Addressing the Challenges of Advanced Compression Ignition Strategies using Optimization Techniques with Machine Learning

By

Naga Krishna Chaitanya Kavuri

A dissertation submitted in partial fulfillment of

the requirements for the degree of

Doctor of Philosophy

(Mechanical Engineering)

at the

UNIVERSITY OF WISCONSIN – MADISON

2018

Date of Final Oral Examination: 02/05/2018

The dissertation is approved by the following members of the Final Oral Committee:
Sage L. Kokjohn, Assistant Professor, Mechanical Engineering
Jaal B. Ghandhi, Grainger Professor of Sustainable Energy, Mechanical Engineering
Christopher J. Rutland, Phil and Jean Myers Professor, Mechanical Engineering
David A. Rothamer, Associate Professor, Mechanical Engineering
James J. Schauer, Professor, Civil and Environmental Engineering

Abstract

Advanced compression ignition strategies like reactivity controlled compression ignition (RCCI) and gasoline compression ignition (GCI) have received substantial interest over the past few years. This is due to their potential to achieve reduced emissions, and higher efficiency, relative to conventional diesel combustion. However, most of the benefits seen in past research from these strategies were demonstrated under mid-load conditions. For these strategies to be implemented practically, similar benefits must be demonstrated across the drive cycle. Two particularly challenging areas of operation are high-load-low-speed and low-load-high-speed. Very limited research has been done with advanced compression ignition strategies in these points of the engine operating map. The reason for this is, at these operating conditions, there exists a mismatch between engine and chemistry time scales. The time scale mismatch results in either increased pressure rise rates or high levels of incomplete combustion, both of which make it difficult to operate. The work presented in this dissertation attempts to fill in these research gaps by using a combination of computational fluid dynamics modeling and genetic algorithm optimization.

Initially, targeting high-load-low-speed conditions, a computational optimization study was performed at 20 bar indicated mean effective pressure and 1300 rev/min. with RCCI and GCI combustion strategies. The study was performed on a low compression ratio (12:1) piston with a "bathtub" geometry, since it was found to be well suited for high-load operation in earlier studies. The optima from the two combustion strategies were compared in terms of combustion characteristics, combustion control, and sensitivity to operating parameter variations. The results showed that both the strategies have similar combustion characteristics, including a two-stage heat release. A near top dead center injection initiated the combustion and its injection timing could be used to control the combustion phasing for both the strategies. Both the strategies required elevated levels of exhaust gas recirculation (EGR) (~55%) at a near stoichiometric global equivalence ratio to control the peak pressure rise rate. This resulted in high sensitivity to variations in EGR. To address this issue, high-load strategies at reduced EGR levels were investigated.

A constraint analysis was performed using the optimization data to identify the constraints preventing operation at lower EGR levels. Results showed that operation at lower EGR rates was

constrained by NOx emissions. Relaxing the NOx constraint enabled lower EGR operation with significant efficiency improvement. Allowing NOx emissions to increase to acceptable levels for selective catalytic reduction after treatment yielded an optimum at a moderate (~45%) level of EGR and a globally lean equivalence ratio of 0.8. This optimum case had near zero soot emissions and a higher net fluid efficiency (which accounted for the pumping loop work and the diesel exhaust fluid mass required to reduce the NOx emissions) compared to the earlier high EGR optima. Furthermore, the optimum case with NOx aftertreatment was compared with the high EGR optima in terms of combustion control and stability to operating condition fluctuations. The optimum with NOx aftertreatment retained the excellent combustion control seen with the high EGR optima, while reducing the sensitivity to operating parameter variations. The improved stability was attributed to operation at a reduced global equivalence ratio (from 0.93 to 0.8), which decreased the sensitivity to fluctuations in EGR rate.

After addressing the issues at the high-load-low-speed operating condition, a low-load-high-speed operating point of 2 bar and 1800 rev/min. was simulated on the same engine used for the high-load studies. The results showed poor thermal efficiency for the low-load point. The poor efficiency was found to be due to an elevated level of incomplete combustion, which was a result of the low compression ratio piston used for the study. This result suggested that an optimum compression ratio should be identified considering the performance at the low-load and high-load conditions simultaneously. In addition, past optimization studies performed at low-load conditions have shown that the optimum bowl and injector design are very different compared to the high-load conditions. Accordingly, an optimization study was performed, considering performance at low- and high-load simultaneously. The optimum from the study was a stepped bowl geometry, with a compression ratio of 13.1:1, which resulted in a gross indicated efficiency of ~46% at both the loads. The study showed that the optimum design obtained from prioritizing one load deteriorates the performance at the other load. The results highlight the importance of considering multiple modes of the drive cycle simultaneously, when optimizing the engine design for advanced combustion strategies.

It was shown that multiple modes of the drive cycle should be considered in optimization studies for advanced combustion strategies; however, the optimization with just two operating points took three months to complete. To consider all the modes of a drive cycle in the optimization, the computational time must be reduced. To address this issue, machine learning through Gaussian process regression was coupled with a genetic algorithm optimization to speed up the optimization process. Including machine learning within the optimization process reduced the computational time of optimization by 62%. The optimization process was further improved by using the Gaussian process regression model to check for the sensitivity of the designs to operating parameter variations during the optimization. The approach was tested with existing optimization data and it was shown that adding the stability check resulted in a reliable and stable optimum solution.

Acknowledgements

I would like to thank my advisor Prof. Sage Kokjohn, for his constant support and advice over the past four years. He took me as his student despite my limited knowledge in engine research and I have learnt a lot under his guidance. It was his extensive knowledge and expertise in combustion modeling and optimization techniques that made this work possible. I am forever indebted to him for everything he has taught me as part of my PhD research. In addition, I would like to thank Prof. Christopher Rutland, Prof. Jaal Gandhi, Prof. David Rothamer and Prof. James Schauer for all their valuable suggestions and insights during my preliminary exam which has helped in the progress of my research.

I would also like to thank my Masters advisor at Carnegie Mellon University, Prof. Satbir Singh. When I started my Masters, I was unsure about what area of research interested me and it was after working with Satbir that I grew fond of engine research. When I wanted to pursue a PhD in this field, it was Satbir who suggested applying to the Engine Research Center (ERC) at University of Wisconsin-Madison.

This work would not have been possible without the financial support from Caterpillar Inc. Furthermore, the comments and inputs from Adam Dempsey, Chad Koci, John Bobby and Christopher Gehrke during our weekly meetings have been very helpful in providing direction to my research.

During my PhD, I have met several interesting people at ERC who have become good friends. I would particularly like to thank Dr. Jae Lim (currently at Ford Motor Company) and David Klos (currently at Space X) who were one of the first people I interacted with when I started at ERC. Jae and David took time out of their research and helped me get up to speed with the KIVA code and GA optimization which I later used extensively in my research. Throughout my research, I have used a lot of experimental data to validate the computational models. This data was provided to me, from the single cylinder experiments, run by Mike Tiry (currently at Harley Davidson) and Jordan Paz (currently at Bosch), for which I am very grateful. I also want to thank Flavio Chuahy who has helped me numerous times to fix errors in my MATLAB and KIVA codes and for taking time to discuss ideas related to my research. Special mention goes to my fellow lab mates Tyler Strickland, Arun Ravindran and Dr. Anand Nageswaran Bharath (currently at Cummins) with whom I had several insightful discussions regarding combustion research.

None of my computational work would have been possible without the help of Joshua Leach. He works throughout the day to keep the computer systems and the servers running for which I am extremely thankful. I also would like to thank Dr. Randy Hessel for taking time to organize the seminars every Tuesday. I have learnt a lot from the seminars, by listening to other students present their research.

Over the past four years, I have made many wonderful friends at Madison. A big thank you to my Madison buddies, Ayushi, Abhinav, Chai, Mrunmayi, Ishanti, Rahul and Arjun for all the game nights and outings, which I am sure to miss when I leave Madison. A big hug to my best friends Shravya, Mrudula, Shalini, Tanuja and Khyati. They have been my family away from home. Our regular phone conversations, the numerous trips we made and continue to make, have always kept me happy and strong throughout my PhD.

Most importantly I would like to thank my family. My mom, Vijaya Lakshmi, and dad, Dr. Gopala Rao, who have been my biggest support system. Everything I am and have achieved till date is because of them. They have always encouraged me to pursue my interests and have never hesitated in providing me the means to achieve my goals. They have patiently cheered me when my research was not going as expected and kept me motivated. I would also like to thank my brother Giri and my sister-in-law Souju. They have helped me since the time I have come to USA, and never made me miss my family and home. I will be forever grateful to them for this.

The work presented in this dissertation is dedicated to my late grandmother, Ammaji, who expired during my PhD. She raised me since I was a child and has dreamed of seeing me with my doctorate degree. She was a strong motivation for me throughout my research and will continue to be, for the rest of my life.

Table of Contents

Abstract	i
Acknowledgements	iv
List of Figures	x
List of Tables	xvii
List of Publications	xix
Nomenclature	xxvi
Chapter 1 Introduction	1
1.1 Motivation and Background	1
1.2 Key Contributions	4
Chapter 2 Literature Review	5
2.1 Advanced Combustion Strategies	5
2.2 GA for Engine Optimization	12
2.3 Machine Learning in Engine Optimization	16
2.4 Problems Identified from Past Research	18
2.4.1 Issues at Low-Load-High-Speed Operating Condition	19
2.4.2 Issues at High-Load-Low-Speed Operating Condition	19
2.4.3 Issues with Optimization Techniques	20
2.5 Objectives and Approach	20
Chapter 3 Setup and Model Validation	22
3.1 Engine Specifications	22
3.2 Model Description	23
3.2.1 Combustion Model	24
3.2.2 Emissions Model	24
3.2.3 Spray Model	26
3.3 Genetic Algorithm Optimization	28
3.3.1 MOGA (NSGA-II)	28
3.3.2 Single Objective GA (DK-GA)	30
3.4 Model Validation	31
3.4.1 Model Validation with CDC	32
3.4.2 Model Validation with RCCI	34
3.4.3 Model Validation with GCI	39
3.4.4 Summary of Model Validation	44
Chapter 4 Optimization Targeting High-Load-Low-Speed Operation	46

4.1 Operating Conditions and Optimization Setup	46
4.2 Results and Discussion	48
4.2.1 Experimental Validation	51
4.2.2 RCCI-GCI Comparison	53
4.2.2.1 Combustion Characteristics	53
4.2.2.2 Control Parameters	58
4.2.2.3 Operating Condition Sensitivity	60
4.2.3 Conclusions	62
Chapter 5 Constraint Analysis on High-Load-Low-Speed Operation with RCCI Combustion.	64
5.1 Results	65
5.1.1 Diesel Exhaust Fluid (DEF) Consumption Estimation	68
5.1.2 Effect of removing the NOx constraint on the Optimum at the same EGR Level	71
5.1.3 Comparison of Optimum Strategy at Moderate (45%) and High (55%) EGR	75
5.1.4 Control Parameters	79
5.1.5 Operating Condition Sensitivity	80
5.2 Conclusions	82
Chapter 6 Optimization considering Low-load and High-load Efficiency	83
6.1 Optimization Setup	83
6.2 Results	87
6.2.1 Combustion Characteristics	94
6.2.1.1 Low-Load Combustion Characteristics	94
6.2.1.2 High-Load Combustion Characteristics	97
6.2.2 Mid-Load Operating Condition (9 bar, 1300 rev/min.)	102
6.2.3 Mode Weighting Factor Effect	104
6.3 Conclusions	110
Chapter 7 Machine Learning in Genetic Algorithm Optimization	111
7.1 Gaussian Process Regression (GPR)	113
7.2 GPR in GA Optimization	116
7.2.1 Validation of CFD + GPR Optimization	118
7.3 Uncertainty Quantification using GPR	122
7.3.1 GIE Sensitivity Constants	127
7.3.2 NOx Sensitivity Constants	132
7.3.3 Soot Sensitivity Constants	136
7.3.4 PPRR Sensitivity Constants	140

7.4 Stability Analysis in GA Optimization using GPR	143
7.5 Conclusions	152
Chapter 8 Summary and Future Work	154
8.1 Addressing the challenges at High-Load Low-Speed Operating Condition	154
8.1.1 Optimization at High-Load-Low-Speed Conditions	154
8.1.2 Constraint Analysis of High-Load-Low-Speed Operation with RCCI strategy	155
8.2 Multi-Mode Optimization	156
8.3 RCCI Operating Strategy vs. Load	157
8.4 Machine Learning in GA Optimization	160
8.5 Future Work	161
8.4.1 Machine Learning in Soot Modeling	161
8.4.2 Machine Learning in CFD Modeling	162
8.4.3 Improving Engine Optimization	162
8.4.4 Optimization Study Considering Fuel Effects	163
References	164
Appendix-A Light-Duty Cycle Optimization	172
A.1 Light-Duty Engine	172
A.2 Operating Conditions	173
A.3 Optimization Setup	174
A.4 Results and Discussion.	175
A.4.1 Light-Duty Drive Cycle Modes	175
A.4.2 Cycle Averaged Emissions	181
A.4.3 High-Speed-High-Load Optimization	183
A.5 Conclusions	184
Appendix-B Investigation of Soot Production from a Load Extension Injection	185
B.1 Operating Conditions and Computational Study Setup	185
B.2 Results	186
B.2.1 Effect of Load Extension SOI Timing	186
B.2.2 Effect of EGR	192
B.2.3 Effect of Injection Pressure	194
B.2.4 Feasible Operating Space for Load Extension Injection	196
B.3 Conclusions	198
Appendix-C Thermodynamic Model – Open Cycle Work Calculation	200
C.1 Compressor Calculations	200

C.2 Turbine Calculations	201
Appendix-D Post-Injection Strategies under High-Load Conditions	203
D.1 Operating Conditions	203
D.2 Soot Trends	205
D.2.1 Effect of Dwell Time	206
D.2.2 Effect of Premixed Fuel	209
D.2.3 Effect of Post-Injection	213
D.2.4 Effect of Post-Injection at Low to Mid-Load Conditions	217
D.3 Conclusions	221

T .	c	т.		
List	· ^t	HI10	nır	AC.
шэ	. (/1	1.15	uı	C.3

Figure 1-1.	CO ₂ emissions standard for light and heavy-duty vehicles in the USA from the years 2014 to 2026
Figure 2-1.	Summary of operating conditions covered in earlier RCCI studies
Figure 2-2.	RCCI operating map developed by Curran et al. [43]
Figure 3-1.	Computational mesh for the stock piston shown at top dead center (TDC)
Figure 3-2.	Computational mesh for the bathtub piston shown at TDC
Figure 3-3.	Convergence metric vs. generation for different number of citizens per generation.30
Figure 3-4.	In-cylinder pressure and AHRR comparison between the experiments and simulations for the operating conditions shown in Table 3-3
Figure 3-5.	Comparison of NOx emissions between experiments and simulations for the operating conditions shown in Table 3-3
Figure 3-6.	In-cylinder pressure and AHRR comparison between the experiments (-) and simulations () for the operating conditions shown in Table 3-4
Figure 3-7.	Comparison of NOx and soot emissions between experiments and simulations for the operating conditions shown in Table 3-4
Figure 3-8.	Measured (\circ) and model-predicted (\triangle) soot emissions for EGR-46% and an injection pressure of 1000 bar as a function of load extension injection SOI timing with acetylene(C ₂ H ₂) as inception species for soot model and soot constants of (a) $A_{sf} = 500$ and $E_{sf} = 1250$, (b) $A_{sf} = 25$ and $E_{sf} = 2000$, and (c) $A_{sf} = 1900$ and $E_{sf} = 2000$
Figure 3-9.	NOx and soot emissions comparison between model and experimental data 38
Figure 3-10.	AHRR comparison between model and experiments. The AHRR is separated into primary (top) and secondary (bottom) heat release rate to highlight the agreement of the model predictions with the experiments for the secondary heat release rate 39
Figure 3-11	. Comparison of cylinder pressure and AHRR for the post-injection strategy with the premixed fuel across all the operating conditions studied
Figure 3-12	. Comparison of cylinder pressure and AHRR for the post-injection strategy without the premixed fuel across all the operating conditions studied
Figure 3-13	. Comparison of cylinder pressure and AHRR for the 'no post injection' strategy across all the operating conditions studied
Figure 3-14	. Comparison of GIE, NOx and soot emissions for the three injection strategies across all the operating conditions studied
Figure 3-15	. CFD predicted results vs. the experimental results over the range of operating conditions covered during model validation
Figure 4-1.	Injection strategy for RCCI and GCI combustion used in the optimization study 47 $$
Figure 4-2.	Comparison of contours of GIE and NIE generated from the best cases for RCCI and GCI strategies at each Φ -EGR combination
Figure 4-3.	Comparison of COSSO predicted and KIVA simulated results for the optima 51

Figure 4-4.	Measured and CFD predicted cylinder pressure and apparent heat release rate for the RCCI and GCI optimum points
Figure 4-5.	Comparison of measured and CFD predicted results for RCCI and GCI optimum points
Figure 4-6.	In-cylinder evolution of key species for RCCI and GCI optimum strategies 54
Figure 4-7.	In-cylinder temperature, equivalence ratio, mass fraction of iso-octane, formaldehyde, and OH contours for the optimum RCCI point
Figure 4-8.	In-cylinder temperature, equivalence ratio, mass fraction of iso-octane, formaldehyde, and OH contours for the optimum GCI point
Figure 4-9.	Φ-T plots of the in-cylinder mixture at various crank angles after start of combustion (°ASOC) for the optimum RCCI and GCI combustion strategies. The symbols show the equivalence ratio, and temperature in each computational cell and the lines show NOx (lower right on each diagram) and soot (upper right on each diagram) islands
Figure 4-10	. Combustion phasing (CA50) as a function of inputs for the RCCI and GCI strategies
Figure 4-11	. In-cylinder temperature and equivalence ratio contours for the GCI strategy at three different premix fraction values
Figure 4-12	Experimental and model predicted CA50 as a function of SOI-Diesel and SOI2-Gasoline for the RCCI and GCI strategies
Figure 4-13	. Sensitivity of outputs to changes in inputs for RCCI and GCI strategies 62
Figure 4-14	. Ignition delay vs. 1000/T from constant volume simulations
Figure 5-1.	Comparison of GIE and NIE for cases with all constraints (NOx, soot, and RI) intact, no NOx constraint and no Soot constraint at each EGR and Φ combination.
Figure 5-2.	Comparison of contour plots of NIE and ΔNIE% between the cases with all constraints intact, no NOx constraint and no Soot constraint
Figure 5-3.	Plot showing the dominant constraining factors and the boundaries within which removing the constraint results in an improved NIE in the EGR and Φ operating space
Figure 5-4.	Contours of NFE compared between cases with all constraints intact and cases with no NOx constraint
Figure 5-5.	Contours of NOx, DEF mass consumed and the % efficiency lost to DEF consumption for the cases with no NOx constraint
Figure 5-6.	NFE, NOx and soot emissions as a function of SOI-Diesel for the case with the NOx constraint shown in Table 5-1
Figure 5-7.	NFE, DEF mass consumed and PP as a function of SOI-Diesel for the case without the NOx constraint shown in Table 5-1
Figure 5-8.	Comparison of in-cylinder pressure and AHRR for the two best cases shown in Table 5-1

Figure 5-9. Comparison of EER for the two best cases shown in Table 5-1
Figure 5-10. Comparison of energy flow for the two best cases shown in Table 5-2
Figure 5-11. Comparison of in-cylinder pressure and AHRR for the two best cases shown in Table 5-2
Figure 5-12. Comparison of in-cylinder contours of temperature, Φ, and soot mass fraction at various CA for the two best cases shown in Table 5-2
Figure 5-13. Soot (-) and O ₂ () mass as a function of CA for the two best cases shown in Table 5-2
Figure 5-14. CA50 as a function of inputs for the two best cases compared in Table 5-2 80
Figure 5-15. Comparison of results from the operating condition sensitivity study for the two cases shown in Table 5-2
Figure 6-1. Examples of bowl geometries that can be generated using the bowl geometry code of Lopez et al. [101]
Figure 6-2. Injection strategy used for the optimization study
Figure 6-3. CR as a function of the run number.
Figure 6-4. Optimum piston geometry
Figure 6-5. Injector design parameters as a function of the run number
Figure 6-6. Fueling and air-handling parameters as a function of run number for low-load 90
Figure 6-7. Fueling and air-handling parameters as a function of run number for high-load 92
Figure 6-8. Outputs as a function of run number for low-load
Figure 6-9. Outputs as a function of run number for high-load
Figure 6-10. In-cylinder pressure () and apparent heat release rate (-) for the low-load optimum point
Figure 6-11. In-cylinder Φ, temperature and PRF contours at different crank angles before and after the combustion event for the low-load optimum point95
Figure 6-12. CA50, the percentage of energy in incomplete combustion, NOx emissions, and NFE as a function of EGR for the low-load optimum point
Figure 6-13. In-cylinder evolution of key species, in-cylinder pressure () and apparent heat release rate (-) for the high-load optimum case
Figure 6-14. In-cylinder temperature, Φ , mass fraction of iso-octane, n-heptane, formaldehyde and OH contours for the high-load optimum case
Figure 6-15. In-cylinder evolution of soot emissions, oxygen, average and peak temperature, and injection velocity profiles for the high-load optimum case
Figure 6-16. Comparison of NFE and PPRR of the optimum case with Case-1 (DI-Diesel added to premixed gasoline) and Case-2 (DI-Diesel added to DI-Gasoline)
Figure 6-17. NFE and soot emissions as a function of gasoline fraction for a fixed premixed fuel mass
Figure 6-18. Energy Flow vs. IMEP for the optimum cases

Figure 6-19	. Comparison of COSSO predicted output (y-axis) to KIVA output (x-axis)	104
Figure 6-20	. Comparison of COSSO predicted and KIVA simulated results for the optima	107
Figure 6-21	. Optimum bowl geometries for the three mode weights	108
Figure 6-22	. GIE and NFE vs. IMEP for different W_{mode} values.	109
Figure 7-1.	COSSO and KIVA predicted results of NOx and Soot emissions as a function of SOI-Diesel. The blue box highlights the center point design used to generate the COSSO response function.	
Figure 7-2.	Response function of the exponential kernel evaluated at different values of the kernel parameter σ_m .	114
Figure 7-3.	Response function of the exponential kernel evaluated at different values of the kernel parameter σ_f .	115
Figure 7-4.	Flowchart outlining the CFD+GPR approach for GA optimization	116
Figure 7-5.	Injection strategy used for the GA optimization study	118
Figure 7-6.	Comparison of GPR predicted output (y-axis) to KIVA predicted output (x-axis) the Latin hypercube DOE dataset	
Figure 7-7.	Fraction of total runs that were estimated with CFD and with the GPR model for GA with the CFD+GPR approach.	
Figure 7-8.	Comparison of the time taken to complete the 50 generations of the GA between GA run completely with CFD and the GA run with the CFD+GPR approach	
Figure 7-9.	Comparison of GPR predicted output (y-axis) to KIVA predicted output (x-axis)	124
Figure 7-10	. Input variable corresponding to the top five SCs of GIE for (a) CDC, (b) RCCI, (c) GCI combustion strategies	
Figure 7-11	. Trends of GIE from the GPR model and CFD for the top four SCs of (a) CDC, (RCCI, and (c) GCI combustion strategies	
Figure 7-12	. Φ contours at various crank angles after SOI (°aSOI) compared between cnst22 10 and cnst22 of 80 for the three combustion strategies	
Figure 7-13	. Incomplete combustion [%] as a function of cnst22 [-] for CDC, RCCI, and GCI strategies.	
Figure 7-14	. GIE and CA50 as a function of EGR and CR for the RCCI and GCI strategies	131
Figure 7-15	. Input variable corresponding to the top five SCs of NOx emissions for (a) CDC, RCCI, and (c) GCI combustion strategies	
Figure 7-16	Trends of soot emissions from the GPR model and CFD for the top four SCs of CDC, (b) RCCI, and (c) GCI combustion strategies.	
Figure 7-17	. Contours of Φ , temperature and mass fraction of NOx emissions for rsc of 1.1 a rsc of 1.5 cases for the CDC strategy	
Figure 7-18	. Contours of temperature and mass fraction of NOx emissions for rpr of 1.1 and of 1.5 cases for the CDC strategy.	

Figure 7-19.	Input variable corresponding to the top five SCs of soot emissions for the (a) CDC, (b) RCCI, and (c) GCI combustion strategies
Figure 7-20.	Trends of soot emissions from the GPR model and CFD for the top four SCs of the (a) CDC, (b) RCCI, and (c) GCI combustion strategies
Figure 7-21.	Φ-T plots of in-cylinder charge for EGR of 53% and EGR of 57% for the RCCI case. Soot islands are shown at the top right corner of the plot in red, and the NOx islands are shown at the bottom right corner of the plot in blue
Figure 7-22.	Contours of Φ and mass fraction of soot emissions for the dS of 2 mm and dS of 4 mm cases for the CDC strategy
Figure 7-23.	Input variable corresponding to the top five SCs of PPRR for the (a) CDC, (b) RCCI, and (c) GCI combustion strategies
Figure 7-24.	Trends of PPRR from the GPR model and CFD for the top four SCs of the (a) CDC, (b) RCCI, and (c) GCI combustion strategies
Figure 7-25.	Flowchart outlining the stability analysis in GA optimization. This procedure is applied individually to every citizen of the GA
Figure 7-26.	Evolution of the standard deviation of all the outputs of interest as a function of the run number for the GA (left) without and (right) with the stability check 148
Figure 7-27.	Standard deviation of the output variables with respect to fluctuations in the input variables for the optimizations (top) without and (bottom) with the stability check
Figure 7-28.	GIE, Incomplete Combustion, and PPRR as a function of EGR fluctuation 150
Figure 7-29.	Soot emissions vs. EGR fluctuation for the optimum case with the stability check
Figure 8-1.	Summary of RCCI strategies as a function of nominal gross IMEP 158
Figure 8-2.	Global Φ as a function of IMEP
Figure A-1.	Computational grid used for the light-duty cycle simulations
Figure A-2.	Injection strategies considered in the two RCCI drive cycle optimizations. The simulations considered the port-injected or valve overlap injected fuel fully premixed at intake valve closure
Figure A-3.	GIE and combustion efficiency – NOx tradeoff for the optimization at Mode 1 (2 bar IMEP and 1500 rev/min.)
Figure A-4.	Energy flow diagram for the optimum cases at Mode 1 (2 bar IMEP and 1500 rev/min.) with a single gasoline injection and split gasoline injection. All cases use DI of diesel fuel. The operating conditions are shown in Table A-4
Figure A-5.	Mode 1 in-cylinder pressure and AHRR for the optimum single gasoline injection case, optimum split gasoline injection case, and split gasoline injection case with the direct-injected gasoline premixed
Figure A-6.	Contours of in-cylinder Φ for the single gasoline injection and split gasoline injection RCCI cases at Mode 1. The contours are shown on a cut-plane coincident with the spray axis.

Figure A-7.	Effect of gasoline mass on GIE, combustion efficiency, and NOx emissions at Mode 1 calculated using the COSSO method. The lines show COSSO predicted response and the symbols show the optimum solutions from the CFD study
Figure A-8.	Cycle averaged performance and emissions for RCCI combustion using DI gasoline (ADF-RCCI) and diesel fuel and the baseline conventional diesel combustion case
Figure B-1.	Measured (\circ) and model predicted (\triangle) soot emissions for EGR-46% and an injection pressure of 1000 bar using E0 fuel as a function of load extension injection SOI timing. The measured and simulation data are shown in symbols, and the lines show spline interpolation. The error bars are based on a 97.5% confidence interval from multiple repeats for the experiments with EGR- 30% and an injection pressure of 1000 bar
Figure B-2.	Φ-T plots of the in-cylinder mixture at various crank angles after start of injection (°ASOI) for two load extension injection SOI timings at EGR-46% and injection pressure of 1000 bar. The symbols show the equivalence ratio, and temperature in each computational cell and the lines show NOx (lower right on each diagram) and soot (upper right on each diagram) islands calculated using HCCI simulations at the operating conditions of the present study
Figure B-3.	Φ-T diagrams of the in-cylinder mixture at various crank angles after start of combustion (°ASOC) of premixed fuel for two load extension injection SOI timings at EGR-46% and an injection pressure of 1000 bar. The symbols show the equivalence ratio, and temperature in each computational cell and the lines show NOx (lower right on each diagram) and soot (upper right on each diagram) islands calculated using HCCI simulations at the operating conditions of the present study
Figure B-4.	Soot mass formed and oxidized for the load-extension injection SOI timing sweep at EGR-46% and an injection pressure of 1000 bar
Figure B-5.	In-cylinder images of soot, Φ, and temperature for the load-extension injection SOI timings of -10 °aTDC, 20 °aTDC and 25 °aTDC at EGR-46% and injection pressure of 1000 bar
Figure B-6.	Measured (○,♦) and predicted (△,□) soot emissions for EGR-46% and EGR-30% using E0 fuel as a function of load extension SOI timing at an injection pressure of 1000 bar. The measured and simulation data are shown in symbols, and the lines show spline interpolation. The error bars show 97.5% confidence intervals for the EGR-30% from randomly ordered repeats on different days
Figure B-7.	Soot mass formed and oxidized for the load-extension injection SOI timing sweep at EGR-46% and EGR-30% at an injection pressure of 1000 bar
Figure B-8.	Measured (○,♦) and predicted (△,□) soot emissions for injection pressures of 1000 bar and 1500 bar for EGR-46% using E0 fuel. The measured and simulation data are shown in symbols, and the lines show spline interpolation. The error bars are based on a 97.5% confidence interval from multiple repeats for the experiments with EGR-30% and an injection pressure of 1000 bar

Figure B-9.	Φ-T diagrams of the in-cylinder mixture at various crank angles after start of injection (°ASOI) for injection pressures of 1000 bar (left) and 1500 bar (right) at EGR-46% and SOI = -10 °ATDC. The symbols show the equivalence ratio, and temperature in each computational cell and the lines show NOx (lower right on each diagram) and soot (upper right on each diagram) islands calculated using HCCI simulations at the operating conditions of the present study
Figure B-10	Residence time (CA) of the in-cylinder charge in various temperature ranges for the EGR-46% case and E0 fuel at injection pressures of 1000 bar and 1500 bar and SOI = 25 °aTDC
Figure B-11	Contours of GIE, NOx, and soot emissions as a function of EGR and SOI timing at an injection pressure of 1500 bar using E0 fuel
Figure B-12	Regions in EGR-SOI operating space which meet constraints of NOx $<$ 2 g/kg-f, FSN $<$ 2 and GIE $>$ 40%. The regions are colored by contours of GIE
Figure C-1.	Layout of the air-handling system for open cycle work calculation. Known values are shown in red font
Figure D-1.	Summary of the injection strategies investigated in the current study
Figure D-2.	Experiment and CFD predicted soot emissions vs. gross IMEP for all the cases studied. Post-injection cases with premixed fuel shown as solid lines with filled markers and post-injection cases without premixed fuel shown as dashed lines with unfilled markers
Figure D-3.	CFD predicted trends for the post-injection cases with premixed fuel. The blue box highlights the cases that will be used to explain the soot trends as a function of the dwell time
Figure D-4.	Φ and soot emissions contours for the three cases highlighted in Figure D-3 208
Figure D-5.	CFD predicted trends for the post-injection SOI timing of 25 °aTDC cases with and without the premixed fuel. The blue box highlights the cases that will be used to explain the soot trends as a function of the dwell time
Figure D-6.	$\boldsymbol{\Phi}$ and soot emissions contours for the two cases highlighted in Figure D-5 212
Figure D-7.	Trends of soot formation, oxidation and production as a function of CA for the post-injection cases with (-) and without () premixed fuel compared in Figure D-6. 213
Figure D-8.	CFD predicted trends for the post-injection SOI timing of 16 °aTDC cases without the premixed fuel and the cases without the post-injection. The blue box highlights the cases that will be used to explain the soot trends as a function of the dwell time.
Figure D-9.	$\boldsymbol{\Phi}$ and soot emissions contours for the two cases highlighted in Figure D-8 214
Figure D-10	. Trends of soot formation, oxidation, and production as a function of CA for the no post-injection case (-) and the post-injection case without premixed fuel () compared in Figure D-9
Figure D-11	. Soot emissions results from the baseline and the post-injection strategy of the current study and the results seen from the study by O'Connor et al. [115] 218
Figure D-12	. Φ and soot emissions contours for the two cases highlighted in Figure D-11 220

List of T	ables
Table 1-1.	Tier 3 emissions standards of criteria pollutants for light-duty vehicles
Table 3-1.	Engine and injector specifications
Table 3-2.	Soot model constants used based on the inception species
Table 3-3.	Operating conditions for model validation with the CDC strategy
Table 3-4.	First set of operating conditions for model validation with the RCCI strategy 34
Table 3-5.	Second set of operating conditions for model validation with the RCCI strategy 36
Table 3-6.	Operating conditions for model validation with the GCI strategy
Table 4-1.	Φ-EGR matrix for optimization setup. The values shown at each $Φ$ -EGR location are the corresponding IVC pressures in bar. 47
Table 4-2.	Range of variation allowed for each design parameter in the optimization study 48
Table 4-3.	Comparison of optimum points for the RCCI and GCI strategies 51
Table 4-4.	Range of variation of inputs for the RCCI and GCI parametric study 58
Table 4-5.	Baseline value and the range of fluctuation of each operating condition
Table 5-1.	Best cases without the NOx constraint and with the NOx constraint at a similar level of EGR
Table 5-2.	Comparison of the best case from the cases with no NOx constraint and the high EGR GA optima from Chapter 4
Table 5-3.	Range of variation of inputs for the combustion control parametric study of the two cases shown in Table 5-2
Table 5-4.	Baseline value and the range of fluctuation of each operating condition, for the two cases shown in Table 5-2
Table 6-1.	Range of variation allowed for each design parameter in the optimization study 84
Table 6-2.	Constraint value and harshness factor assigned to each output
Table 6-3.	Optimized design variables for low-load and high-load
Table 6-4.	Outputs for the optimized design at low-load and high-load
Table 6-5.	Design inputs and results for the mid-load condition of 9 bar and 1300 rev/min \dots 103
Table 6-6.	Optimized inputs for low-load and high-load at different W_{mode} values
Table 6-7.	Optimized outputs for low-load and high-load at different W_{mode} values
Table 7-1.	Kernel functions explored, their functional forms and the R ² values for the fits between the GPR and the CFD predictions for the GIE, NOx, Soot and PP outputs
Table 7-2.	Range of variation allowed for each design parameter in the optimization study used to evaluate the potential of combining the GA with the GPR approach
Table 7-3.	Comparison of the optimum points from the GA with CFD and GA with the CFD+GPR approaches

Table 7-4.	Summary of the input parameters in the DOE for CDC, RCCI, and GCI strategies
Table 7-5.	Input variables with the maximum sensitivity constants for each output for the CDC, RCCI and GCI strategies
Table 7-6.	Fluctuations set for each input variable and the constraints set for the standard deviation of each output variable
Table 7-7.	Comparison of the optimum value from the GA without and with the stability check.
Table A-1.	Engine and injector specification for the light-duty cycle optimization study 173
Table A-2.	Operating conditions and the relative weights of each mode chosen for study 173
Table A-3.	Range of variation allowed for each design parameter used in the GA optimization
Table A-4.	Summary of best results from the optimization and comparison of the optimum RCCI results with CDC results of the corresponding mode. The emissions are shown on a gross indicated basis, and the GIE is defined as the (gross indicated work) / (fuel energy).
Table A-5.	Range of variation allowed for each design parameter in the high-load GCI optimization
Table A-6.	Optimum operating conditions for GCI combustion 16 bar IMEP and 2500 rev/min
Table B-1.	Operating conditions for each parametric study
Table D-1.	Summary of operating conditions for the injection strategies shown in Figure D-1.
Table D-2.	Operating conditions for the study at low to mid-load conditions

List of Publications

There were several publications produced as a part of the research work presented in this dissertation. The list of publications with a short summary of each publication is presented in this section.

1) **Kavuri, C., Kokjohn, S.L., Klos, D.T., and Hou, D.,** Blending the Benefits of Reactivity Controlled Compression Ignition and Gasoline Compression Ignition Combustion using an Adaptive Fuel Injection System, *Int. J. Eng. Res.*, 2016, 17(8), 811-824.

This publication addresses the challenges of operating at low-load conditions with advanced combustion strategies. From an optimization study performed over the light-duty cycle, the study showed that using direct-injection of gasoline avoids formation of overly lean regions that require overly advanced combustion phasing to achieve complete combustion. This enables operation across the light-duty drive cycle with a high cycle-averaged gasoline quantity (91%); thereby enabling the second fuel (diesel fuel in this work) to be treated as an additive with the potential to be filled at oil change intervals.

2) **Kavuri, C., and Kokjohn, S.L.,** Investigating Air-handling Requirements of High-Load Low Speed Reactivity Controlled Compression Ignition (RCCI) Combustion, *SAE Technical Paper 2016-01-0782*, 2016.

This study was performed to fully study the effects of air-handling at high-load, low-speed conditions for RCCI combustion. Through individual optimization studies performed at 20 bar and 1300 rev/min. for different levels of EGR and intake pressure, it was shown that the efficiency increases with increasing EGR and intake pressure. At the low EGR rates, to control the PPRR, the operating strategy had low premixed gasoline fuel and a post TDC direct-injection of gasoline which burned in a mixing controlled heat release, resulting in the tradeoff between soot and NOx emissions. As the EGR rate increased, the chemistry time scales became longer, allowing increased premixed gasoline, resulting in higher efficiencies. After considering the pumping loop work, it was shown that increasing the EGR and global Φ beyond 55% and 0.9, respectively, causes the net indicated efficiency (NIE) to decrease due to a high pumping loop penalty; thereby indicating an optimum in this range of EGR and intake pressures.

3) Kavuri, C., Paz, J., and Kokjohn, S.L., A Comparison of Reactivity Controlled Compression Ignition (RCCI) and Gasoline Compression Ignition (GCI) Strategies at High-Load, Low Speed Conditions, *Energy Conversion and Management*, 2016, 127 (1), 324-341.

This work was a continuation of the work presented in the SAE publication. Since, the optimum operating strategies for RCCI combustion had high gasoline percentages; a similar study was repeated with GCI combustion which resulted in similar optimum operating strategies as RCCI combustion. The work presented in this publication compares the optimum RCCI and GCI operating strategies at the high-load, low speed operating condition of 20 bar and 1300 rev/min., in terms of combustion characteristics, combustion control and stability to fluctuations in operating conditions. Results showed that both the strategies have similar combustion characteristics, with a near TDC injection initiating the combustion followed by a two-stage heat release for both the strategies. The RCCI strategy was found to have superior control over combustion due to the shorter ignition delay of diesel fuel over gasoline but also resulted in higher soot emissions compared to the GCI strategy. In terms of stability to operating condition fluctuations, both strategies were found to be extremely sensitive to EGR fluctuations, with the RCCI strategy showing higher stability than the GCI strategy.

4) Kavuri, C., and Kokjohn, S.L., Combustion Stability-NOx Tradeoff: Pathway to Stable High-Load Operation with Reactivity Controlled Compression Ignition (RCCI), *Proc. Inst. Mech. Eng. D: J. Auto. Eng.*, 2017 (Submitted).

This publication furthers the high-load research by addressing the issues of sensitivity to EGR fluctuations observed with the optimum operating strategy from the high-load RCCI optimization study. The sensitivity was found to be due to operating at high levels of EGR (~55%) with a near stoichiometric global Φ . The optimum strategy was identified under the constraints of NOx \leq 2g/kg-f, Soot \leq 2g/kg-f and ringing intensity (RI) \leq 5 MW/m². In the present study, the impact of these constraints on lower EGR operation is investigated to identify pathways for improving the efficiency at lower EGR rates. Results showed that the operation at lower EGR levels was mainly constrained by the NOx emissions. Relaxing the NOx constraint enables lower EGR operation with significant efficiency improvement. Allowing NOx emissions to increase to acceptable levels for selective catalytic reduction (SCR) after treatment, yielded an optimum at a moderate (~45%) level of EGR that had near zero soot emissions and higher net fluid efficiency (NFE) (which accounts for the pumping loop work and the diesel exhaust fluid (DEF) mass required to reduce the NOx emissions) compared to the previous high EGR optima. The optimum strategy at reduced EGR levels,

addressed the issues of high soot emissions and sensitivity to operating condition fluctuations, while retaining the excellent combustion control observed with the earlier high EGR high-load operating strategy.

5) **Kavuri, C., Tiry, M., Paz, J., and Kokjohn, S.L.,** Experimental and Computational Investigation of Soot Production from a Premixed Compression Ignition Engine using a Load Extension Injection, *Int. J. Eng. Res.*, 2016, 18(5-6), 573-590.

The work presented in the earlier publications showed that under high-load conditions, high EGR operation is optimal but unreliable due to the sensitivity to EGR fluctuations. Though lower EGR operation with NOx after treatment is a feasible option, it would be beneficial to understand and address the issues of operating without after treatment at reduced EGR rates. The optimal strategy at low EGR rates identified from the high-load optimization study was a mixed mode combustion strategy which has a premixed heat release (resulting from premixed fuel) followed by a mixing controlled combustion event (resulting from a post TDC load extension injection). However, the soot emissions from the mixing controlled heat release were found to be problematic. The work presented in this publication uses a combination of experiments and CFD modeling to address this issue. Results showed that, when the load extension injection was close to TDC, the soot emissions are highly dependent on the oxygen availability, but as the injection is delayed, the soot emissions become independent of oxygen availability and become solely dependent on in-cylinder temperatures. Thus, despite undergoing locally rich Φ s during the combustion event, due to the low combustion temperatures, the charge does not enter the soot formation region resulting in low soot production. This study provided a pathway for high-load operation, where splitting the load extension injection event into a near TDC injection and a late post TDC injection, allows operation at reduced EGR rates, while meeting the constraints on soot emissions.

6) Kavuri, C., and Kokjohn, S.L., Computational Study to Identify Feasible Operating Space for a Mixed Mode Combustion Strategy: A Pathway for PCI High-load Operation, *ASME ICEF 2017-3668*, 2017.

This publication furthers the research on the mixed mode combustion strategy where the validated computational model was used to study the effects of varying the premixed fuel mass on the results observed from the experimental study. Operating with high premixed fuel mass resulted in improved GIE; however, PPRR was a major constraint, restricting the feasible operating space to a narrow premix fraction (0.6-0.7)

and EGR (> 38%) space. Injecting a portion of the premixed fuel mass as an early stratified injection relaxed the PPRR constraint and allowed operation at higher premix fractions (> 0.7) and lower EGR rates (< 38%). Stratified injection also lowered the soot emissions by providing better access to oxygen for both directinjections, which allowed the load extension injection to be moved closer to TDC while meeting the soot constraint, resulting in improved efficiency. Finally, the results from the study were used to demonstrate high-load operation at 20 bar and 1300 rev/min. at reduced EGR rates and globally lean Φ s while meeting the soot constraints; thereby addressing the issues of instability and high soot emissions observed with the earlier high-load optimum strategy.

7) **Kavuri, C., and Kokjohn, S. L.,** Computational optimization of a reactivity controlled compression ignition (RCCI) combustion system considering performance at multiple modes simultaneously, *Fuel*, 2017, 207(1), 702-718.

The high-load studies were performed on a low CR (12:1) piston whose geometry and CR where optimized for high-load operation. However, using a lower CR piston affected the operation at the low-load conditions by extending the already long chemistry time scales corresponding to these loads, which resulted in high levels of incomplete combustion. This showed that the optimum CR could be different when both the loads are taken into consideration. Additionally, the optimal injector configuration, bowl geometry and air-handling could all be very different considering the large difference in fuel mass associated with the low-and high-load operating conditions. Accordingly, in this publication, an optimization was performed considering performance at low- and high-load simultaneously. The optimum identified from the study was a stepped bowl geometry with a CR of 13.1 that benefited both the loads. The optima had high NFE (42%) with near zero NOx and soot emissions. Additional parametric studies were performed with the GA data, which showed that the optimum design obtained from prioritizing one load deteriorates performance at the other load. The study highlighted the importance of considering multiple modes simultaneously in an optimization, especially when optimizing the engine and injector design.

8) Kavuri, C., Paz, J., Staaden, D., and Kokjohn, S. L., Experimental and Computational Study of Post Injection Strategies for Gasoline Compression Ignition (GCI) Combustion under High-Load Conditions: Understanding the Role of Premixed, Main and Post Injections in Soot Mitigation and Load Extension, *J. Eng. Gas Turbines Power*, 2017 (Submitted).

This publication explored the effectiveness of post injections for GCI combustion, in reducing soot emissions under high-load operating conditions. A combination of engine experiments and CFD modeling was used to isolate and understand the role of premixed, main and post injections in soot mitigation and load extension. The SOI timing of the post injection was also varied to study the effect of dwell time between the main and the post injection on soot emissions. Results showed that adding the post injection was not effective in reducing the soot emissions under high-load conditions due to the long duration of the post injection which extended late into the cycle causing most of the soot formed from the post injection to remain un-oxidized. When a similar study was repeated at mid load conditions, it was found that the post injections showed a benefit in reducing soot emissions. This was because, similar to the high-load conditions, the fuel from the post injection was targeted at a different region in the combustion chamber relative to the main injection, which provided better access to the oxygen to both the main and the post injections. However, compared to high-load conditions, since the duration of the main and the post injection is shorter, it allowed the SOI timing of the post injection to be advanced closer to TDC without overlapping with the main injection. The advanced post injection timing, combined with the shorter duration of the post injection, resulted in the fuel being delivered sufficiently early in the cycle. This provided enough residence time in high temperature regions to oxidize the soot formed from the post injection completely, resulting in reduced soot emissions compared to the case without the post injection.

9) Wissink, M. L., Curran, S. J., Kavuri, C., Kokjohn, S. L., Spray-Wall Interactions in a Small-Bore, Multi-Cylinder Engine Operating with Reactivity-Controlled Compression Ignition, ASME ICEF 2017-3607, 2017.

Experimental work on RCCI in a small-bore, multi-cylinder engine operating on premixed iso-octane and direct-injected n-heptane has shown an unexpected combustion phasing advance at early injection timings, which has not been observed in large-bore engines operating under RCCI at similar conditions. In this work CFD simulations were performed to investigate whether spray-wall interactions could be responsible for this result. Comparison of the spray penetration, fuel film mass, and in-cylinder visualization of the spray from the CFD results to the experimentally measured combustion phasing and emissions provided compelling evidence of strong fuel impingement at injection timings earlier than -90 °aTDC and transition

from partial to full impingement between -65 °aTDC and -90 °aTDC. Based on this evidence, explanations for the combustion phasing advance at early injection timings were proposed along with potential verification experiments.

10) Kavuri, C., and Kokjohn, S. L., Exploring the Potential of Machine Learning in Reducing the Computational Time/Expense for Engine Optimization Studies performed with Computational Fluid Dynamics (CFD) Modeling, *SAE Int. J. Engines*, 2018 (Submitted).

Though the multi-mode optimization study showed the importance of considering multiple operating conditions during optimization to achieve the best output, it took nearly 3 months to complete the GA with 2 operating conditions. To consider all the points of a drive cycle it would take significantly longer. This motivated the need to investigate ways to reduce the computational time of the GA optimization. This publication addresses this issue using machine learning through gaussian process regression (GPR). Initially the effectiveness of GPR in replicating the GA data was studied, by comparing GPR with different kernel functions, using previous high-load GA data. Results showed that GPR with the Matern 3/2 kernel performed the best with R² values greater than 0.95 for all the outputs of interest. Accordingly, GPR with a Matern 3/2 kernel was used in combination with CFD in GA optimizations to speed up the optimization process. After every generation of the GA, the data from the prior generations was used to train the GPR model and then the GPR model was used to predict the outputs for the latest generation. To ensure that the GPR predictions are reliable, the data from a latin hypercube DOE that was run prior to starting the GA was used to validate the GPR model predictions. The optimization study, which took 50 days to complete with CFD, took just 19 days to finish with the CFD+GPR approach with the same amount of computational resources. This study highlights the potential of machine learning in reducing the computational time/expense for engine optimization studies.

11) Kavuri, C., and Kokjohn, S. L., Uncertainity Quantification Applied in Engine Computational Fluid Dynamics (CFD) Modeling: A Comparison of Conventional Diesel Combustion (CDC), Reactivity Controlled Compression Ignition (RCCI) and Gasoline Compression Ignition (GCI) under High-load Low Speed Operating Conditions, *Applied Energy*, 2017 (Submitted).

One major issue with engine optimization studies is the uncertainty in the CFD predictions. The CFD model has a combination of numerical and physical input parameters which are sometimes estimated or

approximated resulting in uncertainty in the CFD predictions. The study presented in this publication uses GPR to quantify the uncertainty arising from each input and helps identify the key input variables the CFD model is sensitive to for a combustion strategy, which provides a pathway to using machine learning with GPR, to achieve reliable optima from engine CFD optimization studies. A total of 39 input variables comprising of numerical and physical inputs were considered and the uncertainty quantification study was performed with CDC, RCCI and GCI strategies under high-load conditions. Results from the study showed that for high-load CDC operation it is important to get the correct injection profile and the mixing field (breakup and transport), to get reliable CFD predictions. For the high-load RCCI and GCI strategies, it is important to get the measurements of CR and the intake conditions (Pivc, Tivc, EGR) correct as even the slightest error would result in large variations in cylinder pressure and emissions predictions.

Nomenclature

Abbreviations

AHRR Apparent heat release rate
ASOC After start of combustion
ATDC After top dead center
BDC Bottom dead center

BMEP Break mean effective pressure

BTDC Before top dead center
BTE Break thermal efficiency
CA50 Crank angle at 50% burn
CARB California air resources board
CDC Conventional diesel combustion
CFD Computational fluid dynamics

CI Compression ignited CO Carbon monoxide

COSSO COmponent Selection and Smoothing Operator

CR Compression ratio
CRIN Common rail injector
DEF Diesel exhaust fluid
DI Direct-injection

DOE Design of experiments
DOI Duration of injection
DPF Diesel particulate filter
DTBP Di-tertiary butyl peroxide
ECN Engine combustion network
EER Effective expansion ratio
EGR Exhaust gas recirculation

EHN Ethyl hexyl nitrate

EPA Environmental Protection Agency

ERC Engine Research Center
EVO Exhaust valve opening
FSN Filter smoke number
FTIR Fourier transform infrared
FTP Federal test procedure
GA Genetic algorithm

GCI Gasoline compression ignition

GDI Gasoline direct-injection
GIE Gross indicated efficiency
GPR Gaussian process regression
GRI Gas Research Institute

HCCI Homogeneous charge compression ignition

HRR Heat release rate

IMEP Indicated mean effective pressureISFC Indicated specific fuel consumption

IVC Intake valve closureKH Kelvin Helmholtz

LDEF Lagrangian drop Eulerian fluid

LES Large eddy simulation
LHV Lower heating value
LNT Lean NO_x trap

LTC Low temperature combustion
MOGA Multi objective genetic algorithm

NFE Net fluid efficiencyNIE Net indicated efficiencyNMOG Non-methane organic gases

NO_x Nitrogen oxides

NSGA Non-dominated sorting genetic algorithm

NTC Negative temperature coefficientPAH Polycyclic aromatic hydrocarbonPCCI Premixed charge compression ignition

PCI Premixed compression ignition

PFS Partial fuel stratification

PID Proportional integral derivative

PM Particulate matter PP Peak pressure

PPC Partially premixed combustion

PRF Primary reference fuel PPRR Peak pressure rise rate

RCCI Reactivity controlled compression ignition

RI Ringing intensity

RNG Re-normalization group RSM Response surface model

RT Rayleigh Taylor SC Sensitivity constant

SCR Selective catalytic reduction

SI Spark ignited SOI Start of injection

SFTP Supplementary federal test procedure

SWP Short wave pass TDC Top dead center

UHC Unburnt hydrocarbons

Chapter 1 Introduction

1.1 Motivation and Background

CO₂ emissions regulations are becoming increasingly stringent. Figure 1-1 [1] shows a trend of CO₂ emissions regulations for light- and heavy-duty vehicles in the United States from the years 2014 to 2026. By 2025, the trend shows an expected reduction in CO₂ emissions of ~33% and 7%, for light- and heavy-duty vehicles, respectively. There also exist stringent standards on criteria pollutants, imposed by the US Environmental Protection Agency (EPA). Table 1-1 [2] shows the Tier-3 emissions standards of non-methane organic gases and nitrogen oxides combined (NMOG+NO_x) and particulate matter (PM) for light-duty vehicles. Compared to current standards, the NMOG and NO_x tailpipe standards represent an 80% reduction on a fleet average basis and the PM standards represent a 70% reduction per-vehicle. For the heavy-duty, on-highway engine, the regulations for NOx and PM are currently 0.2 g/bhp-hr and 0.001 g/bhp-hr, respectively. In 2013, the California Air Resources Board (CARB) established an optional low-NOx heavy-duty standard of 0.02 g/bhp-hr (i.e., 90% below the current regulated levels) [3]. While these standards are currently optional, it is expected that they will become the new standards in the future. These strict emissions regulations have motivated research into developing clean and efficient engines. Additionally, the demand for transportation energy continues to increase and projections show that the increase is skewed towards heavy-fuels (i.e., the demand for diesel fuel is expected to increase, and the demand for gasoline is expected to remain constant or decrease [4]). To simultaneously address the transportation fuel imbalance and the need for engines with high efficiencies that meet the emissions standards, several researchers have proposed gasoline compression ignition (GCI) combustion as a solution.

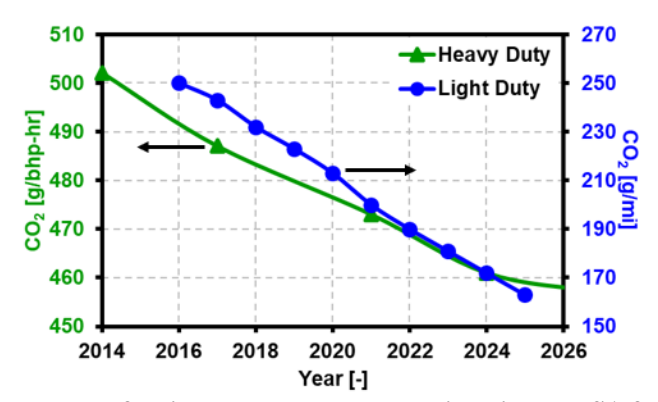


Figure 1-1. CO₂ emissions standard for light and heavy-duty vehicles in the USA from the years 2014 to 2026.

Table 1-1. Tier 3 emissions standards of criteria pollutants for light-duty vehicles.

	NMOG+N	PM (g/mi)		
Test Cycle	FTP	SFTP	FTP	SFTP
2016	160	200	10	10
2025	30	50	3	6
% Reduction	81.25	75	70	40

GCI combustion is a low temperature combustion (LTC) strategy that uses gasoline or other light-fuels in a compression ignition (CI) application. Unlike diesel fuel, the low cetane number of gasoline allows for early cycle injections and higher fuel premixing (dilute mixture). This gives it the potential to achieve high efficiencies with low NO_x and soot emissions. Although GCI combustion has its benefits, several researchers (e.g., Liu et al. [5]) have shown that the low auto-ignition quality of gasoline makes it challenging to achieve combustion at the low-load and cold-start conditions.

An alternative to allowing the use of light-fuels in high efficiency CI engines, while retaining coldstart performance, is the use of dual-fuel engines. Diesel fuel, with its superior auto-ignition qualities compared to gasoline makes combustion at low-loads easily achievable. In a dual-fuel LTC strategy like reactivity controlled compression ignition (RCCI) combustion [6], a blend of low reactivity fuel (e.g., gasoline) and a high reactivity fuel (e.g., diesel fuel) is created in-cylinder. The blend is adjusted, based on the operating condition, to control the combustion phasing. By doing this, the RCCI strategy enables the use of light-fuels in CI engines, while addressing the low-load challenges. In a study comparing RCCI and conventional diesel combustion (CDC) strategies, Kokjohn and Reitz [7] used a design of experiments (DOE) to optimize RCCI combustion in a light-duty engine. They showed that RCCI offers a 4% improvement in fuel consumption and a 7.3% reduction in total fluid consumption. However, the mode weighted gasoline percentage was only 58%. That is, on a full drive cycle, the RCCI engine would consume nearly equal proportions of gasoline and diesel fuel. This result shows that the RCCI strategy might be infeasible for passenger car applications, as it would require two equal sized fuel tanks on board. Also, to achieve operation across the drive cycle, high-load operation must be demonstrated. Several researchers [8, 9, 10] have demonstrated strategies to achieve high-load RCCI operation at loads exceeding 20 bar indicated mean effective pressure (IMEP). These strategies used a low compression ratio (CR) piston, in combination with a mixing controlled combustion strategy (combination of a premixed combustion event and a mixing controlled combustion event), at high intake pressure and exhaust gas recirculation (EGR). However, the use of a low CR piston could affect the efficiencies at low-load and mid-load conditions. Additionally, with the mixing-controlled combustion strategy, the classic tradeoff between soot and NO_x emissions was observed. Furthermore, the use of high intake pressure and EGR increases the pumping losses, which could reduce the gross indicated efficiency (GIE). Based on this discussion, operation at high-load remains a challenge with the RCCI strategy.

From the above discussion, it is understood that despite the benefits shown with advanced combustion strategies like GCI and RCCI combustion, to enable their use in practical engines, challenges at the low-load (~2 bar IMEP) and high-load (~20 bar IMEP) conditions should be addressed. Mainly, at high-loads and low-speeds, or vice versa, there exists a mismatch between the chemistry and the engine time scales (i.e., when one timescale becomes short, the other becomes long based on the load and speed combination). This makes operation under these conditions even more challenging. Accordingly, this dissertation will focus on addressing the challenges of operating with the advanced combustion strategies at the points on an engine operating map where the time scale mismatch exists. A combination of detailed computational fluid dynamics (CFD) modeling and genetic algorithm (GA) optimization will be used to perform the study.

The optimization approaches currently followed are based on the approaches used for the CDC strategy. Several improvements need to be made in the optimization procedure to get the best possible results for advanced combustion strategies. The optimization procedure needs to be modified to enable optimization of multiple operating conditions simultaneously. This is because, unlike the CDC strategy, the advanced combustion strategies are extremely sensitive to CR. As a result, the optimal CR could be completely different at different operating conditions. However, performing optimizations considering multiple operating conditions will be computationally expensive and time-consuming. Therefore, the optimization approach needs to be modified to reduce the computational time and expense. The advanced combustion strategies have also shown higher sensitivity to operating parameter variations relative to CDC

strategies. Hence, it is essential to verify the stability of the optima to fluctuations in operating conditions to ensure reliable and stable optima are obtained. The improvements suggested in the above discussion will be implemented and discussed in more detail in the coming chapters.

1.2 Key Contributions

There are four key contributions from the research presented in this thesis. This section outlines those contributions and the chapters in which they are presented.

- 1. Identifying feasible operating strategies with advanced combustion strategies for high-load-low-speed (Chapter 4, Chapter 5, Chapter 6) and low-load-high-speed operation (Chapter 6, Appendix-A).
- 2. Modifying the optimization approach, to simultaneously optimize multiple modes of the drive cycle (Chapter 6).
- 3. Reducing the computational time of optimization using a combination of machine learning and CFD modeling (Chapter 7).
- 4. Using machine learning in optimization, to check for the stability of the designs to operating parameter variations (Chapter 7).

Chapter 2 Literature Review

2.1. Advanced Combustion Strategies

With the regulations on CO_2 emissions becoming increasingly stringent, diesel engines have become important, due to their superior efficiency potential. However, diesel combustion has issues with controlling soot and NOx emissions, simultaneously [11]. Current diesel engines use after-treatment solutions like lean NOx traps (LNT) [12], selective catalytic reduction (SCR) [13], or a combination of both [14, 15] to reduce NOx emissions. Similarly, diesel particulate filters (DPF) [13] are used to reduce soot emissions. However, these devices either add to the cost of the engine or cause additional fuel consumption [12, 13]. This has motivated research into advanced combustion strategies that aim to eliminate the need for after-treatment devices by reducing the NOx and soot in-cylinder, while achieving diesel-like efficiencies or higher. Most of these advanced combustion strategies can be lumped into one group called LTC. The common theme of LTC strategies is, firstly, to give sufficient time for the premixing of fuel and air. This prevents the formation of fuel rich zones (peak equivalence ratio (Φ) < 2) and avoids soot formation. Secondly, combustion is controlled such that the peak combustion temperatures are low enough (T_{peak} < 2000 K) to avoid NO_x formation. Lastly, the combustion temperatures must be maintained above 1400 K, to avoid low combustion efficiencies.

Several researchers (e.g., [16, 17, 18]) have investigated LTC using diesel fuel. Researchers at Lund University [18] performed an EGR sweep at three different load points of 8 bar, 12 bar and 15 bar IMEP with a partially premixed combustion (PPC) strategy using diesel fuel. They found that a minimum EGR of 70% was needed, in combination with a low CR of 12.5:1, to simultaneously reduce the NO_x and soot emissions. The low CR and high EGR percentage resulted in increased incomplete combustion and poor overall efficiency. The high level of EGR and low CR were necessary to keep the diesel fuel from igniting prematurely due to its high reactivity. In addition, due to its low volatility, diesel fuel could cause wall wetting if injected early in the cycle. Due to its high reactivity and low volatility, diesel fuel may not be the most suitable fuel for LTC strategies. In comparison to diesel fuel, gasoline has higher volatility and lower reactivity, which makes it a very suitable fuel for LTC operation. Additionally, the increase in transportation

demand is skewed towards heavier fuels like diesel fuel [4]. Exploring advanced combustion strategies with gasoline could provide a pathway to addressing this transportation fuel imbalance.

Strategies that use gasoline in CI engines can be grouped under a single name called GCI. The most basic GCI strategy is homogenous charge compression ignition (HCCI) combustion [19]. In HCCI combustion, the fuel is completely premixed with air, before it is inducted into the cylinder, to achieve a homogeneous, fuel lean mixture. Upon induction, the charge is compressed until auto-ignition occurs. Since the entire fuel-air mixture is at nearly the same equivalence ratio and temperature, combustion occurs throughout the combustion chamber at nearly the same time, resulting in a short combustion duration. Due to the fuel lean mixtures, the combustion temperatures are low, which reduces the wall heat transfer losses. The short combustion duration, in combination with the reduced wall heat transfer losses, has been shown to yield high efficiencies. Dec et al. [20] demonstrated operation with a boosted HCCI strategy, in a load range of ~5 bar to 16 bar IMEP, with a peak indicated thermal efficiency of ~47%, while meeting the US-2010 NOx and PM standards. They found that a maximum load of 9 bar IMEP could be achieved with the HCCI strategy without the use of EGR. Further increases in load were constrained by PPRR and required the use of EGR. To extend the load range to 16 bar IMEP, high levels of EGR (~60%) had to be used to control the PPRR. Such high levels of EGR are feasible in a lab environment but may not be suitable in production applications where transient operation is required. In addition, HCCI combustion is difficult to control in practical engines because there is no direct, in-cycle control over the combustion phasing.

To address the challenges of combustion control seen with the HCCI strategy, researchers have investigated partial fuel stratification (PFS) strategies [21, 22]. In the PFS strategy, local equivalence ratio stratification is used to control the heat release rate. Dec et al. [21] repeated their earlier study [20], but, rather than operating fully premixed, injected a portion of the fuel as a direct-injection (DI) to introduce incylinder equivalence ratio stratification. The fraction of the fuel injected as a DI and the injection timing of this injection were varied to control the stratification level. They found that increasing the stratification resulted in reduced ringing intensity (RI). For the same RI, the PFS strategy showed an improvement in IMEP of ~1.5 bar compared to the HCCI strategy. However, the EGR required to achieve high-load

operation remained near 60%. The PFS strategy was also implemented by Marriot et al. [23]. They studied the effect of charge stratification by performing a start of injection (SOI) timing sweep. They showed that the efficiency increased with increasing charge stratification (i.e., injection timing retard); however, if the injection timing was retarded beyond -150 °aTDC, NO_x and PM increased rapidly.

Kalghatgi et al. [24, 25] used a strategy similar to the CDC strategy with a high pressure, near top dead center (TDC) injection of gasoline, in combination with high levels of EGR. The low auto-ignition quality of gasoline, combined with the high levels of EGR, enabled operation with low NO_x and soot emissions at an IMEP of 14.9 bar. Kalghatgi et al. [26] also demonstrated that adding an early gasoline injection reduces the maximum heat release for a given IMEP. They were able to operate the engine at ~16 bar IMEP with very low soot and NO_x emissions. Ra et al. [27, 28] performed a numerical study of multiple injection gasoline sprays, in a heavy-duty CI engine, at 16 bar IMEP and 2500 rev/min. They found that improved mixing before ignition reduces the carbon monoxide (CO) and unburnt hydrocarbon (UHC) emissions. Furthermore, splitting the fuel into multiple injections was effective at reducing PPRR.

Though GCI combustion has shown benefits at the mid- to high-load conditions, to be implemented in production engines, operation with similar benefits over the full load range needs to be demonstrated. Researchers [5, 29] have shown that the poor auto-ignition qualities of gasoline can make it difficult to achieve combustion at low-load conditions. Sellnau et al. [30, 31] used a combination of exhaust rebreathing, intake air heating, and supercharging, to enable light-load operation. With this setup, they demonstrated operation over the full load-speed range of a light-duty cycle with diesel-like efficiencies. While the strategy is promising, the thermal management system to heat the intake air adds to the cost and complexity of the engine. In addition, the use of a supercharger requires substantial energy addition, which reduces the efficiency.

The previous discussion has shown that, though GCI combustion has several advantages, the low auto-ignition quality of gasoline makes operation at low-load conditions challenging. In contrast to gasoline, the high reactivity of diesel fuel makes it easier to achieve combustion under low-load conditions. However, diesel fuel has difficulty controlling combustion phasing at increased loads, as was explained

earlier. This led to research into exploring LTC operation with fuel blends. Bessonette et al. [32] found that the best fuel for HCCI operation may have auto-ignition qualities between that of diesel fuel and gasoline. Additionally, they showed that the optimal auto-ignition quality changes with operating condition. Inagaki et al. [33] implemented a dual fuel premixed compression ignition (PCI) strategy with port-injected gasoline and direct-injected diesel fuel and was able to achieve 12 bar IMEP with NO_x less than 10 ppm and soot less than 0.1 FSN. Based on the work of Bessonette et al. [32] and Inagaki et al., [33] Kokjohn et al. [34, 35, 36] developed a dual-fuel PCI strategy using in-cylinder fuel blending of gasoline and diesel fuel (low and high reactivity, respectively). They named this strategy, RCCI combustion [6]. In this combustion mode, two fuels with different auto-ignition characteristics are blended in-cylinder. By controlling the fuel blend, they were able to achieve combustion phasing control. The in-cylinder fuel blending allows spatial stratification of the fuel reactivity in the cylinder and enables control over the combustion duration. Several studies were done with RCCI combustion to demonstrate operation over the full load-speed range. Kokjohn and Reitz [7] compared RCCI combustion and CDC over the most heavily weighted portions of the lightduty cycle (i.e., loads ranging from 2 bar to 9 bar IMEP). They found that RCCI combustion can improve the thermal efficiency by over 10%, while yielding an order of magnitude reduction in NO_x and soot emissions. However, at the lightest load condition, they found that a diesel LTC strategy offered better efficiency than RCCI combustion. The reason for the lower efficiency with RCCI combustion was high levels of CO and UHC emissions from the over-lean mixture of premixed gasoline. Reverting to a diesel LTC strategy at the lightest load caused the mode weighted gasoline percentage to be only 58%. Due to the need to manage two fuel systems (i.e., monitor and fill two fuel tanks), this solution is not ideal for passenger car applications.

Splitter et al. [37] proposed a "single fuel" RCCI strategy. Instead of using diesel fuel, gasoline doped with a small quantity of di-tertiary butyl peroxide (DTBP) was used as the high reactivity DI fuel. The strategy used port-fuel-injection (PFI) of gasoline and DI of gasoline doped with 0.75%, 1.75%, and 3.5% DTBP by volume, which accounts for ~0.2% of the total fueling. At the mid-load condition, they achieved a peak GIE of ~57%, while meeting the US-2010 standards for NOx and PM emissions. Hanson

et al. [38] compared single and dual fuel RCCI strategies at low-load conditions of 2 bar and 4.5 bar IMEP, with the engine speed varied from 800 rev/min. to 1700 rev/min. The single fuel RCCI strategy used 3.5% by volume of 2-ethyl hexyl nitrate (2-EHN) to increase the reactivity of gasoline. Both the strategies resulted in low NOx and soot emissions across all the engine speeds, but the thermal efficiency reduced with increased engine speed due to increased levels of incomplete combustion.

Kokjohn et al. [6] demonstrated RCCI combustion on a heavy-duty engine in the load range of 4.5 bar IMEP to 14.5 bar IMEP. The study resulted in a peak GIE of 56%, at a mid-load condition of 9 bar and 1300 rev/min. They found that, at the lightest loads, operation bordered on the lean limit for the premixed gasoline, with complete oxidation of UHC and CO being difficult. At higher engine loads, they had near stoichiometric operation, where the DI event had to be carefully controlled to avoid rich regions and incomplete combustion due to insufficient oxygen. This result suggested the use of increased intake pressure for load extension.

Focusing on load limit extension, Wang et al. [39] performed an experimental parametric study of operating parameters to study the limiting factors for extension of upper and lower load limits of RCCI combustion. Similar to Kokjohn et al. [7], they found that, at the lower load limits, a high fraction of diesel fuel was required to achieve good combustion efficiency. The upper load limits required a combination of high gasoline fraction, an early diesel injection, and high levels of EGR to avoid excessive pressure rise rates from premature combustion. The combination of high EGR and early SOI timing resulted in challenges controlling combustion phasing.

Zhang et al. [40] demonstrated operation on a heavy-duty engine over loads ranging from 5 bar to 11 bar brake mean effective pressure (BMEP) at an engine speed of 1200 rev/min. using a gasoline-diesel fuel RCCI strategy. They compared two injection strategies; one with an early injection of diesel fuel and the other with a late injection of diesel fuel. For both the strategies, the upper load limit was constrained at 11 bar BMEP due to the PPRR constraint. They repeated the study by using an 85% ethanol-15% gasoline blend (E85) as the premixed fuel. With E85, they achieved load extension up to 19 bar BMEP. The lower

reactivity of E85 relative to gasoline resulted in a wider spread in reactivity stratification, which was effective in achieving the load extension.

Dempsey and Reitz [41] used a low CR (11.7:1) piston to demonstrate operation in the load range of 4 bar IMEP at 800 rev/min. to 23 bar IMEP at 1800 rev/min. Their study considered operating conditions ranging from low-load-low-speed to high-load-high-speed. They performed computational optimizations with a gasoline-diesel fuel RCCI strategy. Using a split injection of diesel fuel, they achieved a maximum load of 23 bar IMEP with near zero NOx and soot emissions.

Benajes et al. [42] explored the potential of the RCCI strategy across a wide range of loads and speeds, ranging from idle to full load and 900 rev/min. to 1800 rev/min., respectively. Using a piston with CR of 14.4:1, they were able to operate up to 50% of full load with ultra-low NO_x and soot emissions. As the load increased, they were limited by a tradeoff between noise and soot emissions. By reducing the CR to 11:1, they were able to operate at full load. However, the use of the low CR piston resulted in poor combustion efficiency (~70%) at the low-load conditions.

Figure 2-1 shows a summary of the operating conditions covered in the RCCI studies described in the previous discussion. From the figure, it is seen that most of the research is focused in the mid-load range of 4 bar to 14 bar IMEP. There is very limited research performed at the low-load-high-speed and high-load-low-speed conditions, as highlighted by the two boxes overlaid on the figure. The limited research at high-load-low-speed used a low CR piston to achieve high-load extension, resulting in in poor combustion efficiency at the low-load-high-speed operating condition. Alternately, when a high CR piston was used it improved the low-load combustion efficiency, but resulted in high PPRR at the high-load-low-speed condition. Clearly, more work is required to understand the key tradeoffs in these areas.

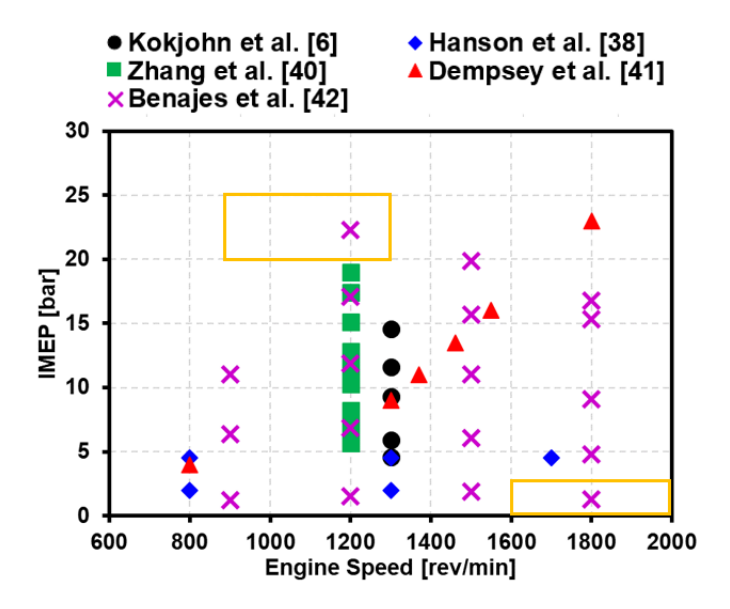


Figure 2-1. Summary of operating conditions covered in earlier RCCI studies.

Similar results were also seen from a study performed by Curran et al. [43]. They explored RCCI operation with gasoline and diesel fuel over a wide load-speed range in a light-duty multi-cylinder diesel engine. This led to the creation of an RCCI engine map, which is shown in Figure 2-2. The map was developed under the constraints of PPRR of 10 bar/deg, and a CO limit of 5000 ppm. The maximum brake thermal efficiency (BTE) was at a mid-load condition of 8 bar BMEP. At 8 bar BMEP, the BTE was 5% better and the NOx emissions were an order of magnitude lower than the CDC case. Despite the benefits seen at mid-load conditions, it is clear from the map that operation became increasingly challenging as they approached high-load-low-speed or vice versa. This was due to the difficulty in meeting the constraints on PPRR at high-load-low-speed and CO emissions (i.e., incomplete combustion) at low-load-high-speed conditions. At the high-load-low-speed conditions, the chemistry timescales are short due to the pressure and equivalence ratio sensitivity of typical hydrocarbons and the engine timescales are long due to the slow rotational speed. This mismatch in timescales causes difficulties in controlling the combustion phasing to avoid excessive PPRR. Conversely, at the low-load-high-speed conditions, the opposite situation presents a challenge. That is, the chemistry timescales are long due to the low intake pressures and low equivalence ratios, while the engine timescales are short, due to high rotational speed. This leads to issues with high

levels of incomplete combustion. Due to these challenges, there is very limited advanced combustion research in these operating points of the engine map.

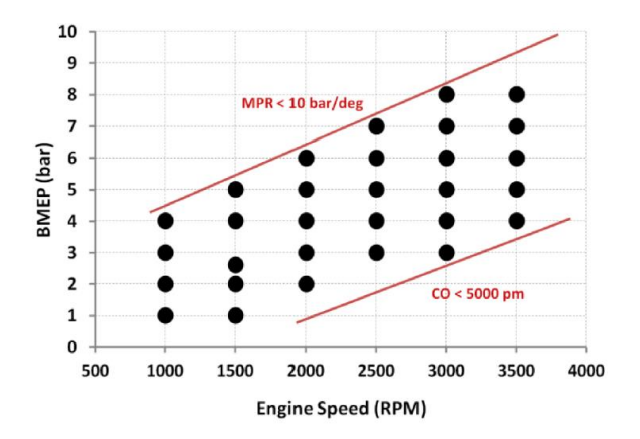


Figure 2-2. RCCI operating map developed by Curran et al. [43]

From the previous discussion, it is clear that GCI and RCCI strategies have several benefits, but to demonstrate operation over the entire load range, challenges at the low-loads (~2 bar IMEP) and high-loads (~20 bar IMEP) need to be addressed. This challenge will be addressed using CFD modeling in combination with GA optimization to identify feasible operating strategies at these operating conditions.

2.2. GA for Engine Optimization

Engine design involves numerous fuel system, air system, and geometric variables. Accordingly, the design space is often too large to fully cover using traditional design of experiments techniques. To address this challenge, evolutionary search algorithms (e.g., GAs) techniques are useful due to their ability to efficiently cover a large design space. Wickman et al. [44] used a single objective GA to optimize a heavy-duty diesel engine at high-load conditions. Their optimization study included design parameters for bowl design, injector design, injection strategy, and air handling. The optimum design from the study coupled a shallow bowl geometry, small nozzle holes, and high injection pressure. The optimal SOI timing and EGR rate were found to be sensitive to the NOx constraint used. Kim et al. [45] also used a single objective GA to optimize the injection strategy and air handling for a heavy-duty diesel engine at mid-load conditions. Their study showed that the GA preferred early injections with high EGR rates to achieve simultaneously low NOx and soot emissions. Since combustion optimizations have multiple objectives (e.g., efficiency, emissions, noise, etc.). Single objective GA studies require the use of a merit function.

This function encompasses the effects of the multiple objectives through a weight assigned to each of the objectives. Though the above-mentioned studies have shown satisfactory results, other authors [46, 47] have found the single objective GA results to be extremely sensitive to the choice of the merit function and the weights assigned to the objectives.

To avoid these issues, multi objective GA (MOGA) methods were explored for engine optimization studies [48, 49, 50]. To identify the best MOGA method, Shi and Reitz [51] compared different MOGA methods, in optimizing a heavy-duty diesel engine, under high-load conditions. Upon comparison, they found that the non-dominated sorting GA (NSGA-II) performed the best. Using the MOGA with NSGA-II, optimal combinations of bowl geometry, spray-targeting, and swirl ratio were identified to simultaneously minimize the NOx and soot emissions. MOGA optimization with NSGA-II has also been used to optimize advanced combustion strategies. Kokjohn et al. [52] used NSGA-II to optimize the injection strategy for RCCI combustion. Non-reacting simulations were performed at 11 bar IMEP to identify the strategy that yields the most homogenous charge. The optimum strategy identified had a low pressure first injection at -67 °aTDC, which conditioned the squish, and a high pressure second injection at -33 °aTDC, that was targeted into the bowl. The optimal SOI timings were such that, the fuel was optimally distributed between the bowl and the squish regions, to minimize the inhomogeneity. Dempsey and Reitz [53] used NSGA-II to optimize gasoline PCI operation in a heavy-duty engine at mid- and high-load conditions. They achieved a GIE of ~50%, but at the high-load conditions, controlling soot emissions and PPRR was found to be a challenge. Lim et al. [9] performed an optimization with NSGA-II and demonstrated operation with the RCCI strategy at 21 bar IMEP using gasoline and diesel fuel. The optimum strategy indicated that, by injecting a part of the low-reactivity fuel (gasoline) into the squish region, the temperatures in that region can be lowered due to evaporative cooling of the fuel. This thermal stratification led to reduced PPRR.

In a more recent study, Klos and Kokjohn [54] found that, as the number of design variables increased, the convergence rate of NSGA-II decreased. When the number of variables was 12 or higher, they found that the NSGA-II did not converge to an optimum. To address this issue, Klos and Kokjohn [54]

developed a new single objective GA, called the DK-GA. This GA blends the broad search coverage of a MOGA with the rapid convergence of a single objective GA. It has been shown to efficiently work with a large number of design variables. The performance of the DK-GA was compared with the NSGA-II for a design problem with 12 variables and it was found that the DK-GA significantly outperformed the NSGA-II. This is contrary to the results seen in the previous studies [47, 48], where the MOGA was found to be beneficial compared to the single objective GA's. There are two primary differences between the DK-GA and the earlier single objective GA's. The first difference is the objective function. In previous single objective GA techniques, a merit function, combining the effect of all the outputs of interest, was used as the objective function. As a result, by optimizing the merit function, the GA was effectively attempting to optimize all the outputs simultaneously. In doing this, this approach was found to be sensitive to the weight assigned to each output in the merit function. However, in the DK-GA, there is only one output or objective function (e.g., efficiency or fuel consumption), that is optimized. The rest of the outputs (e.g., NOx, PPRR etc.,) are included in the optimization as constraints. The DK-GA ensures that these outputs meet their corresponding constraints, through a penalty function imposed on the objective. Even with the DK-GA, weights in the form of a harshness factor are assigned to each output, in the penalty function. The harshness factor would determine the strictness of the constraint imposed on the output. However, since the DK-GA is only ensuring that the outputs meet the constraints, rather than aiming to optimize them simultaneously, this approach was not as sensitive to the assigned weights or harshness factors, as the earlier single objective GA's.

The second difference is in the coverage of the design space. Previous single objective GA's used fixed mutation rates to force the GA to target an optimum solution as quickly as possible. This was necessary due to the limited amount of computing resources available when these GA's were applied (early-to-mid 2000's). Recent advances in high throughput computing makes it possible to easily run hundreds of simulations simultaneously. Accordingly, Klos and Kokjohn [54] proposed the use of a variable mutation rate. The mutation rate is very high during early generations to fully cover the design space and decreases

in later generations to force convergence. Using this approach, they were able to achieve design space coverage similar to a MOGA with convergence rates similar to a single-objective GA.

Klos and Kokjohn [54] used the DK-GA to optimize the bowl design, injector design, injection strategy, and air handling for high-load RCCI combustion. The optimum design had a hemispherical bowl, with a low CR of 12:1. The GA picked a case with the maximum intake pressure and EGR rate as the optimum strategy. The study resulted in a high GIE of 48.7%, with near zero NOx and soot emissions.

In the above discussion, though several different GA optimization studies were mentioned, one common aspect among all these studies is that they were all performed at a single load point. Practically, it would be of more interest to have optimizations performed across multiple load points. That is, the optimal design obtained at one operating condition may not be suitable for a different operating condition. For example, when bowl design optimizations are performed separately at different operating conditions, it is likely that a different optimal bowl geometry would be found for each operating condition. In practice, this is not a useful solution since the bowl geometry cannot be changed with operating condition. To tackle this issue, Shi and Reitz [55] repeated their earlier high-load optimization study [51] at low-load conditions. They found that, unlike the high-load operating condition, the low-load results were insensitive to the bowl and injector geometry variations. Based on these results, they suggested an approach where, firstly, the hardware design is optimized at the high-load conditions. Using this hardware, the controllable design parameters (e.g., fueling strategy and air handling) are optimized at low-load and high-load conditions, separately. With this approach, they demonstrated simultaneous reduction in fuel consumption, NOx, and soot emissions at both the load conditions. Similar results were demonstrated by Ge et al. [56]. It is to be noted that both these studies were performed using a CDC strategy, which is relatively insensitive to changes in CR, due to the lack of premixed fuel.

For advanced combustion strategies, this approach may not be suitable because the premixed charge is extremely sensitive to changes in CR. Secondly, at low-load conditions, over-mixing is often a limiting factor for advanced combustion strategies. Accordingly, using DI and a bowl geometry that contains the fuel from the DI in one location to create a locally rich mixture may be the key to improving

the low-load combustion efficiency. However, using the same bowl geometry at high-load conditions may inhibit mixing and result in high soot emissions. This indicates that, unlike the CDC studies mentioned above, the optimal advanced combustion bowl geometry may have equal importance at multiple load conditions. Furthermore, previous studies [57] have shown that advanced combustion strategies are significantly more sensitive to operating parameter variations than the CDC strategy. Hence, in addition to the commonly explored objectives (i.e., efficiency, emissions, and noise), the sensitivity to variations in operating conditions, should also be minimized, to ensure that a stable and reliable optimum is obtained.

The above discussion highlights the improvements that need to be made in the optimization approach to achieve practical and robust solutions for advanced combustion strategies. Firstly, a new approach will have to be developed such that the bowl geometry can be optimized considering the low-load and high-load conditions simultaneously. Secondly, the GA optimization will have to be modified to check for the stability of the designs to operating condition fluctuations and ensure a reliable optimum is obtained.

2.3. Machine Learning in Engine Optimization

An issue that was not mentioned in the previous discussion is the large amount of data from the optimization studies that is wasted. Usually, the focus is on the optimum obtained from the GA; however, the rest of the data generated has useful information on interactions between the design variables and the outputs across the entire design space. Most of this data remains unused. Kavuri and Kokjohn [58, 59] have shown that using machine learning techniques to perform non-parametric regression analysis with the GA data, is one way of isolating these interactions and identifying the response functions of the objectives as a function of the design parameters.

In the simplest sense, machine learning relies on training an analytical model to enable a computer to make a data-driven decision. As the amount of data increases, the model is refined and becomes more accurate. While machine learning is not a new technique, substantial advancements have been made in recent years. These advancements have been driven by the need, and potential value, to analyze and make decisions based on large quantities of data made available by online activities (e.g., consumer preferences for online shopping [60]).

A non-parametric regression technique used in previous engine optimization studies [51, 58, 59] is a method called component selection and smoothing operator (COSSO). COSSO is based on the smoothing spline analysis of variance (SS-ANOVA) model [61]. The COSSO method was used in the earlier GA studies to estimate the response surfaces for the objectives as a function of the design parameters and to perform additional parametric studies on the optimum design.

There are several other machine learning techniques that can be used with non-parametric data sets. Ge et al. [62] used the k-nearest neighbor's method [63] to analyze the GA data from a heavy-duty diesel engine optimization. With this approach, the trends between the outputs and inputs were isolated with similar success as the COSSO method. The response functions were then used to study the sensitivity of engine performance to the design parameters of interest. Kodavasal et al. [64] used another machine learning technique, the random forest method [65], to predict the variation in peak cylinder pressure (PP) due to cycle-to-cycle variations, in a spark ignited (SI) engine. Data from large eddy simulation (LES) of 123 cycles was split into training and test data sets. 85% of the data was assigned to training and the rest assigned to test the model. The training data was used to train the random forest model and estimate the correlation between PP and the 10 metrics chosen to represent PP. Verification with the test data showed that the random forest model was capable of predicting the highs and lows in PP as a function of the cycle number.

Bin and Wenlai [66] used an approach called Gaussian Process Regression (GPR) [67], to estimate the correlation between thermal comfort index and design parameters including activity level, clothing insulation, air temperature, air relative humidity, air velocity, and mean radiant temperature. They found that the GPR approach showed good agreement with the analytical results. Additionally, they compared the performance of the GPR approach with other machine learning approaches, including neural networks and support vector machines. They found that the GPR approach showed superior performance and resulted in higher fitting precision than the other two approaches. Richardson et al. [68] used the GPR approach to predict the state of health and useful life, remaining in a lithium ion battery. In their work, they explain that battery degradation modeling is a challenge due to the complex interactions between the design parameters.

The large amount of data available from several cycles of lithium ion battery degradation was used to train the GPR model. They compared different GPR kernel functions, including matern 3/2, matern 5/2, squared exponential, and periodic kernel functions. They showed that the matern 3/2 kernel yielded superior performance among the various kernel functions investigated.

Shi and Reitz [69] compared four different machine learning techniques; k-nearest neighbors [63], kriging (or GPR) [67], neural networks [70], and radial basis functions [71] with the aim of using machine learning to substitute few of the CFD runs during the optimization. They initially ran a GA with 50 generations, which had design parameters for bowl design, injector angle, and swirl ratio. Upon the completion of the GA, the GA data was used to compare the machine learning approaches. They used the machine learning models trained with the GA data to predict the outputs for every 10th generation of the GA, and compared the error between the machine learning outputs and the actual CFD predicted outputs from the GA. They found that the k-nearest neighbor and the kriging approaches performed the best, among the four approaches studied. Though the approach showed promise, they were unable to implement it because, as the number of generations increased (i.e., as the trained data set size increased), the learning process took nearly as much time as the CFD simulation. Furthermore, they did not have a verification approach to identify which cases should be predicted using machine learning and which cases should use CFD. Addressing these issues, could provide a pathway to implementing machine learning in GA optimization, which has the potential to reduce the optimization time significantly.

2.4. Problems Identified from Past Research

The literature review summarized the potential of advanced combustion strategies, like RCCI and GCI combustion, in meeting the stringent emissions and fuel consumption targets expected in the coming years. However, several challenges were also identified, limiting the practical application of these strategies. The key issue highlighted was the lack of research, in the low-load-high-speed and high-load-low-speed regions of the drive cycle with the advanced combustion strategies. This section will provide a brief summary of the challenges faced at these two operating conditions. GA optimization will be used in combination with CFD, to address the challenges with advanced combustion strategies. The literature

review also covered the issues with the existing optimization approaches followed for advanced combustion strategies. Accordingly, this section will also summarize those issues.

2.4.1. Issues at Low-Load-High-Speed Operating Condition

At low-load-high-speed operating condition, the over-lean mixtures of premixed gasoline resulted in elevated levels of incomplete combustion. Resorting to a CDC strategy at low-load conditions has shown to improve the combustion efficiency, but it reduced the cycle-averaged gasoline percentage. This is mainly a concern for light-duty passenger vehicles, due to the need to monitor and fill two fuel tanks. Investigating strategies with direct-injected gasoline, could reduce the over-lean zones in the combustion chamber, and improve the low-load combustion efficiency. This would provide a pathway to improving the cycle-averaged gasoline percentage.

2.4.2. Issues at High-Load-Low-Speed Operating Condition

At the high-load-low-speed operating condition, controlling the combustion to avoid high PPRR, was found to be challenging. Optimization studies performed at high-load-low-speed operating conditions, suggested operation at the maximum intake pressure and EGR rate, allowed within the optimization study. However, the use of high intake pressure and EGR rate, could increase the pumping loop work, and reduce the net efficiency. Since the optimization study was performed over a closed cycle (i.e., from intake valve closure (IVC) to exhaust valve opening (EVO)), the pumping loop work was not accounted for in the efficiency calculations. Additionally, the use of excessive EGR rate, poses challenges during transient operation. This motivates the need to perform a thorough investigation of air-handling requirements, under high-load-low-speed conditions. Understanding the constraints on high-load-low-speed operation, at reduced EGR rates, could provide a solution to reducing the EGR burden during high-load operation.

It was also pointed out during the literature review that gasoline is well suited for high-load operation, due to its low reactivity. This makes it of interest to compare RCCI and GCI strategies under high-load-low-speed conditions to understand if having a diesel injection provides any benefits or if a complete GCI strategy is preferable under these conditions.

2.4.3. Issues with Optimization Techniques

From the literature review on GA optimization for engine applications, the main issue highlighted was the need to perform optimization studies considering multiple operating conditions simultaneously. This is particularly important for advanced combustion strategies, when optimizing the bowl design, considering the high sensitivity of premixed fuel to CR. Furthermore, the advanced combustion strategies have shown higher sensitivity to operating parameter variation than CDC strategies. Accordingly, the optimization approach should also be modified to check for the stability of the operating strategy to variations in inputs. Lastly, it was observed that engine optimizations generate large data sets, but the focus is usually on the optimum design. As a result, the majority of the GA data is not used. Machine learning techniques have shown potential to simplify large non-parametric data sets, like the GA data.

2.5. Objectives and Approach

The objective of the research presented in this thesis, is to address the challenges of advanced combustion strategies, at high-load-low-speed and low-load-high-speed operating conditions. This would fill in the research gaps existing in the literature for advanced combustion strategies and provide a pathway to practical implementation of these strategies. In this thesis, the focus will be on RCCI and GCI combustion strategies since they have shown significant benefits over CDC in previous studies. Furthermore, the optimization approach currently followed for advanced combustion strategies will be improved, to better suit these strategies.

In this thesis, CFD modeling is primarily used to perform the research. Therefore, to achieve confidence in the CFD model predictions, a thorough model-validation is performed. Experimental data from CDC, RCCI and GCI combustion strategies, across a range of operating conditions, will be used to validate the CFD model. The model-validation study will be presented in Chapter 3. Upon completing model-validation, a combination of CFD modeling and GA optimization will be used to address the challenges of advanced combustion strategies that were summarized in the previous section. It is necessary to perform an optimization study because the number of input variables and the design space of interest are too large to be covered manually to find a suitable operating strategy. Initially, optimizations targeting high-load-low-speed condition will be performed, since the challenges at this operating condition could

potentially cause structural damage to the engine. This study will investigate the effects of air-handling on high-load-low-speed operation with RCCI and GCI strategies. A detailed comparison of the two strategies, in terms of combustion characteristics, combustion control and operating parameter sensitivity will be presented. Operating constraints preventing operation at reduced EGR rates will be studied. Eventually, feasible operating strategies at various levels of EGR rates will be presented and their respective benefits and tradeoffs will be explained. The research performed at high-load-low-speed conditions will be shown in Chapter 4 and Chapter 5..

Upon completing the high-load study, the optimization approach is modified to optimize multiple operating conditions simultaneously. From this study, feasible operating strategies for both the low-load-high-speed and high-load-low-speed operating conditions will be presented. This study will be shown in Chapter 6. It is to be noted that all the studies mentioned so far will be performed on a heavy-duty engine. A separate study focusing solely on the light-duty drive cycle was also performed. The goal of that study was to investigate the potential of gasoline direct-injection to improve the combustion efficiency of light-load RCCI combustion. This is important, particularly for light-duty applications, as it would increase the drive-cycle gasoline percentage and provide a pathway for practical implementation of the RCCI strategy. The details of this study are shown in Appendix-A.

Lastly, machine learning techniques will be implemented in GA-based optimization to reduce the computational time and to evaluate the robustness of the selected designs. These studies will be presented in Chapter 7.

Chapter 3 Setup and Model Validation

3.1. Engine Specifications

The engine modeled in this study is a single cylinder version of a Caterpillar C-15, 15-L. six-cylinder engine. The C-15 is typical of a heavy-duty size-class diesel engine with a bore of 137 mm and a stroke of 171 mm. The work presented in this thesis uses two pistons. One is the stock piston with a CR of 16.4:1 and the other is a "bathtub-type" piston with a CR of 12:1. The "bathtub-type" piston was used to allow high-load premixed operation. A custom cylinder head was cast to allow the use of two identical Bosch CRIN II common-rail fuel injectors, for high-pressure DI of two fuels. The injector tips have seven 141-micron holes with included angles of 148°. Table 3-1 shows a summary of the engine and injector specifications.

Table 3-1. Engine and injector specifications.

Parameter Parameter	Stock	Bathtub	
Engine Specifications			
Displacement [L/cylinder]	2.5	2.5	
Bore x Stroke [mm]	137 x 171	137 x 171	
Compression Ratio [-]	16.4:1	12:1	
Swirl Ratio [-]	0.7	0.7	
IVC [°ATDC]	-154	-154	
EVO [°ATDC]	113	113	
Bosch Common Rail Injectors			
Number of holes	7		
Hole Diameter [mm]	0.141		
Included Spray Angle [°]	148		

In the experiments, though there are two independent injectors delivering gasoline and diesel fuel, the simulations assumed that both injectors were at the axis of the cylinder. This allowed the use of a sector mesh to reduce the computational burden. This simplification was validated in a previous study [72], and the results were found to be a good match with the experiments. Figure 3-1 shows the computational grid representing the stock piston. The grid represents a 51.42° sector mesh which includes one spray hole from the injector. The grid is made up of 34,634 cells at bottom dead center (BDC), with a cell size of 2 mm in the axial and vertical directions and 2° in the azimuthal direction. The study presented in Appendix-D uses the stock piston.

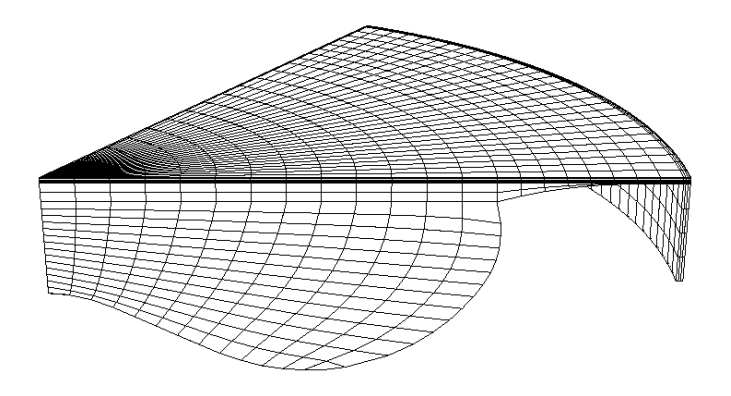


Figure 3-1. Computational mesh for the stock piston shown at top dead center (TDC).

The studies presented in Chapter 4, Chapter 5, Chapter 7, and Appendix-B use the "bathtub" piston. Figure 3-2 shows the computational grids used for this piston. The coarse grid has 16,258 cells at BDC, with an average mesh size of 3 mm. The fine grid has 39,647 cells at BDC, with an average mesh size of 1 mm. A mesh sensitivity study [73] for this bowl showed that the trends in the results remain unchanged with the mesh size for a cell size of 3 mm or smaller, although, differences in magnitudes exist. For cell size less than or equal to 1 mm, the results were found to be independent of the mesh size with variation in magnitudes reducing to less than five percent. Considering the large number of cases involved, the GA optimization study presented in Chapter 4 and Chapter 5 used the coarse mesh. The optimum cases identified from this study were re-run on the fine mesh. For the GA optimization, since the trends in the outputs are more important than the actual magnitudes, this approach was considered acceptable. The studies presented in Chapter 7 and Appendix-B used the fine mesh.

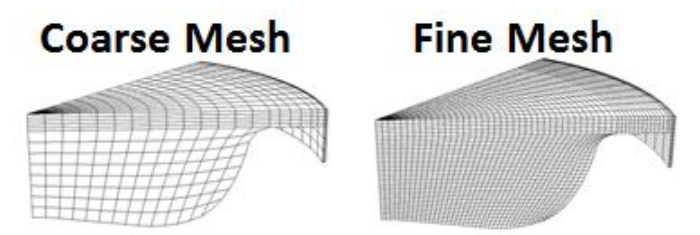


Figure 3-2. Computational mesh for the bathtub piston shown at TDC.

3.2. Model Description

Computational modeling was performed using the KIVA-3v release 2 code, which includes improved physical and chemistry models developed at the Engine Research Center (ERC) [74]. This section provides an overview of the physical models essential to the present study.

3.2.1. Combustion Model

The chemistry calculations were performed using a sparse analytical Jacobian solver coupled to the code, called SpeedChem [75]. It has been shown to perform calculations three to four times faster than CHEMKIN-II without significant changes in the combustion and emissions predictions [76]. The following study uses four fuels; diesel fuel, 93 AKI gasoline, 87 AKI gasoline, and 91E10 gasoline. The physical properties of diesel fuel are represented using tetradecane (C₁₄H₃₀), and the chemical kinetics are represented using n-heptane (nC₇H₁₆). For the 93 AKI gasoline, iso-octane (iC₈H₁₈) is used as the physical and the chemical surrogate. 87 AKI gasoline is represented as a blend of 13% n-heptane and 87% isooctane. The physical and the chemical properties of the 91E10 gasoline are represented using four surrogates; iso-octane with a mass fraction of 0.576, n-heptane with a mass fraction of 0.110, toluene (C₇H₈) with a mass fraction of 0.213, and ethanol (C_2H_6O) with a mass fraction of 0.101. The mass fractions of the surrogates were estimated by minimizing the relative error between the surrogate fuel properties and the reference fuel properties. A reduced reaction mechanism consisting of 80 species and 349 reactions [77] is used to model the fuel chemistry for the work presented in all the chapters, except for the high-load optimization study presented in Chapter 4 and Chapter 5. The high-load optimization study used a reduced reaction mechanism consisting of 47 species and 142 reactions [78]. Both the mechanisms had similar base primary reference fuel (PRF) chemistry, but the new mechanism [77] had polycyclic aromatic hydrocarbon (PAH) chemistry added up to pyrene formation. The new mechanism [77] was used to improve the predictions of soot formation. 91E10 gasoline was used for the study presented in Appendix-D. This study required ethanol chemistry to be added to the mechanism to model the combustion of the ethanol content in the fuel. Hence, ethanol chemistry from another reaction mechanism [79] was added to form a new reduced mechanism having 87 species and 412 reactions. This mechanism was used solely for the study presented in Appendix-D.

3.2.2. Emissions Model

NOx is predicted using a 12-reaction NOx mechanism based on the Gas Research Institute (GRI) NO mechanism [80]. The two-step phenomenological soot model based on the approach of Hiroyasu,

predicts the soot formation and oxidation [81]. The rate of change of soot mass within a computational cell, \dot{M}_s , is given by the competition between the soot formation rate, \dot{M}_{sf} , and the soot oxidation rate, \dot{M}_{so} , as

$$\dot{M}_S = \dot{M}_{Sf} - \dot{M}_{SO},\tag{1}$$

The soot formation rate is given by the Arrhenius expression

$$\dot{M}_{sf} = A_{sf} M_{inception} P^{0.5} e^{\frac{-E_{sf}}{RT}}, \tag{2}$$

where $M_{inception}$ is the mass of the inception species¹ in the computational cell, P is the pressure, R is the ideal gas constant, and T is the cell temperature. A_{sf} and E_{sf} are the soot formation pre-exponential, and the activation energy for soot formation respectively. The soot oxidation rate is given by the carbon oxidation model of Nagle and Strickland-Constable [82]. The oxidation rate is discussed by Liu et al. [83], and given by

$$\dot{M_{so}} = A_{so} \frac{6M_s}{\rho_s D_s} R_{total} MW_C, \tag{3}$$

where A_{so} is an empirical constant, M_s is the mass of soot in each computational cell, and R_{total} is the net reaction rate. The soot density, ρ_s , and soot particle diameter, D_s , are taken as 2 g/cm³ and 0.025 micron, respectively. MW_C is atomic weight of carbon atom. The soot model constants for each inception species are shown in Table 3-2. Discussion of the selection of inception species is described in §3.4.2.

Table 3-2. Soot model constants used based on the inception species.

Inception Species	C_2H_2	$C_{16}H_{10}$
$A_{sf} [1/s.bar^{0.5}]$	30	500
E _{sf} [cal/gmol]	1250	1250
A _{so} [-]	1	0.5

 $^{^{1}}$ Initially, acetylene ($C_{2}H_{2}$) was used as the inception species for the soot model. But, later in a study focused on soot emissions (shown in the Model Validation section), it was found that using a PAH species like pyrene resulted in improved soot predictions. Using pyrene as the inception species gave good predictions across a range of operating conditions, without the need for adjusting the soot model constants. Accordingly, pyrene ($C_{16}H_{10}$) was used as the inception species for the soot model in all the chapters, except for Chapter 4, where acetylene ($C_{2}H_{2}$) was used as the inception species.

3.2.3. Spray Model

The spray model uses the Lagrangian-Drop and Eulerian-Fluid (LDEF) approach where liquid fuel is treated as Lagrangian parcels, and the gas is discretized into Eulerian cells. The Lagrangian fuel parcels and the Eulerian gas phase are coupled using source terms in the mass, momentum, and energy conservation equations. In a grid dependency study of spray models for diesel engines, Abraham [84] found that the minimum grid size required would be of the order of the injector nozzle radius, which is approximately 0.1 mm. Performing the large number of calculations presented in this work, on a mesh that large (~ 1 million cells), would be highly impractical. Abani et al. [85] found that most of the grid dependence arises from the momentum exchange between the liquid and the gas phases near the injector nozzle. When a coarse mesh is used, the computational cell volume is significantly larger than the actual volume of influence of the spray. This extra volume increases the drag force on the liquid parcels due to the surrounding gas phase, leading to an underprediction of the spray penetration. To allow accurate spray simulation on a coarse grid, Abani et al. [85, 86] developed the Gasjet model. The Gasjet model assumes that the relative velocity between the liquid droplet and the gas phase is equal to the relative velocity between the liquid droplet and a turbulent gas jet which, has the same mass and momentum of the injected liquid fuel. This approach imposes an axial component for the gas phase velocity, as a function of the distance from the nozzle, which is used in the droplet acceleration equation given by

$$\frac{dU}{dt} = \frac{3}{8} C_D \frac{\rho_g}{\rho_l r_d} |U - V_{gas}| (U - V_{gas}), \tag{4}$$

where U is the droplet velocity vector, C_D is the droplet drag coefficient, which is a function of the Reynolds number, ρ_g and ρ_l are the gas and liquid phase densities respectively; r_d is the droplet radius, and V_{gas} is the gas phase velocity vector given as $V_{gas} = (V_x, V_y, V_z)$. The velocity components perpendicular to the spray axis (i.e., V_y and V_z) are obtained from the Eulerian gas phase solution, and the axial component, V_x , of the gas phase velocity, is found from gas-jet theory as

$$V_{x} = \min \left[U_{inj}, \frac{3U_{inj}d_{noz}\sqrt{\frac{\rho_{I}}{\rho_{g}}}}{K_{entr}x} \left(\frac{1}{\left(1 + \frac{12r^{2}}{K_{entr}^{2}x^{2}}\right)^{2}} \right) \right], \tag{5}$$

where U_{inj} is the injection velocity, d_{noz} is the nozzle diameter, K_{entr} is a model constant taken to be 0.7 as suggested by Abani et al. [85], x is the position downstream of the nozzle on the spray axis, and r is the radial position. Accordingly, to reduce the grid size dependency of the LDEF spray model, the Gasjet model of Abani et al. [85, 86] is used to model the relative velocity between the droplets and gas phase in the near nozzle region.

Spray breakup is modeled using the Kelvin Helmholtz–Rayleigh Taylor (KH-RT) model described by Beale and Reitz [87]. The Kelvin Helmholtz (KH) instability model is used to predict the primary breakup of the initially injected fuel parcels, and the secondary breakup is modeled using a competition between the KH and the Rayleigh-Taylor (RT) instabilities. The primary breakup process is evaluated to occur after a breakup time predicted by the KH model as

$$\tau_{KH} = \frac{3.726B_1r}{\Omega_{KH}\Lambda_{KH}},\tag{6}$$

where Ω_{KH} and Λ_{KH} are the calculated frequency and wavelength of the fastest growing wave respectively, B_1 (called cnst22 in KIVA) is an adjustable parameter used to adjust the breakup time. In the current study, a B_1 value of 80 is used. The radius of the child parcel resulting from the primary breakup is predicted using the KH model as

$$r_c = B_0 \Lambda_{KH}, \tag{7}$$

B₀ (called balpha in KIVA) is an adjustable parameter, which is given a constant value of 0.6. The RT model is used to predict secondary breakup beyond a breakup length from the injector tip, which is estimated as

$$L_b = C_b d_0 \sqrt{\frac{\rho_{fuel}}{\rho_{air}}},\tag{8}$$

where d_0 is the parent parcel diameter and C_b (called distant in KIVA) is another adjustable parameter, which is given a value of 1.9. The radius of the child parcel resulting from the secondary breakup is predicted using the RT model as

$$r_c = \frac{\pi C_{RT}}{K_{RT}},\tag{9}$$

where K_{RT} is the calculated wave number and C_{RT} is an adjustable constant set to 0.1. These values of spray parameters have been shown to predict spray penetration and mixture distributions accurately for diesel jets (see Chuahy and Kokjohn [88]).

The renormalization group (RNG) k–ε model modified by Han and Reitz [89] for compressible flows, is used for the turbulent flow calculation. The droplet collision model is based on O'Rourke's model, and a radius of influence method is used to determine the collision partners to reduce the mesh dependency. Additionally, the model was expanded by Munnanur [90] to include a complete list of collision outcomes that consider the effects of bounce, coalescence, fragmenting, and non-fragmenting separations. A wall film sub model was used to model droplet interaction with the wall [91], which includes the effects associated with splash, film spreading, and motion due to inertia.

3.3. Genetic Algorithm Optimization

Optimization was performed using a GA, which is a search technique inspired by the theory of evolution. Initially, for the high-load optimization study presented in Chapter 4 and Chapter 5, a MOGA was used. However, later Klos and Kokjohn [54] found that the MOGA does not work efficiently when there are more than 12 input variables, as explained in Chapter 2. Consequently, they developed a GA called the DK-GA, which works efficiently for optimizations with a large number of variables, and verified its improved performance over the MOGA. Accordingly, this GA was used for the optimizations presented in the later chapters. Both the GA approaches will be explained in detail in this section.

3.3.1. MOGA (NSGA-II)

The MOGA used for the high-load optimization study has multiple objective functions. It generates a range of optimal solutions called the Pareto solutions, to identify the ideal design space of operation. From this set of Pareto solutions, the optimum point was identified by applying a set of filters which are explained

later in Chapter 4. Shi and Reitz [51] explored several MOGA techniques and have shown that the NSGA-II proposed by Deb et al. [92] is well suited for engine optimizations. Hence, NSGA-II was coupled to the CFD code and used for the optimization presented in Chapter 4. The NSGA-II code randomly populates the citizens for the first generation and uses crossover and mutation to populate the next generation. From the second generation onwards, crowding tournament selection is used to compare the results from the two generations and populate the further generations. Citizens having a higher rank are given preference, and if two citizens have the same rank, a citizen is chosen such that the crowding of citizens is avoided. In this way, the GA aims to achieve diverse solutions.

Before performing the high-load optimization study, considering the large number of cases involved (see Chapter 4), an optimization study was performed to identify the optimum number of citizens required per generation. The optimum was chosen as the number of citizens required to achieve an optimum between the convergence speed and the computational expense. Optimization was performed by varying the number of citizens per generation in steps of 32 from 32 to 192 and the convergence rates were compared. Optimization convergence was monitored using the convergence metric proposed by Shi and Reitz [51]. The metric calculates the minimum normalized Euclidean distance, d_i , of each Pareto solution from the current generation, $f_k(i)$, to the Pareto solutions from the pool of all the previous generations, $f_k(j)$, for each objective, k, as

$$d_{i} = \min_{j=1} \sqrt{\sum_{k=1}^{M} \left(\frac{f_{k}(i) - f_{k}(j)}{f_{k}^{max} - f_{k}^{min}} \right)^{2}},$$
(10)

where f_k^{max} and f_k^{min} are the maximum and minimum values of the k-th objective in the pool of Pareto solutions and M is the number of objectives. The convergence metric is then calculated by averaging the normalized distance for all the Pareto solutions and normalizing it by the maximum average distance to keep the convergence metric between 0 and 1. Figure 3-3 shows the convergence metric as a function of generation number for the citizen sweep study. The case with 96 citizens converges much faster than the 32 and 64 citizen cases. However, increasing the citizen number beyond 96 adds to the computational cost,

but does not improve the convergence rate. Hence, 96 citizens per generation was chosen as the optimum number and used for the high-load optimization study in Chapter 4.

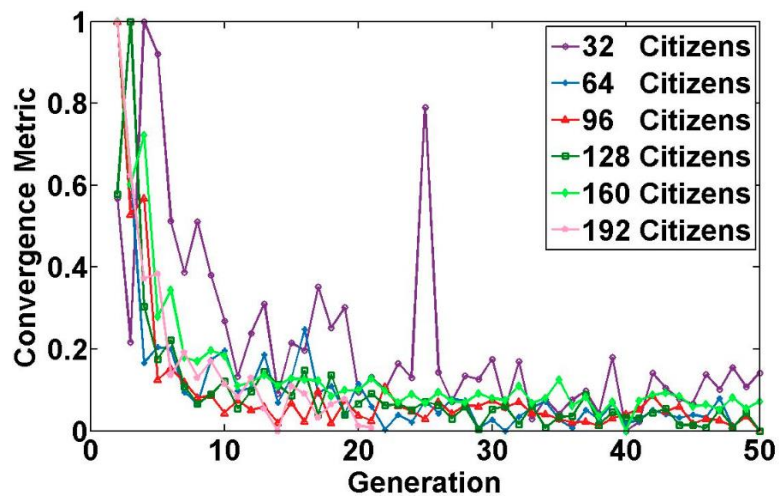


Figure 3-3. Convergence metric vs. generation for different number of citizens per generation.

3.3.2. Single Objective GA (DK-GA)

Most engine optimization problems can be considered constrained minimizations, where fuel consumption is minimized, subject to emissions and mechanical constraints. Accordingly, Klos and Kokjohn [54] developed a new single-objective GA with a penalty function for the constraints, which they called the DK-GA. They verified its improved performance over the NSGA-II with several objective functions. DK-GA differs from the NSGA-II in three key aspects.

- 1. Cross breeding of parents to select a new generation is done by a Punnett square technique. In this technique, the top n designs from the previous generations become the parents of the new generation. Each parent has a child with every other parent twice and once with themselves, producing a new generation of n^2 children.
- 2. Once the new generation is created, mutation occurs for each variable of each child. In DK-GA, the mutation rate is not constant. A normally distributed random number with its mean set to the current value and standard deviation set by a decaying time constant is generated to add mutations to the system. As the GA progresses, the time constant that dictates the mutation rate exponentially decays. The rate at which it decays is defined as

$$\tau_{GA,i} = \tau_{GA,0} * \exp\left(-\sigma_{GA} \frac{i}{n_{end}}\right), \tag{11}$$

where $\tau_{GA,i}$ is the time constant at the i^{th} generation, $\tau_{GA,0}$ is the user specified initial time constant, σ_{GA} is the standard deviation, and n_{end} is the user specified total number of generations. This approach allows the GA to fully explore the design space in the early generations but then forces the GA to converge to a solution in the later generations. For the studies involving DK-GA, presented in Chapter 6 and Chapter 7, $\tau_{GA,0}$ of 0.6 and σ_{GA} of 4 are used.

3. The fitness function involves minimizing (e.g., indicated specific fuel consumption (ISFC)) or maximizing (e.g., GIE) any one output. A penalty function is used to penalize the fitness value based on the constraints set for the other outputs (e.g., soot emissions, PPRR, etc.). This way it ensures that, while the chosen output is being optimized the other outputs also meet the set constraint values. The penalties are estimated based on a penalty function given by

$$P_{j} = \frac{1}{\left(\max\left(1, 1 + sign(H_{j}) * \left(\frac{y_{j} - c_{j}}{|c_{j}|}\right)\right)\right)^{H_{j}}},$$
(12)

where P_j is the penalty, y_j is the CFD calculated value of the j^{th} output, c_j is the user specified constraint value for the j^{th} output, and H_j is a user specified harshness factor. The magnitude of H_j determines how severely the constraint should be enforced and the sign defines if the output needs to be higher or lower than the constraint value (i.e., if the harshness variable is positive, the output value must be less than the constraint and vice versa). Once the penalties are estimated for all the outputs, all the penalties are multiplied together to create the total penalty. The total penalty is then multiplied by the optimization variable to create the final fitness function. This function will be maximized or minimized based on the problem definition.

3.4. Model Validation

The primary focus of the present work is to use the computational tools to investigate advanced combustion at conditions where it is difficult to investigate experimentally without prior knowledge of the

desired injection and air handling (e.g., intake pressure and EGR) strategies. Accordingly, the model validation effort focuses on ensuring the models are predictive over a wide range of operating conditions. The models used in the present study have been extensively validated and applied for low-load and midload operation using RCCI, GCI and CDC strategies. For example, Kokjohn et al. [6] showed good agreement between simulations and experiments of RCCI combustion at loads spanning from 4 to 14 bar IMEP. Dempsey et al. [93] have shown accurate prediction of mid-load GCI combustion. The authors early work (see Kavuri et al. [50]) investigated model performance at loads spanning from 2 bar IMEP to 14 bar IMEP in CDC, RCCI, and GCI modes in a light-duty engine. Accordingly, the present effort will focus on high-load model validation in a heavy-duty engine. Experimental data for the present test engine (see Table 3-1) was available for CDC, RCCI, and GCI combustion at near 20 bar IMEP. These will be discussed in the coming sub-sections. Further model validation efforts are performed later in the study after the models have been exercised to identify relevant operating conditions. These studies are described in the coming chapters (see §4.2.1, §4.2.2.2, §B.2, §D.2).

3.4.1. Model Validation with CDC

The operating conditions for the CDC model validation experiments are shown in Table 3-3. The experimental data for these studies was obtained from Caterpillar. The data provided was for a diesel SOI sweep where the SOI timing of the diesel injection was varied from -18 °aTDC to 6 °aTDC at a fixed diesel fuel mass of 244.25 mg. This resulted in a variation in IMEP in the range of 15 bar to 20 bar. The study was performed at a fixed engine speed of 1800 rev/min. The measured injection rate profile and the IVC species composition corresponding to the EGR rate used in the experiments were provided and used in the CFD simulations.

Table 3-3. Operating conditions for model validation with the CDC strategy.

Parameter	Input	
Fuel	Diesel Fuel	
IMEP [bar]	15 to 20	
Engine Speed [rev/min]	1800	
Fuel Mass [mg/cycle]	244.25	
SOI-Diesel [°aTDC]	-18 to 6	
P _{inj} [bar]	1490	
EGR [%]	20	

Figure 3-4 shows the in-cylinder pressure and apparent heat release rate (AHRR) comparison between the experiments and CFD. The SOI timing for each case is shown on the corresponding plot. The peak AHRR is slightly under-predicted at the early SOI timings but matches well with the experiments as the SOI timing is retarded. This was found to be due to under-prediction of CO oxidation at the early SOI timings, which could be happening due to differences in the mixing field between the experiments and CFD. Despite the differences at the early SOI timings, there is a reasonable agreement between the experiments and simulations across the SOI sweep.

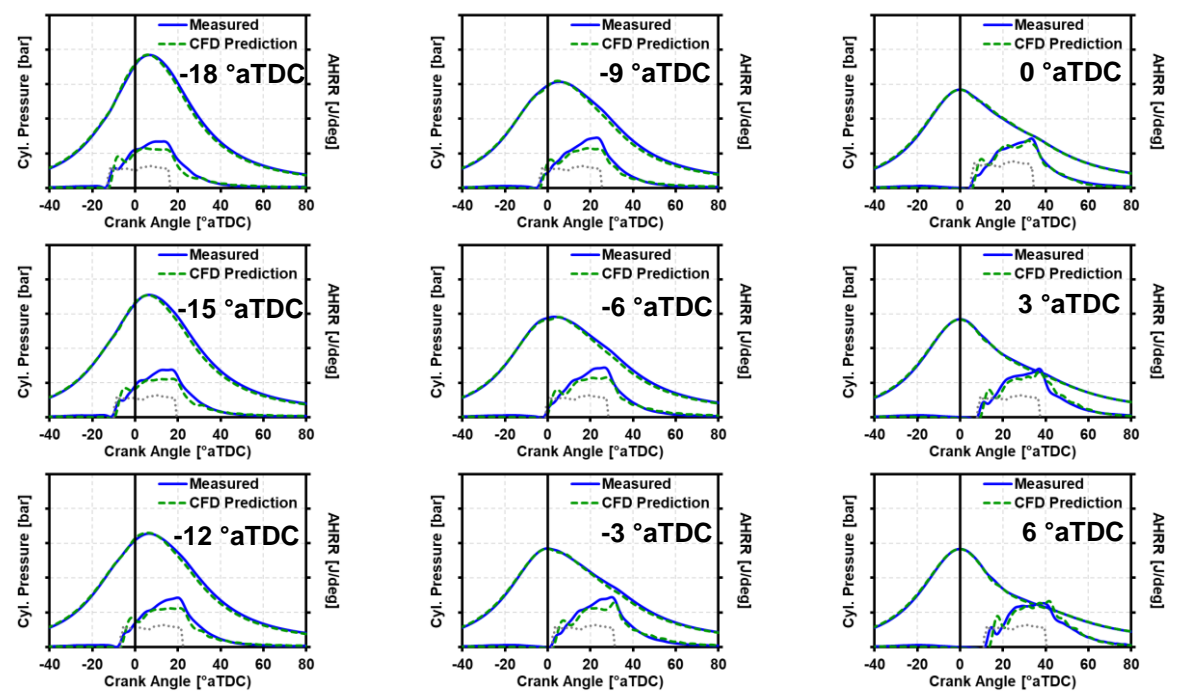


Figure 3-4. In-cylinder pressure and AHRR comparison between the experiments and simulations for the operating conditions shown in Table 3-3.

Figure 3-5 shows a comparison of the NOx emissions between experiments and CFD. The NOx emissions were normalized to set the range between zero and one. As seen from the figure, there is a good agreement in the trends and magnitudes of NOx emissions between the experiments and simulations. A comparison of soot emissions is not shown because the experimental data for soot emissions was not provided.

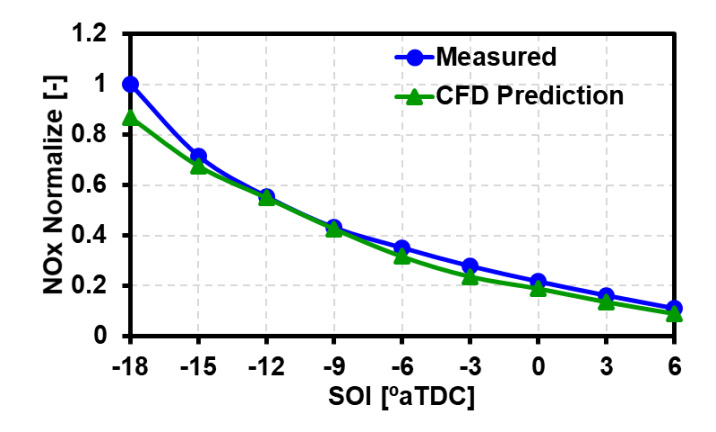


Figure 3-5. Comparison of NOx emissions between experiments and simulations for the operating conditions shown in Table 3-3.

3.4.2. Model Validation with RCCI Combustion

The first set of RCCI model validation experiments [94] were performed at 20 bar gross IMEP and 1800 rev/min. with a single- and split-injection strategy for the diesel fuel. The gasoline was injected during the intake stroke in the experiments but was modeled as a homogenous mixture at IVC in the simulations. Both cases used over 50% EGR. Table 3-4 shows the operating conditions. Figure 3-6 shows a comparison of the in-cylinder pressure and AHRR between the experiments and CFD. For both strategies, there is a reasonable agreement in ignition delay, combustion duration, and peak AHRR between the simulations and experiments. Figure 3-7 shows the NOx and soot emissions comparison between the experiments and simulations. For both the NOx and soot emissions, the trends and magnitudes were predicted reasonably well between the two cases shown in Table 3-4.

Table 3-4. First set of operating conditions for model validation with the RCCI strategy.

Parameter	20 bar 1800 rev/min (Single Inj.)	20 bar 1800 rev/min (Split Inj.)
IMEP [bar]	20	20
Engine Speed [rev/min.]	1800	1800
Premix Mass [mg/cycle]	217	225
Mass in Inj-1 [mg/cycle]	24	17.85
Mass in Inj-2 [mg/cycle]	N/A	16.15
SOI-1 [°aTDC]	-74	-74
SOI-2 [°aTDC]	N/A	-8
EGR [%]	57	52
Inj. Pressure [bar]	741	741
IVC Pressure [bar]	3.96	3.96

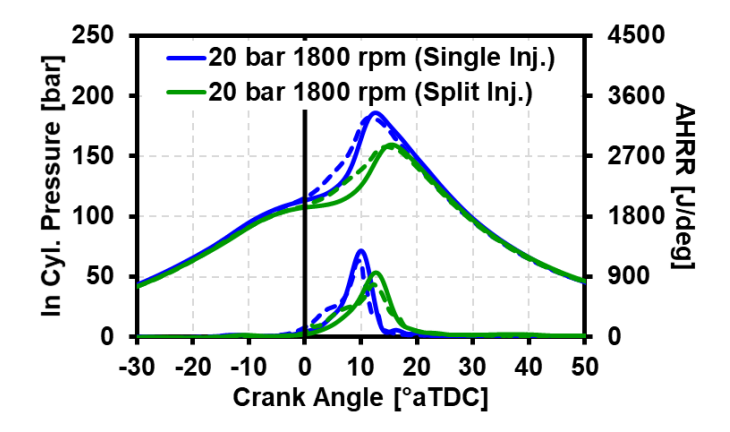


Figure 3-6. In-cylinder pressure and AHRR comparison between the experiments (-) and simulations (- -) for the operating conditions shown in Table 3-4.

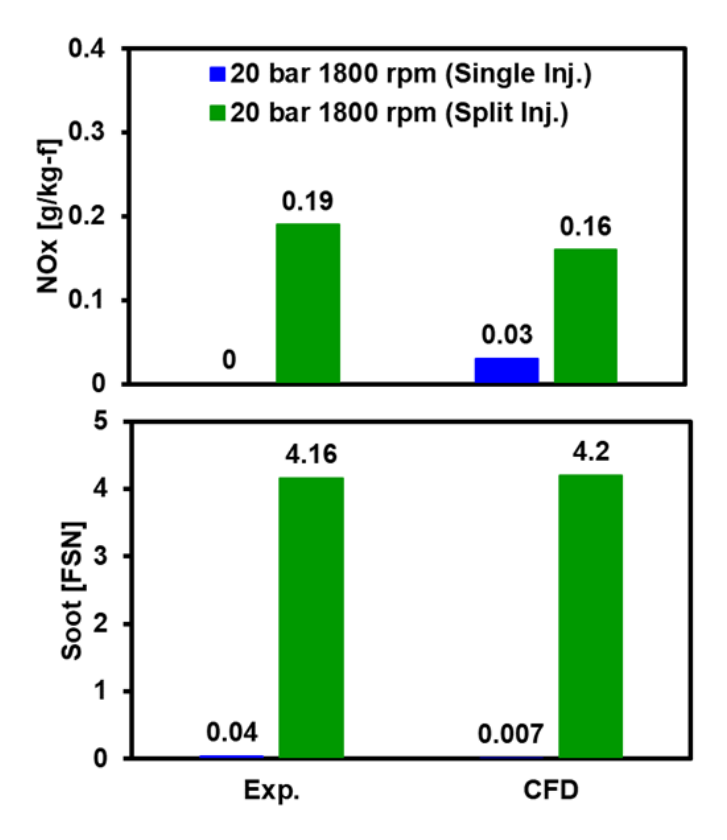


Figure 3-7. Comparison of NOx and soot emissions between experiments and simulations for the operating conditions shown in Table 3-4.

The operating conditions for the experimental data [71, 94] used as the second set of model validation data for RCCI combustion are shown in Table 3-5. In these experiments, performed at 13 bar and 1300 rev/min., a premixed charge of gasoline and n-heptane was created using injections during the intake stroke. The quantity of gasoline and n-heptane was set to reach a load of 10 bar gross IMEP from

the premixed fuel alone. A load extension injection consisting of 46 mg of gasoline was added at -10 °aTDC to reach a load of 13 bar gross IMEP. The ratio of gasoline and n-heptane in the premixed fuel was adjusted to set the 50 percent burn location of the premixed heat release to TDC. The load extension injection was swept from -10 °aTDC to +30 °aTDC in steps of 5 °CA while holding all other parameters constant. The study was performed at various levels of EGR and injection pressure. Although the data-set is for a midload condition of 13 bar IMEP, where the model was thoroughly validated in earlier studies, it was still used for model-validation because it has a premixed (low temperature, locally lean) and a mixing-controlled (high temperature, locally rich) combustion event occurring in the same cycle. Such mixed-mode strategies were not validated in earlier studies, which makes this data-set unique. The broad range of local equivalence ratios and temperatures covered during the two combustion events makes it an idea data-set for model-validation. Achieving good agreement with these experiments would give us high confidence in the model predictions.

Table 3-5. Second set of operating conditions for model validation with the RCCI strategy.

Parameter\Effect Investigated	Load Extension SOI	EGR	Inj. Pressure
Nominal gross IMEP (bar)	13		
Speed (rev/min)	1300		
Intake Temp (°C)	60		
Intake Pressure (bar)	2.31		
Load Extension SOI Timing (°ATDC)	-10 to +30		
Load Extension Mass (mg/cycle)	46		
Total Gasoline Mass (mg/cycle)	158	160, 158	158
Total n-heptane Mass (mg/cycle)	17	5,17	17
EGR Rate (%)	46	30, 46	46
Inj. Pressure (bar)	1000	1000	1000, 1500

Figure 3-8 shows the soot emissions comparison between the experiments and the model, as a function of the load extension SOI timing, for the 46% EGR case and injection pressure of 1000 bar. For these results, acetylene was used as the inception species for the soot model. Figure 3-8 (a) shows the soot trends for an initial set of soot constants (Asf = 500, Esf = 1250). With these values of soot constants, the soot is overpredicted across the SOI sweep. The soot constants were then adjusted to Asf of 25 and Esf of

2000, to match the soot magnitude of the experiments for SOI of 25 °aTDC. The same soot constants were used to simulate the remaining SOI timings in the study, and the resulting trends are shown in Figure 3-8 (b). As illustrated, the soot is significantly under-predicted for the SOI timings before TDC. The same study was then repeated by adjusting the soot constants to Asf of 1900 and Esf of 2000, to match the soot magnitude of the SOI of -10 °aTDC case. However, when these constants were used, soot was grossly overpredicted for the SOI timings later than TDC (see Figure 3-8 (c)). These results show that using acetylene as the inception species a common set of soot constants which gave a good agreement across the SOI sweep, could not be found.

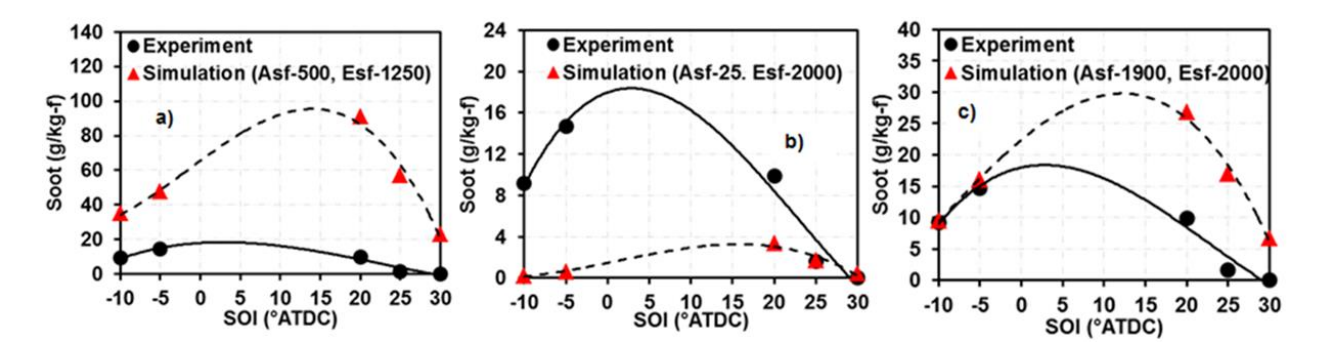


Figure 3-8. Measured (\circ) and model-predicted (\triangle) soot emissions for EGR-46% and an injection pressure of 1000 bar as a function of load extension injection SOI timing with acetylene(C₂H₂) as inception species for soot model and soot constants of (a) $A_{sf} = 500$ and $E_{sf} = 1250$, (b) $A_{sf} = 25$ and $E_{sf} = 2000$, and (c) $A_{sf} = 1900$ and $E_{sf} = 2000$.

In addition to the soot model constants, the soot inception species is another input to the two-step soot model, which could be modified to improve the soot predictions. Previous studies [95, 96] have identified that soot inception is very closely represented by PAH growth. PAH growth starts from merging of smaller aliphatics of which acetylene is a key contributor. PAH growth continues through the "H-abstraction-C₂H₂-addition" (HACA) mechanism, which is initiated by H-atom abstraction from a reactive radical. This is followed by the addition of an acetylene molecule to the radical site. After a certain size, PAH species begin to collide and stick to each other while individual PAH's continue to increase in size via the HACA process. This combination of molecular chemical growth reactions and physical collisions leads to the formation of soot particles. Since acetylene plays a key role in the inception process, it is commonly used as the inception species in the two-step soot model. This is done to avoid having reaction

chemistry with higher carbon chains, which saves computational time. However, including PAH formation and growth in the reduced chemistry mechanism represents soot inception more accurately and might give a closer prediction compared to using acetylene as the inception species. During the time of this research, Wang et al. [77] developed a reduced PRF mechanism considering PAH chemistry up to pyrene formation. Accordingly, this mechanism was investigated and pyrene was used as the inception species in the two-step soot model. Figure 3-9 shows the NOx and soot emissions comparison between the experiments and simulations. When the soot model was modified to use pyrene as the inception species instead of acetylene, a common set of soot constants that gave good agreement with the experimental soot emissions could be identified, as shown in Figure 3-9.

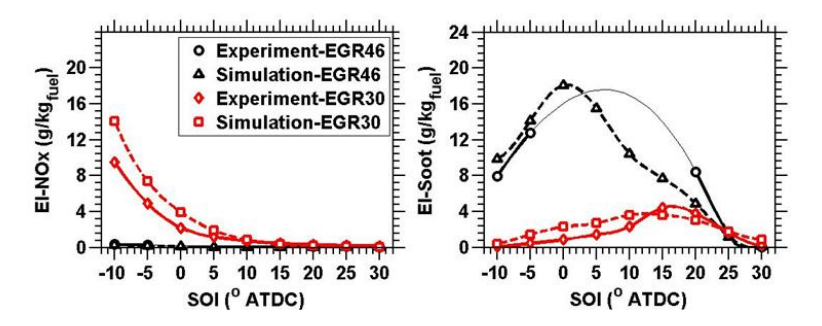


Figure 3-9. NOx and soot emissions comparison between model and experimental data.

Figure 3-10 shows the AHRR comparison between the model and the experiments for this data. Since the primary and secondary heat releases have different scales, they are shown on separate plots to highlight the agreement of the model predictions with the experiments for the secondary heat release rate. The experimental AHRR curves are an ensemble average of 250 cycles. The peak heat release rate is overpredicted for the cases with 30% EGR in the simulations, but the combustion duration agrees well with the experiments for all the cases. Despite the differences in peak heat release rate, the model does a decent job of predicting the combustion characteristics over the range of SOI timings for both EGR rates.

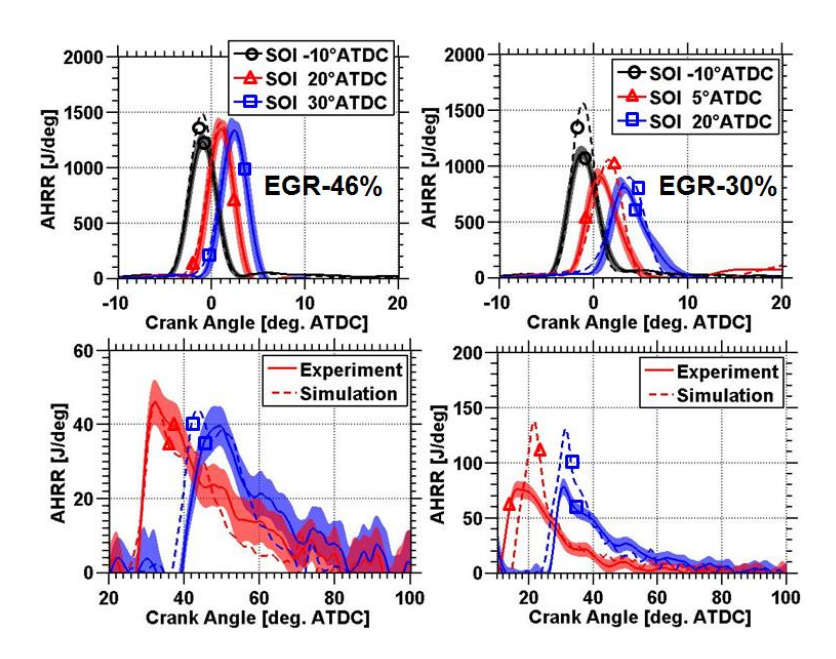


Figure 3-10. AHRR comparison between model and experiments. The AHRR is separated into primary (top) and secondary (bottom) heat release rate to highlight the agreement of the model predictions with the experiments for the secondary heat release rate.

3.4.3. Model Validation with GCI Combustion

The operating conditions for the experimental data used for model validation with GCI strategy are shown in Table 3-6.

Table 3-6. Operating conditions for model validation with the GCI strategy.

Parameter \ Injection Strategy	No Post Injection	Post Inj. w/ no Premix Fuel	Post Inj. w/ Premix Fuel	
Fuel	91E10			
Nominal gross IMEP [bar]		16 to 21		
Engine Speed [rev/min.]	1300			
Intake Temperature [°C]	65			
Intake Pressure [bar]	2.85			
EGR [%]	0			
Injection Pressure [bar]	1360			
Main Inj. SOI Timing [°aTDC]	-8			
Total Fuel Mass [mg/cycle]	~ 215 to 290			
Premixed Fuel Mass [mg/cycle]	0	0	68	
Main Inj. Fuel Mass [mg/cycle]	~ 215 to 290	215	147	
Post Inj. Fuel Mass [mg/cycle]	0	~ 0 to 75	~ 0 to 75	
Post Inj. SOI Timing [°aTDC]	N/A	16, 25, 40	12, 25, 40	

The injection strategy for this data set has premixed fuel, a main injection, and a post TDC injection.

Like the earlier data-set, this set of experiments also covers a wide range of operating conditions and

combustion characteristics, but at high-load conditions. The premixed fuel results in a primary heat release which undergoes combustion under locally lean equivalence ratios and is controlled by the chemical kinetics of the fuel. On the contrary, the main and the post-injection combust in a mixing-controlled heat release. Among them, the main injection combusts close to TDC where the oxygen levels are reasonably high, and the post-injection combusts late in the cycle in an oxygen-depleted environment. Achieving good agreement with the experimental results from this data-set would validate the model under various combustion modes and in-cylinder conditions. Furthermore, this data-set includes the range of operating conditions that will be covered during the optimization studies performed in the later chapters. This makes it an ideal data-set for model validation, to instill confidence in using this model in the later chapters for performing the optimization studies.

Figure 3-11, Figure 3-12, and Figure 3-13 show the experimental and CFD predicted in-cylinder pressure and AHRR trends for the post-injection strategy with premixed fuel, the post-injection strategy without the premixed fuel, and the no post-injection strategy respectively. The main and the post-injection duration for each case are shown on the corresponding plots. There is good agreement between the measured and the predicted profiles across all the operating conditions.

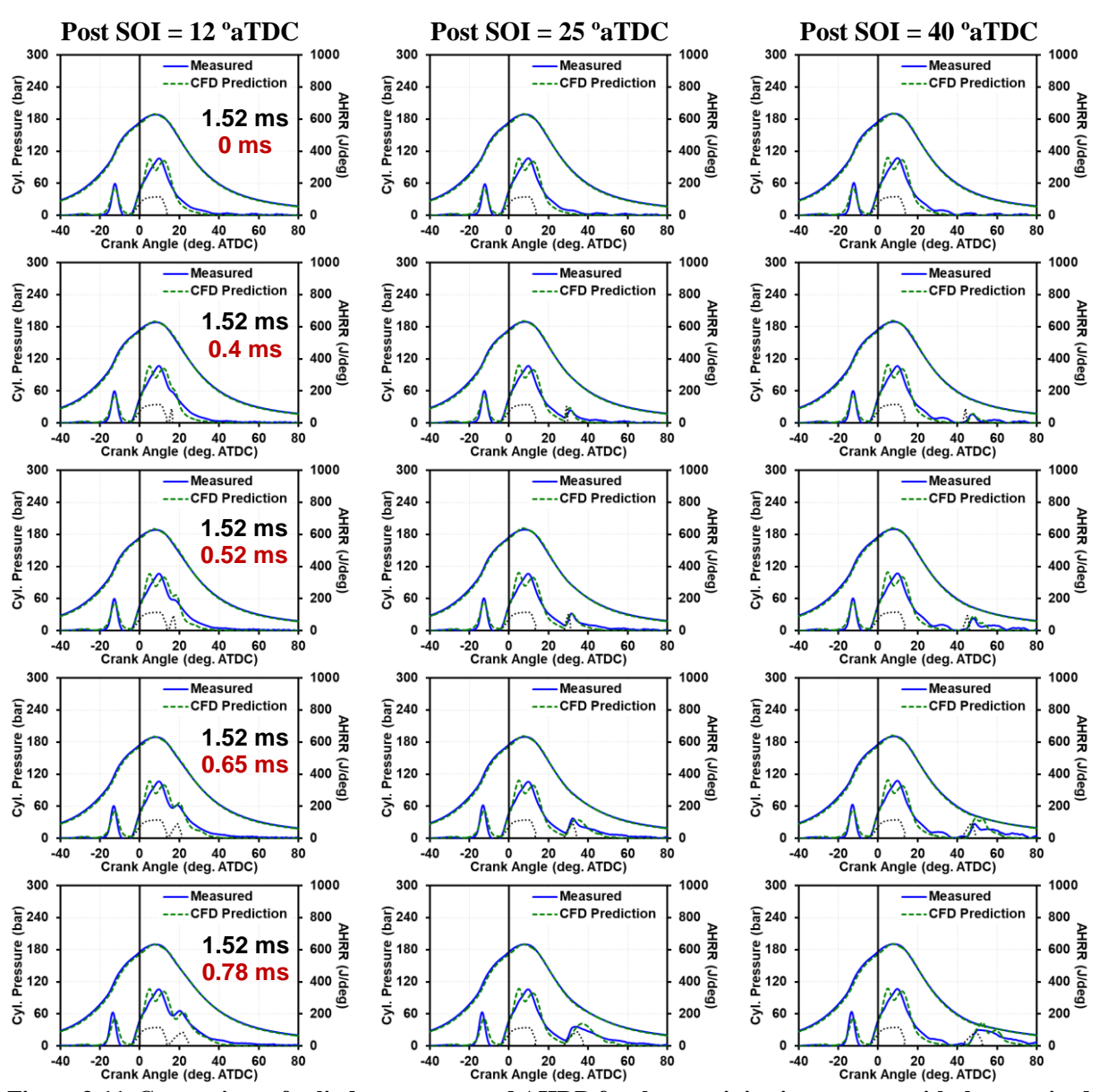


Figure 3-11. Comparison of cylinder pressure and AHRR for the post-injection strategy with the premixed fuel across all the operating conditions studied.

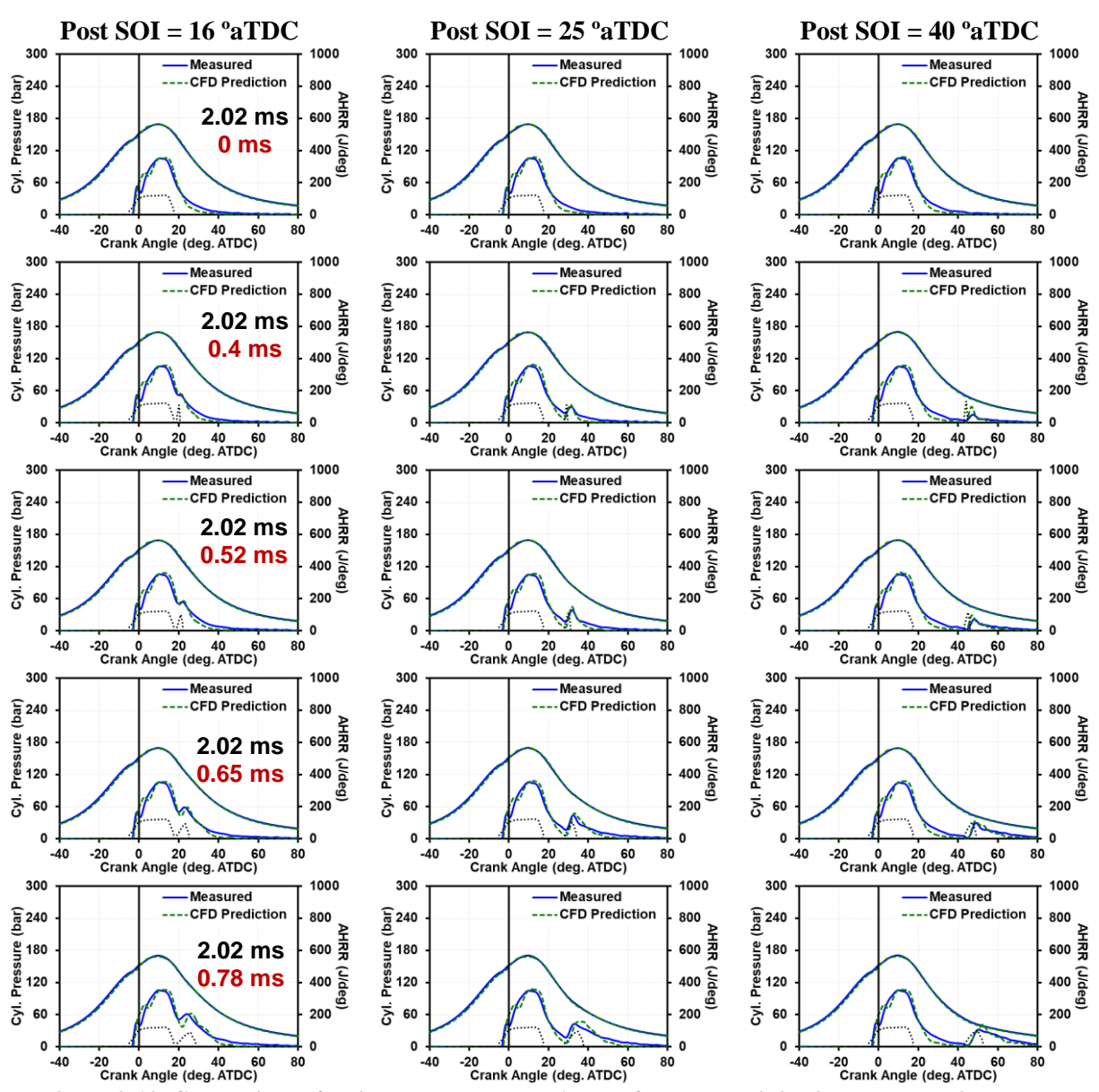


Figure 3-12. Comparison of cylinder pressure and AHRR for the post-injection strategy without the premixed fuel across all the operating conditions studied.

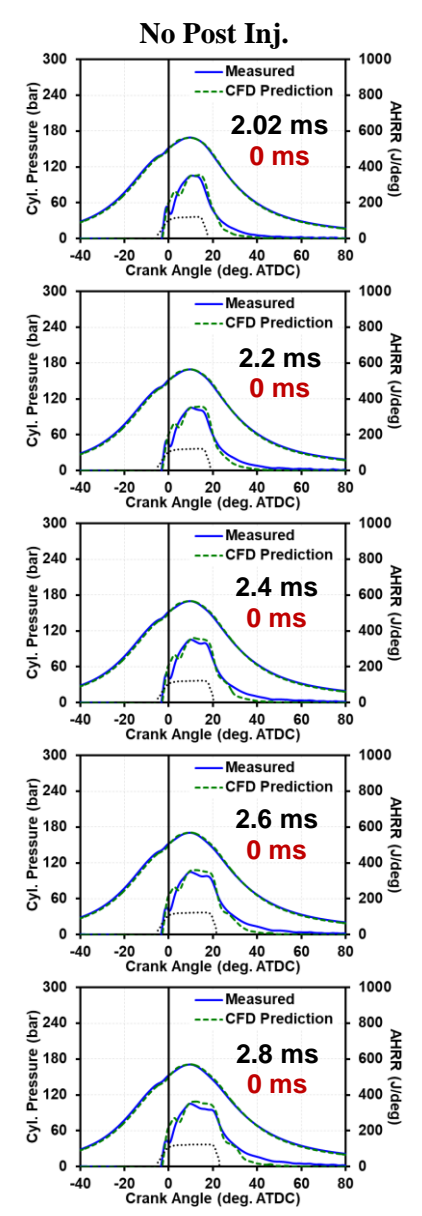


Figure 3-13. Comparison of cylinder pressure and AHRR for the 'no post injection' strategy across all the operating conditions studied.

Figure 3-14 shows the experimental and CFD predicted trends of GIE, NOx, and soot emissions at all the operating conditions for the three post injection strategies studied. Similar to the in-cylinder pressure and AHRR, a good agreement is seen between the measured and the CFD predicted GIE, NOx, and soot emissions in terms of trends and magnitudes. It is seen once again that, using pyrene as the inception species, the two-step soot model does an excellent job at predicting the soot trends and magnitudes without having to adjust the soot constants.

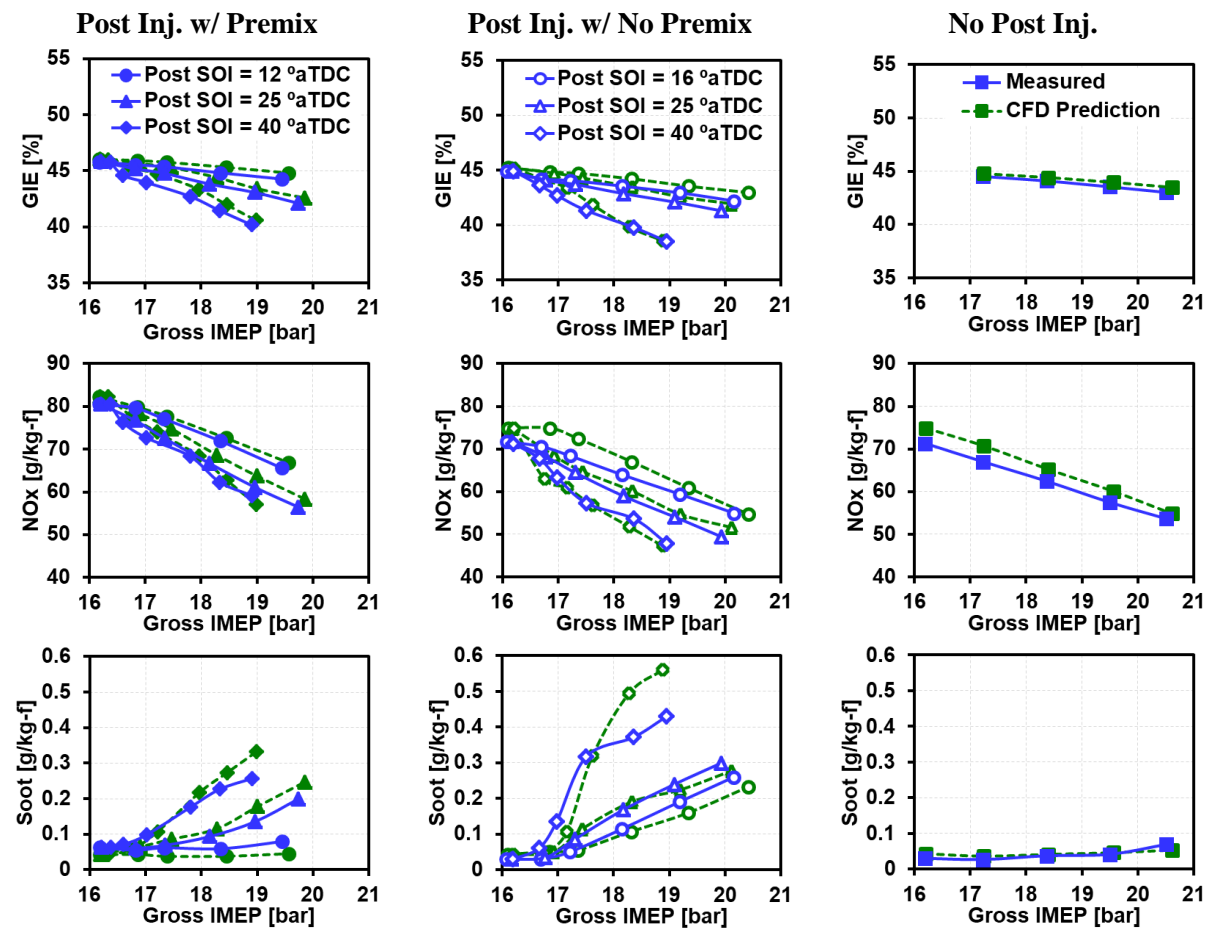


Figure 3-14. Comparison of GIE, NOx and soot emissions for the three injection strategies across all the operating conditions studied.

3.4.4. Summary of Model Validation

In the previous discussion, a wide range of operating conditions was covered during model-validation, over which the model has shown good agreement. To concisely demonstrate the efficiency of the CFD model in predicting the experimental results, Figure 3-15 shows the trends of the CFD predicted results versus the experimental results. Trends of GIE, NOx, and soot emissions are shown for operating conditions ranging from low-load to high-load that were covered during the model-validation study. A straight line with a slope of one would indicate a perfect match. Firstly, the range of the axis for the three outputs shows that a broad range of operating conditions was covered during the study. Secondly, looking at the R² values for the three outputs, it is seen that the model does a decent job at predicting the outputs over the wide range covered. The agreement shown in Figure 3-15 provides high confidence in the model

predictions. Accordingly, the model will be used to perform the optimization studies and to identify operating strategies for high-load-low-speed and low-load-high-speed conditions.

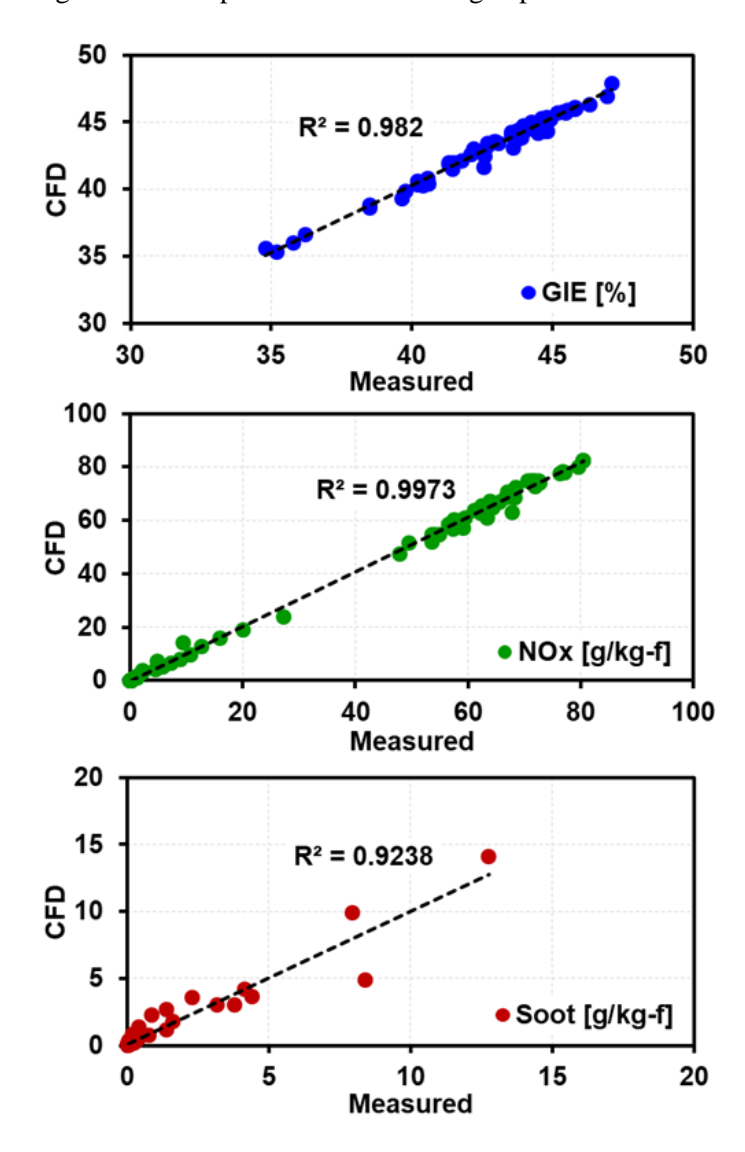


Figure 3-15. CFD predicted results vs. the experimental results over the range of operating conditions covered during model validation.

Chapter 4 Optimization Targeting High-Load-Low-Speed Operation

Experimental investigation of advanced combustion at high-load-low-speed conditions is challenging due to the high in-cylinder pressures. That is, if the operating conditions are selected incorrectly, the experimental setup could be damaged. Accordingly, this point was selected for the initial computational optimization to guide the complementary experimental effort. Optimizations were performed using the heavy-duty engine with a CR of 12:1 (specifications shown in Table 3-1), targeting a high-load low-speed condition of 20 bar and 1300 rev/min., with the RCCI and GCI strategies. All the studies presented in this chapter and the coming chapters will focus on this heavy-duty engine. A complete optimization study focused solely on a light-duty engine can be found in Appendix-A.

4.1. Operating Conditions and Optimization Setup

Past high-load optimization studies [54] with RCCI and GCI strategies have shown that the GA tends to pick the highest EGR point as the optima. This is because the closed cycle optimizations have minimal penalties for using EGR. However, to thoroughly evaluate the effects of air handling (e.g., EGR and intake pressure), the injection strategy must be fully optimized at each condition. Accordingly, instead of varying the intake pressure and EGR within the GA, a full factorial DOE of GA optimizations was setup at 20 bar IMEP and 1300 rev/min. for three fixed values of EGR (30%, 45%, and 55%) and equivalence ratio (Φ) (0.8, 0.9, and 1.0). Throughout this dissertation, EGR rate is defined as the ratio between the intake CO₂ and exhaust CO₂ concentration with the assumption of complete combustion of fuel. To get the intake charge composition, first, the temperature and pressure at IVC are used to calculate the density at IVC. The calculated density along with the premixed mass of fuel and the EGR rate is used to iteratively solve for the mole fractions at IVC. EGR is assumed to consist of complete combustion products (O₂, N₂, CO₂, and H₂O) only. The equivalence ratio for each case was set by the corresponding EGR and IVC pressure, as shown in Table 4-1. Though optimizations were performed at various combinations of EGR and Φ , the present discussion only focuses on the peak efficiency point. A more detailed analysis on the performance across the EGR and Φ space studied will be shown in Chapter 5 and can also be found in Kayuri et al. [58]. The injection strategies used for the optimization study are shown in Figure 4-1. The GA was allowed to

vary four design parameters each for the RCCI and GCI strategies. For the RCCI cases, the design parameters were

- 1. Fraction of the total gasoline that is premixed (Premix Gas. Frac),
- 2. Fraction of the total fuel that is gasoline; this includes premix and DI gasoline (Gas. Frac),
- 3. SOI of gasoline (SOI-Gas.),
- 4. SOI of diesel fuel (SOI-Diesel).

For the GCI cases, the design parameters were

- 1. Fraction of the total fuel that is premixed (Premix Frac);
- 2. Fraction of the total direct-injected fuel that is in the first injection (DI Frac);
- 3. SOI of first gasoline injection (SOI1-Gasoline);
- 4. SOI of second gasoline injection (SOI2-Gasoline);

The ranges for each design parameter are shown in Table 4-2. Optimizations were performed using the NSGA-II code with the aim of minimizing four objectives; ISFC, NOx, soot, and PPRR.

Table 4-1. Φ-EGR matrix for optimization setup. The values shown at each Φ-EGR location are the corresponding IVC pressures in bar.

corresponding 1 ve pressures in surv			
Φ [-] \ EGR [%]	30	45	55
0.8	2.93	3.76	4.6
0.9	2.61	3.35	4.12
1.0	2.36	3.03	3.72



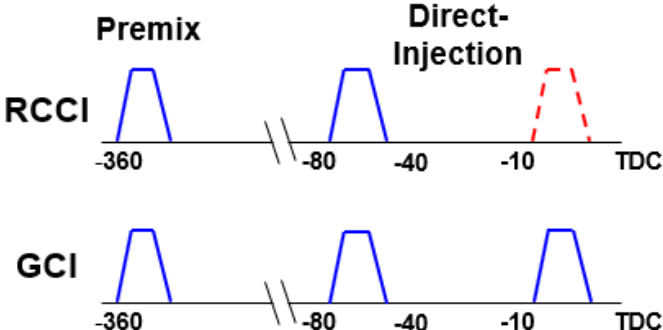


Figure 4-1. Injection strategy for RCCI and GCI combustion used in the optimization study.

Table 4-2. Range of variation allowed for each design parameter in the optimization study.

RCCI Strategy			
Design Parameter	Range		
Premix Gas. Frac [-]	0 to 1.00		
Gas. Frac [-]	0 to 1.00		
SOI-Gas. [°aTDC]	-100 to +40		
SOI-Diesel [°aTDC]	-100 to +40		
GCI Strategy			
GCI Strategy			
GCI Strategy Design Parameter	Range		
	Range 0 to 1.00		
Design Parameter			
Design Parameter Premix Frac [-]	0 to 1.00		

To fill the four-dimensional Pareto front, the GA's were setup to run for 50 generations with 96 citizens per generation at each Φ -EGR combination. For the matrix shown in Table 4-1, the total CFD calculations are 86,400 for the two combustion strategies combined with each run taking ~12 hrs.

4.2. Results and Discussion

The solutions for each Φ -EGR combination were filtered for cases with low emissions (NOx \leq 2g/kg-f, Soot \leq 2g/kg-f) and acceptable pressure rise rates (PPRR \leq 20 bar/deg). From these results, the cases with the maximum net indicated efficiency (NIE) were selected. The pumping loop work for the cases selected was estimated using a thermodynamic model, prepared in CANTERA [97], to allow the calculation of NIE. The details of the thermodynamic model are given in Appendix-C. Figure 4-2 shows contours of GIE and NIE in Φ -EGR space generated as a result of gridded interpolation between the optimum cases at each Φ -EGR combination. GIE increases with increasing intake pressure (decreasing Φ) and increasing EGR for both strategies. The high levels of EGR help in extending the chemistry timescales and achieving the optimal combustion phasing. The high intake pressure in combination with the high EGR helps achieve leaner mixtures. This provides enough oxygen to combust the fuel, thereby maintaining nearly 100% combustion efficiency. Hence, with increasing intake pressure and EGR, GIE is maximized. However, with increasing intake pressure, the pumping loop penalty also increases. At the lower EGR rates (30% EGR), the intake pressures are low, resulting in minimal pumping losses. As the EGR increases, to achieve the same equivalence ratios, higher intake pressures are needed, resulting in higher pumping losses. Despite

the increased pumping losses, the trends in NIE remained similar to those of GIE until an EGR rate of 55% and equivalence ratio of 0.9 for both the strategies. That is, the increase in GIE outweighed the increase in pumping losses. Operating at an EGR of 55% with an equivalence ratio leaner than 0.9 resulted in reduced NIE as the increase in pumping losses began to outweigh the increase in GIE. The tradeoff between increased intake pressure and losses from pumping work yields an optimum operating range that maximizes NIE while meeting the NOx, soot, and PPRR constraints. For the RCCI strategy, this range contains equivalence ratios from 0.8 to 0.93 and EGR rates from 43% to 55%. For the GCI strategy, the optimum space includes equivalence ratios from 0.85 to 0.92 and EGR rates from 53% to 55%. Though the optimum operating spaces are different for the GCI and RCCI strategies, within the range of equivalence ratios from 0.8 to 0.98 and EGR rates of 43% to 55%, the efficiencies differ by less than 1%. This is within the range of uncertainty for the gridded interpolation method used to generate the operating space maps. Similar contour plots were generated for the input parameters as well and the trends were explained using the COSSO tool [61]. The details of this study can be found in Kavuri et al. [58].

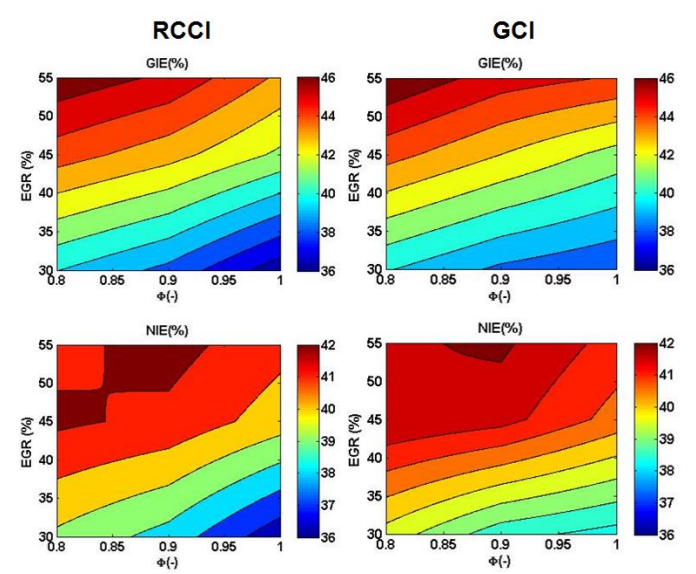


Figure 4-2. Comparison of contours of GIE and NIE generated from the best cases for RCCI and GCI strategies at each Φ-EGR combination.

To select a single optimum operating point for comparison of the RCCI and GCI strategies, the COSSO tool was used. COSSO fits a response surface model to the GA data from all the runs combined. From the model, the response surface equations for each objective were generated and used to predict the

output for a given set of input parameters. This allowed EGR and intake pressure to be used as inputs to the model in addition to the parameters shown in Table 4-2, thereby enabling coverage of the entire Φ-EGR design space. The COSSO models were exercised using a DOE approach to identify the cases with maximum NIE, NOx $\leq 2g/kg-f$, soot $\leq 2g/kg-f$, and PPRR ≤ 20 bar/deg. Table 4-3 shows the operating conditions for the optimum points chosen from the COSSO DOE study for the RCCI and GCI strategies. The optimum points were simulated with the KIVA code using the fine mesh shown in Figure 3-2 to verify the COSSO results. Figure 4-3 shows a comparison of the COSSO predicted and KIVA simulated results of the optimum points for the RCCI and GCI strategies. The COSSO model gives a good agreement in trends with the KIVA simulated results for both the combustion strategies. The magnitudes differ slightly between the COSSO and KIVA results, but the trends are consistent. The optimum strategies for the RCCI and GCI cases are similar. Most of the fuel (~70%) is introduced early into the combustion chamber in the form of premixed fuel and an early injection at -100 °aTDC and -78 °aTDC for the GCI and RCCI strategies respectively. The rest of the fuel is injected as a stratified injection close to TDC at -14 °aTDC and -12 °aTDC for the GCI and RCCI strategies respectively. The optimums for both the strategies were similar in terms of air handling as well. Both required an EGR of 55%, with the RCCI optimum having a slightly higher intake pressure. It is to be noted that the optimum points fall in the optimum EGR and equivalence ratio range observed in Figure 4-2 for the RCCI strategy. However, for the GCI strategy, the equivalence ratio is slightly outside the range. This could be because Figure 4-2 was generated as an approximation based on a gridded interpolation of the best cases at each EGR and equivalence ratio combination. These results show that the upper limit of optimum operation range of equivalence ratio extends up to 0.98, rather than 0.92, as pointed out earlier from Figure 4-2, for the GCI strategy.

INPUTS		
Design Parameter	RCCI Optimum	GCI Optimum
Premix Gas. Frac (-)	0.63	1
Gas. Frac (-)	0.72	1
SOI-Gas. (°aTDC)	-78	ı
SOI-Diesel (°aTDC)	-12	1
Premix Frac (-)	-	0.56
DI Frac (-)	-	0.46
SOI-Gas.1 (°aTDC)	-	-100
SOI-Gas.2 (°aTDC)	-	-14
EGR (%)	55	55
Φ (-)	0.93	0.98
IVC-Pressure (bar)	3.97	3.79
OUTPUTS		
GIE (%)	46.3	45.6
NIE (%)	43.8	44.1
NOx (g/kg-f)	0.3	0.08
Soot (g/kg-f)	1.78	0.17
PPRR (bar/deg)	19.91	17.1

Table 4-3. Comparison of optimum points for the RCCI and GCI strategies.

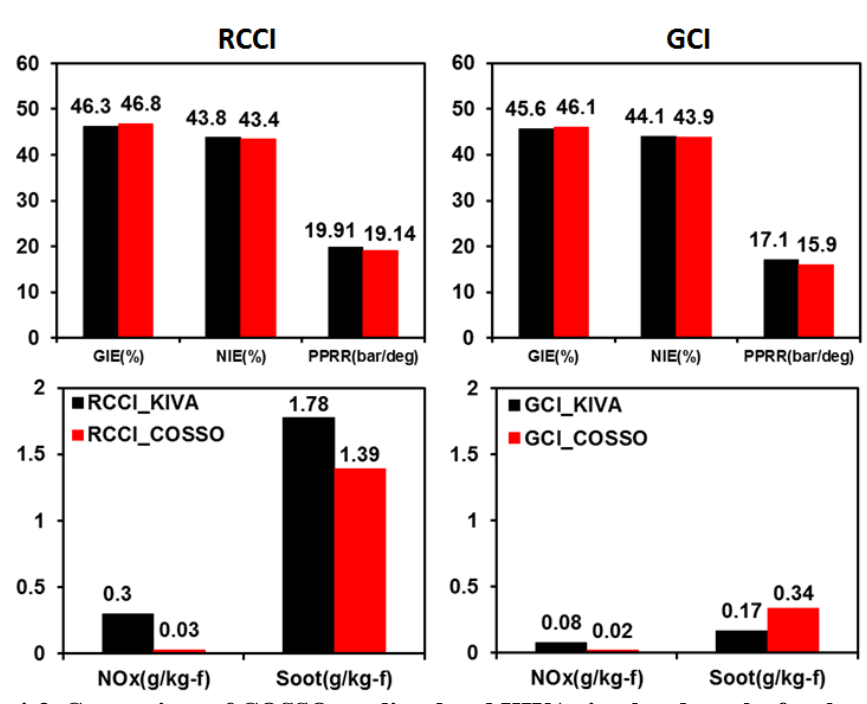


Figure 4-3. Comparison of COSSO predicted and KIVA simulated results for the optima.

4.2.1. Experimental Validation

The optimum points from the DOE study were verified with single cylinder engine experiments run by Jordan Paz [49]. Figure 4-4 shows the measured and model predicted in-cylinder pressure and AHRR for the RCCI and GCI optimum points.

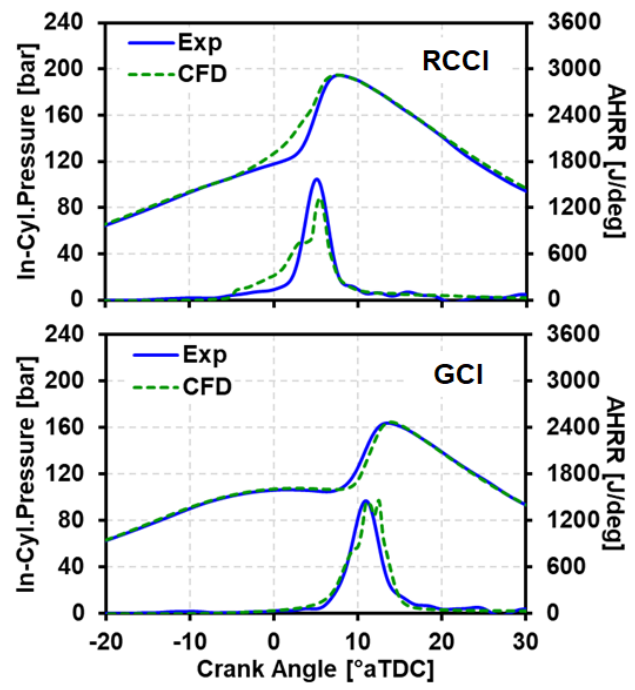


Figure 4-4. Measured and CFD predicted cylinder pressure and apparent heat release rate for the RCCI and GCI optimum points.

For both combustion strategies, the model predicts the combustion duration reasonably well. The peak heat release is accurately predicted for the GCI strategy while it is slightly under-predicted for the RCCI strategy. This difference in peak heat release for the RCCI strategy could be due to mixing effects since the combustion from the diesel fuel injection for this strategy is mixing-controlled. For the GCI strategy, the model predicted start of combustion matches accurately with the experiments. Whereas, for the RCCI strategy, there are slight differences in the rising part of the heat release.

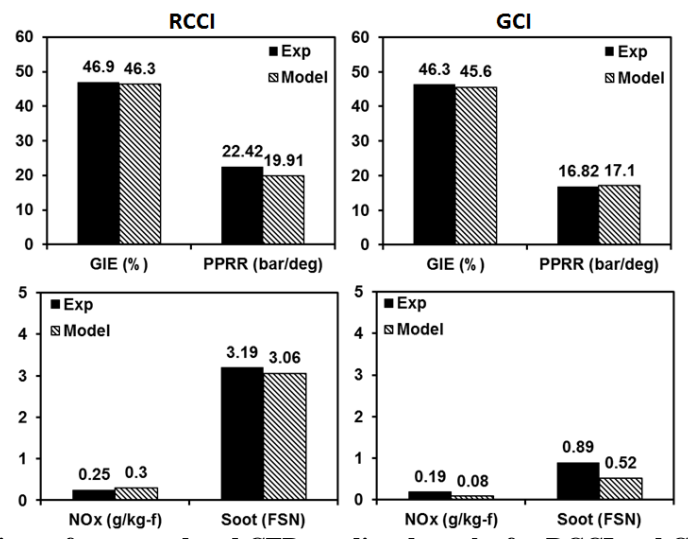


Figure 4-5. Comparison of measured and CFD predicted results for RCCI and GCI optimum points.

Figure 4-5 shows a comparison of the measured and model predicted GIE, PPRR, soot, and NOx emissions for the RCCI and GCI optimum points. For both the combustion strategies, the model agreement with experiments, for all the outputs, is considered acceptable. Soot magnitudes are slightly under-predicted by the model, but the model accurately predicts the trends in soot shown by the two combustion strategies. Note that the soot model parameters were held constant for this study. Despite the slight differences, the model does a decent job of predicting the overall combustion characteristics of the two combustion strategies studied. Accordingly, the model will be used to explain the sources of the differences and similarities in combustion and emissions characteristics of the two strategies.

4.2.2. RCCI-GCI Comparison

With the validated optimum points, the combustion characteristics of the two strategies were compared using the CFD model. Further analysis was performed to identify the input parameters that provide control over combustion for the two strategies. Finally, an operating condition sensitivity study was performed. In this analysis, the sensitivity to fluctuations in operating conditions on each output was studied. The results from these studies are shown in the following sections.

4.2.2.1. Combustion Characteristics

From Figure 4-4, it can be seen that the AHRR profiles are similar for the two strategies, but the RCCI strategy has a significantly shorter ignition delay than the GCI strategy. To explain the combustion characteristics, Figure 4-6 shows a comparison of the in-cylinder evolution of several key species for the RCCI and GCI strategies. The heat release rate, average in-cylinder temperature, and injection velocity are also shown to explain the species trends. Figure 4-7 and Figure 4-8 show cut planes colored by temperature, equivalence ratio, mass fractions of iso-octane, n-heptane (RCCI only), formaldehyde (CH₂O), and OH for the RCCI and GCI combustion strategies respectively. The species profiles of the two strategies are very similar. For both the strategies, formaldehyde starts forming around -30 °aTDC, which coincides with the low temperature consumption of iso-octane from the first gasoline injection. In Figure 4-7 and Figure 4-8, at -9 °aTDC and 6 °aTDC respectively, there is a high concentration of iso-octane in the squish region. This is from the first gasoline injection for both the strategies. The location of this concentration of iso-octane

coincides with the location of the peak concentration of formaldehyde. This indicates that the low temperature consumption of gasoline (represented in the simulations by iso-octane) from the first injection, is the source of formaldehyde formation. The near TDC injections have an ignition delay period (longer for GCI than RCCI) during which the formaldehyde mass fraction continues to increase. This is from the low temperature consumption (the heat release is still close to zero, and the in-cylinder temperatures are less than 1000 K) of n-heptane and iso-octane for the RCCI and GCI strategies respectively. For the RCCI strategy, once the thermal ignition of n-heptane occurs, which is marked by the sharp increase in in-cylinder temperature, the iso-octane consumption speeds up considerably. Iso-octane consumption tracks with formaldehyde consumption and OH accumulation, which does not occur until the high temperature ignition of n-heptane. This indicates that the near TDC diesel fuel injection initiates the combustion for the RCCI strategy. This can also be seen from Figure 4-7 at -4 °aTDC and 0 °aTDC, where the consumption of nheptane causes the increase in temperature leading to the consumption of iso-octane present in the bowl. The locations of iso-octane consumption correspond with the locations of increasing OH and reducing formaldehyde concentration. The energy release spreads into the squish to consume the iso-octane from the first gasoline injection. These clearly results show the two-staged combustion for the RCCI strategy initiated by the near TDC diesel fuel injection.

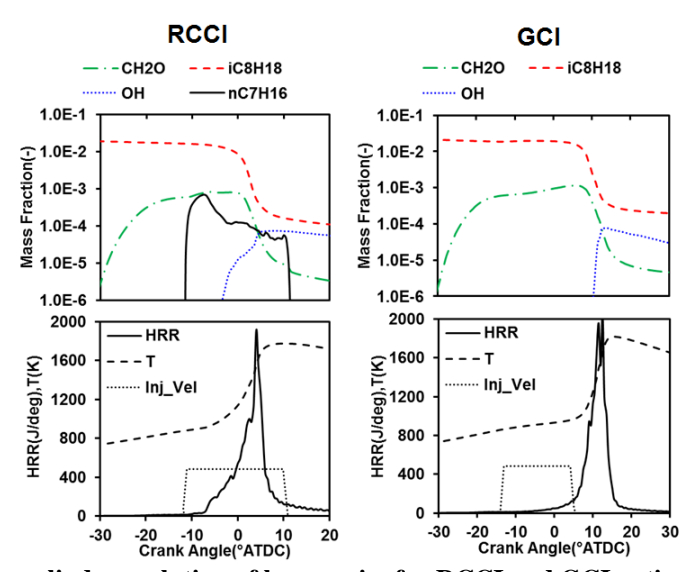


Figure 4-6. In-cylinder evolution of key species for RCCI and GCI optimum strategies.

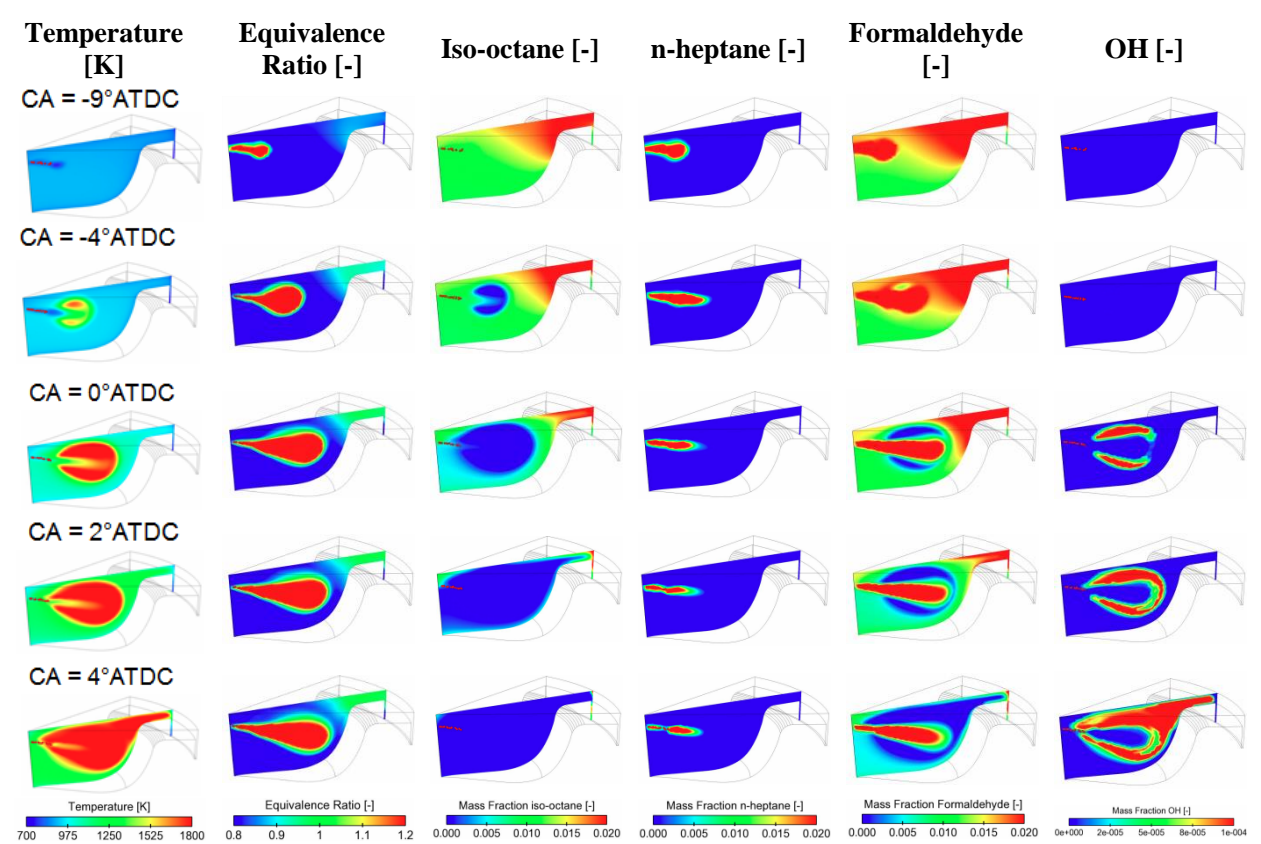


Figure 4-7. In-cylinder temperature, equivalence ratio, mass fraction of iso-octane, formaldehyde, and OH contours for the optimum RCCI point.

A similar fuel distribution in the combustion chamber as the RCCI case is seen for the GCI strategy as well, as shown in Figure 4-8. For the GCI strategy, when the near TDC gasoline injection at -14 °aTDC is introduced, the local equivalence ratio in the combustion chamber increases. The equivalence ratio contours in Figure 4-8 show a fuel rich region formed in the center of the bowl with regions of Φ equal to unity along the edge of the fuel rich region. These regions are a result of the interaction of DI gasoline with the premixed fuel present in the bowl. This region initiates the combustion. This can be seen from the temperature contours at 6 °aTDC and 8 °aTDC where a gradient in temperature is visible around the fuel rich region, with the regions of Φ equal to unity having the highest temperatures. Two crank angles later, at 10 °aTDC, the rest of the DI fuel mass combusts. The energy release from this combustion event progresses throughout the combustion chamber rapidly, igniting the fuel in the squish and the rest of the premixed fuel in the bowl. Similar to the RCCI strategy, the high temperature consumption of iso-octane is marked by a simultaneous increase in OH concentration and reduction in formaldehyde concentration, as

shown in Figure 4-6. However, this does not occur until the thermal ignition of the near TDC gasoline injection. In Figure 4-8, comparing the regions of high temperature (formed from the ignition of the near TDC gasoline ignition) with the locations of formaldehyde consumption and OH accumulation, it is seen that they occur at the same locations. This indicates that similar to the RCCI strategy, a two-staged combustion occurs for the GCI strategy as well, with the near TDC gasoline injection initiating the combustion event.

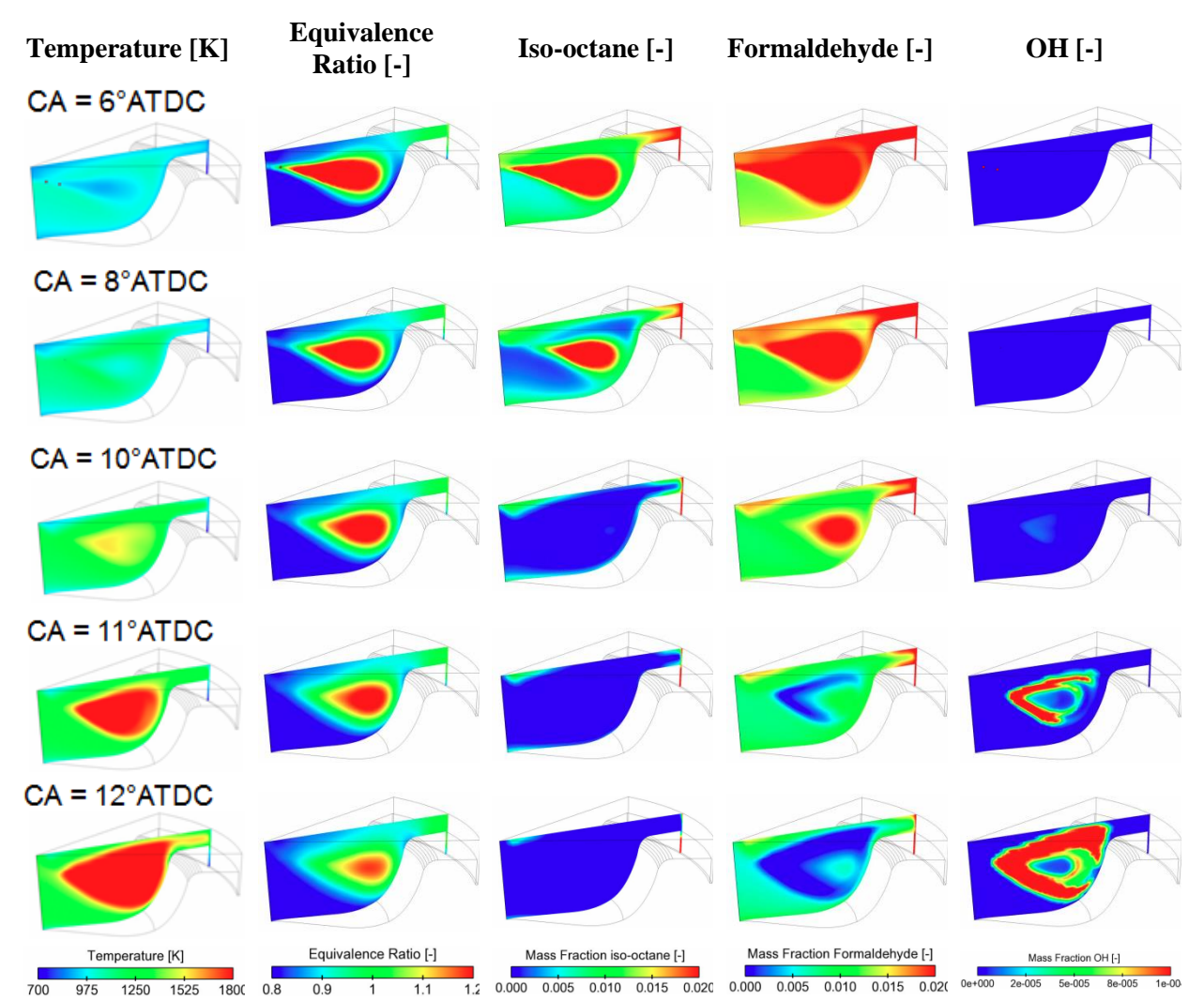


Figure 4-8. In-cylinder temperature, equivalence ratio, mass fraction of iso-octane, formaldehyde, and OH contours for the optimum GCI point.

Though slight differences exist in the heat release rates, the overall combustion characteristics are very similar, with the near TDC injection initiating the combustion for both the strategies. Soot emissions are the primary difference between the optimum RCCI and GCI strategies. The difference in soot emissions

between the two strategies is explained by investigating the state of the in-cylinder charge in equivalence ratio – temperature $(\Phi$ -T) coordinates. Φ is the local equivalence ratio, evaluated as

$$\Phi = \frac{4[C] + [H]}{2[O]},\tag{13}$$

where [C], [H], and [O] are the moles of carbon, hydrogen, and oxygen respectively. Figure 4-9 shows the Φ -T diagrams for the optimum RCCI and GCI cases at several crank angles after the start of combustion (°ASOC). The regions producing NOx and soot in Φ -T space, identified from HCCI simulations of mixtures of gasoline and air, are overlaid on the plot. The outer most contour of each region shows soot and NOx of 2 g/kg-f.

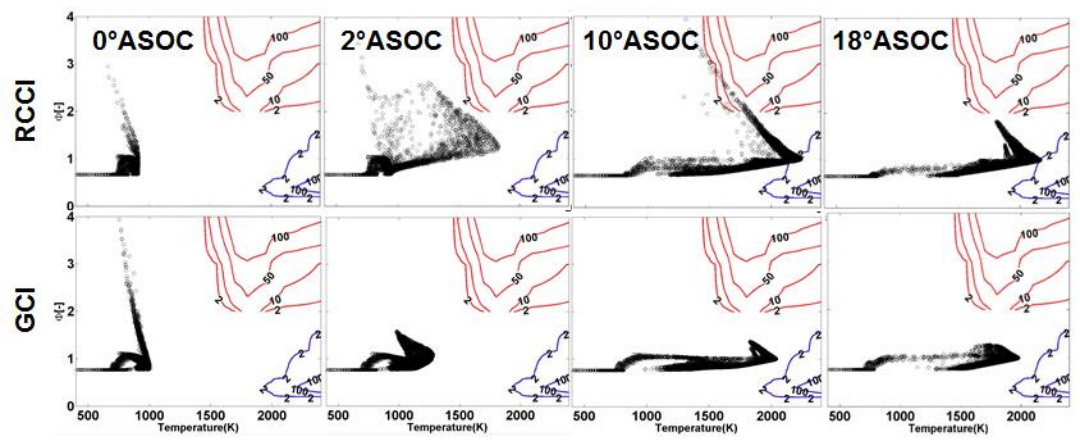


Figure 4-9. Φ-T plots of the in-cylinder mixture at various crank angles after start of combustion (°ASOC) for the optimum RCCI and GCI combustion strategies. The symbols show the equivalence ratio, and temperature in each computational cell and the lines show NOx (lower right on each diagram) and soot (upper right on each diagram) islands.

Though the SOI timings of the near TDC injection are very similar for both the combustion strategies, the more prolonged ignition delay of gasoline compared to diesel fuel, delays the start of combustion for the GCI strategy. The ignition delays of the RCCI and GCI case are 6 °CA and 16 °CA respectively. The shorter ignition delay of diesel fuel causes combustion to occur during the injection event for the RCCI strategy. At 10 °ASOC (near the 50% burn location for both cases), the final diesel fuel injection of the RCCI case is ~60% complete, and this case has regions in the combustion chamber with equivalence ratios above 3. In contrast, the final gasoline injection of the GCI case has been finished for 7 °CA, and post injection mixing has reduced the peak equivalence ratio to ~1.2. The higher local equivalence

ratios during combustion results in higher soot formation for the RCCI strategy in comparison to the GCI strategy. The high EGR levels result in peak temperatures of 2242 K and 2056 K, for the RCCI and GCI cases respectively. The low peak temperatures explain the low NOx emissions.

4.2.2.2. Control Parameters

Though the optimum points indicate good performance for both the combustion strategies, combustion control can be a challenge for highly premixed strategies. To evaluate the control of combustion phasing, a parametric simulation study was performed for both the combustion strategies where every input was varied fixing the rest of the inputs at the optimum value. The range of variation of the inputs is shown in Table 4-4. EGR was not chosen as an input for the parametric study because the timescale for EGR changes is long (on the order of 10 engine cycles), making it a poor control variable. Figure 4-10 shows the variation in combustion phasing (CA50) with each control parameter, for the RCCI and GCI strategies. A steeper slope indicates better control over combustion phasing. For the RCCI strategy, it is evident that the SOI of diesel fuel is the primary control parameter. The response of SOI-Diesel is 0.56° CA50 per degree SOI-Diesel. CA50 is insensitive to the rest of the inputs for the RCCI strategy. It is interesting to see that, gasoline fraction, which was found to be a strong control parameter in earlier RCCI studies [98, 99], shows little control over combustion (0.13° CA50 per percent of gasoline fraction) under the operating conditions of the parametric study. This could be because, under these conditions, the ignition delay of diesel fuel is so short that it combusts immediately upon injection irrespective of the quantity of diesel fuel being injected.

Table 4-4. Range of variation of inputs for the RCCI and GCI parametric study.

RCCI Strategy			
Design Parameter	Range	Step Size	Optima
Premix Gas. Frac (-)	0.4 to 0.7	0.01	0.63
Gas. Frac (-)	0.5 to 0.8	0.01	0.72
SOI-Gas. (°ATDC)	-95 to -65	2	-78
SOI-Diesel (°ATDC)	-30 to 0	2	-12
GCI Strategy			
Design Parameter	Range	Step Size	Optima
Premix Frac (-)	0.4 to 0.7	0.01	0.56
DI Frac (-)	0.3 to 0.7	0.01	0.46
SOI1-Gas. (°ATDC)	-100 to -65	5	-100
SOI2-Gas. (°ATDC)	-30 to 0	2	-14

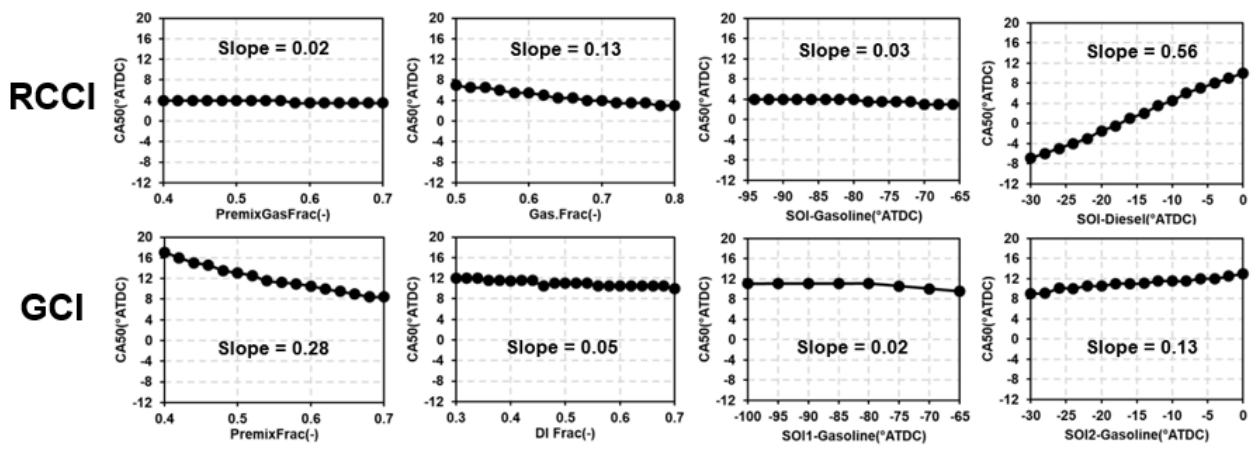


Figure 4-10. Combustion phasing (CA50) as a function of inputs for the RCCI and GCI strategies.

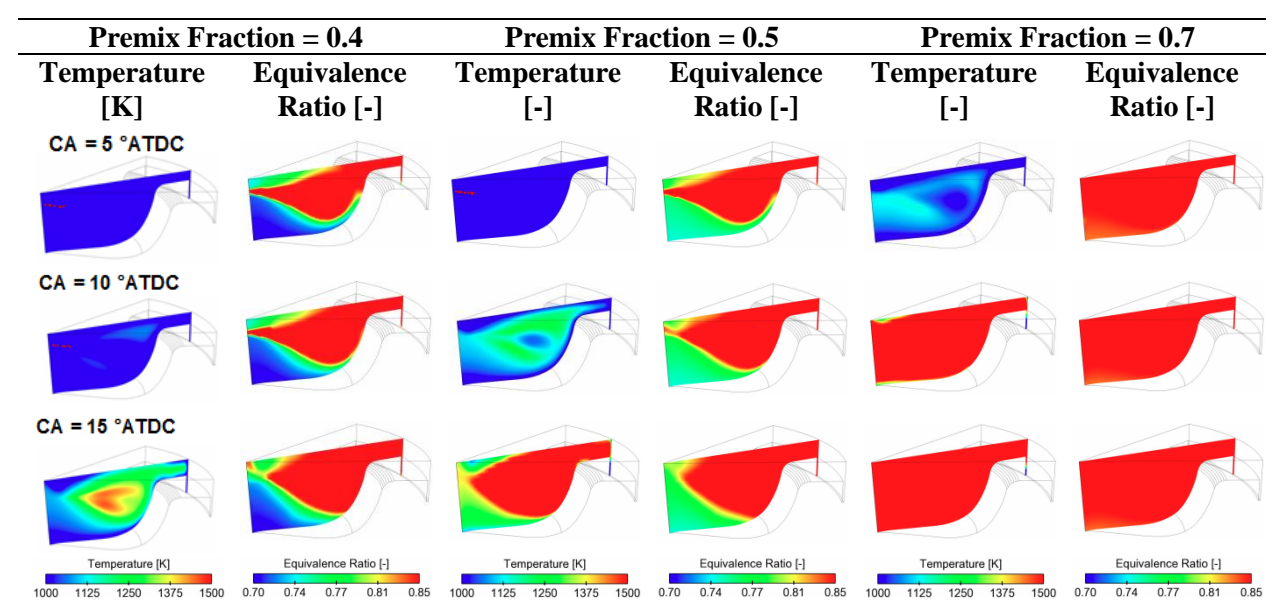


Figure 4-11. In-cylinder temperature and equivalence ratio contours for the GCI strategy at three different premix fraction values.

For the GCI strategy, the premix fraction and the SOI of the second gasoline injection provide similar control over combustion phasing. Although the premix fraction gives a higher slope than SOI2-Gasoline, excessively high PPRR (>20 bar/deg) was observed at premix fractions greater than 0.5. This makes premix fraction a less desirable control parameter than SOI2-Gasoline. To explain the rapid increase in PPRR with increasing premixed fraction, Figure 4-11 shows the in-cylinder temperature and equivalence ratio contours for the GCI strategy, at three different premix fraction values. The figure shows a transition to homogenous combustion at a premix fraction of 0.7, where the entire combustion chamber combusts at

once. Therefore, SOI2-Gasoline is considered the preferable control parameter. The response of SOI2-Gasoline is 0.13° CA50 per degree SOI2-Gasoline.

Additional engine experiments were performed by Jordan Paz [49] for both the combustion strategies, at two SOI timings, one degree before and after the optimum SOI value, to verify the control of RCCI and GCI combustion at high-load-low-speed conditions. Advancing or retarding the SOI timing more than one degree from the optimum value caused excessively high soot emissions and PPRR respectively. This limited the range of SOI timing for the experimental study, unlike the simulations, where a more extensive range of SOI timings was studied. Figure 4-12 shows the experimental and model predicted CA50 as a function of SOI-Diesel and SOI2-Gasoline, for the RCCI and GCI strategies respectively. Good agreement is seen between the experimental and simulated CA50 for both the strategies. Comparing the two strategies, the RCCI strategy shows stronger control over combustion phasing than the GCI strategy. This is directly related to the close coupling between SOI-Diesel and the start of combustion. In contrast, the longer ignition delay of the GCI case reduces the level of control over combustion phasing. Recall that the short ignition delay of the RCCI case resulted in significantly higher soot emissions than the GCI case. This comparison highlights a tradeoff in soot emissions and combustion phasing control.

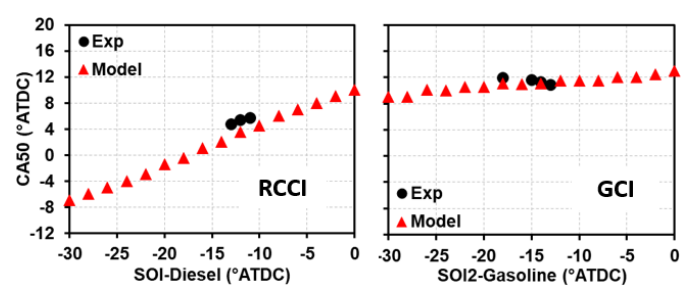


Figure 4-12. Experimental and model predicted CA50 as a function of SOI-Diesel and SOI2-Gasoline for the RCCI and GCI strategies.

4.2.2.3. Operating Condition Sensitivity

The previous sections showed that controllable RCCI and GCI operation is achievable at 20 bar IMEP and 1300 rev/min. However, other work has shown that cycle-to-cycle variation can be problematic for PCI strategies [57]. Cycle-to-cycle variability may stem from bulk fluctuations in charge conditions (e.g., operating parameter variations) and fueling rates or local fluctuations in the mixture conditions due

to turbulence. The present work focuses on identifying potential sources due to sensitivity to fluctuations in charge conditions and fueling rates.

A sensitivity analysis was performed by running full factorial DOE's about the optimum RCCI and GCI conditions. The baseline value and the DOE range of each operating condition are shown in Table 4-5. The rest of the inputs are fixed at the values shown in Table 4-3. The results from the DOE were used to build a response surface model (RSM) as described in Klos et al. [57]. A full quadratic response surface model with linear, squared, and interaction terms was used. All variables had R² values higher than 0.98 and maximum errors less than 3%, indicating that the RSM model is very accurate in the range of conditions considered in Table 4-5. The details of the model coefficients and the term each coefficient multiplies can be found in Kavuri et al. [49]. The sensitivity analysis is then performed by taking the partial derivative of the RSM equations of each objective with respect to each input parameter.

Table 4-5. Baseline value and the range of fluctuation of each operating condition.

Operating Condition	Baseline RCCI	Baseline GCI	Range
$T_{ivc}(K)$	406	406	± 3
P _{ivc} (bar)	3.97	3.79	± 0.05
EGR (%)	55	55	± 2
Premix Fuel Mass (mg/cycle)	108	135	± 4
DI Fuel Mass (mg/cycle)	133	106	± 4

The results of this analysis are shown in Figure 4-13. The first observation that can be made is that both the strategies are very sensitive to fluctuations in EGR. This is in contrast with the study performed by Klos et al. [57] at a mid-load condition where they found the RCCI strategy to be insensitive to EGR. Notice that the GCI strategy is more sensitive to EGR than the RCCI strategy. The global equivalence ratio of the GCI strategy is 0.98 (i.e., nearly stoichiometric), causing it to be very sensitive to oxygen concentration. An increase in EGR from 55% to 56% leads to fuel rich operation, which causes a substantial decrease in GIE, as shown in Figure 4-13. In comparison, for the RCCI strategy, the global equivalence ratio is 0.93, which makes the sensitivity to EGR slightly lower than that of the GCI strategy. In addition to EGR, IVC temperature and pressure also affect the combustion phasing considerably for the GCI strategy, whereas, the RCCI strategy is relatively insensitive to these fluctuations. Like EGR, fluctuations in IVC pressure also affect oxygen concentration, which explains the sensitivity of the GCI strategy to IVC

pressure. To explain the difference in IVC temperature sensitivity, Figure 4-14 shows calculated constant volume ignition delays for stoichiometric mixtures of gasoline and diesel fuel, with air and EGR, at 80 bar (i.e., similar to the TDC pressure of the two cases). The relevant range of temperatures near TDC for both the cases is in the range of 850 K to 1000 K. The combustion phasing of the GCI and RCCI strategies are controlled by the ignition delay of the near TDC injected gasoline and diesel fuel respectively. Figure 4-14 shows that, in the relevant temperature range, the sensitivity of gasoline ignition delay to temperature is 0.043 ms/K. On the other hand, due to the NTC behavior of diesel fuel, the sensitivity of diesel fuel is 0.002 ms/K. Accordingly, the GCI strategy is sensitive to fluctuations in the IVC temperature while the RCCI strategy shows minimal sensitivity.

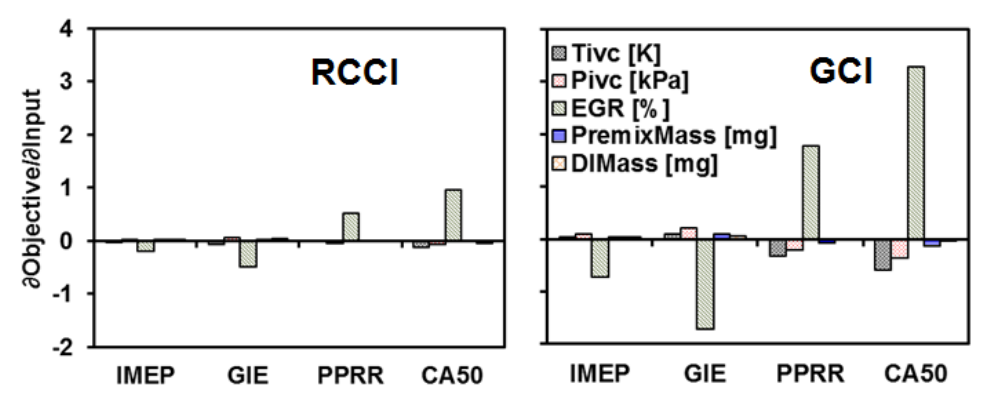


Figure 4-13. Sensitivity of outputs to changes in inputs for RCCI and GCI strategies.

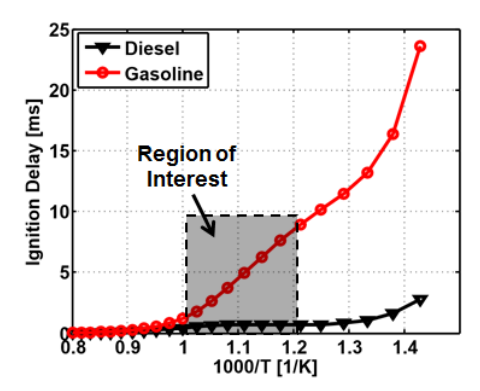


Figure 4-14. Ignition delay vs. 1000/T from constant volume simulations.

4.2.3. Conclusions

In this chapter, RCCI and GCI combustion strategies were compared at a high-load-low-speed operating condition of 20 bar IMEP and 1300 rev/min. GA optimizations were performed for the two combustion strategies, and the respective optimums were compared in terms of combustion and

performance characteristics. Further analysis was done to study the effect of input and operating condition variation on combustion control, performance, and combustion stability. The results showed that both combustion strategies have similar combustion characteristics with a near TDC injection initiating and controlling the combustion phasing. However, the RCCI strategy was found to have better control over combustion phasing than the GCI strategy. The increased control was found to be due to the shorter ignition delay of diesel fuel compared to gasoline. This benefit, however, comes at the expense of increased soot emissions, as the combustion event occurs during the near TDC injection event. The longer ignition delay of the GCI strategy results in less control over combustion phasing but enables near-zero soot emissions. In terms of other performance parameters, both strategies were found to have high GIE (47%) with near zero NOx emissions. The RCCI strategy was found to have a higher PPRR than the GCI strategy due to advanced combustion phasing, but it was still within reasonable operation level (PPRR ≤ 20 bar/deg) for high-load operation in a heavy-duty engine. The sensitivity analysis showed that both strategies were most sensitive to fluctuations in EGR with the GCI strategy being more sensitive than the RCCI strategy.

Chapter 5 Constraint Analysis on High-Load-Low-Speed Operation with RCCI Combustion

In the previous chapter, feasible operating strategies were identified for RCCI and GCI combustion at high-load-low-speed conditions. However, due to operation at a high EGR rate and near stoichiometric global Φ , both the strategies showed strong sensitivity to EGR fluctuations, which makes these strategies difficult to implement in production applications. Furthermore, operation under high EGR rate is a burden on the air handling system, and it would be preferable to operate at a reduced EGR rate. Both these points motivate the need to identify high-load operating strategies that work at reduced EGR rates and leaner global Φ 's.

In the high-load optimization study shown in Chapter 4, the optimum operating strategy was identified as the case with the maximum NIE that met the constraints of NOx \leq 2g/kg-f, Soot \leq 2g/kg-f and ringing intensity (RI) ≤ 5 MW/m². Operating under these constraints could have negatively affected the efficiency at the low and moderate levels of EGR. The RI constraint is a necessity to prevent the structural damage of the engine parts. However, the constraints on NOx and soot emissions could be relaxed by using after-treatment devices if it offers significant efficiency benefits. Accordingly, in the present study, the effect of removing these constraints on the efficiency in EGR-Φ operating space is investigated. The constraints on NOx and soot emissions are removed alternatively while keeping the other two constraints fixed (i.e., when the NOx constraint is removed, the soot and RI constraints are fixed and vice versa). The motivation of the study is to investigate if removing either of these constraints improves the efficiency in the low and moderate EGR operation range while meeting the remaining constraints. This could enable high-load operation at lower levels of EGR than the GA optima shown in Chapter 4. If significant benefits are observed from removing either the NOx or the soot constraint, the highest efficiency point upon removing the constraint shall be identified. This case shall be compared with the high EGR optimum operating point from Chapter 4 in terms of combustion characteristics, combustion control and stability. Investigation of high-load-low-speed operating strategies at reduced EGR rates keeping all the constraints intact was also performed. The details of this study can be found in Kavuri et al. [100].

In Chapter 4, RCCI and GCI combustion were shown to be similar in terms of combustion characteristics at high-load-low-speed conditions. However, the RCCI strategy had superior control over combustion phasing and higher stability to operating parameter variations compared to the GCI strategy. Since these factors are essential for the practical implementation of any advanced combustion strategy, it can be said that the RCCI strategy is better suited than the GCI strategy for high-load-low-speed operation. Accordingly, the constraint analysis presented in this chapter will focus solely on the RCCI strategy.

5.1. Results

As explained in the previous section, the constraints on NOx and soot emissions were removed while keeping the other two constraints intact. From this data-set, the highest efficiency point was chosen at each EGR and Φ combination to see if it results in an efficiency benefit in the lower EGR regions. Figure 5-1 shows a comparison of the GIE and NIE for the cases with no NOx constraint (only the soot and RI constraints), no soot constraint (only the NOx and RI constraints), and with all constraints (NOx, Soot, and RI constraints) intact at each EGR and Φ combination.

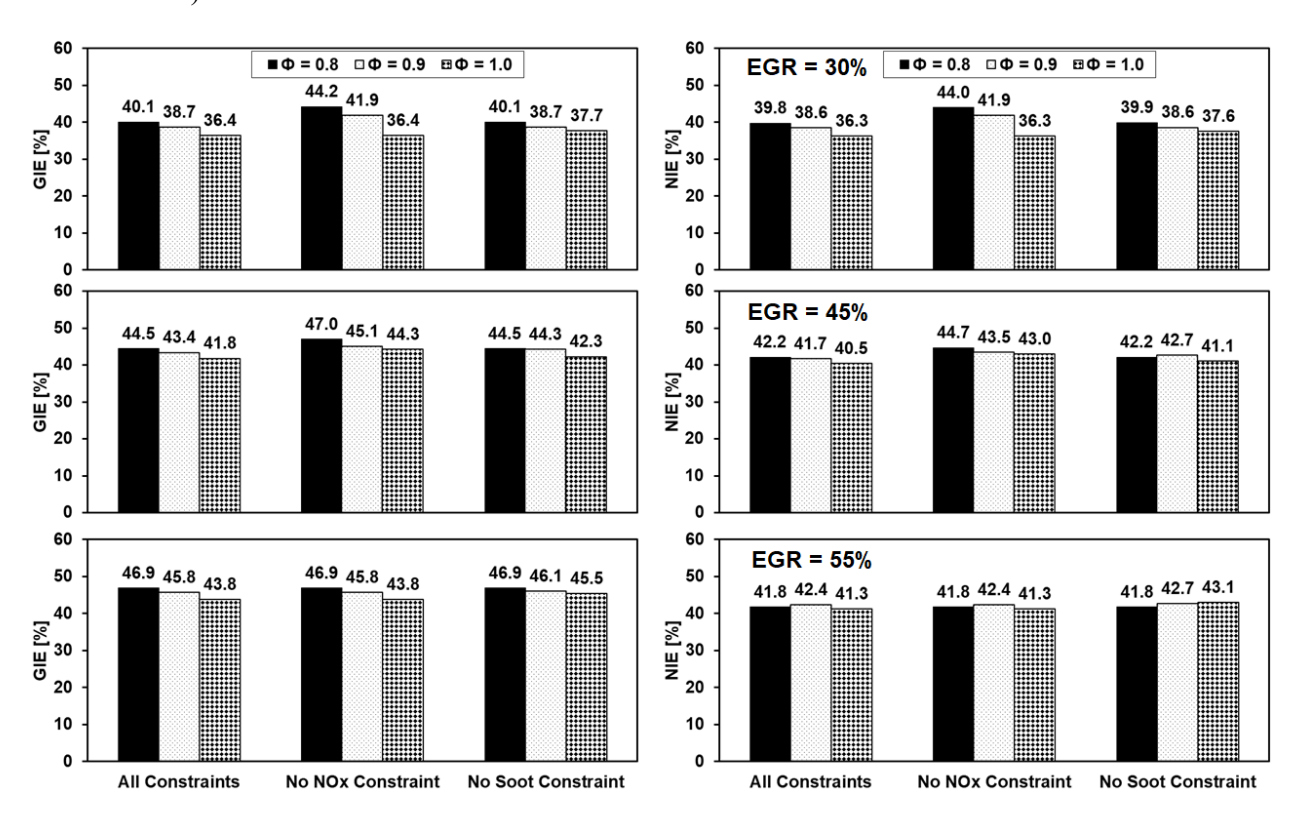


Figure 5-1. Comparison of GIE and NIE for cases with all constraints (NOx, soot, and RI) intact, no NOx constraint and no Soot constraint at each EGR and Φ combination.

Figure 5-1 shows that removing the NOx constraint results in a significant improvement in GIE and NIE at EGR of 30% and 45%. The maximum increases in efficiency are seen at the leanest Φ (Φ = 0.8) (or the highest intake pressure) cases. The improvement in efficiency reduces as EGR or Φ increases. Eventually, at an EGR of 55%, removing the NOx constraint does not result in any improvement in efficiency. On the contrary, removing the soot constraint results in the opposite trends. Without the soot constraint, increases in efficiency are seen mainly at the high EGR (45% and 55%) and high Φ (0.9 and 1.0) operating points. The improvement in efficiency increases with increasing EGR and Φ when the soot constraint is removed.

Contour plots of NIE were generated to identify the regions in EGR and Φ operating space where an efficiency benefit is seen from removing the NOx and soot constraints. The contour plots are the result of a gridded interpolation performed between the optimum cases shown in Figure 5-1. From these results, a percentage increase in NIE (Δ NIE %) is estimated as

$$\Delta NIE \% = \frac{NIE_{ConstraintRemoved} - NIE_{AllConstraintsIntact}}{NIE_{AllConstraintsIntact}}, \tag{14}$$

Figure 5-2 shows the contour plots of NIE and the Δ NIE% as a function of EGR and Φ , compared between the cases with all constraints intact, no NOx constraint, and no Soot constraint. Removing the NOx constraint resulted in increased NIE over the majority of EGR and Φ operating space for EGR rates less than 50%. A substantial increase (\geq 5%) in NIE is seen in the EGR and Φ range of 30% to 45% and 0.8 to 0.94, respectively. A peak increase in NIE of 10% occurs at 30% EGR and Φ of 0.8. Removing the NOx constraint results in a maximum NIE of 44.71%, and this occurs at an EGR of 45% and Φ of 0.8. Interestingly, this value is higher than the peak NIE (43.8%) observed from the high EGR (55%) optima at the same high-load-low-speed operating condition. Removing the soot constraint does not result in as significant an increase in NIE as removing the NOx constraint. This is evident from the Δ NIE% plot shown in Figure 5-2. Without the soot constraint, a reasonable increase (~5 %) in NIE is seen in the EGR and Φ range of 50%-55% and 0.96-1 respectively.

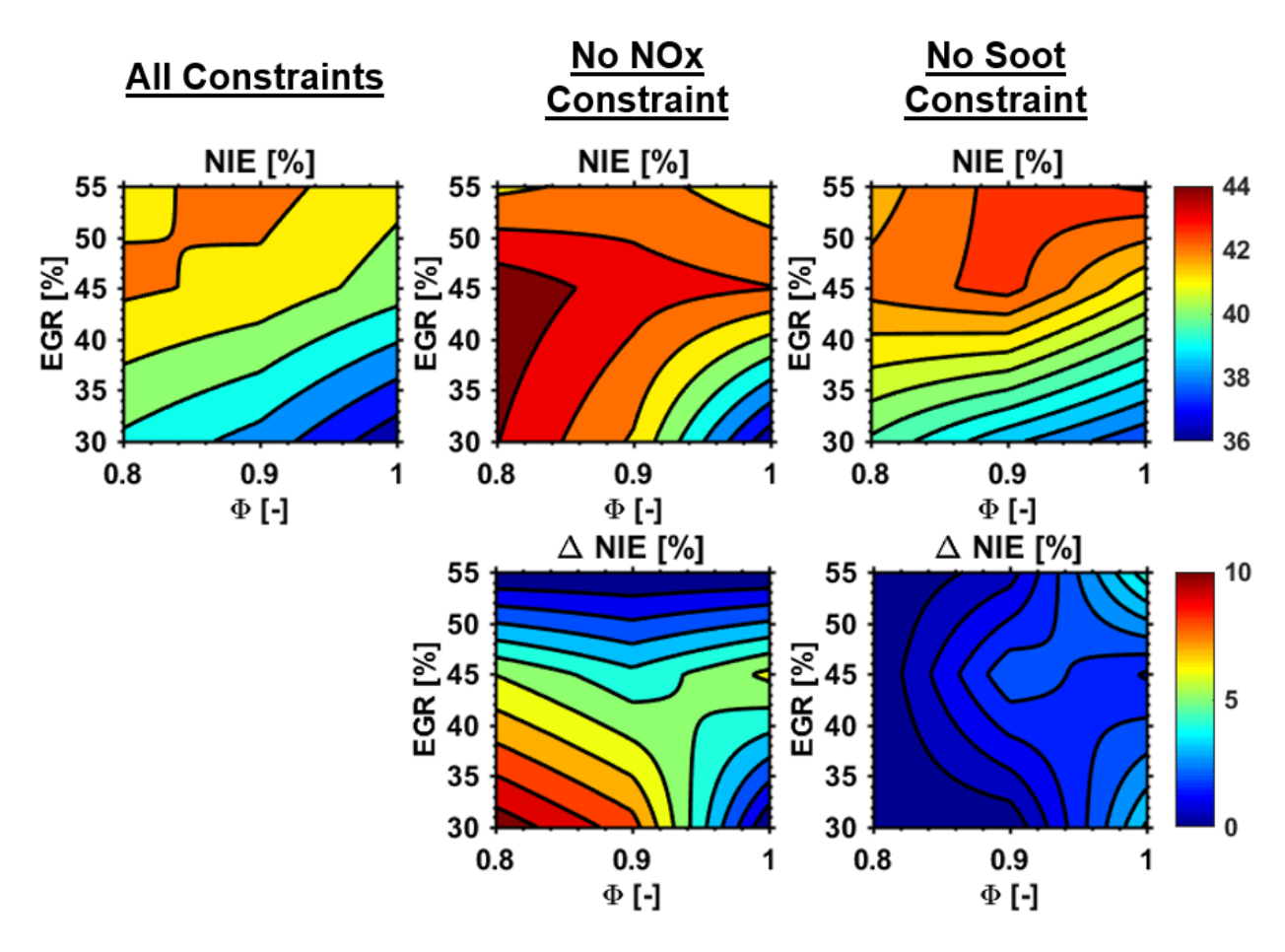


Figure 5-2. Comparison of contour plots of NIE and Δ NIE% between the cases with all constraints intact, no NOx constraint and no Soot constraint.

Based on the results seen in Figure 5-2, the key constraining factors across the EGR and Φ space were identified. Figure 5-3 shows a plot highlighting the dominant constraints and the bounds within which removing these constraints resulted in an improvement in NIE in the EGR and Φ space. The boundary lines for the constraining regions were estimated from the Δ NIE% plots shown in Figure 5-2 by identifying the contour lines with boundaries at Δ NIE% > 0. From the plot, it is observed that operation at high EGR is mainly constrained by the RI constraint. This explains the reason for the GA picking a high EGR operating point as the optima in the high-load optimization study presented in Chapter 4, where all the constraints had to be met. As the EGR reduces, NOx starts becoming a dominant constraint, with the low EGR (\leq 45%) regions primarily constrained by NOx emissions. In the near stoichiometric regions, either at extremely low EGR's (\sim 30%) or extremely high EGR's (\sim 55%), soot emissions seem to be the primary

constraining factor. However, in the low EGR (\leq 45%) regions which are the focus of the current study, removing the soot constraint did not result in as significant a benefit as removing the NOx constraint.

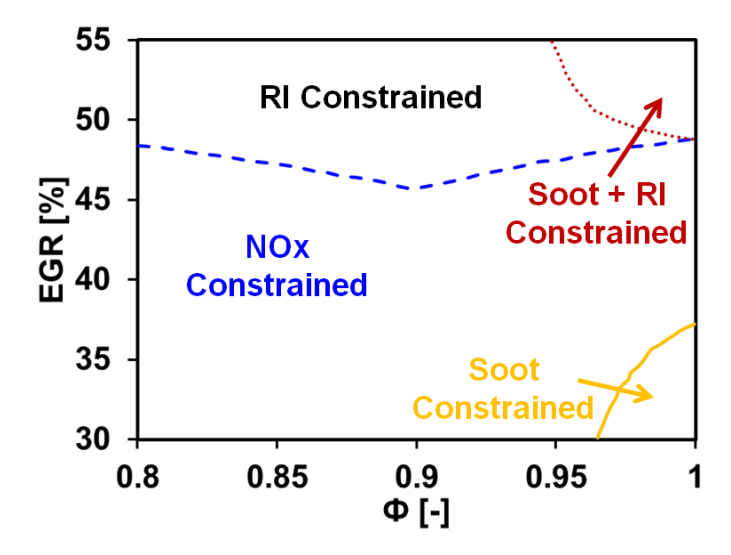


Figure 5-3. Plot showing the dominant constraining factors and the boundaries within which removing the constraint results in an improved NIE in the EGR and Φ operating space.

Based on the previous discussion, removing the NOx constraint and using SCR after-treatment seems to be a viable solution to enable low EGR operation at high efficiencies under high-load-low-speed conditions. Accordingly, further discussion will focus on the cases with the NOx constraint removed.

5.1.1. Diesel Exhaust Fluid (DEF) Consumption Estimation

Removing the NOx constraint resulted in an efficiency benefit, but it also resulted in a simultaneous increase in NOx emissions. Hence, NOx after-treatment using SCR would be required to bring the NOx emissions down to acceptable tailpipe levels. Reducing the NOx emissions using SCR will result in an efficiency penalty from consumption of DEF in the SCR. In the present section, the DEF mass required to bring the NOx emissions to zero is estimated for the cases shown in Figure 5-1, which have the NOx constraint removed. Equations 15 and 16 show the reactions for ammonia (NH₃) and urea (CO(NH₂)₂) consumption involved in reducing the NOx emissions.

$$4NO + 4NH_3 + O_2 \rightarrow 4N_2 + 6H_2O \tag{15}$$

$$CO(NH_2)_2 + H_2O \rightarrow 2NH_3 + CO_2$$
 (16)

The reactions show that one mole of ammonia is required to reduce one mole of NO and half a mole of urea is consumed to produce that one mole of ammonia. Converting it to a mass basis, 30 g of NO (one mole) requires 30 g of urea (half a mole) to reduce it (i.e., 1 g of NO would require 1 g of urea to reduce it). Accordingly, based on the NO_x emissions, the urea mass can be estimated as

$$m_{urea} = \frac{m_{NO_x}}{\left(MW_{NO_2}/MW_{NO}\right)},\tag{17}$$

where m_{urea} is the mass of urea, m_{NO_x} is the mass of NOx emissions, MW_{NO_2} is the molecular weight of NO₂, and MW_{NO} is the molecular weight of NO. Since the NO_x emissions are expressed in terms of NO₂, the ratio of molecular weight of NO₂ to NO is used in equation 17 to convert the NO_x mass to NO mass. Since the DEF is 32.5% urea solution, from the mass of urea, the DEF mass is calculated as

$$m_{DEF} = \frac{m_{urea}}{0.325},\tag{18}$$

where m_{DEF} is the mass of DEF. Using the mass of fuel (m_{fuel}) and the mass of DEF, the net fluid efficiency (NFE) is estimated as

$$NFE = \left(\frac{NIE * m_{fuel}}{m_{fuel} + m_{DEF}}\right) * 100, \tag{19}$$

In estimating NFE, the DEF and diesel fuel are assumed to have the same cost. The cost equivalency can be demonstrated using the following set of equations. The total fluid cost C can be calculated as

$$C = m_{fuel}C_{fuel} + m_{DEF}C_{DEF}, \tag{20}$$

where C_{fuel} is the cost of the fuel and C_{DEF} is the cost of the DEF. The equivalent fuel mass (m_{eq}) that could have been purchased with equal cost can be evaluated as

$$m_{eq}C_{fuel} = m_{fuel}C_{fuel} + m_{DEF}C_{DEF}, (21)$$

Solving for m_{eq} gives

$$m_{eq} = m_{fuel} + m_{DEF} \frac{C_{DEF}}{C_{fuel}}, \tag{22}$$

The NFE is defined as

$$NFE = \left(\frac{NIE * m_{fuel}}{m_{eq}}\right) * 100, \tag{23}$$

Substituting for the equivalent fuel mass (from equation 22) in equation 23 results in

$$NFE = \left(\frac{NIE * m_{fuel}}{m_{fuel} + m_{DEF} \frac{C_{DEF}}{C_{fuel}}}\right) * 100, \tag{24}$$

Finally, assuming equal cost on a mass basis between DEF and diesel fuel, it results in equation 19. Estimating the efficiency this way ensures that the cases with unreasonably high NOx emissions are penalized for high DEF consumption. Figure 5-4 shows a comparison of the contours of NFE between the cases with all the constraints intact and the cases with the NO_x constraint removed.

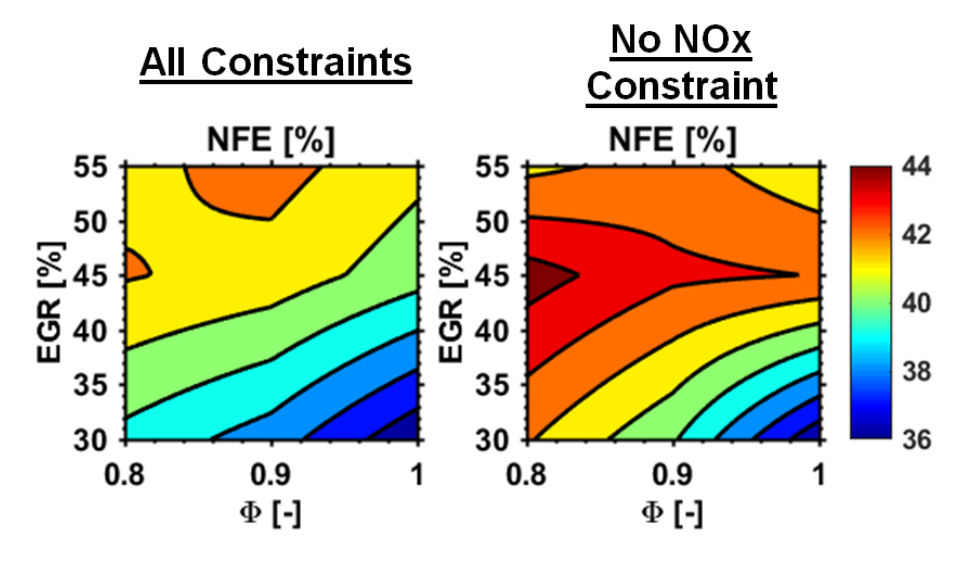


Figure 5-4. Contours of NFE compared between cases with all constraints intact and cases with no NOx constraint.

Results show that even after accounting for the DEF consumption, removing the NOx constraint resulted in an improvement in efficiency. The peak efficiency remains at an EGR of 45% and Φ of 0.8. However, as EGR is reduced below 45%, the penalty of DEF consumption on efficiency becomes more evident. To quantify this penalty, Figure 5-5, shows the contours of the efficiency lost to DEF consumption estimated as a percentage change between NFE and NIE for the cases with no NOx constraint. The contours of NOx and DEF mass consumed are also shown in Figure 5-5 to explain the trends. As the EGR is reduced below 45%, the DEF consumption increases due to an increase in the NOx emissions. This results in an increased loss in efficiency to DEF consumption at the low EGR rates (< 45%), as shown in Figure 5-5. Near an EGR of 45%, there is near zero loss in efficiency to DEF consumption, making it an optimal zone

for operation. In other words, operating at moderate EGR rates (~45%) results in a significant improvement in efficiency for a minor increase in NOx emissions and, therefore, helps in realizing the maximum benefit from using the SCR.

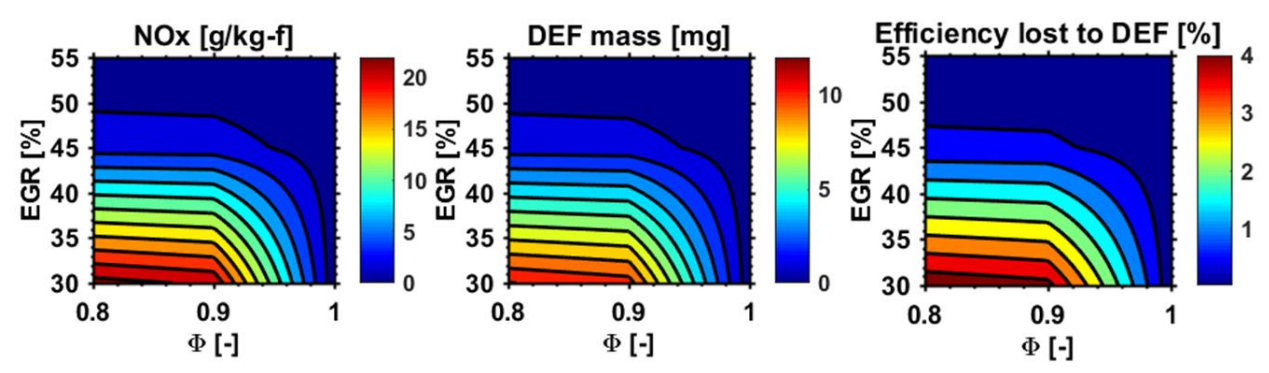


Figure 5-5. Contours of NOx, DEF mass consumed and the % efficiency lost to DEF consumption for the cases with no NOx constraint.

5.1.2. Effect of removing the NOx constraint on the Optimum at the same EGR Level

From the data-set, an optimum case was picked, to understand how the optimum strategy changes when the NOx constraint is removed. The optimum was chosen as the case with the highest NFE that meets the constraints of soot ≤ 2 g/kg-f and RI ≤ 5 MW/m². The results of this case were compared with the best case (highest NFE) at the same EGR level, but with the NOx constraint intact (i.e., NOx ≤ 2 g/kg-f, soot ≤ 2 g/kg-f, and RI ≤ 5 MW/m²). Table 5-1 shows a comparison of these two cases.

Table 5-1. Best cases without the NOx constraint and with the NOx constraint at a similar level of EGR.

INPUTS				
Design Parameter	Best Case (no NOx constraint)	Best Case (with NOx constraint)		
Premix Gas. Frac [-]	0.68	0.78		
Gas. Frac [-]	0.63	0.602		
SOI-Gas. [°aTDC]	-83.2	-63.2		
SOI-Diesel [°aTDC]	-17.3	-6		
EGR [%]	45	45		
Φ[-]	0.8	0.8		
IVC-Pressure [bar]	3.76	3.76		
OUTPUTS	OUTPUTS			
GIE [%]	47.2	44.8		
NIE [%]	44.7	41.9		
NFE [%]	44.4	41.8		
NOx [g/kg-f]	3.04	1.52		
Soot [g/kg-f]	0.81	1.71		
PPRR [bar/deg]	14.49	7.29		
PP [bar]	199.78	162.09		
RI [MW/m ²]	4.98	1.47		

The key difference between the two points compared in Table 5-1 is the SOI of diesel fuel. The diesel fuel injection is significantly advanced from -6 ⁰aTDC to -17.3 ⁰aTDC upon removing the NOx constraint. Figure 5-6 shows the NFE, NOx, and soot emissions as a function of the SOI of diesel fuel for the case with NOx constraint shown in Table 5-1. Across the SOI sweep there exists the classical tradeoff between soot and NOx emissions. When the NOx constraint was intact, the SOI of diesel fuel had to be delayed closer to TDC to keep the NOx emissions below the constraint. This results in an increase in soot emissions and a simultaneous reduction in NFE. Hence an optimum SOI timing of -6 ⁰aTDC was chosen since it is the earliest SOI for diesel fuel injection that results in simultaneously low (≤ 2g/kg-f) NOx and soot emissions. Removing the NOx constraint allows the near TDC diesel fuel injection to be advanced significantly, resulting in an improvement in NFE of ~6% and a reduction in soot emissions of ~53%.

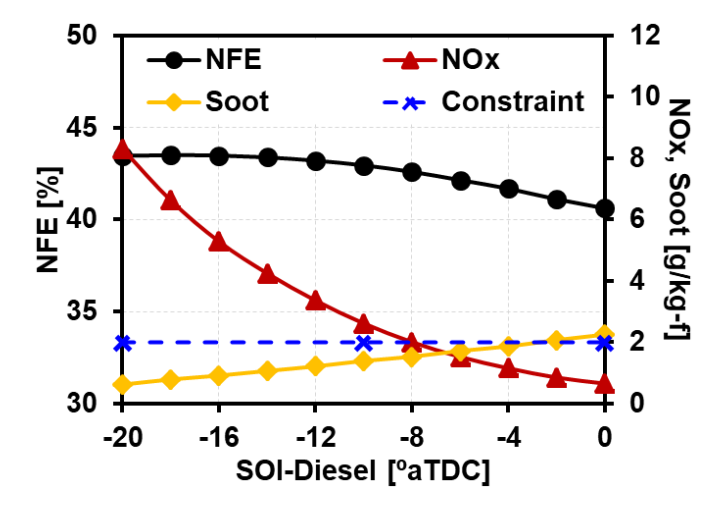


Figure 5-6. NFE, NOx and soot emissions as a function of SOI-Diesel for the case with the NOx constraint shown in Table 5-1.

Figure 5-7 shows the NFE, DEF mass consumed, and PP as a function of the SOI of diesel fuel for the case without the NOx constraint shown in Table 5-1. Advancing the SOI of diesel fuel results in an increase in NFE. However, as the injection is advanced beyond -17 °aTDC, the DEF consumption penalty starts to increase due to increased NOx emissions causing the NFE to decrease. Additionally, we can see that the in-cylinder PP also increases as the injection is advanced. Hence, PP also acts as an additional constraint on how advanced the diesel fuel injection can be while operating without the NOx constraint. While experimentally running the engine that was modeled in the current study, the operation is usually

restricted to a maximum PP of 200 bar to avoid structural damage. Accordingly, from the SOI sweep, the optimum SOI timing of -17.3 $^{\circ}$ aTDC was chosen as the SOI timing for which, the peak NFE of 44.4% is achieved while having a PP \leq 200 bar.

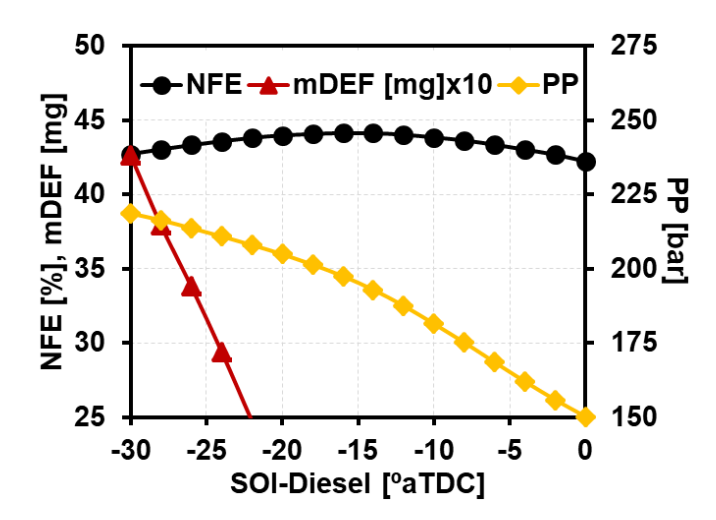


Figure 5-7. NFE, DEF mass consumed and PP as a function of SOI-Diesel for the case without the NOx constraint shown in Table 5-1.

To explain the improvement in NFE for the case with the NOx constraint removed, Figure 5-8 shows a comparison of the in-cylinder pressure and the AHRR for the two cases shown in Table 5-1. For both the cases the diesel fuel injection combusts in a mixing-controlled fashion, which explains the strong tradeoff that was seen between the soot and NOx emissions in Figure 5-6. When the NOx constraint is removed, since the SOI of diesel fuel is advanced, it results in an advancement in start of combustion (SOC) (identified by the CA at which 10% of the total heat release occurs) from 1.2 °CA to -6.7 °CA. It also results in a simultaneous reduction in combustion duration (estimated as the absolute difference between the SOC, and the CA at which 90% of the total heat release occurs) from 27.2 °CA to 19 °CA. Due to the combination of advanced SOC and shortened burn duration, there is a higher percentage of combustion occurring closer to TDC for the case with the NOx constraint removed. Combustion closer to TDC has a higher potential to perform work, due to an improved utilization of the expansion stroke.

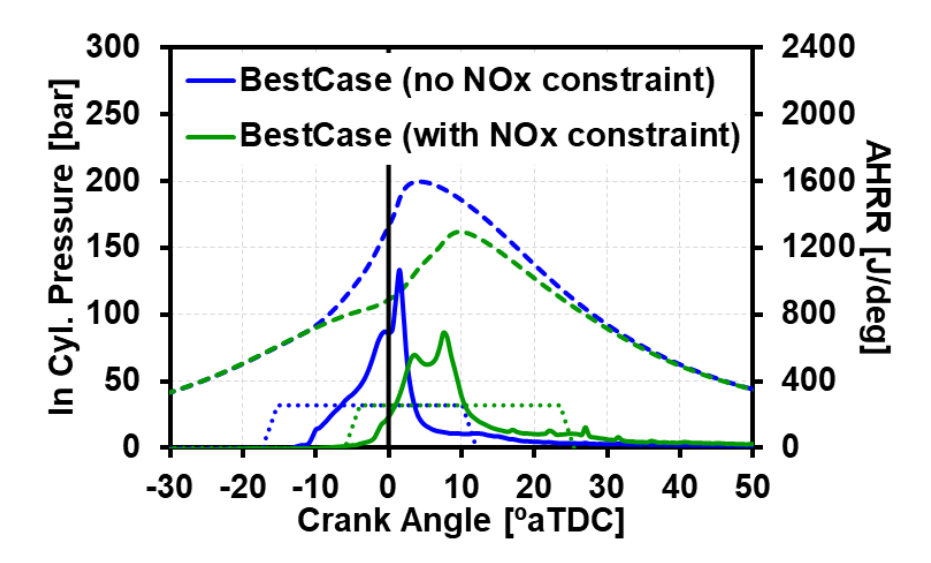


Figure 5-8. Comparison of in-cylinder pressure and AHRR for the two best cases shown in Table 5-1.

To quantify the improvement in expansion stroke utilization, the effective expansion ratio (EER) was defined as

$$EER = \frac{\int_{SOC}^{EOC} HRR(\theta) * \left(\frac{V_{BDC}}{V(\theta)}\right) d\theta}{m_{fuel} * LHV_{fuel}},$$
(25)

where $HRR(\theta)$ is the chemical heat release rate at each CA, V_{BDC} is the cylinder volume at BDC, and $V(\theta)$ is the volume of the cylinder at each CA. The closer the EER is to the geometric CR (12:1 for the engine modeled in the current study), the higher is the work extraction potential. Figure 5-9 shows a comparison of the EER for the two cases shown in Table 5-1.

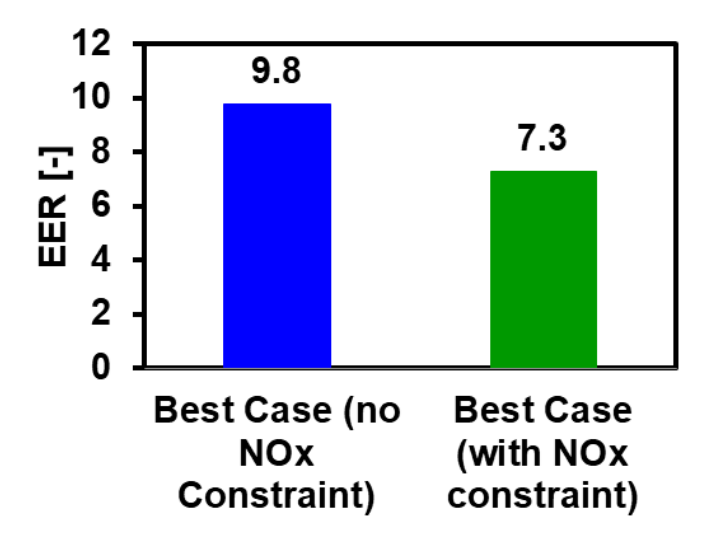


Figure 5-9. Comparison of EER for the two best cases shown in Table 5-1.

The case without the NOx constraint has a higher EER of 9.8 compared to the case with the NOx constraint which has an EER of 7.3. Removing the NOx constraint allowed the SOI timing of diesel fuel to be advanced, resulting in an improvement in EER of ~34.25%. The improvement in expansion stroke utilization explains the improved NFE when the NOx constraint is removed.

5.1.3. Comparison of Optimum Strategy at Moderate (45%) and High (55%) EGR

The best case with the NOx constraint removed (shown in Table 5-1) is compared with the high EGR (55%) RCCI optima from the high-load GA optimization study shown in Chapter 4. The two cases were compared in terms of combustion characteristics, combustion control, and stability to operating condition fluctuations. The motivation of this study is, firstly, to understand the difference between the two optima in terms of combustion characteristics and performance. Secondly, to verify if the benefits of high combustion control seen with the high EGR GA optima are retained at the reduced EGR operation. Lastly, to see if the issues of high soot emissions and sensitivity to EGR fluctuations observed with the high EGR GA optima are eliminated by operating at a reduced EGR rate. Table 5-2 shows a comparison of the best case from the cases with no NOx constraint compared with the high EGR GA optima from Chapter 4.

Table 5-2. Comparison of the best case from the cases with no NOx constraint and the high EGR GA optima from Chapter 4.

Tom empter ii			
INPUTS			
Design Parameter	Best Case (no NOx constraint)	GA Optima	
Premix Gas. Frac [-]	0.68	0.63	
Gas. Frac [-]	0.63	0.72	
SOI-Gas. [°aTDC]	-83.2	-78	
SOI-Diesel [°aTDC]	-17.3	-12	
EGR [%]	45	55	
Φ[-]	0.8	0.93	
IVC-Pressure [bar]	3.76	3.97	
OUTPUTS			
GIE [%]	47.2	46.3	
NIE [%]	44.7	43.8	
NFE [%]	44.4	43.8	
NOx [g/kg-f]	3.04	0.3	
Soot [g/kg-f]	0.81	1.78	
PPRR [bar/deg]	14.49	19.91	
PP [bar]	199.78	194.9	
RI [MW/m ²]	4.98	6.59	

The operating strategy remains very similar for the two cases compared in Table 5-2. Most of the fuel is gasoline, which is introduced early into the combustion chamber in the form of premixed fuel and an early DI. The SOI timing of the gasoline injection is -83.2 °aTDC and -78 °aTDC for the best case with no NOx constraint and the GA optima respectively. The rest of the fuel is injected as a stratified injection close to TDC at -17.3 °aTDC and -12 °aTDC for the best case with no NOx constraint and the GA optima respectively. The two cases differ mainly in terms of the air handling. Removing the NOx constraint allows operation at a reduced EGR rate of 45% and a relatively lean global Φ of 0.8. This results in a minor increase in NFE from 43.8% to 44.4%. It also results in a significant reduction (~54.5%) in soot emissions from 1.78 g/kg-f to 0.81 g/kg-f.

To explain the improvement in efficiency for the case with no NOx constraint, Figure 5-10 shows a comparison of the energy balance for the two cases shown in Table 5-2. Though the GA optimum has reduced wall heat transfer and reduced exhaust losses, it also has higher combustion losses which offset the benefits, resulting in a lower GIE.

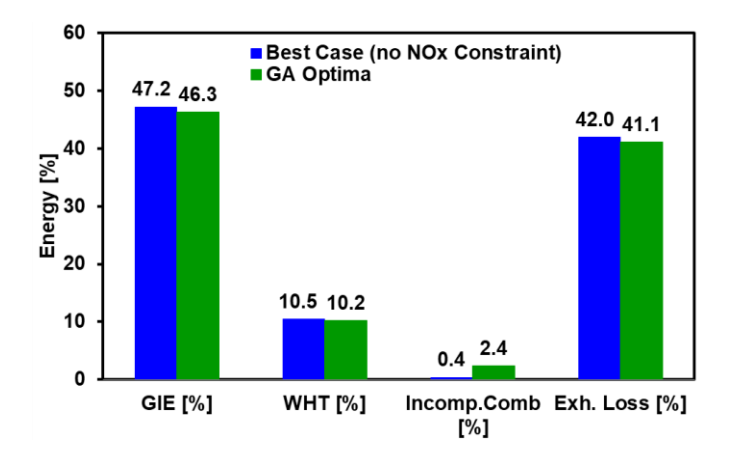


Figure 5-10. Comparison of energy flow for the two best cases shown in Table 5-2.

Figure 5-11 shows a comparison of the in-cylinder pressure and AHRR for the two cases compared in Table 5-2. The SOI of diesel fuel is at -17.3 °aTDC for the case with no NOx constraint, which is slightly early relative to the SOI of diesel fuel for the GA optima occurring at -12 °aTDC. This results in an advanced SOC of -6.73 °CA for the case with no NOx constraint relative to the SOC of the GA optima which occurs at -2.99 °CA. The advanced SOC leads to reduced combustion losses and an improved GIE. From Figure

5-11, it is also seen that the case with no NOx constraint has a higher mass (longer injection duration) in the near TDC diesel fuel injection that is combusting in a mixing-controlled fashion. However, interestingly, this case yields lower soot emissions than the GA optima. To explain this result, Figure 5-12 shows the in-cylinder contours of temperature, Φ , and soot mass fraction at various crank angles for the two cases compared in Figure 5-11.

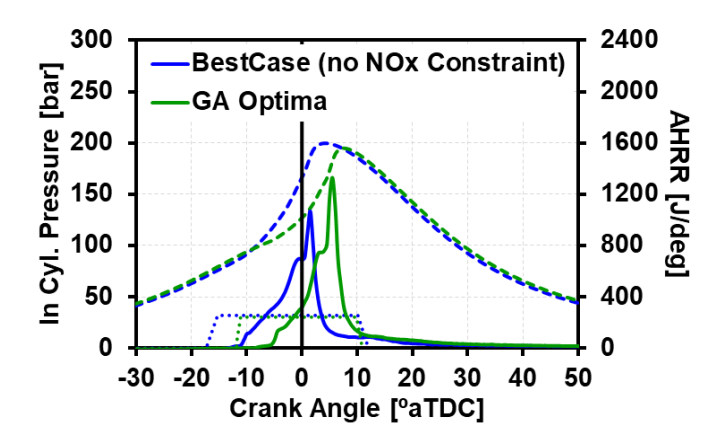


Figure 5-11. Comparison of in-cylinder pressure and AHRR for the two best cases shown in Table 5-2.

Firstly, it is seen that both cases are very similar in combustion characteristics with the near TDC diesel fuel injection acting as the ignition source and causing the rest of the fuel in the combustion chamber to ignite. For the case with no NOx constraint, the larger fuel mass in the diesel fuel injection results in higher soot formation, as seen in Figure 5-12 at CA timings of 20 $^{\circ}$ aTDC and 30 $^{\circ}$ aTDC. However, the best case with no NOx constraint has a global Φ of 0.8 at a moderate EGR rate of 45% which is much leaner compared to the GA optima having a global Φ of 0.93 at a higher EGR rate of 55%. This results in a leaner background Φ in the bowl, for the case with no NOx constraint, as seen in Figure 5-12 at all the crank angles. This causes more oxygen to be available later in the cycle. Figure 5-13 shows the mass of soot (solid line) and O_2 (dashed line) as a function of crank angle. The difference in O_2 mass between the two cases is evident until EVO. Due to the higher availability of oxygen, the case with no NOx constraint has a higher soot oxidation rate, which is evident from the steeper slope of the falling part of the soot mass curve during the expansion stroke. This higher soot oxidation rate eventually results in lower soot emissions at EVO for the case with no NOx constraint relative to the GA optima. This is seen from the reduced soot mass fractions

at a CA of 50 °aTDC and 60 °aTDC in Figure 5-12 and from the soot mass trend shown in Figure 5-13. A detailed discussion of soot formation and oxidation for near TDC and post-injections under advanced combustion conditions is shown in Appendix-B and in Kavuri et al. [73]. The soot study was not included in the main text for brevity and continuity.

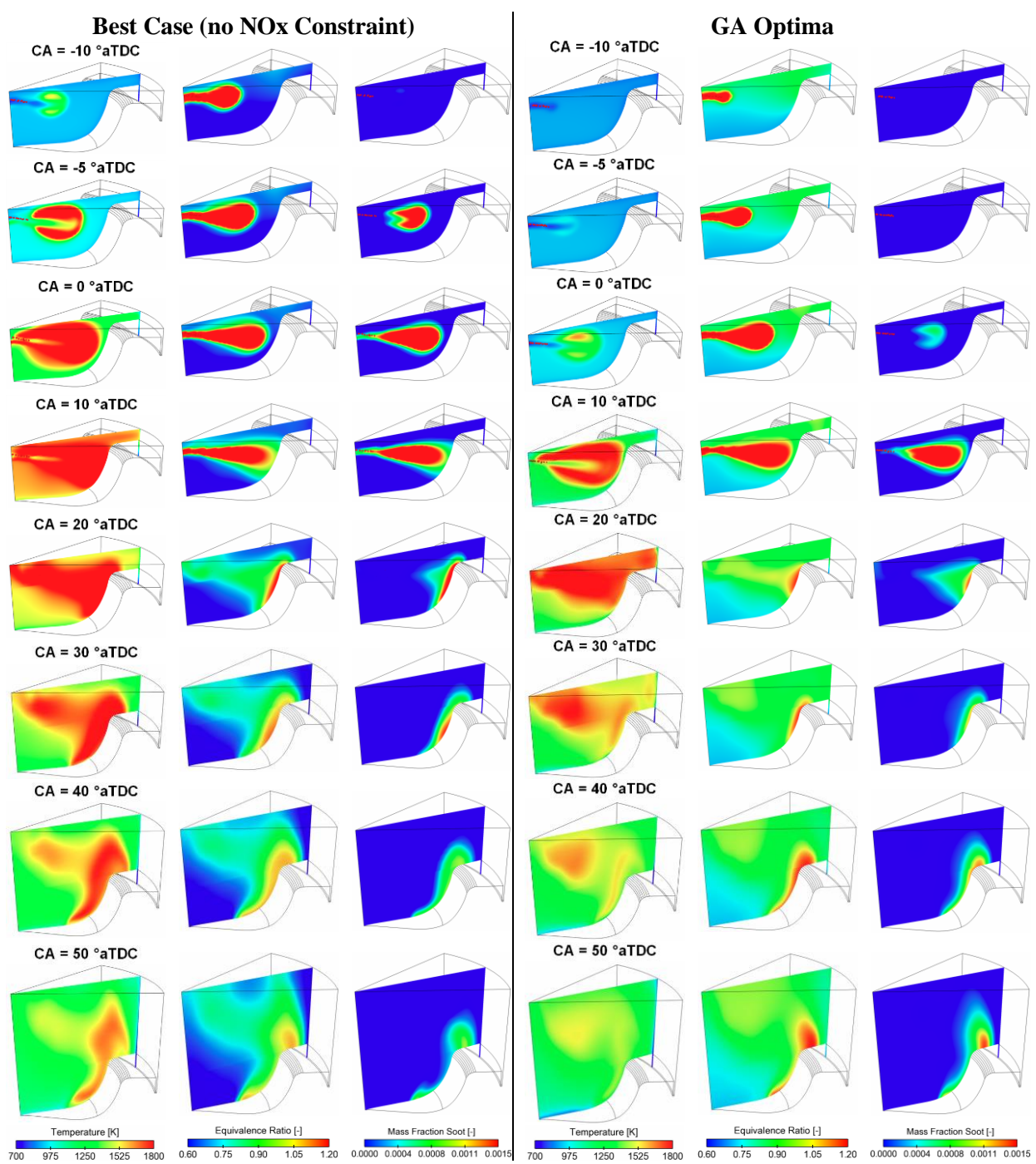


Figure 5-12. Comparison of in-cylinder contours of temperature, Φ , and soot mass fraction at various CA for the two best cases shown in Table 5-2.

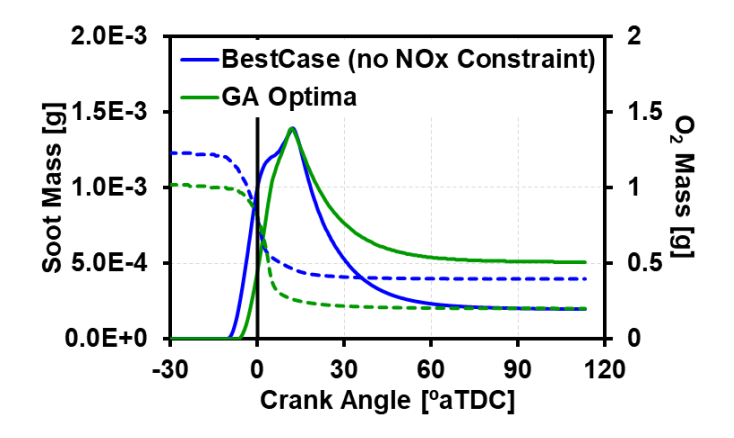


Figure 5-13. Soot (-) and O₂ (--) mass as a function of CA for the two best cases shown in Table 5-2.

5.1.4. Control Parameters

To verify that the combustion control seen with the GA optima is retained in the lower EGR optima with no NOx constraint, a parametric study was performed for the optima with no NOx constraint. Each input (excluding EGR) was varied individually fixing the rest of the inputs at the optimum value shown in Table 5-2. The results from the sweep were compared to the results from a similar parametric study performed on the GA optima (details shown in §4.2.2.2). Table 5-3 shows the range of variation of inputs for the combustion control parametric study.

Table 5-3. Range of variation of inputs for the combustion control parametric study of the two cases shown in Table 5-2.

Best Case (no NOx Constraint)			
Design Parameter	Range	Step Size	Optima
Premix Gas. Frac [-]	0.6 to 0.9	0.01	0.68
Gas. Frac [-]	0.5 to 0.8	0.01	0.63
SOI-Gas. [°aTDC]	-95 to -65	2	-83.2
SOI-Diesel [°aTDC]	-30 to 0	2	-17.3
GA Optima			
Design Parameter	Range	Step Size	Optima
Premix Gas. Frac [-]	0.4 to 0.7	0.01	0.63
Gas. Frac [-]	0.5 to 0.9	0.01	0.72
SOI-Gas. [°aTDC]	-100 to -60	2	-78
SOI-Diesel [°aTDC]	-30 to 0	2	-12

Figure 5-14 shows the variation in CA50 with each control parameter for the two cases shown in Table 5-2. A steeper slope indicates better control over combustion phasing. For both the cases, it is evident that SOI of diesel fuel is the primary control parameter. The response of SOI-Diesel is 0.62° and 0.58° CA50 per degree SOI-Diesel for the case with no NOx constraint and the GA optima respectively. The

strong control over combustion was found to be due to the short ignition delay of the mixing-controlled diesel fuel injection, as was explained in §4.2.2.2. CA50 is insensitive to the rest of the inputs for both the strategies. These results indicate that, similar to the GA optima, there is an excellent control over combustion phasing for the case with no NOx constraint. However, removing the NOx constraint allows operation at a leaner global Φ , which results in significantly lower soot emissions. Therefore, operating at reduced EGR rates with SCR after-treatment addresses the tradeoff between combustion control and soot emissions observed with high EGR GA optimum (in Chapter 4).

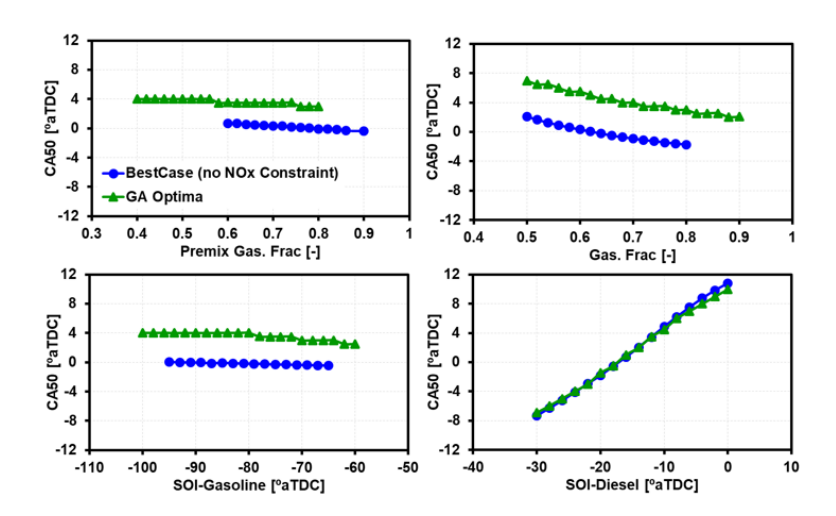


Figure 5-14. CA50 as a function of inputs for the two best cases compared in Table 5-2.

5.1.5. Operating Condition Sensitivity

One of the motivations for investigating the reduced EGR strategies was to see if operating at a lower EGR rate reduces the sensitivity to variations in EGR observed with the high EGR GA optima. Accordingly, the current section shows a comparison of the sensitivity of the outputs to variations in charge conditions and fueling rates for the two cases shown in Table 5-2. To perform the sensitivity analysis, a similar procedure as explained in §4.2.2.3 is followed. Initially a full factorial DOE is run about the optimum cases shown in Table 5-2. The baseline value and the range of fluctuation for each operating condition are shown in Table 5-4. The rest of the inputs are fixed at the values shown in Table 5-2. The results from the DOE were used to build a full quadratic RSM with linear, squared, and interaction terms. The sensitivity analysis is then performed by taking a partial derivative of the RSM equations of each objective with respect to each input parameter.

Table 5-4. Baseline value and the range of fluctuation of each operating condition, for the two cases shown in Table 5-2.

Operating Condition	Best Case	GA Optima	Range
	(no NOx Constraint)		
T _{ive} [K]	406	406	± 3
P _{ivc} [bar]	3.76	3.97	± 0.05
EGR [%]	45	55	± 2
Premix Mass [mg/cycle]	103	108	± 4
DI Mass [mg/cycle]	138	133	± 4

Figure 5-15 shows a comparison of the results from the sensitivity study for the two cases shown in Table 5-2. For the GA optima, all the outputs are significantly more sensitive to EGR than the other inputs. This was found to be due to operating at a near stoichiometric global Φ of 0.93, where an increase in EGR was causing the global Φ to increase beyond 1, resulting in a rapid drop in PPRR and GIE. Removing the NOx constraint resulted in an optimum operating strategy that has a significantly leaner global Φ of 0.8. This reduces the sensitivity to EGR substantially, as seen in Figure 5-15. To give an example to explain the improved stability, an increase in EGR rate from 55% to 56% for the GA optimum results in a change in CA50 of 0.97 deg. To achieve the same change in CA50 for the best case without a NOx constraint, the EGR rate would have to increase to 58%. Therefore, removing the NOx constraint and using SCR after-treatment resulted in a high-load-low-speed operating strategy with improved stability.

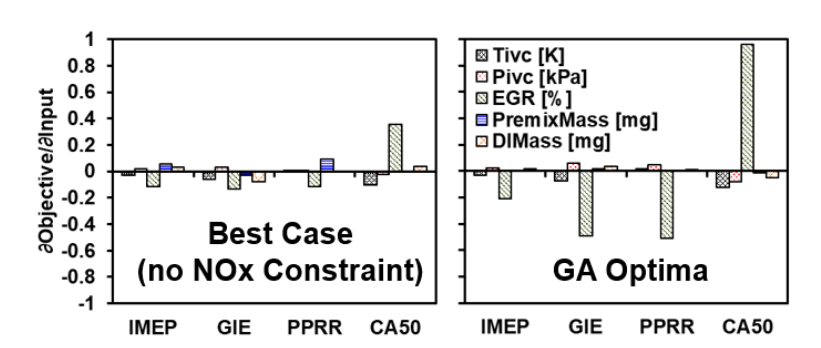


Figure 5-15. Comparison of results from the operating condition sensitivity study for the two cases shown in Table 5-2.

The results in this chapter have shown that removing the NOx constraint and using SCR aftertreatment results in a feasible high-load-low-speed RCCI operating strategy that addresses the issues of high soot emissions and sensitivity to operating condition (EGR) fluctuations observed with the high EGR operating strategy in Chapter 4.

5.2. Conclusions

The study presented in this chapter investigated operating strategies at reduced (< 50%) EGR levels for high-load-low-speed operation with RCCI combustion. A constraint analysis was performed to identify the constraints preventing operation at lower EGR levels. It was found that the lower EGR regions are mainly constrained by NOx emissions. Removing the NOx constraint resulted in increased efficiency at the lower EGR rates, but had a simultaneous tradeoff with increased NOx emissions. This led to increased consumption of the DEF mass required for SCR after-treatment. By optimizing between the efficiency and the DEF consumption, it was identified that operating at moderate EGR rates (\sim 45%) helps in realizing the maximum benefit of using SCR after-treatment. An optimum case without the NOx constraint was identified, which had a moderate EGR rate of 45% and a globally lean Φ of 0.8. In terms of performance, the optimum case had a NFE of 44.4% and near zero soot emissions. The improved efficiency upon removing the NOx constraint was identified to be due to advancing the diesel fuel injection which resulted in a more optimal combustion phasing and led to a better utilization of the expansion stroke.

Furthermore, the optimum operating strategy was compared with the high EGR (\sim 55%) optimum shown in Chapter 4. It was found that the optimum with SCR after-treatment resulted in similar combustion control as the high EGR optima without the tradeoff of high soot emissions. This was found to be due to the increased oxygen availability from operating under globally lean conditions, which resulted in improved soot oxidation rates and lower soot emissions. Comparing the two strategies in terms of stability to operating parameter variation showed that the optimum with SCR after-treatment was significantly more stable compared to the GA optima. The improved stability was found to be due to the reduced sensitivity to EGR fluctuations from operating at a leaner global Φ . These results indicate that removing the NOx constraint and using SCR after-treatment addresses the issues of high soot emissions and sensitivity to EGR fluctuations while retaining the excellent combustion control observed with the high EGR GA optimum, under high-load-low-speed conditions.

Chapter 6 Optimization considering Low-load and High-load Efficiency

The results presented in Chapter 4 and Chapter 5 identified several approaches to enable RCCI and GCI combustion at high-load-low-speed conditions. Recall, however, that these studies used a piston with a CR of 12:1. Preliminary simulations at the low-load-high-speed condition were performed using this piston. The operating strategy (e.g., injection schedule) used was based on a light-duty optimization performed at low-load-high-speed conditions (see Appendix-A). Note that the study presented in Appendix-A used a CR of 16.7:1, a re-entrant piston bowl, and a narrow angle injector. Applying this strategy to the present heavy-duty engine, with a wide-angle injector and a CR of 12:1, resulted in a GIE of only 39.1%. The poor efficiency was attributed to the combination of low CR piston, open bowl geometry, and wide-angle injector. This set of hardware works well at high load conditions, but at low load, the geometry extends the already long chemistry time scales, leading to high levels of incomplete combustion. This result indicates that the optimal hardware set may be different when low-load and high-load are taken into consideration.

Accordingly, to get a feasible solution that works at both the loads, a common optimization that accounts for the performance at low-load and high-load conditions should be performed. In this chapter a computational optimization will be presented, that considers the performance at low-load-high-speed (2 bar, 1800 rev/min.) and high-load-low-speed (20 bar, 1300 rev/min.) operating conditions simultaneously. The motivation of this study is to demonstrate an approach that can identify optimal solutions that work across the drive cycle. The two operating conditions were chosen based on the earlier optimization studies performed separately at each of these operating conditions. Choosing similar operating conditions allows us to compare the optimization approaches and isolate any difference in the results due to the modified optimization approach.

6.1. Optimization Setup

GA optimizations were setup at 2 bar, 1800 rev/min. and 20 bar, 1300 rev/min. targeting low-load-high-speed and high-load-low-speed operating modes, respectively. 28 design inputs were varied in the optimization which includes parameters for defining bowl geometry, injector design, air-handling, and

fueling strategy. The complete list of the inputs and the range of variation allowed for each input is shown in Table 6-1.

Table 6-1. Range of variation allowed for each design parameter in the optimization study.

	Low-Load	High-Load			
Design Parameter	(2 bar, 1800 rev/min.)	(20 bar, 1300 rev/min.)			
Bowl Design					
CR [-]	9 t	o 22			
Point 1 [-]	-0.1 1	to 0.99			
Point 2 to Point 3 [-]	0.01	to 0.99			
Point 4 [-]	-0.18	to 0.99			
Point 5 to Point 15 [-]	0.01	to 0.99			
Injector Design					
Tiltxz-Gas. [⁰]	5 t	o 85			
Tiltxz-Diesel[0]	5 t	o 85			
dnoz-Gas. [µm]	100	to 400			
dnoz-Diesel [µm]	100 to 400				
Fueling Strategy					
Gas. Frac. [-]	0 to 1	0 to 1			
Premix Gas. Frac. [-]	0 to 1	0 to 1			
SOI-Gas. [OATDC]	-100 to 40	-100 to 40			
SOI-Diesel [OATDC]	-100 to 40	-100 to 40			
Pinj-Gas. [bar]	500 to 2500	500 to 2500			
Pinj-Diesel [bar]	500 to 2500 500 to 2500				
Air-handling					
Pivc [bar]	1 to 1.5	2.36 to 4.5			
EGR [%]	0 to 60	0 to 60			

For every generation and every citizen of the GA, it was ensured that the inputs generated for bowl geometry and injector design parameters shown in Table 6-1 would remain the same for the two operating modes. The inputs for air-handling and fueling strategy can be controlled at each operating condition and could be different at the two operating modes. This ensures that the best fueling strategy possible at each mode is identified for a bowl geometry and injector configuration that is optimized considering the performance at both the operating modes.

To define the bowl geometry, a bowl geometry code developed by Lopez et al. [101] was used. The code uses six control points that make up a Bezier spline to define the piston geometry. The six control points are defined by 15 variables (shown as Point1 to Point 15 in Table 6-1), which can be varied to generate a wide variety of geometries ranging from re-entrant bowls to open bowls. Figure 6-1 shows examples of a few bowl geometries that can be generated by varying each of the 15 bowl parameters.

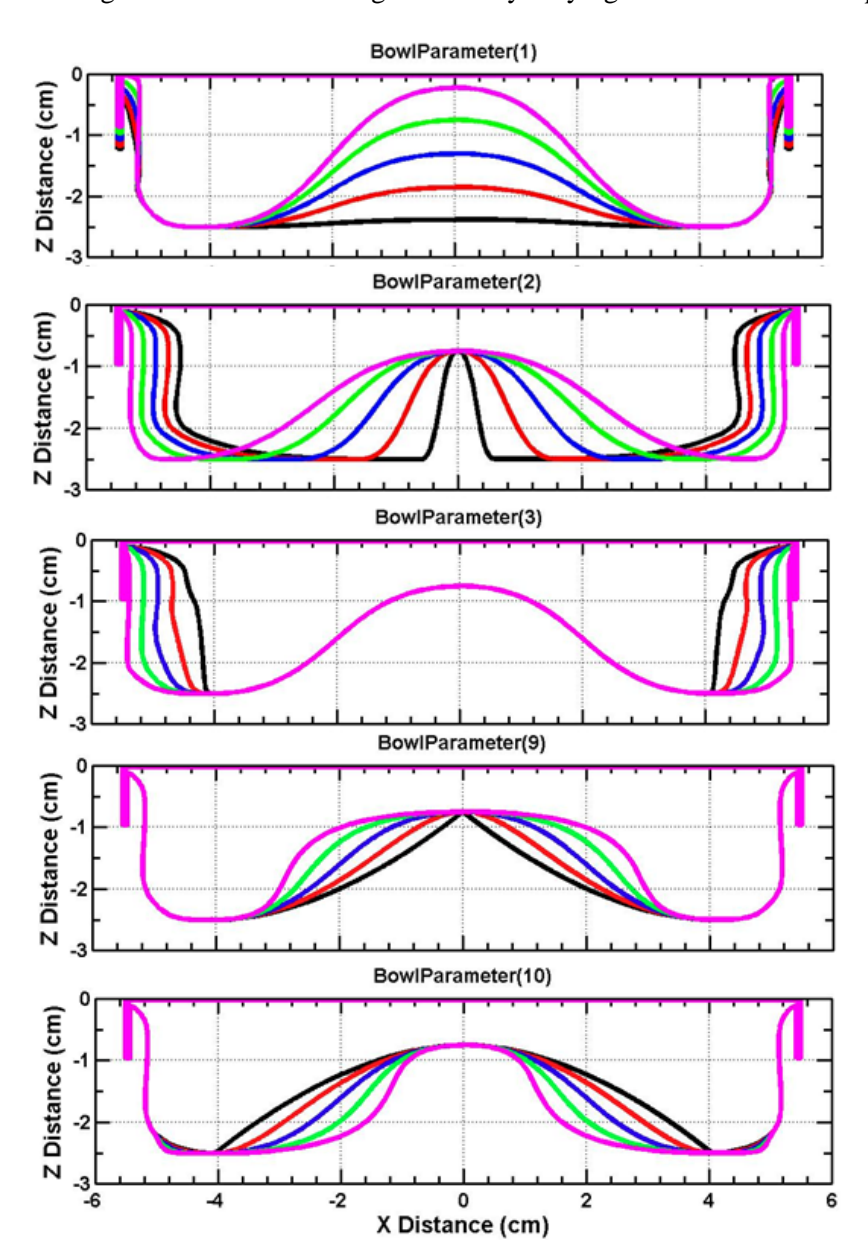


Figure 6-1. Examples of bowl geometries that can be generated using the bowl geometry code of Lopez et al. [101].

The injection strategy shown in Figure 6-2 was used for the optimization study. The SOI of DI gasoline (SOI-Gas.) and diesel fuel (SOI-Diesel) and their corresponding injection pressures (Pinj) are varied in the GA. Additionally, the fraction of the total gasoline that is premixed (Premix Gas. Frac) and the fraction of the total fuel that is gasoline (Gas. Frac) are also varied in the GA. Similar to the earlier chapters, the premixed gasoline was modeled as a homogenous mixture at IVC.

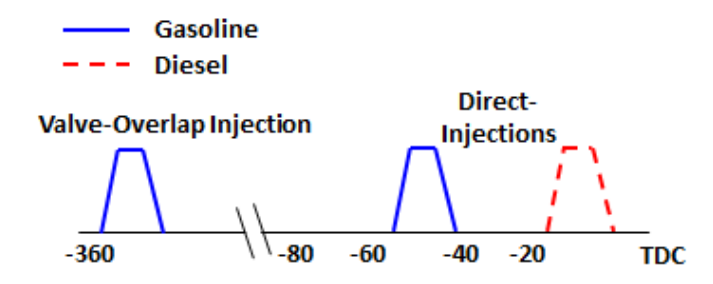


Figure 6-2. Injection strategy used for the optimization study.

The injector included half angle (Tiltxz) and the injector nozzle diameters (dnoz) for the gasoline and diesel injectors were varied independently. The injectors were modeled as having seven holes each and were assumed to be centrally mounted. This allowed the simulations to be performed on a 51.42° sector mesh. For any bowl profile generated in the GA a computational mesh with approximately 40,000 cells at BDC and an average cell size of 1 mm was used. The variation in intake pressure was represented by varying the pressure at intake valve closure (Pivc). The amount of EGR used was also varied.

Optimizations were performed with the aim of maximizing the mode-weighted NFE while having constraints on soot emissions, PPRR, and PP. The constraint value assigned to each output and the harshness factors used are mentioned in Table 6-2.

Table 6-2. Constraint value and harshness factor assigned to each output.

Output Constrain		Harshness Coefficient
Soot [g/kg-f]	2	0.5
PPRR [bar/deg]	15	0.5
PP [bar]	200	1

In Chapter 5, removing the constraint on NOx emissions and using SCR after-treatment was found to be beneficial for high-load-low-speed operation. Accordingly, for the current study, there was no direct constraint on NOx emissions. As shown in Chapter 5, accounting for the DEF consumption in the NFE

calculation indirectly constraints the NOx emissions from being unreasonably high. Once the NFE is estimated for every citizen of a generation in the GA at low-load and high-load conditions, the mode-weighted NFE is estimated as

$$NFE_{total} = (1 - W_{mode}) * NFE_{LL} + W_{mode} * NFE_{HL}, \tag{26}$$

where NFE_{total} is the mode-weighted NFE, NFE_{LL} and NFE_{HL} are the NFE at low-load and high-load respectively for every citizen, and W_{mode} is the mode weighting factor. For the current study W_{mode} is set to 0.5 (i.e., the two modes were equally weighted). In a later section of this chapter, the effect of varying this weighting factor on the optimization results will be discussed. The GA was run for 40 generations with 250 citizens per generation. This sums to 20,000 CFD calculations for the two operating modes. The optimum design was chosen as the citizen with the highest mode-weighted NFE that meets the constraints on soot emissions, PPRR, and PP.

6.2. Results

Upon completion of the GA, the optimized points for low-load and high-load were identified, and their corresponding design variables are listed in Table 6-3.

Table 6-3. Optimized design variables for low-load and high-load

Table 0-3. Optimized design variables for low-load and high-load						
Design Parameter	Low-Load	High-Load				
Design 1 arameter	(2 bar, 1800 rev/min.)	(20 bar, 1300 rev/min.)				
Bowl and Injector Design						
CR [-]	13	3.1				
Tiltxz-Gas. [⁰]	73	3.05				
Tiltxz-Diesel[0]	55	5.14				
dnoz-Gas. [µm]	1	15				
dnoz-Diesel [µm]	1	06				
Fueling Strategy						
Gas. Frac. [-]	0.15	0.92				
Premix Gas. Frac. [-]	0.05	0.66				
SOI-Gas. [OATDC]	-15	15				
SOI-Diesel [OATDC]	-45	-7				
Pinj-Gas. [bar]	881	2154				
Pinj-Diesel [bar]	537	1541				
Air-handling						
Pivc [bar]	1	3.69				
EGR [%]	40	46				

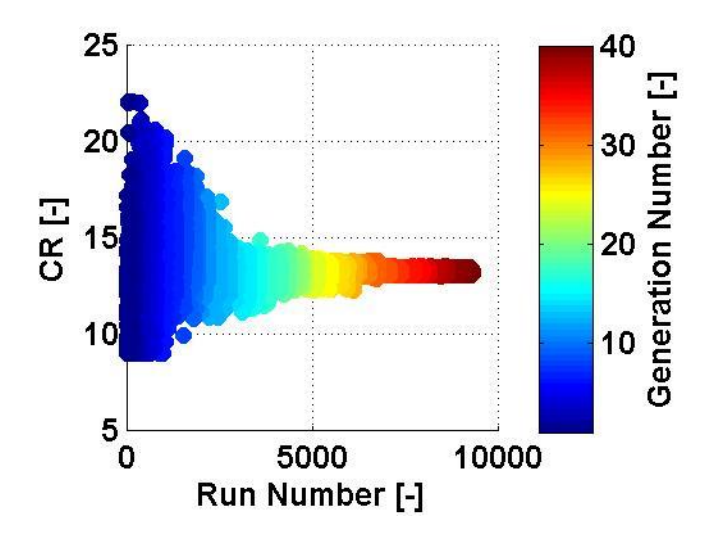


Figure 6-3. CR as a function of the run number.

The optimum piston geometry with the optimum spray included half angles of the gasoline and diesel injectors is shown in Figure 6-4. The piston geometry has two distinctive regions in the lower and the upper part of the bowl. Figure 6-5 shows the evolution of injector parameters.

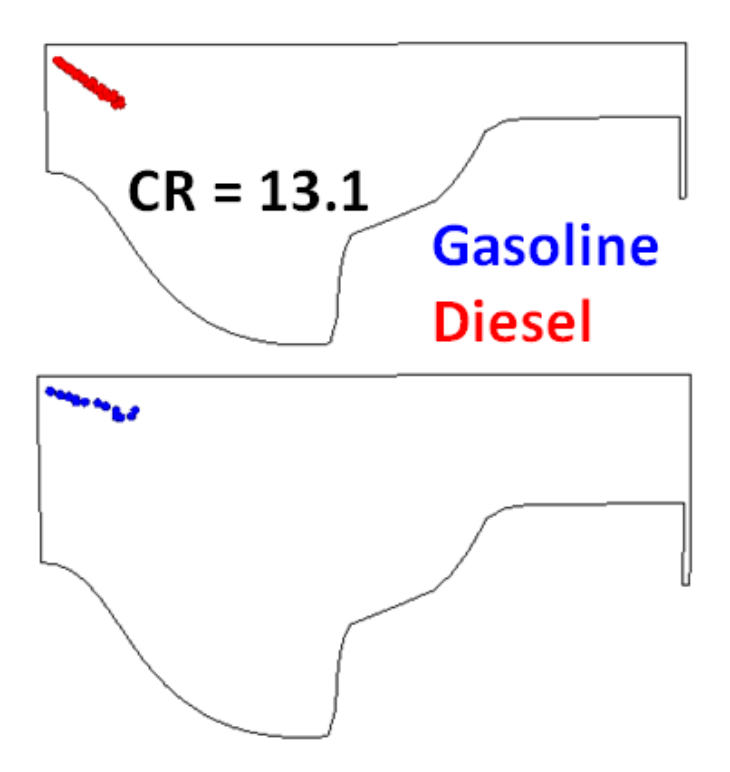


Figure 6-4. Optimum piston geometry.

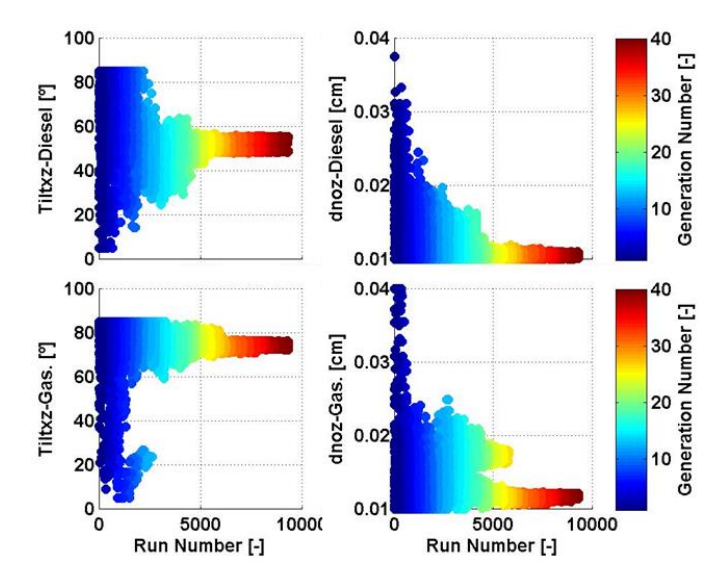


Figure 6-5. Injector design parameters as a function of the run number.

The GA eliminated extremely wide or narrow spray included half angles for the diesel fuel injector and finally converged to a spray angle near the middle of the design space. For the gasoline spray included half angle, the GA converged very quickly to a wide spray angle. The optimum gasoline injector had an included half angle of 73.1°. The diesel fuel injector had a narrow included half angle of 55.1°. Interestingly, the optimum included half angles are such that the gasoline spray is targeted into the upper region while the diesel fuel spray is targeted into the lower region of the bowl. Both the injectors converge to relatively small nozzle diameters. The optimum configuration had nozzle diameters of 115 μ m and 106 μ m for the gasoline and diesel fuel injectors, respectively.

Figure 6-6 shows the evolution of the fueling strategy and air-handling design parameters for the low-load operating condition. The GA immediately converges to a low quantity of premixed gasoline to minimize the incomplete combustion resulting from the over-lean and low reactivity premixed fuel commonly seen at low-loads. As mentioned earlier, at the low-load-high-speed conditions, the chemistry timescales are long while the engine timescales are short. One way to shorten the chemistry time scale and address the mismatch would be to use a high percentage of the higher reactive fuel (i.e., diesel fuel in the current study). Accordingly, the GA converges to low levels of gasoline fraction very quickly. Interestingly, the GA does not settle on neat diesel fuel operation and prefers having a small, but non-negligible

percentage of gasoline. Of the total fuel mass, 15% was gasoline, most of which is direct-injected. The premixed fuel mass was only 5% of the gasoline mass, which is 0.55% of the total fuel mass. The GA converges to an early SOI timing for the diesel fuel injection with an optimum SOI timing of -45 °aTDC. The gasoline injection converged to a near TDC injection timing with an optimum SOI of -15 °aTDC. The optimal SOI timings for low-load were such that the fuel spray is matched with the bowl geometry to create a sufficiently high local Φ (~0.4 to 0.5) mixture that is favorable for combustion at low-load conditions. The injection pressure for the diesel fuel injection converges to 537 bar. The gasoline injection pressure has two species progressing into the final generations. However, considering that there is very little fuel in the gasoline injection, the results were insensitive to the gasoline injection pressure at the low-load condition. The optimum design chosen had a gasoline injection pressure of 881 bar.

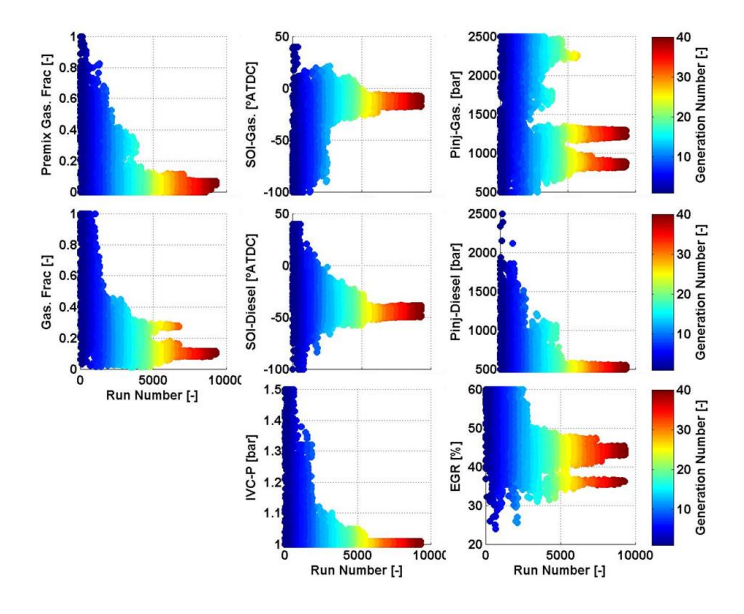


Figure 6-6. Fueling and air-handling parameters as a function of run number for low-load.

The intake pressure converges to a naturally aspirated condition of 1 bar absolute. Two EGR species progress to the final generation with optimal EGR rates of 36% and 42%. The two species have NFE within 0.5% of each other. The species with the lower EGR rate has higher combustion efficiency, but also higher engine-out NOx, requiring higher DEF consumption. Conversely, the higher EGR case has lower combustion efficiency, but a lower DEF penalty. Since the NFE of the two species are nearly the same, the higher EGR case was preferred due to its ability to meet NOx targets without relying on SCR after treatment

at low-loads. Practically, this is preferred to minimize the complications of low exhaust temperature (~650 K) which may result in reduced SCR efficiency.

Figure 6-7 shows the evolution of the fueling strategy and air-handling design parameters for the high-load operating condition. The GA converged to high premixed gasoline fraction values and eventually settled at an optimum value of 0.66 (i.e., 66% of the total gasoline mass is premixed). This mass is the maximum amount of fuel that could be premixed while meeting the constraints on PPRR and PP. The GA converged rapidly to operation on 92% gasoline. Contrary to the low-load case, at high-load-low-speed conditions, the chemistry timescales are short, and the engine time scales are long. Operating at high gasoline fractions helps extend the chemistry time scales because of the low reactivity of gasoline. The diesel fuel SOI timing has two species evolving into the final generations. One species has a diesel fuel SOI timing around -50 oaTDC which is representative of the classical RCCI strategy seen in past research. The second species has SOI timing close to TDC. Eventually, the species with a near TDC injection dominates and progresses to the final generations. The optimal case has a diesel fuel SOI timing of -7 °aTDC. The gasoline SOI timing converges quickly to a value after TDC. If gasoline is to be introduced before TDC, it is preferable to premix the gasoline. However, a further increase in premixed fuel mass is constrained by PPRR and PP. Accordingly, the rest of the gasoline mass is injected in the post TDC injection to achieve the necessary load. The GA converges to an optimum gasoline SOI timing of 15 °aTDC. This is the closest to TDC that the gasoline injection can occur to maximize the efficiency while meeting the soot constraint. That is, early post-injection timings resulted in increased soot emissions. A detailed analysis on soot emissions from post-injections can be found in Appendix-B and Appendix-D. Considering that there is substantial fuel mass in both the direct-injections and since the SOI timings are in the near TDC region, the GA converges to high injection pressures for both the injections. The gasoline injection has an optimum injection pressure of 2154 bar and the diesel fuel has an optimum injection pressure of 1541 bar. The higher injection pressure for the gasoline injection could be because of the significantly larger fuel quantity in the gasoline injection compared to the diesel fuel injection. Also, as will be shown later in this chapter, the gasoline injection is the primary source of soot emissions for the high-load case. The higher injection

pressure is essential to keep the soot emissions low as it enables better air entrainment and a longer residence time in the high-temperature regions. This improves the soot oxidation rates and results in reduced soot emissions at EVO.

IVC pressure and EGR converge to values near the middle of the design space for each variable. EGR converges to an optimum value of 46%. IVC pressure has two species with values of 3.41 bar and 3.69 bar progressing to the final generations. The combination of IVC pressure and EGR results in global Φ of 0.82 and 0.93 for the 3.69 bar and 3.41 bar cases respectively. Both species ended up having NFE within 2% of each other at similar levels of NOx (0.08 g/kg-f difference) and soot emissions (0.2 g/kg-f difference). The globally leaner case achieved higher GIE but suffered from higher pumping losses due to the higher intake pressure. The near stoichiometric cases had lower pumping losses, but also lower GIE due to the reduced availability of oxygen. Eventually, the species with the higher IVC-pressure of 3.69 bar was picked as the optimum as it ended up having a slightly higher efficiency. Also, the results presented in Chapter 4 have shown near stoichiometric operation to be extremely sensitive to variations in the EGR rate. Hence, the globally leaner operating condition was preferred as the optimum.

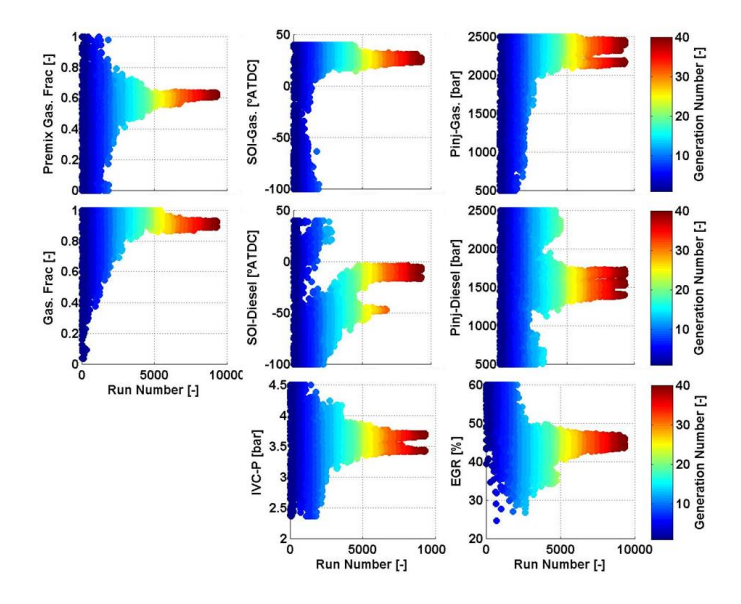


Figure 6-7. Fueling and air-handling parameters as a function of run number for high-load.

The outputs for the optimum design are shown in Table 6-4. The optimum designs met the constraints on all the outputs for both the loads as shown in Table 6-4.

Table 6-4. Outputs for the optimized design at low-load and high-load

Output	Low-Load (2 bar, 1800 rev/min.)	High-Load (20 bar, 1300 rev/min.)
GIE [%]	46.5	44.7
NFE [%]	41.9	41.6
NOx [g/kg-f]	0.18	0.31
Soot [g/kg-f]	0.00	1.88
CO [g/kg-f]	112.23	33.36
UHC [g/kg-f]	10.29	2.64
PPRR [bar/deg]	2.45	14.69
PP [bar]	42.05	194.58
CA50 [°ATDC]	-0.25	-0.38

Figure 6-8 shows the evolution of the constrained outputs as a function of run number for the low-load operating condition. The initial generations have a few points that are above the constraint value for soot emission. However, within a few generations, the GA converges to soot emissions less than 2 g/kg-f. There was no constraint set on NOx emissions, but as the generations progress, the GA minimizes the NOx emissions to reduce the DEF consumption penalty and maximize the NFE. The PPRR and PP outputs were well below the constraint value for the low-load cases. The low-load optimum case yielded a GIE of 46.5% and NFE of 41.9%. It is to be noted that the NOx emissions are near zero for this case indicating that the difference between the GIE and NFE is due to pumping losses.

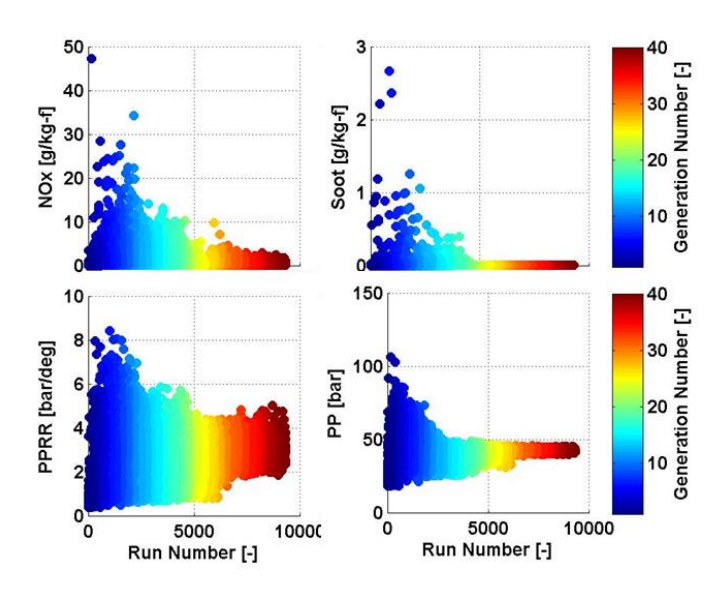


Figure 6-8. Outputs as a function of run number for low-load.

Figure 6-9 shows the evolution of constrained outputs for the high-load operating condition. Unlike the low-load cases, most of the high-load cases exceeded the constraints in the early generations. The soot emissions, PPRR, and PP outputs eventually converge to their respective constraint values and remain around the constraint value until the final generation. This indicates that all three outputs are limiting factors on achieving the maximum possible efficiency for the high-load-low-speed operating condition. Notice that the optimum cases had NOx emissions of 0.18 g/kg-f and 0.31 g/kg-f for the low-load and high-load optimum respectively. This indicates that, although SCR was considered in the optimization, the optimum strategies do not require the use of SCR. The high-load optimum case had a GIE of 44.7% and NFE of 41.6%. Similar to the low-load optimum case, the difference between the GIE and NFE is due to pumping losses.

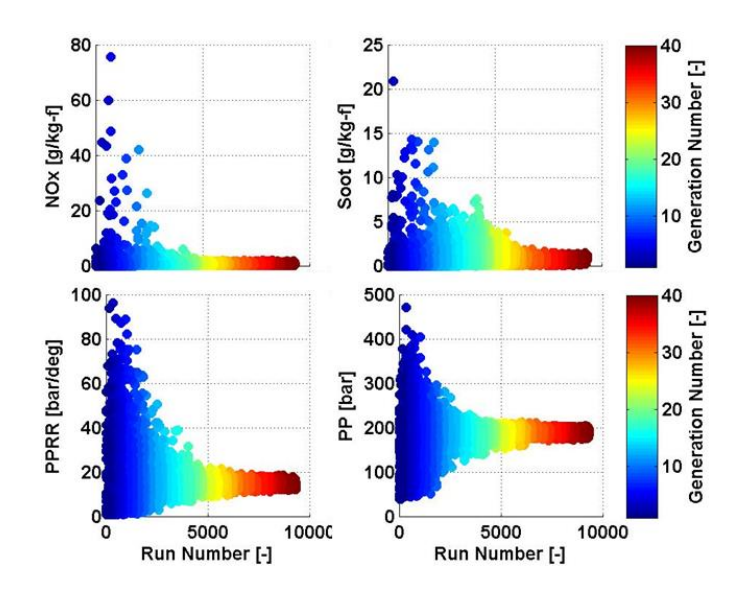


Figure 6-9. Outputs as a function of run number for high-load.

6.2.1. Combustion Characteristics

Once the optimum points were identified, in-cylinder visualization was used to understand the combustion characteristics for the low-load and the high-load optimum operating strategies.

6.2.1.1. Low-Load Combustion Characteristics

Figure 6-10 shows the in-cylinder pressure, AHRR and Figure 6-11 shows the contours of in-cylinder Φ , temperature, and PRF number at several crank angles before and after the combustion event for the low-load optimum case.

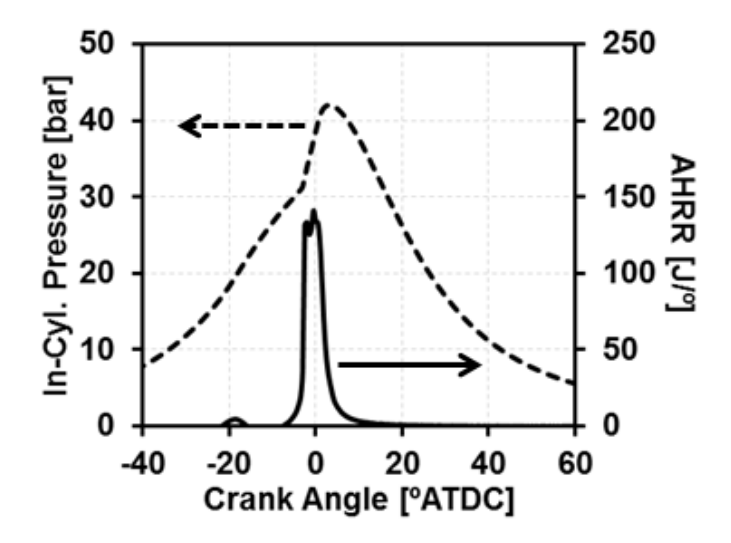


Figure 6-10. In-cylinder pressure (- -) and apparent heat release rate (-) for the low-load optimum point.

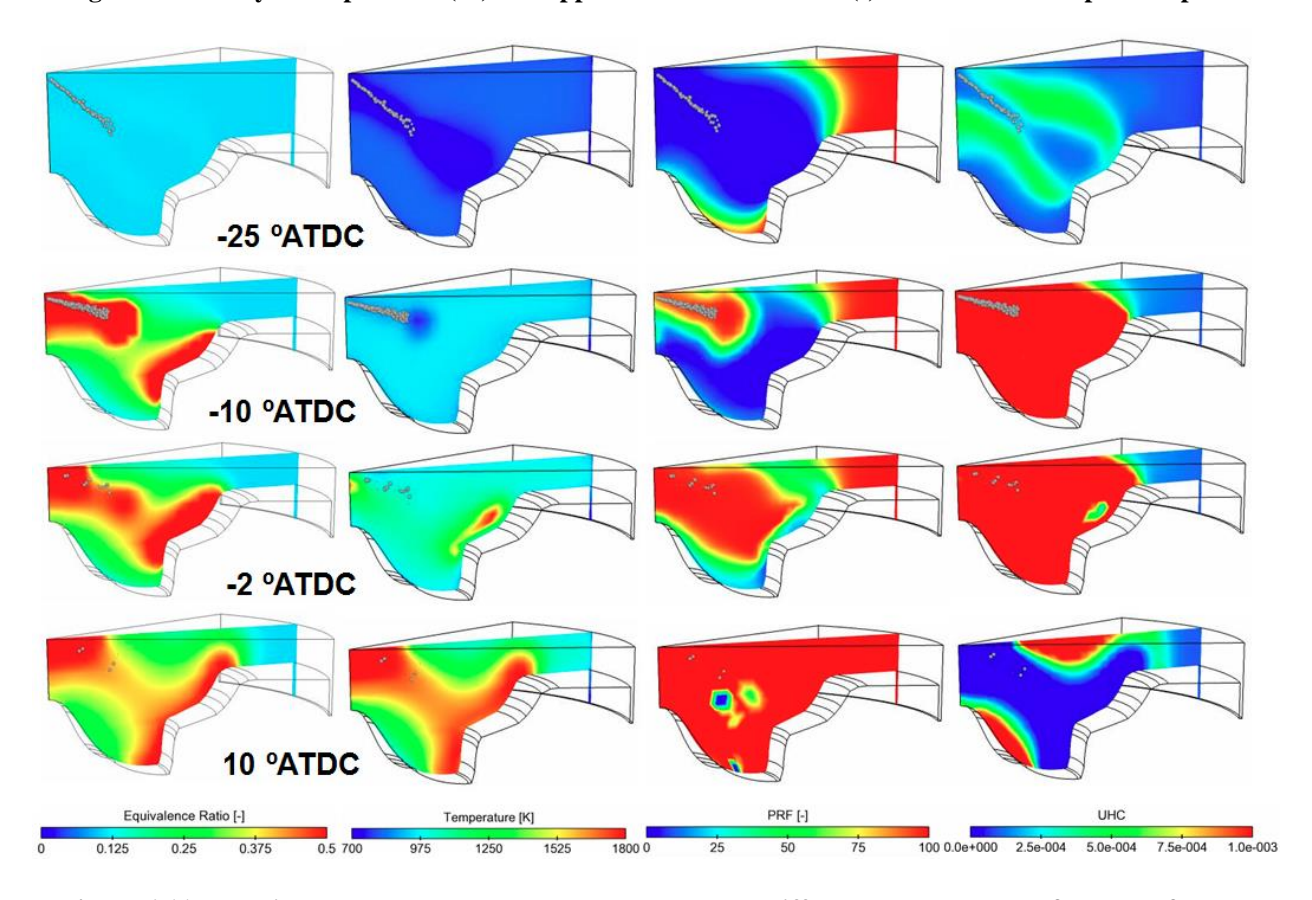


Figure 6-11. In-cylinder Φ , temperature and PRF contours at different crank angles before and after the combustion event for the low-load optimum point.

As discussed in Chapter 2, a primary challenge of low-load RCCI combustion is the high levels of incomplete combustion that result from the over lean and low reactive premixed fuel. This explains why the GA picked a case with nearly zero premixed fuel as the optimum strategy. Having a narrow angle and

an early SOI timing for the high reactivity diesel fuel ensures that the diesel fuel is contained within the bowl. This is evident from the high Φ and low PRF regions in the bowl at CA of -10 °aTDC in Figure 6-11. The injection pressure of the diesel fuel injection is only 537 bar to minimize mixing and overly lean regions. Though the gasoline injector has a wide spray angle, the optimum SOI timing is such that it sprays into the fuel rich zones created by the diesel fuel injection. The injection pressure of the gasoline injection was also low (881 bar) to avoid overmixing. Ignition occurs in the piston bowl at -2 °aTDC. Comparing the location of the ignition site with the Φ and PRF contours, we see that ignition occurs in the fuel rich region in the bowl with the highest reactivity (lowest local PRF). Progressing into the expansion stroke, the richer regions in the center of the bowl continue to combust at high temperatures. Conversely, the leaner regions close to the center of the piston bowl combust at lower temperatures and end up as sources of UHC.

From the images, it is expected that lower UHC emissions would have been achieved if no gasoline were used. This makes it of interest to understand why the GA picked 15% of the fuel to be gasoline as the optimum strategy. Accordingly, a parametric study of gasoline fraction and EGR was performed. Figure 6-12 shows the results of the study where the gasoline fraction and EGR were varied with all other inputs fixed at the optimum value. When the gasoline fraction is reduced from the optimal value of 0.15 to 0, to achieve similar combustion phasing (CA50) as the optimal case (-0.25 °aTDC), a higher percentage of EGR (48%) was required. The increased EGR results in increased levels of incomplete combustion causing the NFE to decrease. Having a part of the fuel as gasoline helps achieve the optimal combustion phasing at lower levels of EGR. This reduces the incomplete combustion and increases the NFE. However, when the gasoline fraction is increased from the optimum of 0.15 to 0.3, the EGR must be reduced from 40% to 22% to maintain the optimal CA50. The reduction in EGR results in an increase in NOx emissions which causes a reduction in the NFE due to excessive DEF consumption. Accordingly, a gasoline fraction of 0.15 in combination with an EGR of 40% was chosen as the optimum because it maximizes the NFE by minimizing incomplete combustion while keeping the NOx emissions to levels that do not require after-treatment.

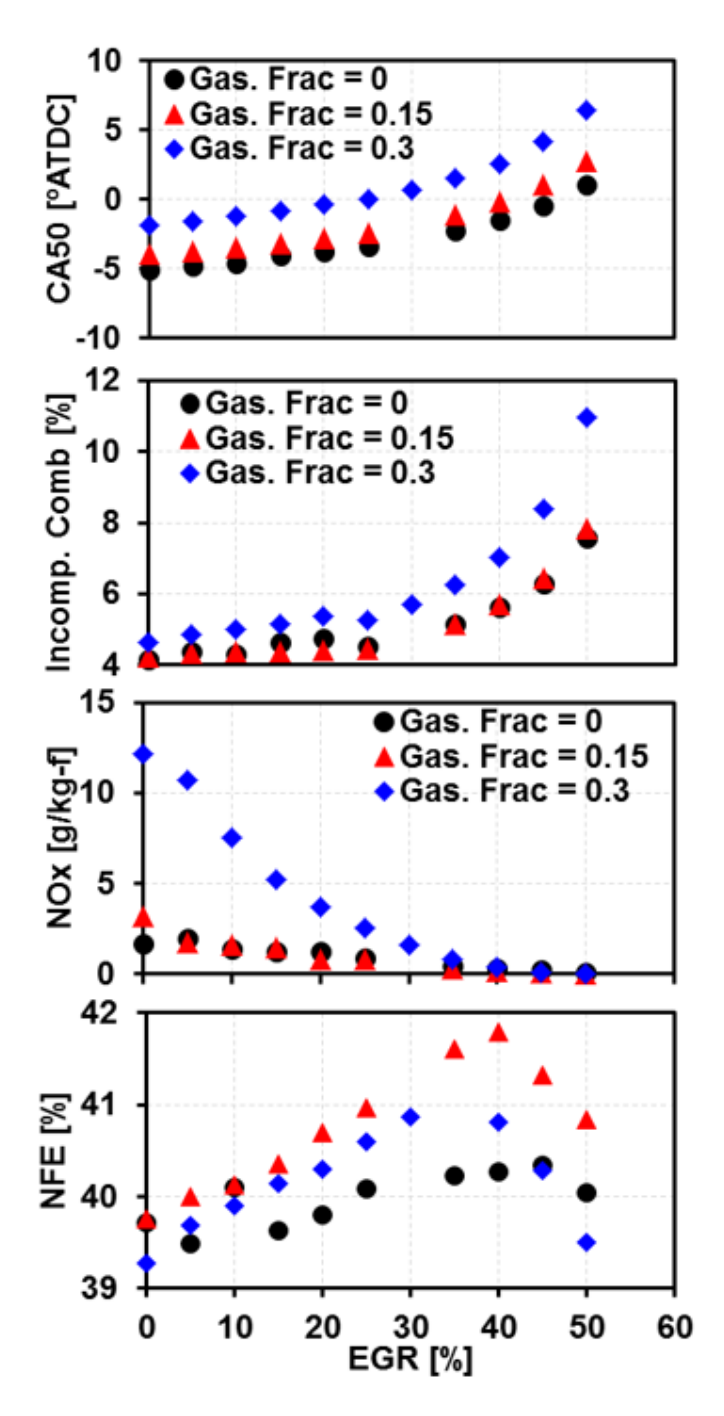


Figure 6-12. CA50, the percentage of energy in incomplete combustion, NOx emissions, and NFE as a function of EGR for the low-load optimum point.

6.2.1.2. High-Load Combustion Characteristics

To explain the combustion characteristics of the high-load optimum case, Figure 6-13 shows the in-cylinder evolution of several key species, the in-cylinder pressure, and AHRR. Figure 6-14 shows cut

planes colored by temperature, Φ , and mass fractions of isooctane, n-heptane, formaldehyde (CH₂O), and OH for the high-load optimum case.

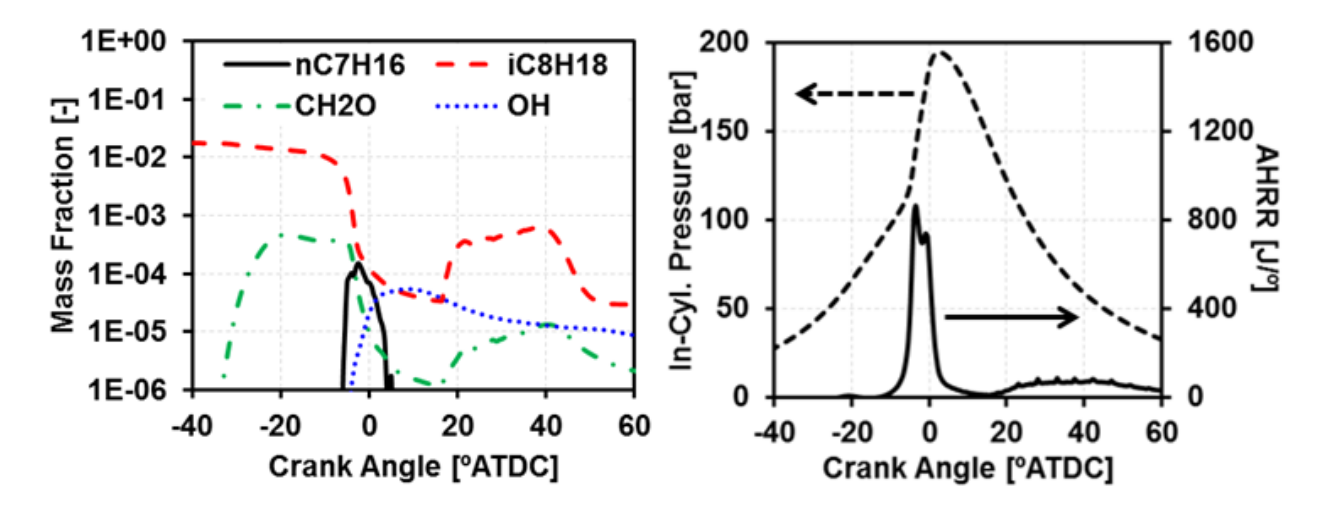


Figure 6-13. In-cylinder evolution of key species, in-cylinder pressure (- -) and apparent heat release rate (-) for the high-load optimum case.

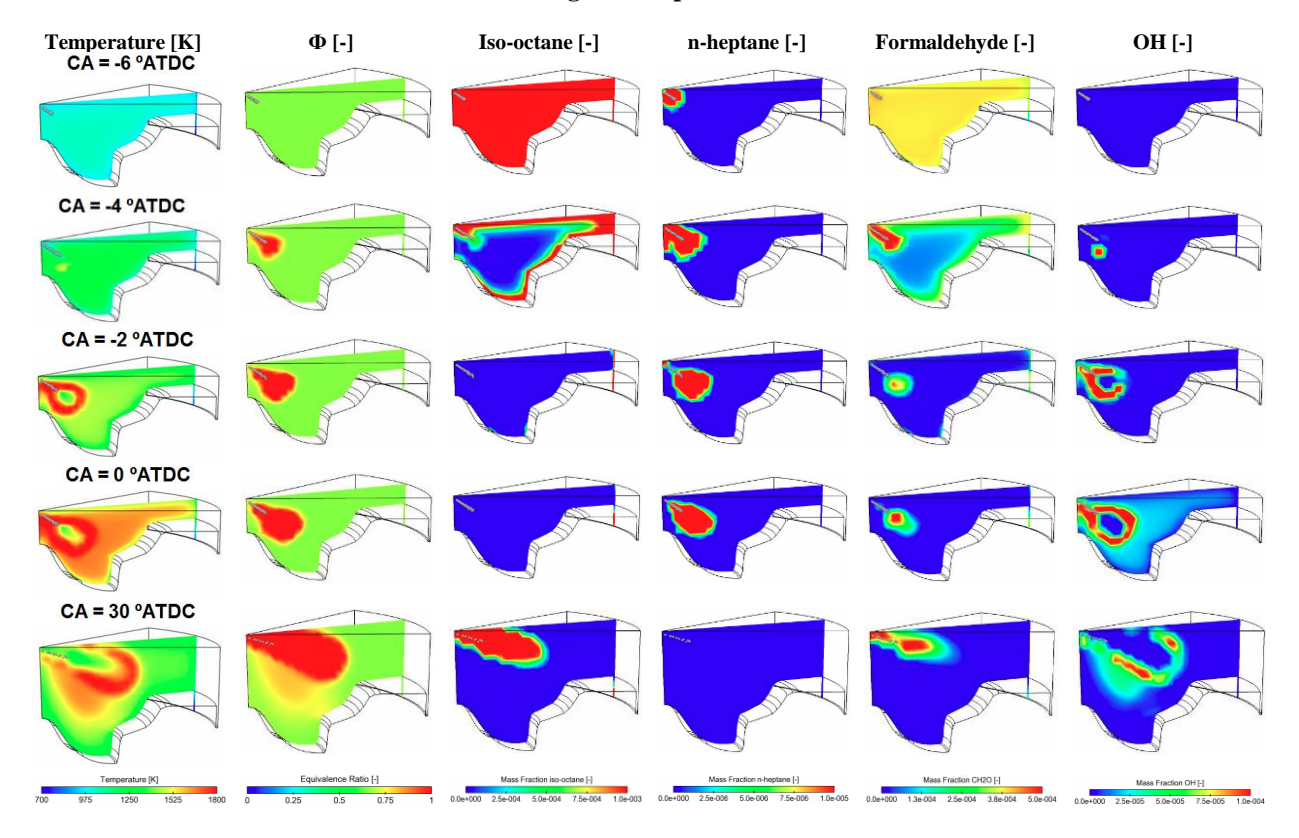


Figure 6-14. In-cylinder temperature, Φ , mass fraction of iso-octane, n-heptane, formaldehyde and OH contours for the high-load optimum case.

Formaldehyde (CH₂O) starts forming around -35 °aTDC from the low-temperature consumption of premixed iso-octane. From the heat release plot shown in Figure 6-13, two distinct peaks are visible. The first peak occurs at -4 °aTDC from ignition of the premixed gasoline triggered by the DI of diesel fuel. Notice that the second stage combustion (signaled by the appearance of OH) occurs approximately 3° after the diesel fuel injection, on the edge of the diesel fuel jet, as shown in Figure 6-14. Two crank angles later, at -2 °aTDC, the second peak in heat release occurs due to the mixing-controlled combustion of diesel fuel (n-heptane).

The gasoline DI is introduced during the expansion stroke and combusts as soon as it is introduced due to the high temperatures from the primary heat release. The late gasoline injection was identified as the main source of the soot emissions for the high-load case. This can be seen from Figure 6-15, which shows the in-cylinder evolution of soot emissions as a function of crank angle. The profiles for oxygen concentration, peak in-cylinder temperature, average in-cylinder temperature, and injection velocity are also shown to help explain the soot trend. The first peak in soot is from the combustion of the initial mixing-controlled diesel fuel combustion. The soot formed from this is mostly oxidized as the temperatures are high and there is sufficient oxygen availability. However, by the time the post-injection occurs, the combustion chamber is severely oxygen-depleted due to the oxygen consumption from the primary heat release. Notice that the oxygen mass fraction after the primary heat release is only ~0.07. Additionally, the injection and combustion event continue late into the expansion stroke (~43 °aTDC and ~60 °aTDC, respectively). During this period the temperatures remain high enough (> 1500 K) to favor soot formation, as can be seen from the peak temperature plot. Soot continues to increase until approximately 60 °aTDC. By this point, the oxygen mass fraction has decreased to 0.04. The low temperatures and low oxygen concentrations do not favor additional soot formation or oxidation and hence cause the soot curve to freeze.

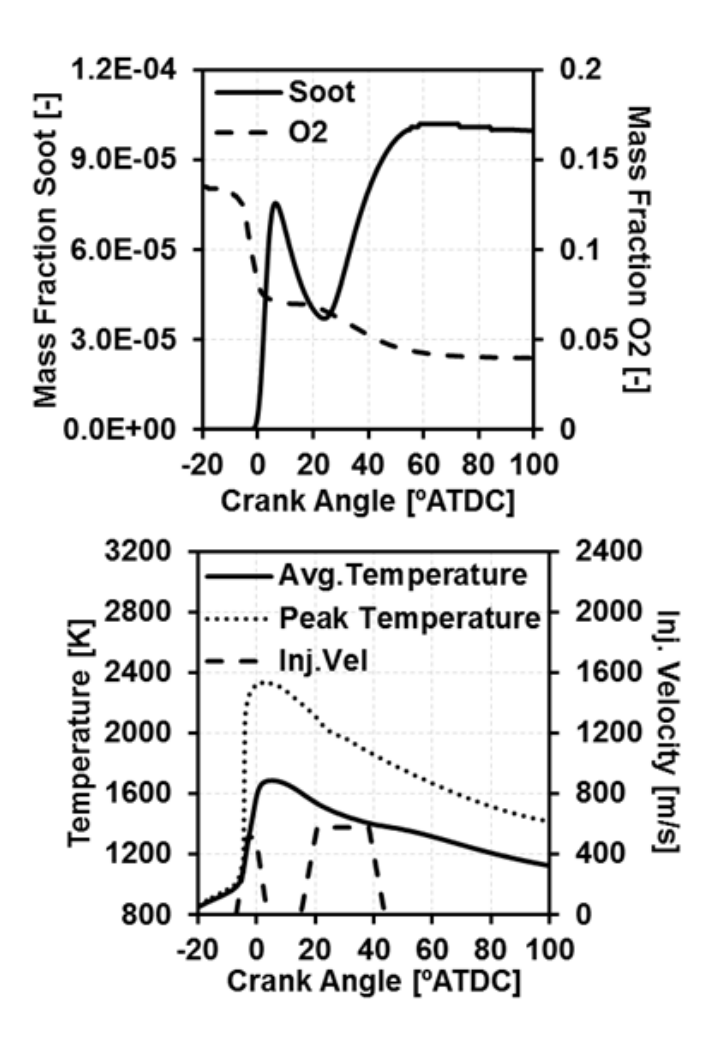


Figure 6-15. In-cylinder evolution of soot emissions, oxygen, average and peak temperature, and injection velocity profiles for the high-load optimum case.

From the in-cylinder visualizations, it was observed that the premixed gasoline was undergoing low-temperature combustion prior to the injection of diesel fuel near TDC. This suggests that the diesel fuel may not be needed to achieve ignition. To understand the importance of the diesel fuel injection and why a completely gasoline operated strategy was not chosen as the optimum, two additional cases were simulated that were completely gasoline operated. In the first case, the diesel fuel mass from the DI was removed and added to the premixed gasoline mass. In the second case, the diesel fuel mass was added to the gasoline DI fuel mass. The rest of the inputs were fixed at the values for the optimum case. Figure 6-16 shows a comparison of the PPRR and NFE from the optimum case with the two additional cases. When the diesel fuel mass was added to the premixed fuel mass, it increases the PPRR from 14.7 bar/deg. to 21.8

bar/deg. The mixing-controlled near TDC diesel fuel combustion event decreases the PPRR without decreasing the thermal efficiency. When the diesel fuel mass was added to the post TDC gasoline injection mass, the thermal efficiency decreases due to a reduction in the expansion stroke utilization. Therefore, the diesel fuel near TDC is necessary to maximize NFE and control PPRR.

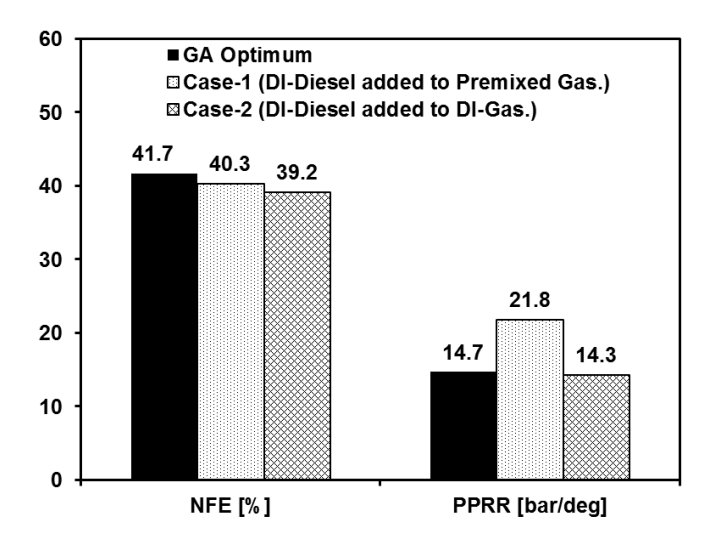


Figure 6-16. Comparison of NFE and PPRR of the optimum case with Case-1 (DI-Diesel added to premixed gasoline) and Case-2 (DI-Diesel added to DI-Gasoline).

Since the late gasoline injection decreases thermal efficiency, it is of interest to understand what has limited the GA from picking an optimum case that had a higher fuel mass in the diesel fuel injection. An additional parametric study was performed where the gasoline fraction was varied while fixing the fuel mass in the premixed fuel at the optimum value. Since the premixed fuel mass is kept constant, varying the gasoline fraction will vary the fuel mass in the gasoline and diesel fuel direct-injections by keeping the total DI fuel mass constant. The rest of the inputs were held fixed at the values of the optimum case. Figure 6-17 shows the NFE and soot emissions as a function of the gasoline fraction. The soot constraint chosen for the optimization study is also overlaid on the plot. The results show that, as the diesel fuel mass is increased, the NFE increases since more fuel is combusting close to TDC. However, increasing fuel in this high temperature mixing-controlled combustion also increases the soot emissions. The maximum NFE possible while meeting the soot constraint is obtained in the gasoline fraction range of 0.9 to 0.92, which agrees with the optimum value selected by the GA.

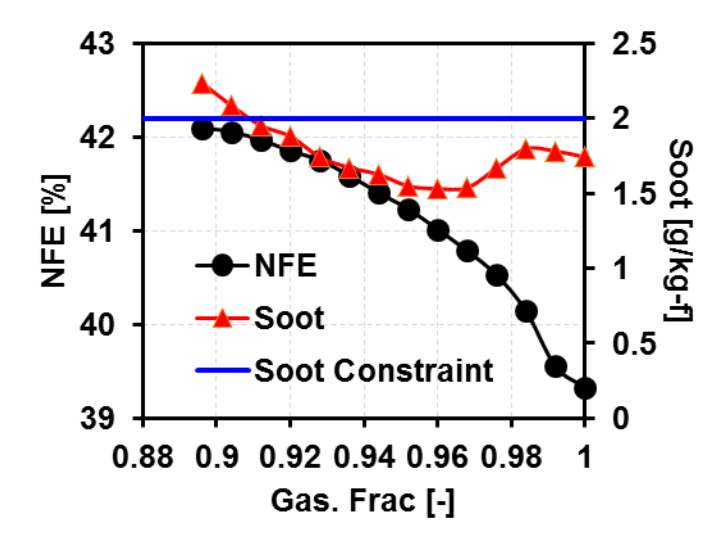


Figure 6-17. NFE and soot emissions as a function of gasoline fraction for a fixed premixed fuel mass.

6.2.2. Mid-Load Operating Condition (9 bar, 1300 rev/min.)

In addition to the low-load and high-load cases, a mid-load operating condition of 9 bar gross IMEP and engine speed of 1300 rev/min. was simulated with the optimum bowl and injector design. The purpose of simulating this case was to ensure that the efficiency and emissions benefits seen with RCCI strategy at mid-load conditions in past research are retained using the selected configuration. The fueling strategy and air-handling inputs for the mid-load operating condition were based on Kokjohn et al. [6] and are shown in Table 6-5. The injection strategy was very similar to the injection strategy considered for the current study, but both the direct-injections used diesel fuel. The gasoline fraction, which is the main control handle for this operating condition was adjusted to achieve the optimal CA50 on the current design. The results from the mid-load simulation are shown in Table 6-5. The mid-load case achieved a GIE of 50.1% and NFE of 47.2% with near zero NOx and soot emissions. This result indicates that the benefits seen with the RCCI strategy at mid-load conditions are retained using the optimized design.

Figure 6-18 shows a comparison of energy flow as a function of IMEP to explain the differences in efficiency seen at the three operating conditions studied. Compared to the mid-load condition, the low-load case has lower exhaust losses and higher wall heat transfer. These two losses offset each other and do not contribute to the efficiency differences. The difference in efficiency is primarily due to the higher incomplete combustion at the low-load operating condition. At high-load, the wall heat transfer and

incomplete combustion are almost the same as the mid-load condition, but the exhaust losses are significantly higher (increase by ~7%). The gasoline injection at 15 °aTDC combusting late into the cycle is the cause of the high exhaust losses for the high-load condition.

Table 6-5. Design inputs and results for the mid-load condition of 9 bar and 1300 rev/min.

DESIGN INPUTS					
Fueling Strategy					
Gas. Frac. [-]	0.92				
Premix Gas. Frac. [-]	1.00				
SOI 1-Diesel. [ºaTDC]	-58				
SOI 2-Diesel [oaTDC]	-37				
Pinj 1-Diesel. [bar]	800				
Pinj 2-Diesel [bar]	800				
Air-handling					
Pivc [bar]	2.1				
EGR [%]	45				
OUTPUTS					
GIE [%]	50.1				
NFE [%]	47.2				
NOx [g/kg-f]	0.07				
Soot [g/kg-f]	0.00				
CO [g/kg-f]	5.78				
UHC [g/kg-f]	4.96				
PPRR [bar/deg]	10.99				
PP [bar]	114.73				
CA50 [°aTDC]	-2.38				

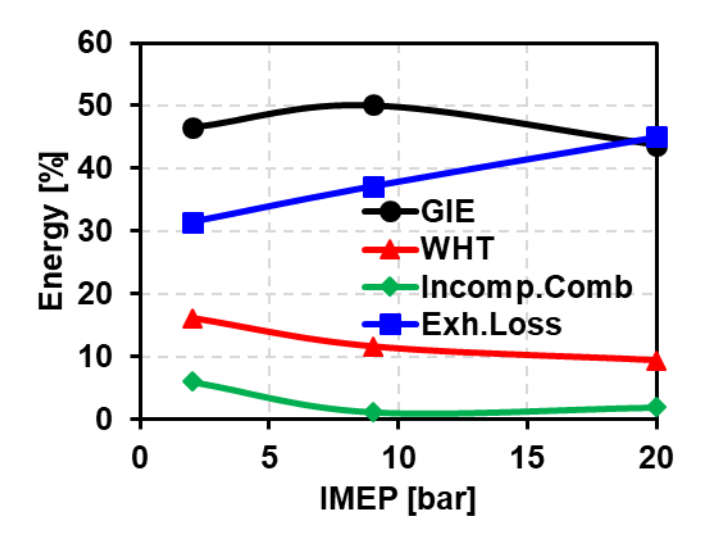


Figure 6-18. Energy Flow vs. IMEP for the optimum cases.

6.2.3. Mode Weighting Factor Effect

The results shown from the optimization study were achieved by equally weighting the efficiencies of the low-load and high-load operating conditions (i.e., by setting the mode weighting factor (W_{mode}) to 0.5). In the current section, the effect of varying W_{mode} on the optimization results will be shown. By setting W_{mode} to 0 (only the low-load NFE will be maximized), we can find a design that is optimized solely for the low-load operating condition. Similarly, by setting W_{mode} to 1 (only the high-load NFE will be maximized), we can find a design optimized exclusively for the high-load operating condition. The results from this study will be compared with the optimization results shown in the earlier section. The purpose of this study is to demonstrate the importance of considering the efficiencies of both the loads when performing an optimization study.

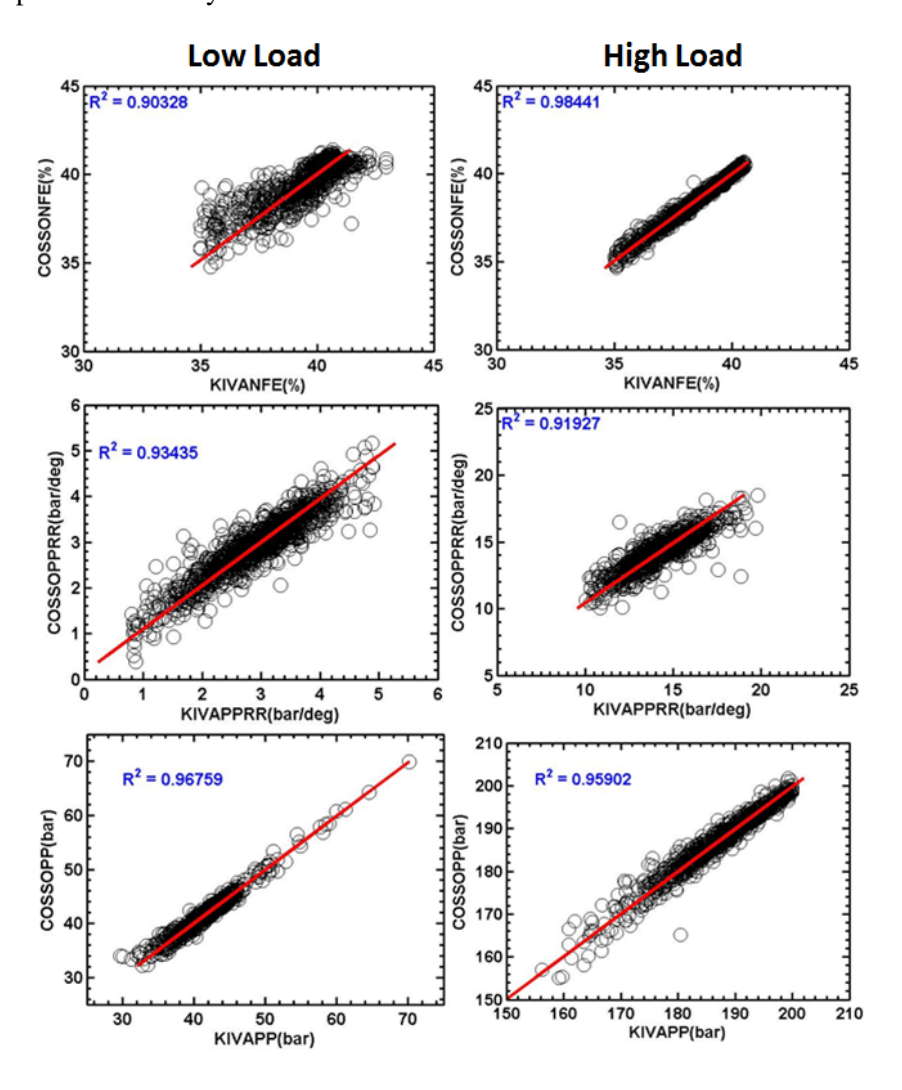


Figure 6-19. Comparison of COSSO predicted output (y-axis) to KIVA output (x-axis).

To perform this study, the COSSO tool [61] was used to fit a response surface model to the GA data. The COSSO model is then used to predict the output for a given set of input parameters. To have confidence in the results predicted by COSSO, the COSSO results were validated with the CFD simulation data from the GA at each load. Figure 6-19 shows the COSSO predicted output versus the CFD (KIVA) simulated output. A straight line with a slope of one would indicate a perfect match. As seen from the figure, all the outputs are predicted suitably for both the combustion strategies over the design space considered for the optimization study.

DK-GA was used for the current optimization study, but instead of using CFD simulations to generate the outputs, the response surface equations generated from COSSO were used to predict the outputs. In the current study, when W_{mode} is set to either 0 or 1, not only the bowl geometry and injector design parameters, but also the fueling strategy and air-handling parameters of only one operating condition (either low-load or high-load based on the value of W_{mode}) are optimized. Since it does not make sense to use the same air-handling and injection strategies for both high-load and low-load, the following procedure was used:

- 1. Assuming W_{mode} is set to 0, the optimization routine is performed to obtain a bowl geometry and injector design that is optimized for the low-load operating condition.
- 2. Keeping the bowl geometry and injector design inputs fixed at the optimum values, the optimization study is repeated by changing W_{mode} to 1- W_{mode} (i.e., from 0 to 1 for this example). Thus, for every citizen of every generation, the bowl geometry and injector design inputs remain fixed at the low-load optima values while the fueling strategy and air-handling inputs are varied. However, since W_{mode} is modified from 0 to 1, the efficiency of the high-load condition is being considered as the objective.
- 3. Following this procedure ensures that the GA is choosing the best low-load and high-load operating strategy possible on a bowl geometry and injector design that is optimized for low-load conditions (or high-load when W_{mode} is 1).

The procedure shown above is assuming W_{mode} is set to 0. A similar procedure is followed when W_{mode} is set to 1, to optimize for the best low-load and high-load operating strategies on a bowl geometry

and injector design optimized for high-load conditions. Table 6-6 and Table 6-7 show a summary of the design parameters and the outputs for the optimum points chosen from this study respectively. The optimum points were simulated with the KIVA code to validate the COSSO results.

Table 6-6. Optimized inputs for low-load and high-load at different W_{mode} values.

Table 6-6. Optimized inputs for low-load and high-load at different W _{mode} values.								
		$\mathbf{W}_{\mathrm{mode}} = 0$		$W_{\mathrm{mode}} = 1$				
DESIGN INPUTS								
	Low-Load (2 bar, 1800 rev/min.)	Mid-Load (9 bar, 1300 rev/min.)	High-Load (20 bar, 1300 rev/min.)	Low-Load (2 bar, 1800 rev/min.)	Mid-Load (9 bar, 1300 rev/min.)	High-Load (20 bar, 1300 rev/min.)		
Bowl and In	njector Design							
CR		15.7			11.8			
Tiltxz-Gas. [°]		81.81			66.91			
Tiltxz- Diesel[°]		58.95			25.51			
dnoz-Gas. [µm]		100			100			
dnoz- Diesel [µm]	100				100			
Fueling Stra	ategy			,				
Gas. Frac.	0.1	0.9	0.88	0.01	0.92	0.995		
Premix Gas. Frac. [-]	0.02	1	0.42	0.03	1	0.71		
SOI-Gas. [°ATDC]	-14	-	14.2	-20.2	-	-5		
SOI-Diesel [°ATDC]	-35	-58/-37	-54	-38.4 -58/-37 -44.4				
Pinj-Gas. [bar]	850	-	2419	500 - 2500				
Pinj-Diesel [bar]	651	800/800	1569	500 800/800 1750				
Air-handlin	g							
Pivc [bar]	1	2.1	3.13	1	2.1	4.25		
EGR [%]	30	45	45.2	0	41	35		

Table 6-7. Optimized	outputs for low-load	l and high-load at	different W _{mode} values
Tuble o / Optimized			

	$\mathbf{W}_{\mathrm{mode}} = 0$ $\mathbf{W}_{\mathrm{mode}} = 1$						
	Low-Load (2 bar, 1800 rev/min.)	Mid-Load (9 bar, 1300 rev/min.)	High-Load (20 bar, 1300 rev/min.)	Low-Load (2 bar, 1800 rev/min.)	Mid-Load (9 bar, 1300 rev/min.)	High-Load (20 bar, 1300 rev/min.)	
GIE [%]	48.4	49.5	35.6	38.1	49.1	47.6	
NFE [%]	43.2	46.4	33.8	32.0	46.3	43.0	
NOx [g/kg-f]	8.32	2.27	0.06	16.3	0.34	6.53	
Soot [g/kg-f]	0.00	0.01	1.73	0.00	0.00	1.16	
PPRR [bar/deg]	6.86	9.03	13.54	3.93	4.67	15.13	
PP [bar]	55.86	105.4	199.36	33.12	90.54	198.3	

Figure 6-20 shows a comparison of the COSSO predicted and KIVA simulated results of the optima for W_{mode} of 0 and 1. Considering the wide range of the design space for the current study, the COSSO model gives a reasonable agreement in trends and magnitudes with the KIVA simulated results for both the mode weights.

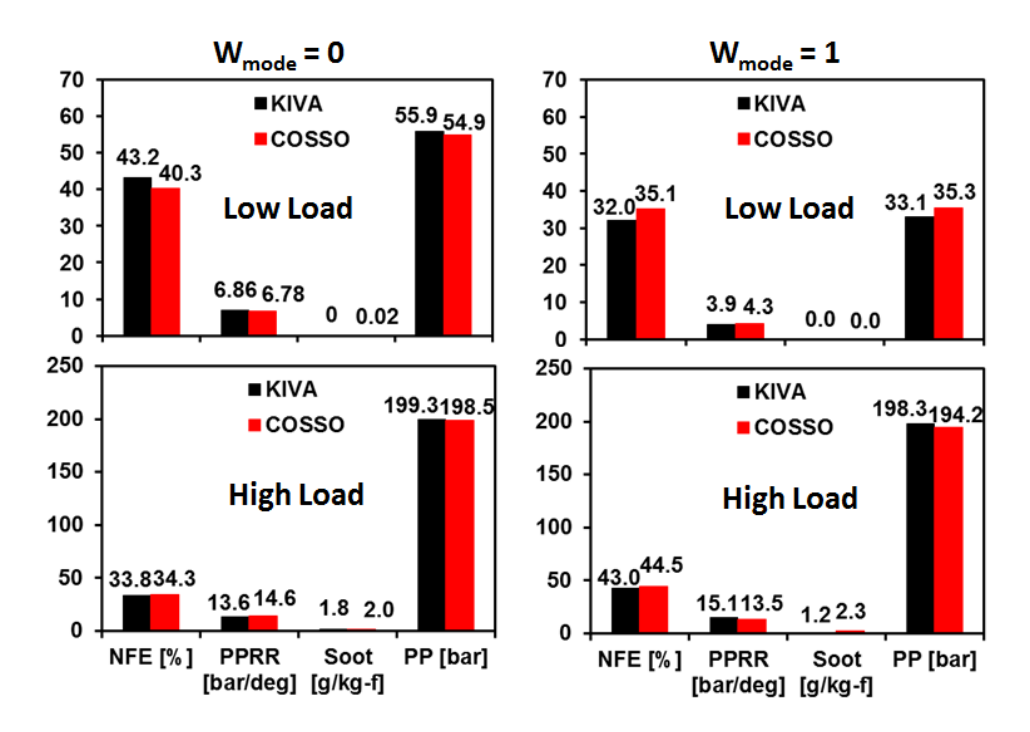


Figure 6-20. Comparison of COSSO predicted and KIVA simulated results for the optima for W_{mode} of 0 and 1.

Investigating the optimum design parameters shows that, when the low-load operating condition is heavily weighted, the optimum converges to a reasonably high CR of 15.7. Conversely, giving the high-

load operating condition, a higher weight leads to a low CR of 11.8 as the optimum value. These two mode weights provide the bounds on the upper and lower limit on CR. Interestingly, when an equal mode weighting was given to both the operating conditions the optimum CR (CR = 13.1) chosen is close to the average of these two CR's. The optimum injector design remained similar across different mode weights. The optimal configuration had a narrow spray angle for the diesel fuel injection and a wide spray angle for gasoline injection with a small nozzle diameter of 100 microns for both the injectors. Figure 6-21 shows the optimum bowl geometries for all the three mode weights studied.

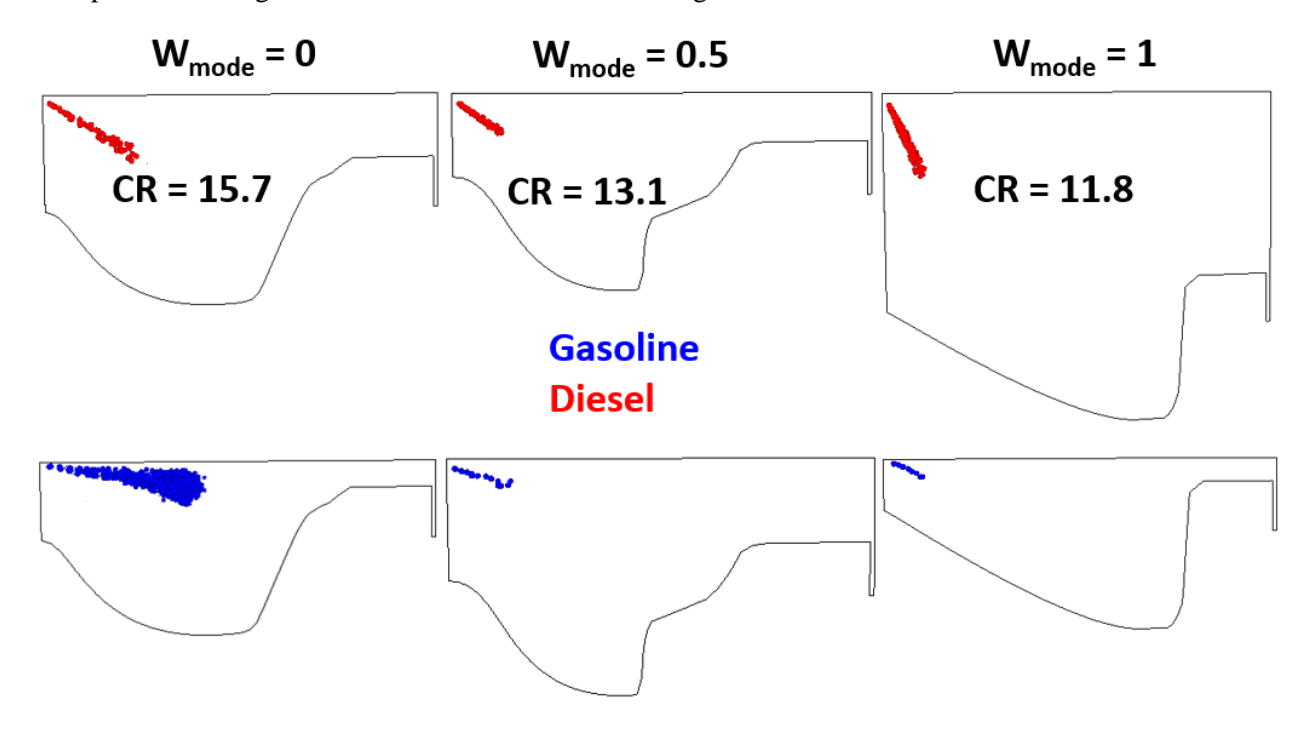


Figure 6-21. Optimum bowl geometries for the three mode weights.

The optimal fueling strategies also were very similar at different mode weights. The low-load optimum at both the mode weights had a diesel LTC strategy with a small amount of fuel being gasoline (\sim 2-3%), like the optimum shown in Table 6-3. The high-load optimums were also similar to the optima shown in Table 6-3, where the majority of the fuel is gasoline. However, for W_{mode} of 1, the SOI timings of gasoline and diesel fuel are before TDC and relative early compared to the optima for W_{mode} of 0.5 (shown in Table 6-3) where the gasoline injection was post TDC. Since the optimum CR for W_{mode} of 1 is lower

than the optimum CR for W_{mode} of 0.5, it was possible to have relatively early SOI timings while meeting the PPRR and PP constraints.

From the outputs in Table 6-7, it is evident that when low-load is given a higher priority (W_{mode} of 0), though the low-load case has an excellent efficiency, the high-load optimum ends up having a poor efficiency. A similar result is seen for W_{mode} of 1 with the low-load operating condition having a poor efficiency. Figure 6-22 shows GIE and NFE as a function of IMEP for the three values of W_{mode} studied.

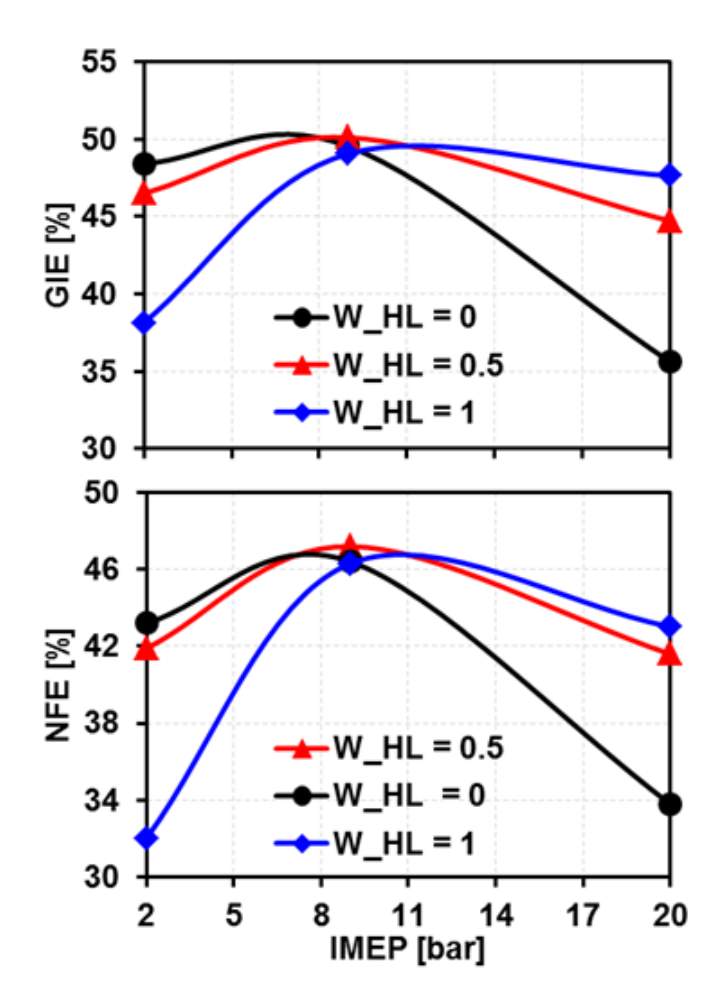


Figure 6-22. GIE and NFE vs. IMEP for different W_{mode} values.

The figure shows that giving preference to one operating condition (low-load or high-load) over the other benefits only the operating condition that was prioritized in the optimization and has a negative impact on the performance at the other operating condition. Giving equal weight to both operating conditions yields an optimum design with efficiencies close to the best possible efficiency at both the loads

and shows good performance across all points considered. It is also interesting to note that the mid-load operating point, 9 bar IMEP and 1300 rev/min., is insensitive to the selected bowl geometry or injector design. This result highlights the importance of considering multiple modes of the drive cycle simultaneously when optimizing the engine design.

6.3. Conclusions

In this chapter, a computational optimization study was performed for RCCI combustion considering the performance at low-load-high-speed (2 bar, 1800 rev/min.) and high-load-low-speed (20 bar, 1300 rev/min.) operating conditions simultaneously. The optimization study considered 28 design inputs which included parameters for piston bowl geometry, injector design, air-handling and fueling strategy. When both conditions were equally weighted, the optimization study resulted in an optimum CR of 13.1 with a stepped piston bowl geometry that had two distinctive regions. Results also showed that a narrow spray angle for diesel fuel and a wide spray angle for gasoline would be necessary to target the two regions of the bowl. The optimal fueling strategy had a diesel LTC strategy at low-load with very little premixed fuel and a low gasoline percentage (~15% of the total fuel mass). At high-load, the optimum strategy was a mixed mode combustion strategy with 92% of the fuel being gasoline and most it being premixed. The small quantity of diesel fuel present was injected close to TDC and this along with the premixed fuel contributed to the primary heat release. The rest of the gasoline was injected as a load extension injection after TDC to achieve the necessary load.

The COSSO response surface model was fit to the GA data and was used to study the effect of weighting the efficiencies on the GA results. It was found that when low-load is given a higher weight, a reasonably high CR piston (CR ~ 15.7) is preferred as the optimum. Conversely, giving a higher weight to high-load results in a low CR (CR ~ 11.8) piston as the optimum. Results also showed that prioritizing one load highly over the other would yield a bowl geometry that affects the performance negatively at the other load condition. The study highlighted the importance of considering multiple loads simultaneously during optimization studies to achieve a realistic optimal design that yields good performance across a range of operating conditions.

Chapter 7 Machine Learning in Genetic Algorithm Optimization

In the previous chapter, it was shown that engine design should be optimized considering multiple operating modes simultaneously to achieve an optimum design that works across the drive cycle. Therefore, to thoroughly optimize an engine design, it would be ideal to perform an optimization considering all the modes of a drive cycle. However, the GA took an extremely long time (~ 3 months) to complete the optimization of two operating points. If the optimization were to be setup considering all the modes of a drive cycle, the optimization process must be made faster to finish the GA in a reasonable time. One approach to address this issue would be to implement machine learning in GA optimizations.

The GA optimizations generate large amounts of data after every generation. For example, the multi-mode GA optimization presented in Chapter 6 generated 25,000 data points upon the completion of the GA. Most of this data is unused because the focus is usually on the optimum point or trends near the optimum point. However, the rest of the data has useful information about the interactions between the inputs and the outputs over the entire design space studied. As shown in Chapter 4 and Chapter 6, non-parametric regression analysis can be used to run additional DOEs and optimization studies within the design space in a much shorter time (less than a day) than the multidimensional CFD code. Nevertheless, so far, non-parametric regression analysis was performed with the GA data only upon completion of the GA. If a similar approach could be used within the GA after every generation, then the regression model could be used instead of the CFD code to predict the outputs. This would reduce the optimization time significantly. However, to perform this study, it is essential to find a regression model that works efficiently with non-parametric data, generates the response function and predicts the response in a short time (ideally, less than an hour).

In the previous chapters, the COSSO tool [61] was used to perform non-parametric regression analysis with the GA data. Though it has worked well in the earlier studies, the COSSO tool has several shortcomings. Firstly, the COSSO tool takes a long time to generate the response function. The time taken to generate the response increases with the number of design variables and the number of training data points. For example, for the multi-mode GA data, when all the 20,000 data points were used, the COSSO

tool took more than a day to generate the response function for each output of interest. Hence, the GA data had to be filtered to 2,000 useful points to reduce the estimation time to a day for each output. Even for the high-load GA in Chapter 4, which had only six design variables, the dataset had to be filtered to 2,000 useful points to ensure that the response function for each output is generated within a day. This is not preferred since the majority of the design space is eliminated upon filtering the dataset. Secondly, the COSSO tool requires the specification of a center point design. When using the COSSO tool with the GA data, the center point design is usually chosen as the optimum point. Hence, the response functions generated can be perceived as a sensitivity analysis about the optimum point. Since a high weight is given to the center point design, the magnitude of the COSSO predictions agree well with the CFD results close to the center point design. However, as the test point deviates from the center point design, sometimes, the COSSO predicted magnitudes deviate from the CFD results. Figure 7-1, shows an example [49] of the COSSO and the KIVA predicted results for NOx and soot emissions as a function of SOI of diesel fuel. The center point design is highlighted on each plot. For both the outputs, the trends predicted by COSSO agree well with the KIVA predicted results. In terms of magnitudes, close to the center point design, there is a good agreement between COSSO and KIVA. However, as the SOI timing moves further away from the SOI of the center point design, the difference increases.

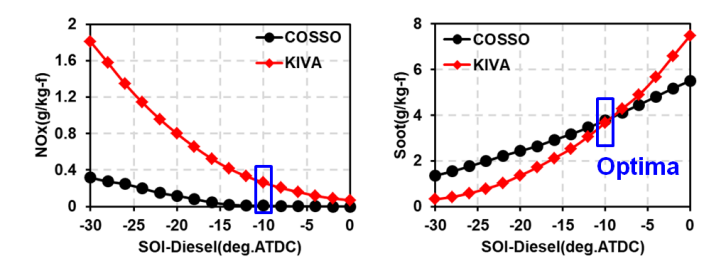


Figure 7-1. COSSO and KIVA predicted results of NOx and Soot emissions as a function of SOI-Diesel. The blue box highlights the center point design used to generate the COSSO response function.

The previous discussion has shown that, although the COSSO tool has worked well with the GA data in the previous studies, due to its shortcomings, it cannot be used within the GA to speed up the optimization process. This motivates the need to find a model generation approach that is fast and works well with large non-parametric datasets like the GA data. Several machine learning approaches that have

been shown to work well with non-parametric datasets were discussed in the literature review (Chapter 2). In previous studies [62, 63] comparing machine learning approaches for non-parametric datasets, the GPR approach has shown superior performance. Accordingly, in the current study, the GPR approach will be used to analyze the GA data.

7.1. Gaussian Process Regression (GPR)

GPR [67] is a non-parametric regression technique that can be applied to any dataset where the functional form is unknown. This approach is named as GPR since the response function has the functional form of a Gaussian (or normal) distribution. Past literature [66, 68] has shown GPR to be a reliable and fast approach for performing non-parametric regression analysis. The reason for the superior performance of the GPR approach is due to the functional form of the response function, also called the kernel function. The most commonly used kernel function for GPR is the exponential kernel, which has a functional form given by

$$f(x_j) = \sum_{i=1}^n \sigma_f^2 \exp(-r), \qquad (27)$$

$$r = \sqrt{\sum_{m=1}^{d} \frac{(x_{im} - x_{jm})^2}{\sigma_m^2}},$$
 (28)

where n is the total number of training data points, d is the total number of input variables, and like COSSO, the kernel parameters σ_f and σ_m are estimated by minimizing the residual function given by

$$R = \frac{1}{n} \sum_{i=1}^{n} [(y_i - f(x_i))^2] + \lambda J(f), \qquad (29)$$

where y_i is the CFD result of the current objective to be fit. The GPR approach works efficiently because the influence of a training data point (x_i) on a test data point (x_j) is based on the distance between the two points. The exponential factor in the kernel function is a function of the distance between the two points. When the two points are close to each other (i.e., $x_i \sim x_j$), the exponential value tends to 1. This indicates that the training data point has the maximum influence on the test data point. Conversely, when the two points are far from each other (i.e., $x_i - x_j \sim \infty$) the exponential value tends to 0, indicating that the training data point has no influence on the test data point. Therefore, through the response function, each training data point gets a weightage. The training data points that are closest to the test data point are given a high weightage. As the distance between the training and the test data point increases, the weightage decreases exponentially. This causes the training algorithm to converge significantly faster than the COSSO approach where the functional form is a spline and all the training data points are given equal weightage.

For the response function to be smooth, the output values at neighboring data points must be alike, and the distant data points should have negligible effect. The kernel parameter σ_m controls the impact of a data point x_i on the response function, based on the distance between x_i and x_j . To demonstrate the effect of changing σ_m , Figure 7-2 shows $f(x_j)$ evaluated for different values of σ_m with x_j varied from 0 to 10 in steps of 0.1, while x_i is set to zero and σ_f is set to one. As seen from the figure, for a small value of σ_m , a minor change in x_j (i.e., distance between x_i and x_j increases) causes a rapid decrease in the response function. This indicates that the corresponding input variable has a large effect on the response function. As the value of σ_m increases, the function starts to respond more gradually to variations in x_i .

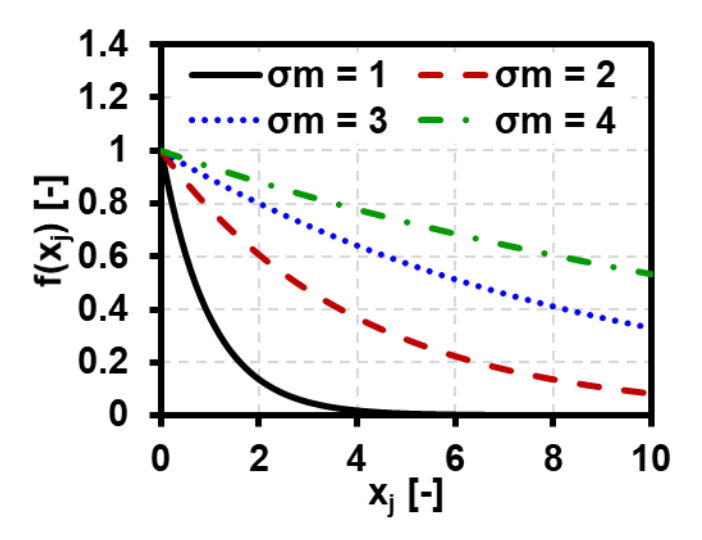


Figure 7-2. Response function of the exponential kernel evaluated at different values of the kernel parameter σ_m .

The kernel parameter, σ_f , gives an estimate of the maximum value the function can have. By adjusting σ_f , the magnitude of the GPR response function is adjusted to match the desired output for a given training data point. To demonstrate the effect σ_f has on the response function, Figure 7-3 shows $f(x_i)$

evaluated for different values of σ_f with x_j varied from 0 to 10 in steps of 0.1 while x_i is set to 0 and σ_m is set to 1. As seen from the figure, by adjusting σ_f , the maximum value of the response function can be modified.

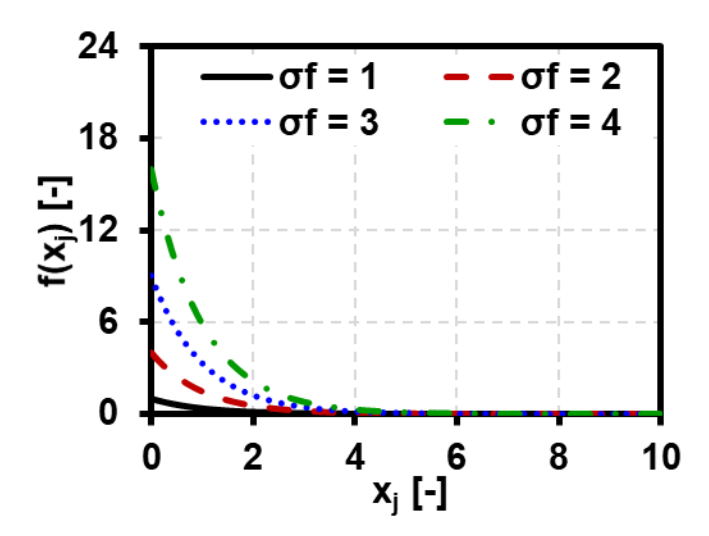


Figure 7-3. Response function of the exponential kernel evaluated at different values of the kernel parameter σ_f .

There are several kernel functions explored in literature for GPR analysis [68]. All the kernel functions have a Gaussian response with the two kernel parameters σ_f and σ_m , which are used to control the shape of the response function. To verify the performance of the GPR approach with GA data, the high-load data from the multi-mode GA was used. The dataset was split up into training and test data with 80% of the data points allocated randomly for training and the remaining 20% for the test data. Various kernel functions were trained with the same training data, and their performance was evaluated with the test data. Table 7-1 shows the various kernel functions explored, their functional forms, and the R^2 values for GIE, NOx, Soot and PP outputs. The R^2 values are estimated for a linear fit between the GPR predicted outputs and the CFD predicted outputs (available from the GA data) of the test data. Results show that all the kernel functions performed reasonably well with R^2 values greater than 0.92 across all the outputs. All the kernel functions investigated took ~15 minutes individually to generate the response function for each output and to estimate the output values for the test data. In comparison, the COSSO approach took more than a day to perform the same task. This study demonstrates the superior efficiency of the GPR compared to the

COSSO approach for non-parametric regression analysis. Of all the response functions explored, the matern 3/2 kernel showed the best agreement with the highest R^2 values for all the outputs. Accordingly, the matern 3/2 kernel will be used for performing further analysis.

Table 7-1. Kernel functions explored, their functional forms and the R² values for the fits between the GPR and the CFD predictions for the GIE, NOx, Soot and PP outputs.

Kernel Function	Functional Form	GIE	NOx	Soot	PP
Exponential	$k(x_i, x_j) = \sigma_f^2 \exp(-r)$	0.92	0.95	0.92	0.97
Squared Exponential	$k(x_i, x_j) = \sigma_f^2 \exp(-r^2)$	0.92	0.95	0.92	0.97
Matern 3/2	$k(x_i, x_j) = \sigma_f^2 (1 + \sqrt{3} r) \exp(-\sqrt{3} r)$	0.95	0.96	0.94	0.98
Matern 5/2	$k(x_i, x_j) = \sigma_f^2 (1 + \sqrt{5}r + \frac{5}{3}r^2) \exp(-\sqrt{5}r)$	0.94	0.96	0.94	0.98

7.2. GPR in GA Optimization

The previous section has shown that the GPR approach with the Matern 3/2 kernel works efficiently with non-parametric datasets and performs regression analysis in a short time. Hence, this approach can be used within the GA to try and speed up the optimization process. Figure 7-4 shows the flow chart outlining the procedure used to speed up the GA optimization.

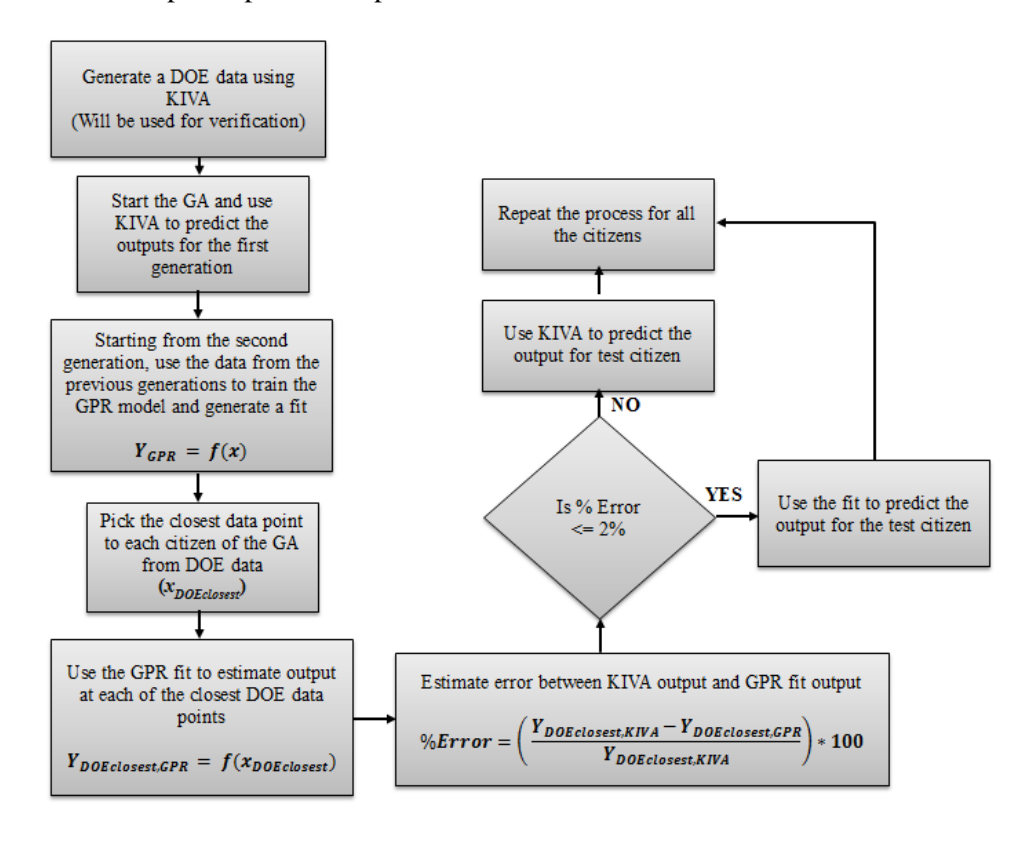


Figure 7-4. Flowchart outlining the CFD+GPR approach for GA optimization.

Before starting the GA, a Latin hypercube DOE dataset of 1000 data points within the input range used for the GA, is simulated in KIVA. This dataset will be used to verify the performance of the GPR model within the GA. Once the DOE runs are complete, the GA is initiated. The first generation is run entirely with KIVA. The data generated from the first generation is used to train the GPR model and generate the response functions for all the outputs of interest. The performance of the GPR model is evaluated using the Latin hypercube DOE dataset generated prior to initializing the GA. From the DOE dataset, the closest point to each citizen of the new generation is estimated. These closest DOE data points will be used to verify the performance of the GPR model. It is reasonably assumed that if the GPR model performs well for the neighboring points of a test citizen, then it is expected to perform well for the test citizen. To identify the closest DOE data point to each citizen, the Euclidean distance from the new generation dataset of the GA to every point in the DOE dataset is estimated. From the estimated distances, the DOE data point with the minimum distance is picked as the closest DOE data point. It is to be noted that prior to estimating the distance, the DOE and the GA data should be normalized to a range between zero and one for all the input variables. This is done to ensure that the relative magnitudes of the inputs do not impact the distance estimation. Upon identifying the closest points from the DOE dataset, the GPR response functions are used to evaluate the outputs for each of these closest DOE data points. However, since the DOE cases were run in KIVA prior to starting the GA, the CFD predicted output for these cases is available. By using the CFD result and the GPR estimated result, a percentage error is estimated for each of the closest DOE data points. If the GPR predicted output for the closest DOE data point has an error of less than 2%, then the output for the corresponding citizen is predicted using the GPR model (i.e., KIVA is not run). On the contrary, if the GPR prediction for the closest DOE data point exceeds an error of 2%, then the corresponding citizen will be simulated in KIVA.

It is to be noted that the GPR model is trained at the start of every new generation. That is, for every new generation, the data from all the previous generations is used to train the GPR model. Therefore, as the number of generations increase and the design space is more thoroughly covered by the GA, it is expected that the number of runs predicted by the GPR model will also increase. As the number of GPR evaluations

increases, the overall time taken for the optimization process reduces. This approach will be referred to as the CFD+GPR approach in the rest of the thesis. The validation of the CFD+GPR approach with GA data will be shown in the next section.

7.2.1. Validation of CFD + GPR Optimization Approach

To validate the approach, initially, an optimization was run completely with CFD (in KIVA) using the DK-GA. Later, the GA was repeated with the CFD+GPR approach to see if a similar optimum as the GA run solely with CFD is obtained. Figure 7-5 shows the injection strategy used for the GA. Table 7-2 shows the design parameters and their corresponding ranges used in the GA. The optimization was performed at a nominal load of 20 bar gross IMEP and engine speed of 1300 rev/min. with a fixed IVC-pressure of 3.96 bar.

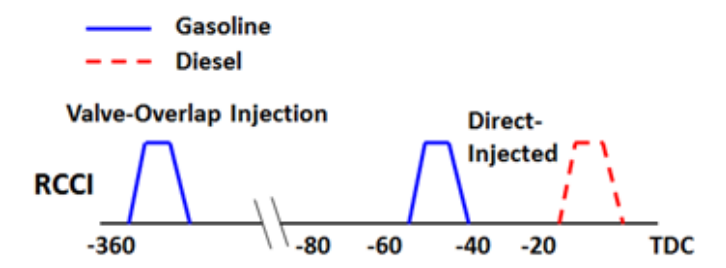


Figure 7-5. Injection strategy used for the GA optimization study used to evaluate the potential of combining the GA with the GPR approach.

Table 7-2. Range of variation allowed for each design parameter in the optimization study used to evaluate the potential of combining the GA with the GPR approach.

Input	Range
Premix Gas. Frac. [-]	0 to 1
Gas. Frac. [-]	0 to 1
SOI-Gas. [°aTDC]	-100 to 40
SOI-Diesel [°aTDC]	-100 to 40
EGR [%]	30 to 60

Both the GA's were run with 100 citizens per generation for 50 generations. Prior to running the GA with the CFD+GPR approach, as explained earlier, a Latin hypercube DOE dataset of 1000 data points within the input ranges shown in Table 7-2, was simulated in KIVA. To ensure that the matern 3/2 kernel is performing as expected with the new dataset, the data obtained from running the GA completely with KIVA was used to train the GPR model with a matern 3/2 kernel. Then the GPR model was tested using

the Latin hypercube DOE dataset. Figure 7-6 shows the agreement between the CFD and the GPR predicted outputs for the DOE dataset.

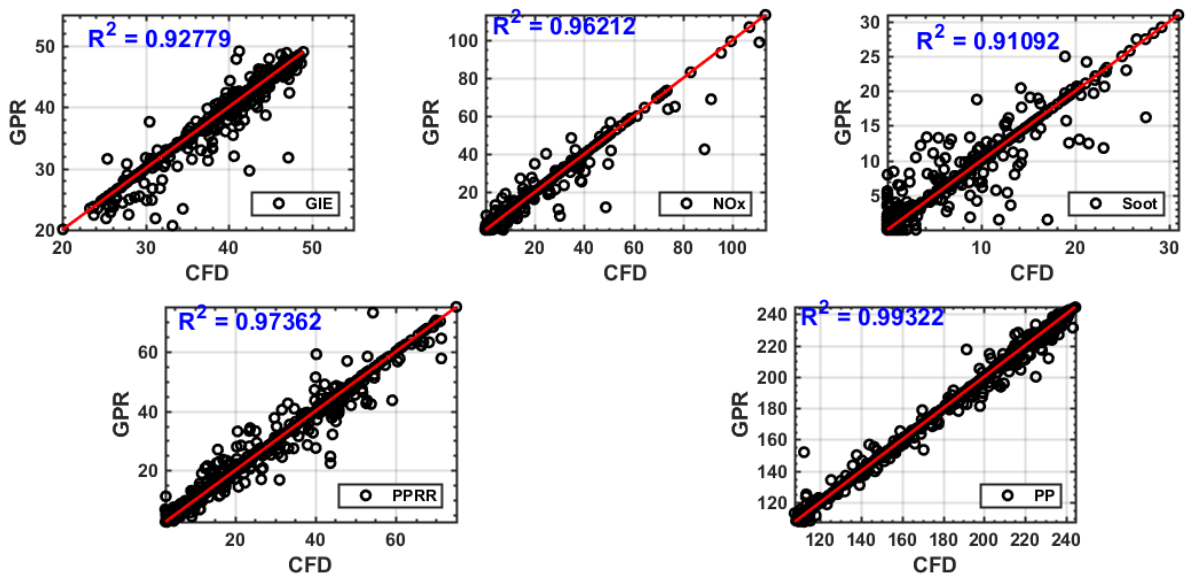


Figure 7-6. Comparison of GPR predicted output (y-axis) to KIVA predicted output (x-axis) for the Latin hypercube DOE dataset.

The results show good agreement between the CFD and GPR predicted results. This study indicates that the GPR model with the matern 3/2 kernel does a reasonable job at predicting the CFD results over the wide design space covered for the GA. Upon the completion of the GA with the CFD+GPR approach, the optimum design was identified, and the results were compared with the optimum from the GA run completely with CFD. Table 7-3 shows a comparison of the optimum points from the two GA's. The results show a very good agreement between the optimum designs of the GA with the CFD and the CFD+GPR approaches. A similar optimum injection strategy is predicted from both the approaches. The optimum fueling quantities were predicted within a maximum error of 0.4%. Though the optimum gasoline SOI timing was different from the two approaches, the overall injection strategy remains similar. Furthermore, since ~99% of the gasoline is premixed, the DI gasoline has negligible fuel mass causing it to have a minimal effect on the performance of the optimum strategy. In terms of the outputs, the optimum cases from both the approaches had an error of less than 2% across all the outputs of interest. To ensure that the GPR predictions were accurate, the optimum point from the CFD+GPR approach was re-run in KIVA and the results from the KIVA run are shown in the last column of Table 7-3. As seen from the table, there is a

good agreement between the GPR and the KIVA results for the optimum point from the GA with the CFD+GPR approach with an error of less than 3% across all the outputs.

Table 7-3. Comparison of the optimum points from the GA with CFD and GA with the CFD+GPR approaches.

approuches.					
Parameter	CFD	CFD+GPR	CFD+GPR (KIVA Validation)		
INPUTS					
Premix Gas. Frac [-]	0.994	0.991	0.991		
Gas. Frac. [-]	0.96	0.964	0.964		
SOI-Gas. [°aTDC]	37.2	19.8	19.8		
SOI-Diesel [°aTDC]	1.53	0.04	0.04		
EGR [%]	59.5	59.5	59.5		
OUTPUTS					
GIE [%]	45.54	45.27	45.13		
NOx [g/kg-f]	0.002	0.001	0.002		
Soot [g/kg-f]	0.012	0.015	0.018		
PPRR [bar/deg]	14.96	14.98	15.31		
PP [bar]	163.45	164.79	165.5		

Figure 7-7 shows the evolution of the fraction of total runs that were evaluated with CFD and with the GPR model for the GA with the CFD+GPR approach. The initial generations have few runs with GPR model and are dominated by CFD evaluations. This is expected since the design space is not yet thoroughly populated by the GA, causing the GPR model to perform poorly in the regions that were not covered by the GA. However, as the generations increase, the GA explores the design space more thoroughly causing the fraction of runs evaluated with GPR model to increase. By the 20th generation, there is a crossover point with the GPR model evaluations overtaking the CFD evaluations. Eventually, by the 31st generation, the CFD evaluations reduce to 0. Beyond the 31st generation, the GA is run completely with the GPR model.

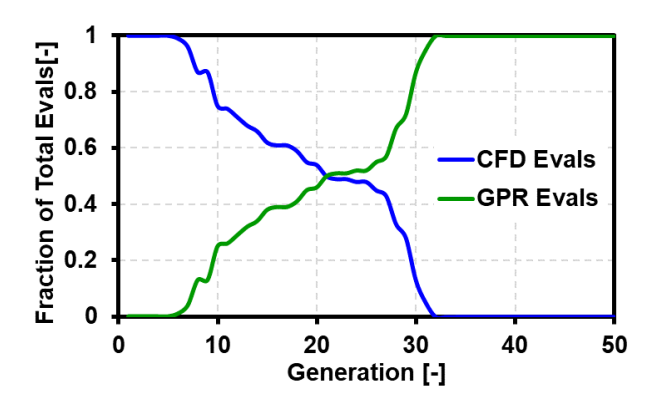


Figure 7-7. Fraction of total runs that were estimated with CFD and with the GPR model for the GA with the CFD+GPR approach.

To understand how much reduction in optimization time, if any, was achieved by using the CFD+GPR approach, Figure 7-8 shows a comparison of the time taken to complete the 50 generations of the GA with the two approaches. The GA run completely with CFD took ~50 days to complete with one day for each generation. However, when the same GA was repeated with the CFD+GPR approach, the GA took ~19 days to complete. This includes the time taken to run the Latin hypercube DOE used for verification within the GA. Using the GPR model in GA optimization has reduced the computational time of optimization by 62%. This reduction in computational time is substantial because the time taken for the GPR runs remains independent of the CFD code being used. Since more than half of the optimization is evaluated by the GPR model, similar optimization studies can be run using higher fidelity approaches (e.g., LES) with suitable computational expense. The results shown in Chapter 6 highlighted the importance of considering multiple modes of a drive cycle simultaneously in optimization studies. However, the primary constraint on such studies was found to be the excessive time taken to complete the optimization. Using the CFD+GPR approach in GA optimizations provides a scope for performing such optimizations within a reasonable time without having to increase the computational expense, which makes this result very useful.

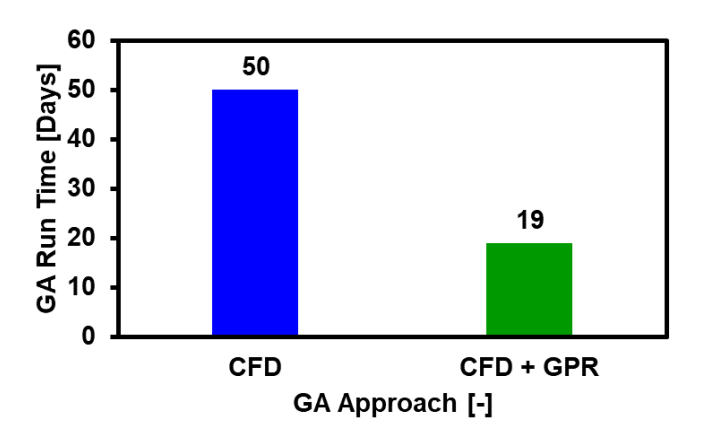


Figure 7-8. Comparison of the time taken to complete the 50 generations of the GA between the GA run completely with CFD and the GA run with the CFD+GPR approach.

Since the GPR model with the matern 3/2 kernel has shown to work efficiently within the GA optimization, using it to further improve the optimization process would help realize its full potential. There are two other areas where regression analysis can be used in optimizations. Firstly, to perform uncertainty quantification, which identifies the input parameters to which the combustion strategy is most sensitive.

Based on this study, the key input parameters that need to be included in an optimization study can be highlighted. Secondly, the GPR model can be used to check for the sensitivity of the designs to operating parameter variations during the optimization process. This would help achieve a reliable and stable optimum. These applications of the GPR model will be discussed in more detail in the coming sections.

7.3. Uncertainty Quantification using GPR

Engine simulation codes, like KIVA used for the work presented in this thesis, have several submodels used to model the complex physics involved in IC engine combustion, including spray, turbulence, chemistry, etc. In the simulation code, each of these sub-models has several input parameters, some of which are numerical parameters, like model constants (e.g., breakup model constants, soot model constants, etc.). These inputs can be tuned to match the model predictions with the experimental data. The remainder of the inputs are physical parameters obtained from experimental data (e.g., SOI, injection pressure, etc.). Uncertainty in CFD predictions arises from errors in the sub-models, the user's choice of these input parameters, and how sensitive the outputs of the CFD model are to these inputs. Assumptions and simplifications need to be made sometimes when choosing the input parameters. For example, when an experimental injection rate profile is not available, it is common practice in CFD studies to use a trapezoidal injection rate profile. Similarly, when running large computational studies, compromises are made on the grid resolution to work efficiently with the available computational resources, as was seen in the optimization studies presented in earlier chapters. These assumptions and simplifications in the choice of model input parameters can cause uncertainty in CFD model predictions. Understanding the sensitivity of the CFD model predictions to the model input parameters could help to establish the relative importance of inputs and model parameters. This will provide insight into the key parameters that must be accurately known and provide guidance for efforts needed in model development and improvement. That is, it does not make sense to invest resources in improving sub-models if their impact on the results of the simulation is limited.

Table 7-4. Summary of the input parameters in the DOE for CDC, RCCI, and GCI strategies.

Table 7-4. Summary	or the inpu	CDC	RCCI GCI			GCI
Input Parameter	Mean	Range	Mean	Range	Mean	Range
Spray Model (KH-RT Breaku)		Kange	Mican	Kange	Wican	Range
balpha [-]	0.6	0.5 to 0.7	0.6	0.5 to 0.7	0.6	0.5 to 0.7
cnst1 [-]	0.18	0.17 to 0.19	0.18	0.17 to 0.19	0.18	0.17 to 0.19
cnst22 [-]	80	10 to 80	80	10 to 80	80	10 to 80
cnst3rt [-]	0.55	0.1 to 1	0.55	0.1 to 1	0.55	0.1 to 1
cnst2b [-]	0.55	0.1 to 1	0.55	0.1 to 1	0.55	0.1 to 1
distant [-]	5.2	0.5 to 10	5.2	0.5 to 10	5.2	0.5 to 10
C _d [-]	0.9	0.85 to 0.95	0.75	0.7 to 0.8	0.75	0.7 to 0.8
Soot Model (Hiroyasu NSC)	0.7	0.03 to 0.73	0.75	0.7 to 0.8	0.73	0.7 to 0.8
$A_{\rm sf}[{\rm s}^{-1}.{\rm bar}^{-0.5}]$	500	400 to 600	500	400 to 600	500	400 to 600
$E_{\rm sf}$ [cal/mol]	1750	1250 to 2250	1750	1250 to 2250	1750	1250 to 2250
Operating Conditions	1730	1230 to 2230	1730	1230 to 2230	1730	1230 to 2230
Engine Speed [rev/min.]	1800	1790 to 1810	1300	1290 to 1310	1300	1290 to 1310
T _{cyl.wall} [K]	440	430 to 450	450	440 to 460	450	440 to 460
T _{cyl.head} [K]	575	565 to 585	475	465 to 485	475	465 to 485
T _{piston} [K]	635	625 to 645	500	490 to 510	500	490 to 510
SOI1-Gas. [°aTDC]			-78	-79 to -77	-100	-101 to -99
SOI2-Gas. [°aTDC]	-	-		-1910-11	-14	-15 to -13
SOI-Diesel [°aTDC]	0	-1 to 1	-12	-13 to -11	1	-13 10 -13
DOI1-Gas. [°CA]			13	11 to 15	10.4	8.4 to 12.4
DOI1-Gas. [°CA]	-	-		11 10 13	12.2	10.2 to 14.2
DOI2-Gas. [CA] DOI-Diesel [°CA]	30	28 to 32	13.4	11.4 to 15.4	1	10.2 to 14.2
Premix Gas. Mass [mg]			109	105 to 113	135	131 to 139
DI1-Gas. Mass [mg]	-	-	64	62 to 66	49	47 to 51
DI2-Gas. Mass [mg]	-	-		02 10 00	57	55 to 59
DI-Diesel Mass [mg]	-	-	67	65 to 69	-	33 10 39
Geometry			07	03 10 09	-	-
CR [-]	16.4	16 to 17	12.4	12 to 13	12.4	12 to 13
tiltxz [°]	65	63 to 67	65	63 to 67	65	63 to 67
cone [°]	10	8 to 12	12	10 to 14	12	10 to 14
dnoz [µm]	242	240 to 244	250	248 to 252	250	248 to 252
smr [μm]	121	120 to 122	125	124 126	125	124 to 126
drnoz [μm]	300	280 to 320	300	280 to 320	300	280 to 320
noz.protrude [mm]	3	2.8 to 3.2	2.1	1.9 to 2.3	2.1	1.9 to 2.3
Initial Conditions		2.0 to 3.2	2.1	1.7 to 2.3	2.1	1.7 to 2.3
Tivc [K]	400	395 to 405	395	390 to 400	395	390 to 400
Pivc [bar]	3.4	3.3 to 3.5	3.97	3.87 to 4.07	3.79	3.69 to 3.89
EGR [%]	20	18 to 22	55	53 to 57	55	53 to 57
Fuel Temperature [K]	333	323 to 343	333	323 to 343	333	323 to 343
tkei	2	1 to 3	2	1 to 3	2	1 to 3
scli	1	0.5 to 1.5	1	0.5 to 1.5	1	0.5 to 1.5
swirl [-]	0.7	0.5 to 1.5	0.7	0.5 to 1.5	0.7	0.5 to 1.5
Numerical Parameters	0.7	0.5 10 1.5	0.7	0.5 to 1.5	0.7	0.5 to 1.5
dtmax [s]	1e-5	1e-4 to 1e-6	1e-5	1e-4 to 1e-6	1e-5	1e-4 to 1e-6
rpr [-]	1.3	1.1 to 1.5	1.3	1.1 to 1.5	1.3	1.1 to 1.5
rsc [-]	1.3	1.1 to 1.5	1.3	1.1 to 1.5	1.3	1.1 to 1.5
tnparc [-]	2000	1000 to 3000	2000	1000 to 3000	2000	1000 to 3000
dS [mm]	2	2 to 4	2	2 to 4	2	2 to 4
dTheta [°]	4	3 to 5	4	3 to 5	4	3 to 5
CAaccord [°CA]	-50	-60 to -40	-50	-60 to -40	-50	-60 to -40
Criaccoru [CA]	50	00 10 -40	50	00 10 -40	50	00 10 -40

To perform this study, a large DOE consisting of a combination of numerical and physical input parameters was setup in KIVA. The study was performed with the three combustion modes that are studied in this thesis: CDC, RCCI, and GCI. The DOE for each combustion strategy had a total of 1200 runs. Table 7-4 shows a summary of the input parameters, their baseline value, and the range of variation for each input parameter in the DOE. The GPR model with the matern 3/2 kernel will be used to perform the uncertainty quantification study.

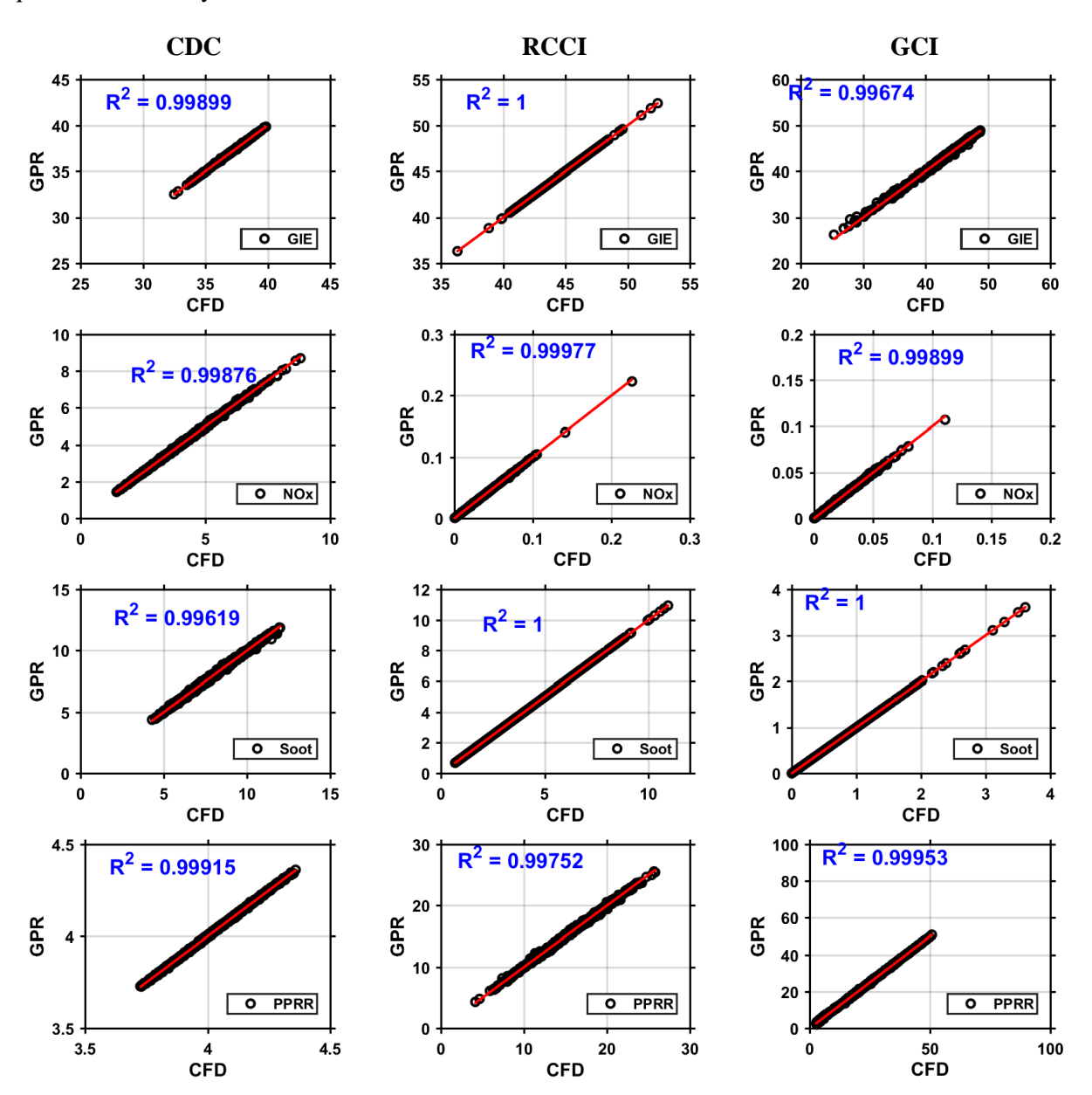


Figure 7-9. Comparison of GPR predicted output (y-axis) to KIVA predicted output (x-axis).

To have confidence in the results predicted by the GPR model, the results were validated with the KIVA predicted results for the DOE data. Figure 7-9 shows the KIVA simulated output versus the GPR predicted output; a straight line with a slope of one indicates a perfect match. All the outputs were accurately predicted for all the three combustion strategies over the design space considered for the study indicating that the GPR model can be used to perform the uncertainty quantification study.

For the uncertainty quantification study, a parameter (i.e., sensitivity constant or SC) is calculated for each output and is used to quantify the importance of an input variable in relation to that output variable. SC is estimated as

$$SC_{j} = \frac{\sigma_{total_{j_{i}}}}{\sum_{i=1}^{n} \sigma_{total_{j_{i}}}},$$
(30)

$$\sigma_{\text{total}_{i}} = \sum_{i=1}^{n} \sigma_{j_{i}} + \sum_{i \neq k}^{n} \sigma_{j_{i,k}},$$
(31)

where j is the output (e.g., GIE, NOx, etc.), n is the number of input variables, and σ is the standard deviation of the output estimated over the total number of data points. The σ_{total} of each output for each input variable is the sum of the standard deviations resulting from the main effect (i.e., where the input variable alone is varied, keeping the rest of the variables fixed at the baseline value), and the two-way interaction effect (i.e., where the input variable in combination with every other input variable is varied while keeping the rest of the variables fixed at the baseline value) of the input variable. To estimate the standard deviation from the main and the total effects, the GPR model is used to run Latin hypercube DOEs while varying the inputs within their corresponding input range, as explained, while fixing the rest at the baseline value. For the current study, each Latin hypercube DOE had data points equivalent to 20 times the number of variables (e.g., in the RCCI case, which has 42 inputs, the Latin hypercube had 840 runs). To cover the main and two-way interactions for each variable, there were 35,280 runs per input variable (i.e., 840 runs for main effect and 840×41 for the two-way interaction effect) for the RCCI strategy. In considering similar runs for all input variables, the RCCI strategy entailed a million runs, which were evaluated in approximately 45 minutes with the GPR model, which shows the potential of this approach. Upon estimating the σ_{total} for

each output with respect to each input variable variation, the SC of the input variable is estimated as the ratio of the σ_{total} of that input variable to the sum of the σ_{total} of all the input variables. Therefore, the larger the SC of an input variable, the more significant the variation in the output due to the variation of the input, thus indicating that the output is sensitive to the input variable.

A similar approach was used in few earlier studies [102, 103, 104] done in Sibendu Som's group at Argonne National Lab. They used an approach called global sensitivity analysis with a sparse regression technique [105] to estimate the sensitivity constants. Pei et al. [102] performed a sensitivity study for CDC at a mid-load condition on a heavy-duty engine. Kodavasal et al. [103] repeated a similar study for GCI combustion at low-load conditions on a light-duty engine. Pal et al. [104] also performed a sensitivity study with GCI combustion, but at mid-load conditions on a heavy-duty engine with low octane (RON70) gasoline.

The uncertainty quantification study presented in this section differs from the earlier studies in several aspects. Firstly, in the present study, along with CDC, sensitivity analysis was performed with advanced combustion strategies like RCCI and GCI as well. Furthermore, a comparison of the sensitivities of the three combustion strategies was presented. Secondly, the number of parameters included in the present study is significantly higher compared to the earlier studies. Though GCI combustion has been explored in earlier studies, the current study differs in terms of operating conditions (i.e., high-load operation) and includes interactions effects which could have a significant effect on the results from the study. Despite the larger number of input parameters, the inclusion of interaction effects was possible because the GPR model was used to perform the sensitivity analysis in the current study. Due to the computational speed of the GPR model, the design space could be thoroughly explored within the range of variation of all the input variables.

The approach discussed earlier was followed to estimate the SCs for CDC, RCCI, and GCI combustion strategies. The SCs are sorted in descending order, and the top five variables to which the output is sensitive are highlighted for each output, for all the three combustion strategies.

7.3.1. GIE Sensitivity Constants

Figure 7-10 shows the plot of input variables corresponding to the top five SCs of GIE for CDC, RCCI, and GCI combustion strategies. The GIE for the CDC and RCCI strategies was found to be most sensitive to the primary breakup time constant (i.e., cnst22) and the duration of the near TDC diesel fuel injection. For the GCI strategy as well, GIE was found to be sensitive to cnst22 and the near TDC gasoline injection duration, but was not as sensitive as the RCCI or CDC strategies. The GCI strategy was found to be more sensitive to EGR and CR. Additionally, the CDC strategy had a relatively high degree of sensitivity to swirl ratio (similar to that of the near TDC diesel fuel injection duration). Additionally, there was some minor sensitivity seen with the computational cell size (dS) and the discharge coefficient (Cd). For the RCCI strategy, the sensitivity to EGR was similar to that of the near TDC diesel fuel injection duration. Furthermore, for the RCCI strategy, GIE was also found to be sensitive to the mesh resolution in the squish region (i.e., CAaccord) and to CR.

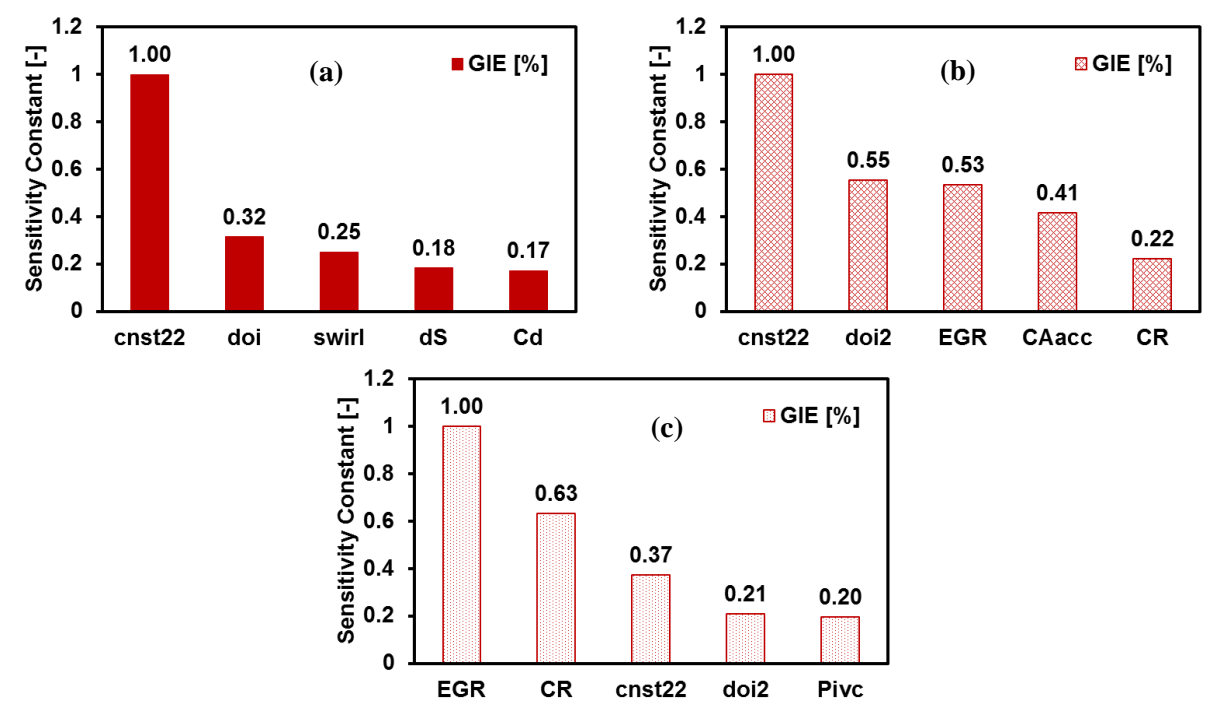


Figure 7-10. Input variable corresponding to the top five SCs of GIE for (a) CDC, (b) RCCI, and (c) GCI combustion strategies.

To verify the performance of the GPR model, the main effects of the top four SCs of GIE for each combustion strategy were simulated in KIVA, and the results were compared with the GPR model trends.

Figure 7-11 shows a comparison of the trends of GIE from the GPR model and KIVA for the top four SCs of the three combustion strategies. As seen from the figure, there is an excellent agreement in magnitude and trends between the GPR model and CFD.

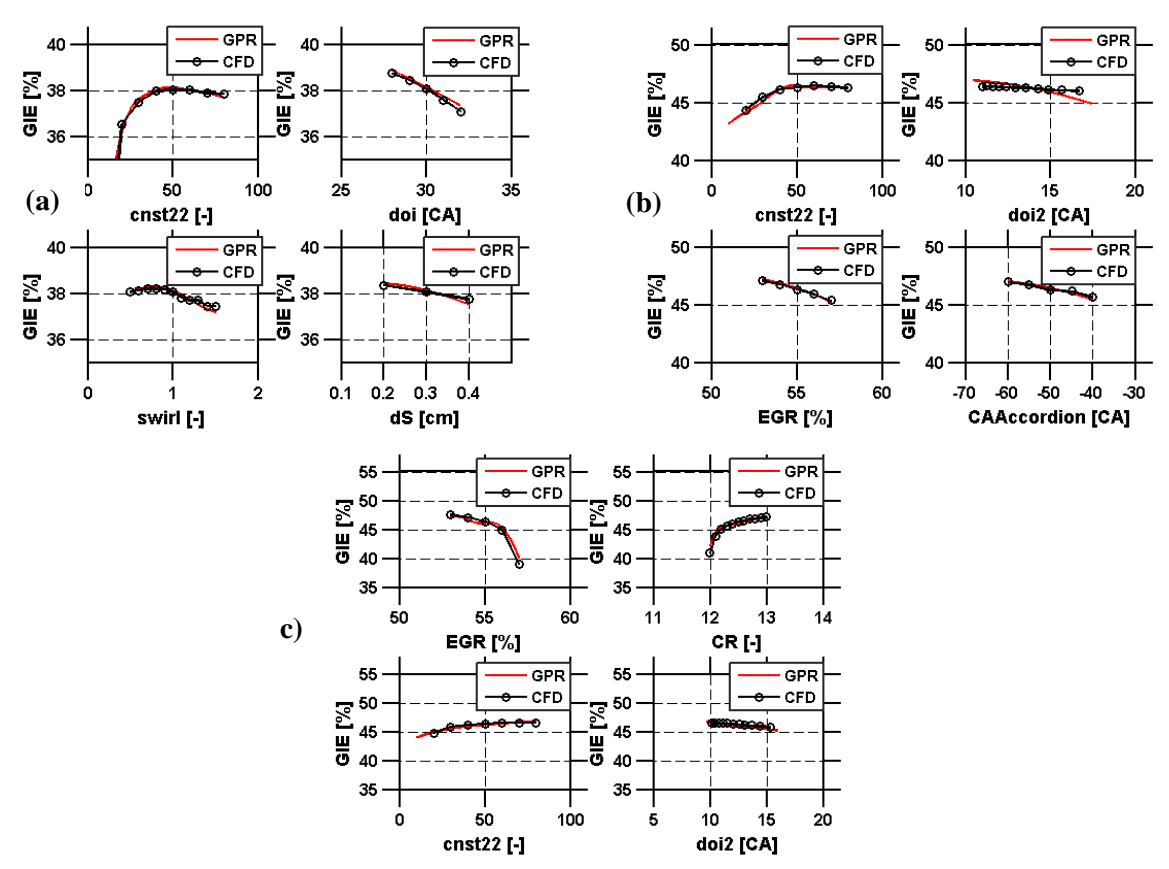


Figure 7-11. Trends of GIE from the GPR model and CFD for the top four SCs of (a) CDC, (b) RCCI, and (c) GCI combustion strategies.

From Figure 7-11, for all three combustion strategies, we see a similar trend of GIE as a function of cnst22. At low cnst22, the GIE drops sharply, and as the cnst22 increases, GIE increases. After a cut off cnst22, the GIE becomes constant. This is contrary to what we would expect because reducing cnst22 reduces the primary breakup time, which results in smaller droplets and improved fuel vaporization. This is expected to result in faster fuel-air mixing and improved GIE. However, we see the opposite trend here, where low cnst22 yields low GIE. To explain the trend with respect to cnst22, Figure 7-12 shows the Φ contours at various crank angles after the start of injection (°aSOI) compared between cnst22 of 10 and cnst22 of 80 for the CDC, RCCI, and GCI combustion strategies.

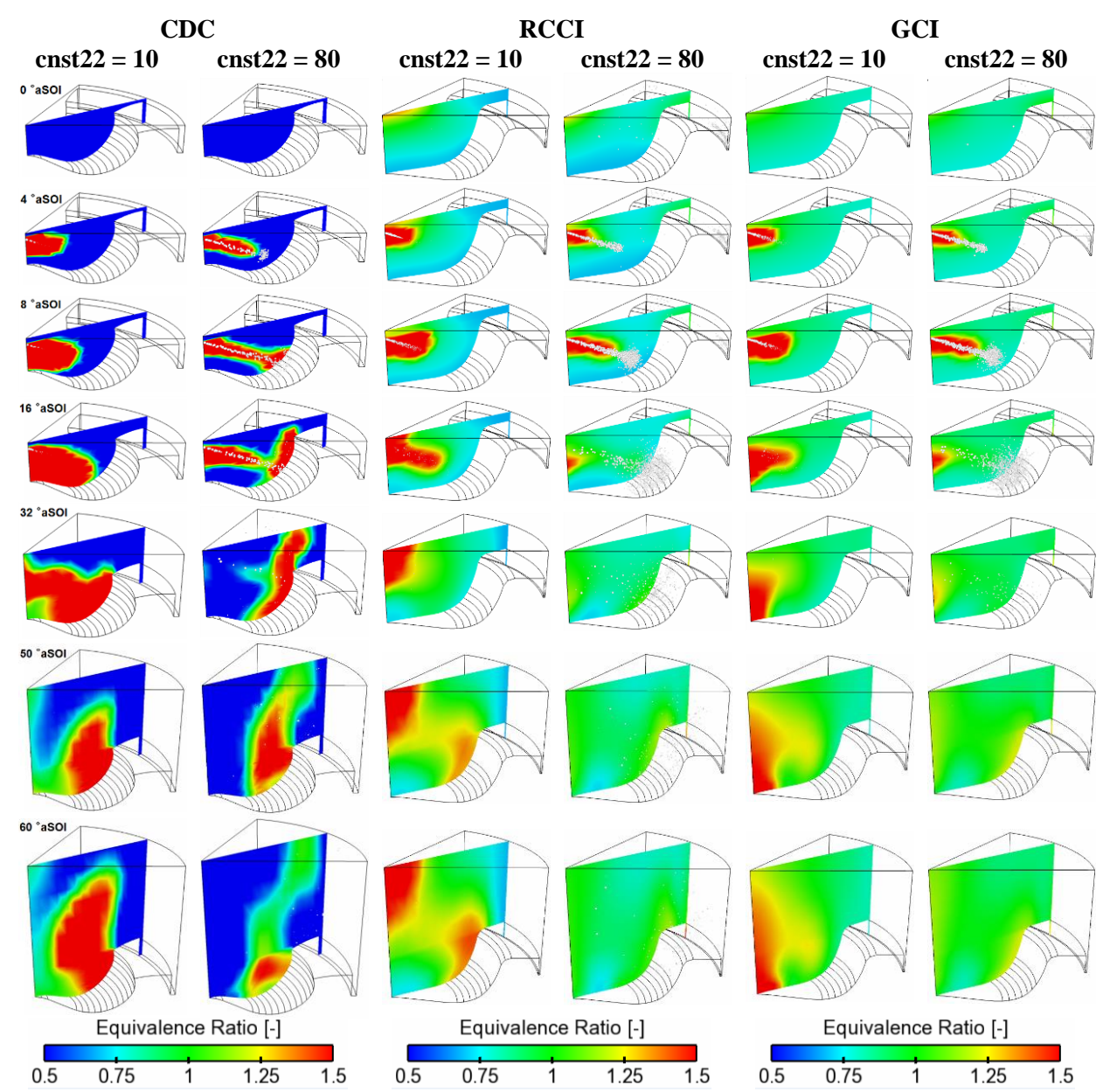


Figure 7-12. Φ contours at various crank angles after SOI (°aSOI) compared between cnst22 of 10 and cnst22 of 80 for the three combustion strategies.

As expected, for the smaller cnst22 of 10, the primary breakup time is short, which results in smaller fuel droplets. However, as the droplet size reduces, so does the spray momentum which results in reduced spray penetration. This is evident from the Φ contours for all the three strategies at crank angles of 4 °aSOI and 8 °aSOI, where the cnst22 of 80 case exhibits higher spray momentum and larger spray penetration relative to the cnst22 of 10 case. Due to the reduced spray momentum at low cnst22, the fuel does not spread in the combustion chamber and results in an increase in the fuel rich regions (Φ > 1) in the

combustion chamber. This is clear from the Φ contours at 16 °aSOI and 32 °aSOI for the cnst22 of 10 cases. Due to the low spray penetration, the fuel accumulates in the bowl in the CDC case, near the nozzle in the RCCI case, and along the cylinder axis in the bowl in the GCI case. However, for the larger cnst22 of 80, due to the increased spray penetration, the fuel hits the piston bowl with greater spray momentum and is better distributed in the combustion chamber. This can be seen from the Φ contours of cnst22 of 80 at the crank angles of 16 °aSOI and 32 °aSOI. Eventually, at a crank angle of 60 °aSOI, the difference between the cnst22 of 10 and 80 becomes very noticeable. Focusing on the Φ contours, for the cnst22 of 10 case, the fuel rich regions are seen to be significantly higher compared to the cnst22 of 80 case.

From these results, it becomes apparent that at low values of cnst22, the spray penetration effect supersedes the vaporization effect, consequently resulting in relatively poor mixing as compared to the higher cnst22 cases. The poor mixing causes increased levels of incomplete combustion for the low values of cnst22, thus leading to the sudden drop in GIE. Figure 7-13 shows the percentage of total fuel energy lost to incomplete combustion as a function of cnst22 for CDC, RCCI, and GCI combustion strategies. The sharp increase in incomplete combustion percentage at low cnst22 values is evident. As the cnst22 increases, the GIE and the incomplete combustion percentage eventually reach saturation because the spray penetration has reached its maximum and no further increase in mixing is seen due to the increase in cnst22.

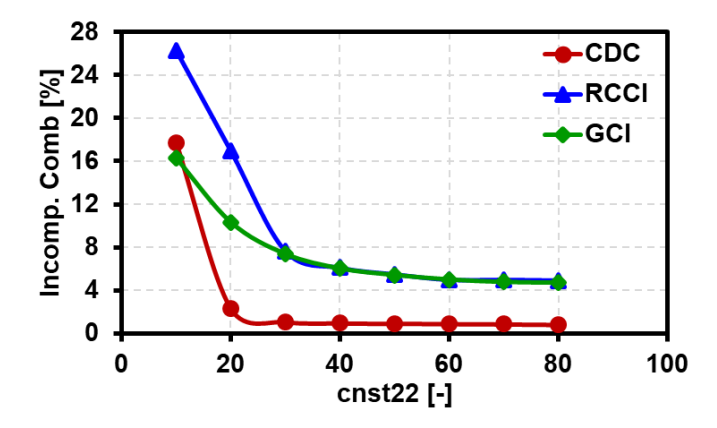


Figure 7-13. Incomplete combustion [%] as a function of cnst22 [-] for CDC, RCCI, and GCI strategies.

From Figure 7-13, it is also apparent that RCCI and GCI strategies have nearly the same response to varying cnst22, but cnst22 had a higher SC for RCCI relative to GCI. This indicates that the difference

in the SC of cnst22 is not due to the reduced impact of cnst22 on GIE of the GCI strategy, but due to the increased impact of EGR and CR on GIE for the GCI strategy relative to the RCCI strategy. To understand this result, Figure 7-14 shows trends of GIE and CA50 as a function of EGR and CR for the RCCI and GCI strategies.

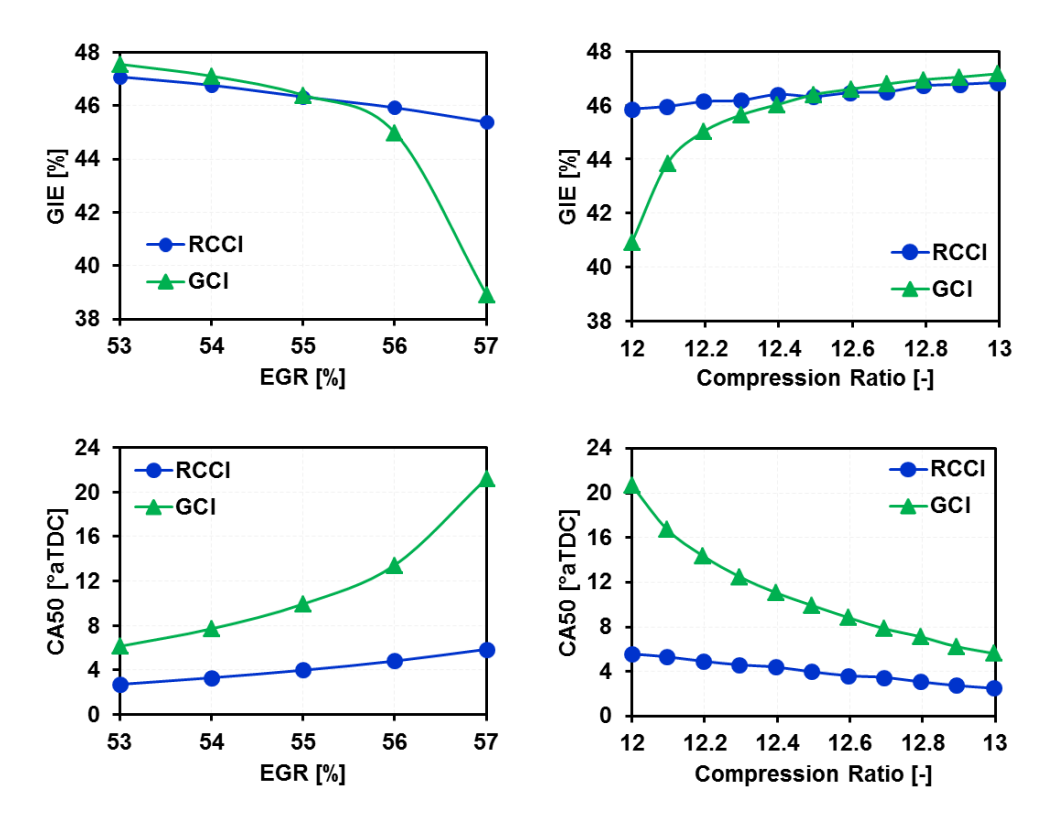


Figure 7-14. GIE and CA50 as a function of EGR and CR for the RCCI and GCI strategies.

From the GIE trends, it is seen that the GCI strategy is significantly more sensitive to EGR and CR relative to the RCCI strategy. Particularly at the high EGR values and low CR values, a rapid drop in GIE is observed for the GCI strategy. Comparing the CA50 trends for the RCCI and GCI strategies, at the baseline EGR of 55% and baseline CR of 12.4, it is apparent that the CA50 for both strategies is after TDC. Increasing the EGR or reducing the CR decreases the oxygen concentration or reduces the in-cylinder pressure and temperature respectively, both of which lead to an increase in ignition delay. This causes the CA50 to be moved further away from TDC, resulting in the reduction in GIE for both strategies. However, the GCI strategy was found to be more sensitive to this effect because, for the same level of EGR, the GCI strategy is operated at a lower IVC pressure (3.79 bar) relative to the RCCI strategy (3.97 bar). Thus, the

GCI strategy has a near stoichiometric global Φ of 0.98, which is higher relative to the RCCI strategy that has a global Φ of 0.93. Increasing the EGR increases the global Φ beyond stoichiometric for the GCI strategy, causing a sharp rise in incomplete combustion, which reduces the GIE rapidly. For the RCCI strategy, despite the increase in EGR, the global Φ remains relatively lean. Therefore, it is not as significantly affected as the GCI strategy due to the EGR reduction. Similarly, the GCI strategy has a CA50 of 10 °aTDC, which is relatively late compared to the RCCI strategy, which has a CA50 of 4 °aTDC. As a result, reducing the CR delays the CA50 late into the expansion stroke where temperatures drop rapidly and increase the level of incomplete combustion causing a steep reduction in GIE.

All the three combustion strategies were also found to be sensitive to the duration of the near TDC injection where an increase in the injection duration resulted in a reduction in GIE. This is because, for all the three strategies, the near TDC injection initiates the combustion and burns in a mixing-controlled heat release. Hence, increasing the duration of the injection increases the combustion duration of the mixing-controlled heat release, causing a larger portion of the total fuel mass to burn away from the TDC. This reduces the EER and results in a reduction in GIE.

7.3.2. NOx Sensitivity Constants

Figure 7-15 shows the plot of input variables corresponding to the top five SCs of NOx emissions for CDC, RCCI, and GCI combustion strategies. For all three combustion strategies, NOx emissions were found to be sensitive to EGR as expected. However, in the CDC case, NOx emissions were found to be more sensitive to the reciprocal Schmidt number (rsc) and the reciprocal Prandtl number (rpr). NOx emissions were also found to be sensitive to cnst22, and some slight sensitivity was seen with the duration of the near TDC injection. For the RCCI and GCI strategies, NOx emissions were significantly more sensitive to EGR as compared to all other inputs.

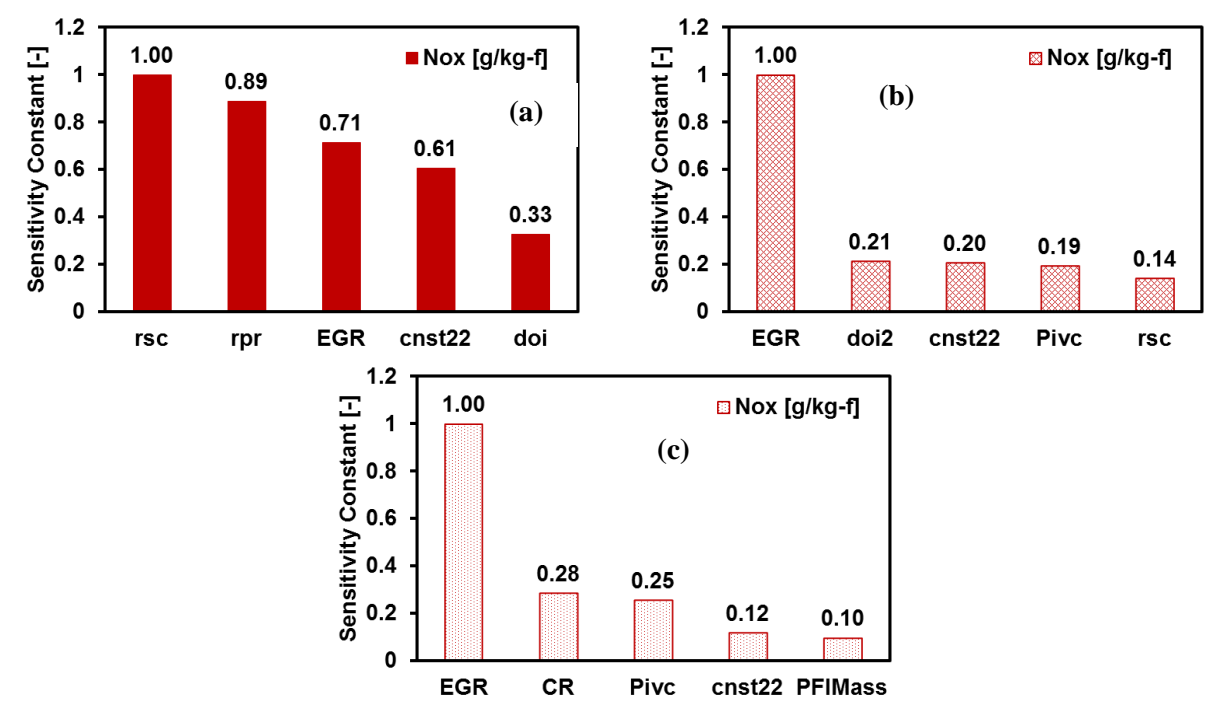


Figure 7-15. Input variable corresponding to the top five SCs of NOx emissions for (a) CDC, (b) RCCI, and (c) GCI combustion strategies.

To verify the performance of the GPR model, the trends from the main effects of the top four SCs of NOx emissions for each combustion strategy were compared between the GPR model and CFD. As seen from Figure 7-16, there is an excellent agreement in magnitude and trends between the GPR model and CFD. From Figure 7-16, firstly, for the RCCI and the GCI strategies, it is seen that NOx emissions are near zero and are significantly lower as compared to the CDC case. The reason for this is the use of high EGR (55%) for the baseline case. Due to the use of high EGR, the RCCI and GCI strategies were found to be insensitive to any input variation other than EGR. With respect to EGR, we see a familiar trend where reducing the EGR results in an increase in NOx emissions. Nevertheless, the increase in NOx emissions is almost negligible since the lower limit of EGR used (53%) is also high enough to keep the NOx emissions close to zero.

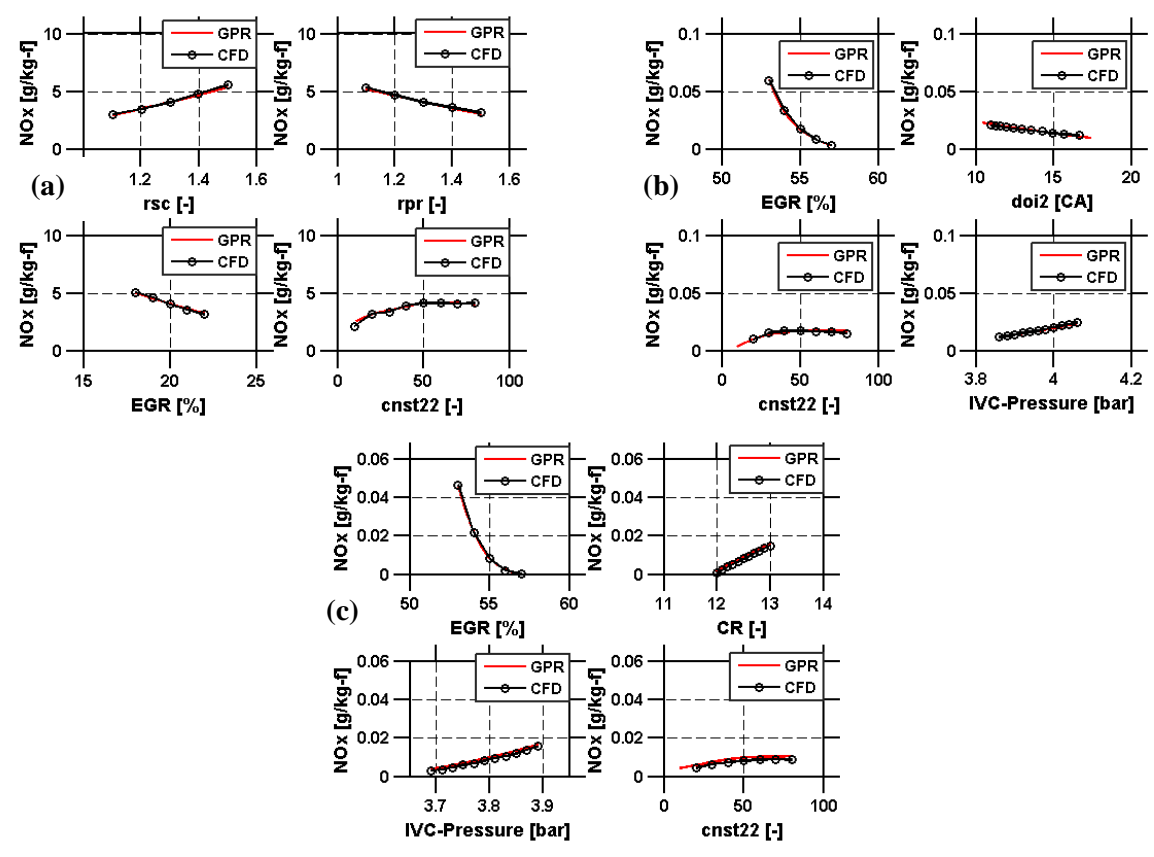


Figure 7-16. Trends of soot emissions from the GPR model and CFD for the top four SCs of (a) CDC, (b) RCCI, and (c) GCI combustion strategies.

For the CDC case, while NOx emissions are high, we see a similar trend with EGR as expected. However, for the CDC case, it is interesting to note that NOx emissions were more sensitive to the reciprocal Prandtl number (rpr) and the reciprocal Schmidt number (rsc). NOx emissions were found to increase with increasing rsc and reduce with increasing rpr. To explain the trends with respect to rsc, Figure 7-17 shows a comparison of the contours of Φ , temperature, and mass fraction of NOx emissions at various crank angles for rsc of 1.1 and rsc of 1.5 for the CDC strategy. Increasing the rsc increases mass diffusivity, which results in leaner local Φ 's. In the initial crank angles during the injection event, the difference in Φ 's between the two rsc cases is not evident. However, upon completion of injection, towards the later part of the expansion stroke at crank angles of 54 °aTDC and 60 °aTDC, the difference in Φ between the two rsc cases becomes more visible. At these crank angles, the fuel distribution in the combustion chamber for both cases is similar, but the rsc of 1.5 case has relatively leaner Φ regions compared to rsc of 1.1. The Φ scale is set to the range in which NOx formation is expected to occur, and it is seen that the lean Φ regions of rsc of 1.5 correspond

to a near stoichiometric Φ . This results in higher in-cylinder temperatures for the rsc of 1.5 case relative to the rsc of 1.1 case. The higher in-cylinder temperatures for the rsc of 1.5 case are clearly visible at all crank angles shown in Figure 7-17. The increased in-cylinder temperatures result in higher NOx emissions for the rsc of 1.5 case relative to the rsc of 1.1 case. This is seen from the NOx emission contours in Figure 7-17, where the rsc of 1.5 case has higher NOx emissions relative to the rsc of 1.1 case at every crank angle. Furthermore, the regions of higher NOx emissions correspond to the regions of higher temperature.

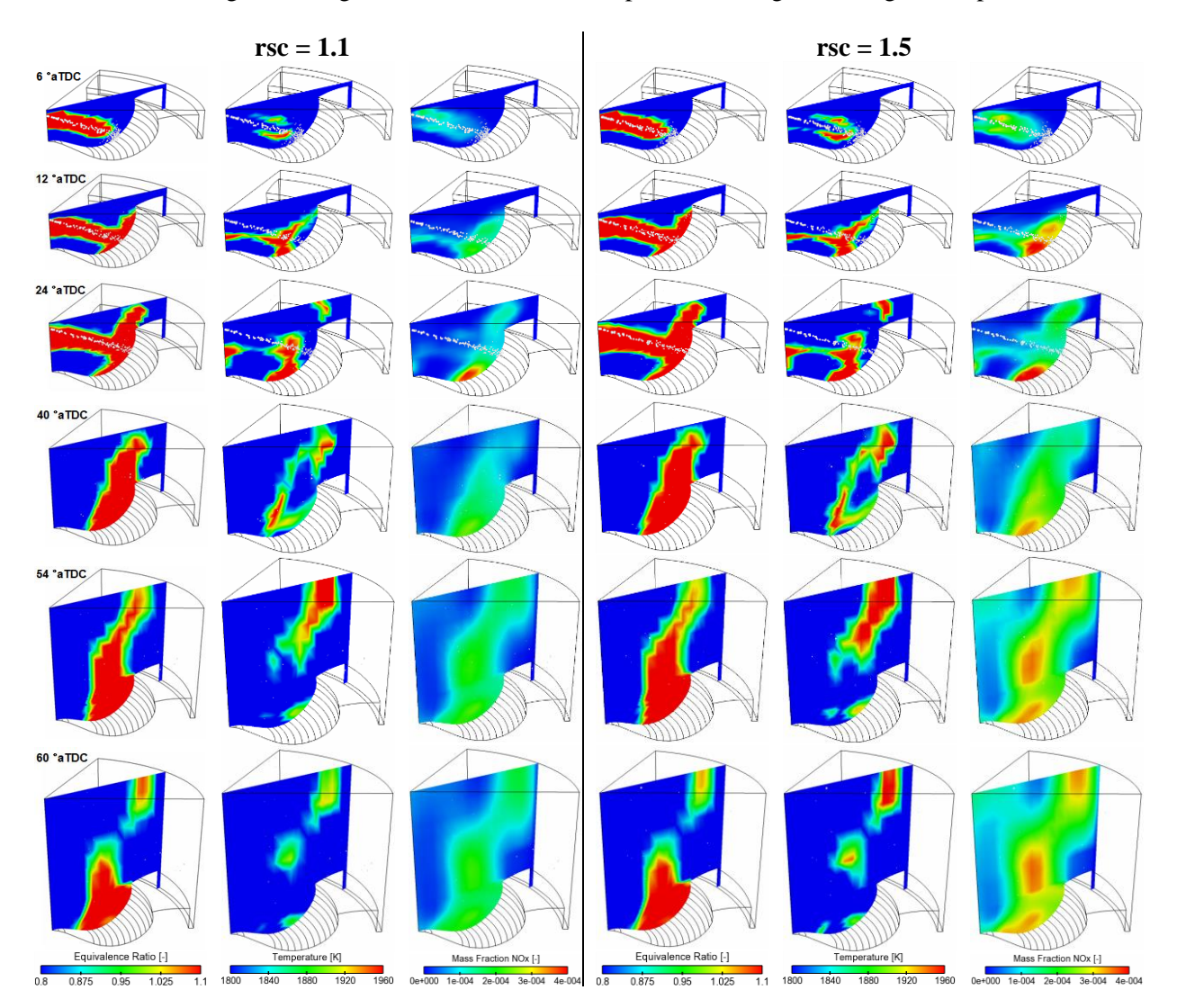


Figure 7-17. Contours of Φ , temperature and mass fraction of NOx emissions for rsc of 1.1 and rsc of 1.5 cases for the CDC strategy.

To explain the trend with respect to rpr, Figure 7-18 shows contours of temperature and mass fraction of NOx emissions at various crank angles for rpr of 1.1 and rpr of 1.5 cases for the CDC strategy.

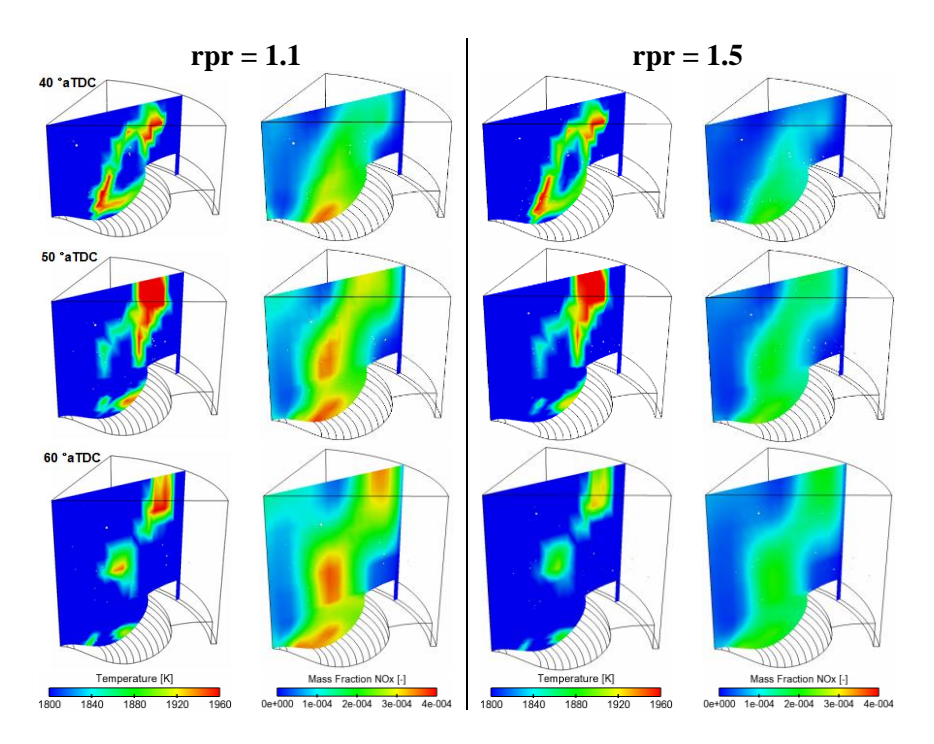


Figure 7-18. Contours of temperature and mass fraction of NOx emissions for rpr of 1.1 and rpr of 1.5 cases for the CDC strategy.

Since the fuel distribution remains the same as shown in Figure 7-17, contours are shown only for the crank angles in the expansion stroke after the injection event. Increasing rpr increases the thermal diffusivity, which in turn increases local heat transfer and prevents pockets of sharp temperature rise. Similar to the rsc cases, the fuel distribution remains the same for both the rpr cases, but the lower incylinder temperatures for the rpr of 1.1 case are evident at all the crank angles shown in Figure 7-18. The reduced in-cylinder temperatures result in lower NOx emissions for the rpr of 1.5 case relative to the rpr of 1.1 case. The lower NOx emissions for the rpr of 1.5 case are noticeable from the mass fraction of NOx contours shown in Figure 7-18.

7.3.3. Soot Sensitivity Constants

Figure 7-19 shows the plot of input variables corresponding to the top five SCs of soot emissions for CDC, RCCI, and GCI combustion strategies. The soot emissions for CDC, RCCI, and GCI strategies were found to be sensitive to cnst22. RCCI and GCI strategies were found to be sensitive to the duration of the near TDC injection, and some minor sensitivity was seen with CR. For the CDC case, soot emissions were most sensitive to cnst22, and some minor sensitivity was seen with the computational cell size (dS).

For all three combustion strategies, although there were additional inputs to which soot emissions were sensitive, they had significantly lower SCs as compared to the top two variables

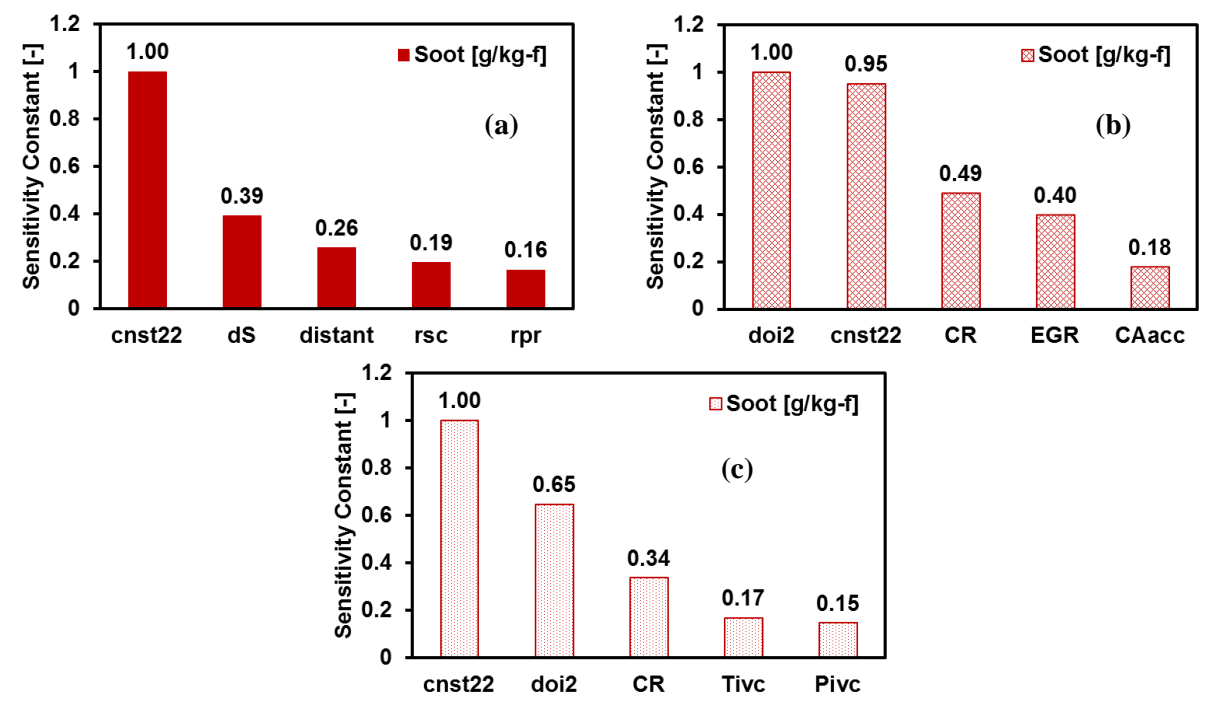


Figure 7-19. Input variable corresponding to the top five SCs of soot emissions for the (a) CDC, (b) RCCI, and (c) GCI combustion strategies.

To verify the performance of the GPR model, the trends from the main effects of the top four SCs of soot emissions for each combustion strategy were compared between the GPR model and CFD. As seen in Figure 7-20, there is a very good agreement in magnitude and trends between the GPR model and CFD. Figure 7-20 shows that soot emissions for CDC, RCCI, and GCI strategies decrease as cnst22 increases. This is due to the higher spray penetration with increased cnst22. As was shown in Figure 7-12, as the cnst22 increases, the droplet size becomes larger, and the spray has greater momentum, leading to a longer spray penetration. This causes the fuel to be better distributed in the combustion chamber and reduces the number of fuel rich mixture ($\Phi \ge 2$) zones, resulting in reduced soot emissions. The effect of cnst22 on the local Φ was shown in Figure 7-12. The soot emissions for the RCCI and GCI strategies were also found to be sensitive to the duration of the near TDC injection. As the duration of the near TDC injection increases, soot emissions increase for both strategies. For the RCCI and GCI strategies, the near TDC injection initiates the combustion and burns in a mixing-controlled heat release. As the duration of this injection

increases, there is more fuel combusting at locally rich Φ 's, thus resulting in soot formation. Additionally, the RCCI and GCI strategies are operated at a high EGR of 55% with near stoichiometric global Φ 's of 0.93 and 0.98, respectively. The reduced oxygen availability lowers the rate of soot oxidation and, combined with the increased soot formation, results in increased soot emissions with increased duration of the near TDC injection. However, the magnitudes of soot emissions for the GCI strategy are significantly less due to the lower reactivity of gasoline relative to diesel fuel. The low reactivity of gasoline increases the ignition delay prior to the mixing-controlled heat release and reduces the locally rich mixtures during combustion. This results in lower soot formation and reduced soot emissions at EVO for the GCI strategy as compared to the RCCI strategy.

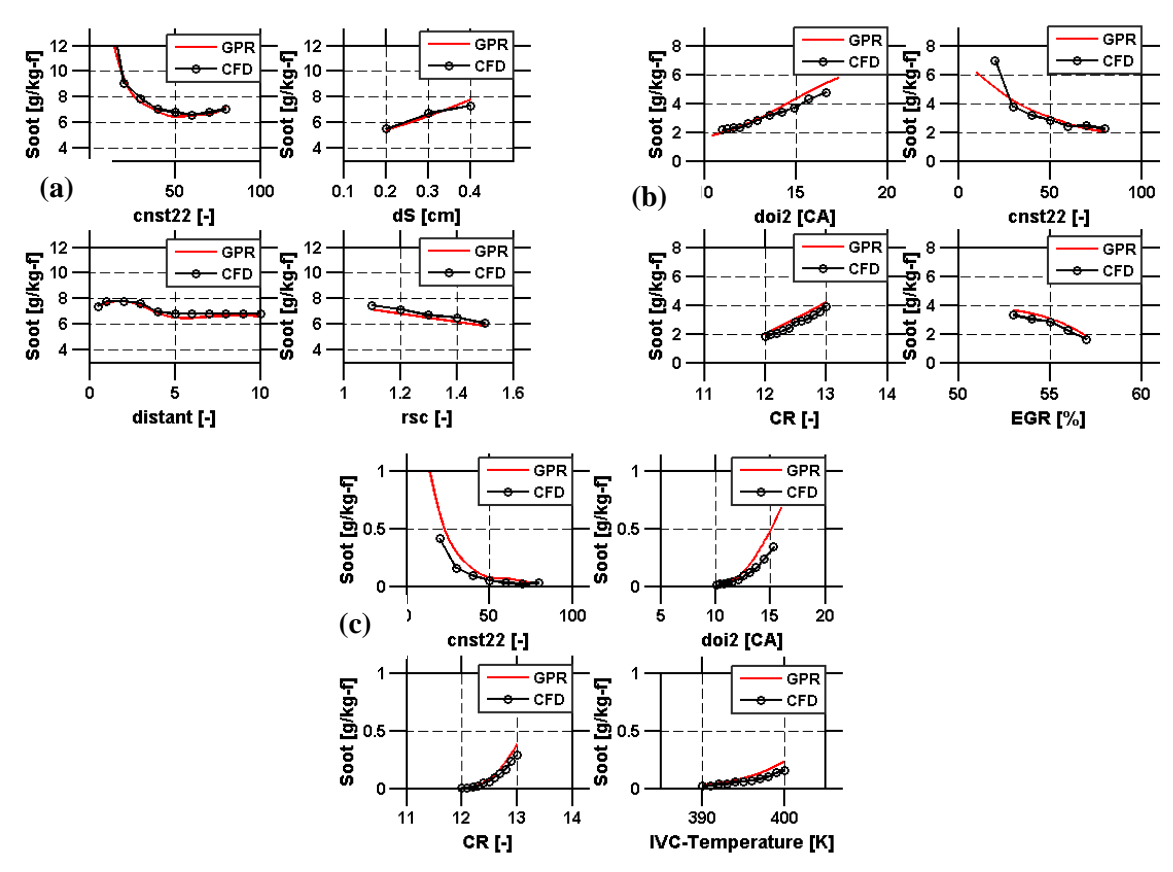


Figure 7-20. Trends of soot emissions from the GPR model and CFD for the top four SCs of the (a) CDC, (b) RCCI, and (c) GCI combustion strategies.

Interestingly, for the RCCI strategy, soot emissions were observed to reduce with increasing EGR. This is contrary to the expected trend because increasing EGR results in the reduced availability of oxygen, which should result in increased soot emissions. To explain this result, Figure 7-21 shows the Φ -T plots of

the in-cylinder charge at various crank angles for the RCCI cases with EGR of 53% and EGR of 57%. For the higher EGR case, although the available oxygen reduces, so does the in-cylinder temperature. Under the operating conditions studied, the reduced temperature effect of EGR dominates the reduce oxygen availability effect. This can be seen from Figure 7-21 where at all the crank angles shown, the charge from the EGR of 53% case reaches higher temperatures and closer to the soot formation regions as compared to the EGR of 57% case. This results in higher soot formation for the EGR of 53% case.

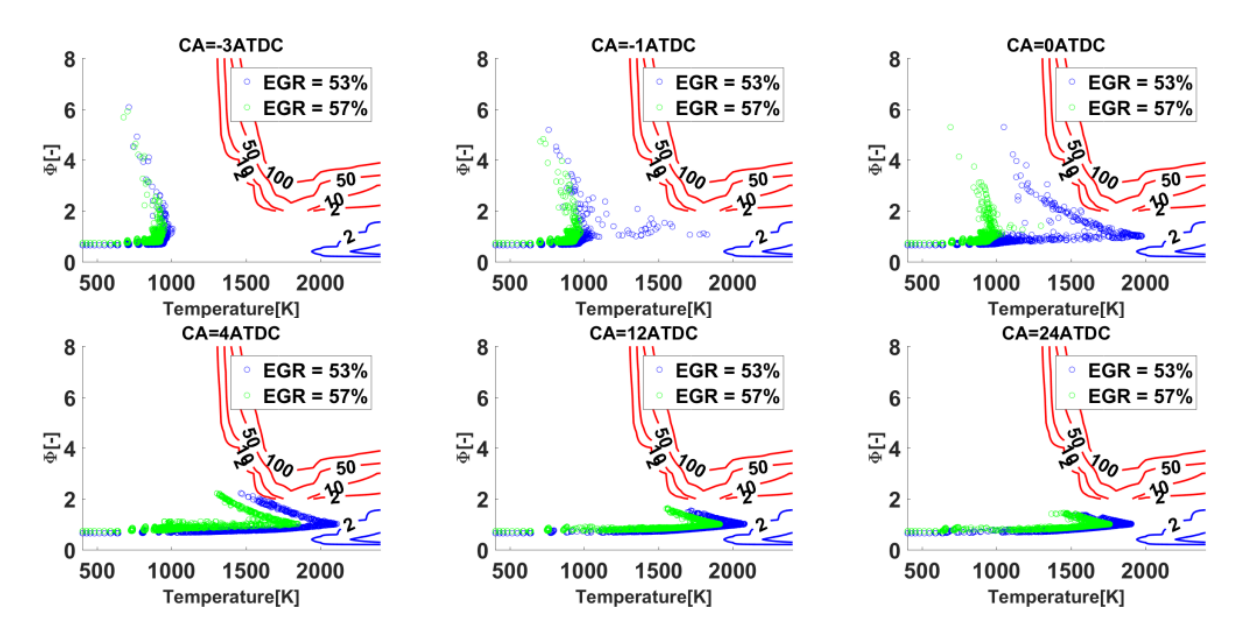


Figure 7-21. Φ-T plots of in-cylinder charge for EGR of 53% and EGR of 57% for the RCCI case. Soot islands are shown at the top right corner of the plot in red, and the NOx islands are shown at the bottom right corner of the plot in blue.

In the CDC case, in addition to cnst22, soot emissions were also found to be sensitive to the computational cell size (dS). Increasing the cell size resulted in increased soot emissions, as shown in Figure 7-20. To explain this trend, Figure 7-22 shows the in-cylinder contours of Φ and mass fraction of soot emissions at various crank angles for the CDC cases with dS of 2 mm and 4 mm. As the value of dS increases, the spray penetration is under-predicted due to the decrease in the spray momentum. This is a result of using a coarse mesh due to which the CFD cell volume ends up being quite different from the actual volume of influence of the spray. Consequently, the momentum transfer to the surrounding gas phase due to drag forces on the liquid droplets is dampened. Ultimately, the gas phase momentum and the liquid droplet penetration are both under-predicted. This is realized from comparing the Φ contours of the two

cases shown in Figure 7-20, in which the dS of 2 mm case has a higher spray momentum. This causes better fuel-air mixing in the dS of 2 mm case. This can be observed from comparing the Φ contours from crank angles of 40 °aTDC to 60 °aTDC, where the dS of 4 mm case has a relatively higher number of locally rich regions as compared to dS of 2 mm. This results in increased soot emissions for the dS of 4 mm case. The increase in soot emissions for the dS of 4 mm case is evident from the soot mass fraction contours at crank angles of 40 °aTDC to 60 °aTDC.

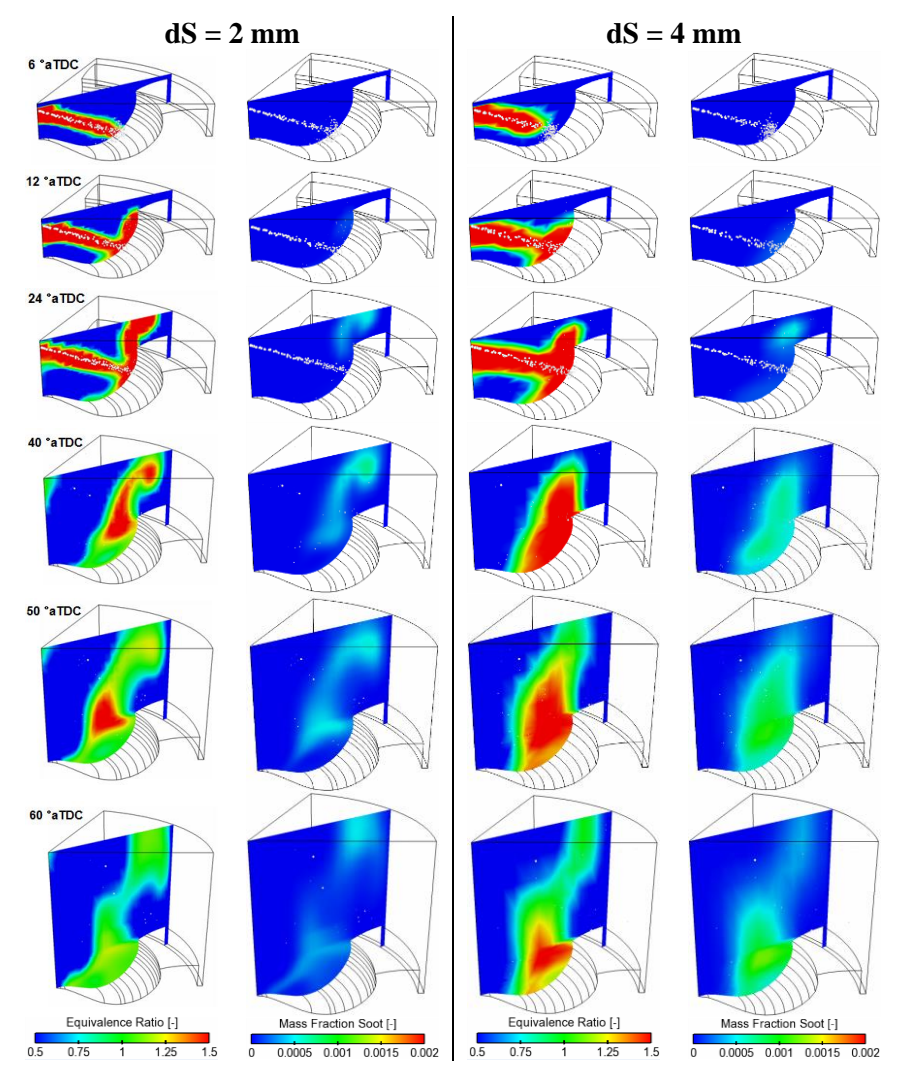


Figure 7-22. Contours of Φ and mass fraction of soot emissions for the dS of 2 mm and dS of 4 mm cases for the CDC strategy.

7.3.4. PPRR Sensitivity Constants

Figure 7-23 shows the plot of input variables corresponding to the top five SCs of PPRR for CDC, RCCI, and GCI combustion strategies.

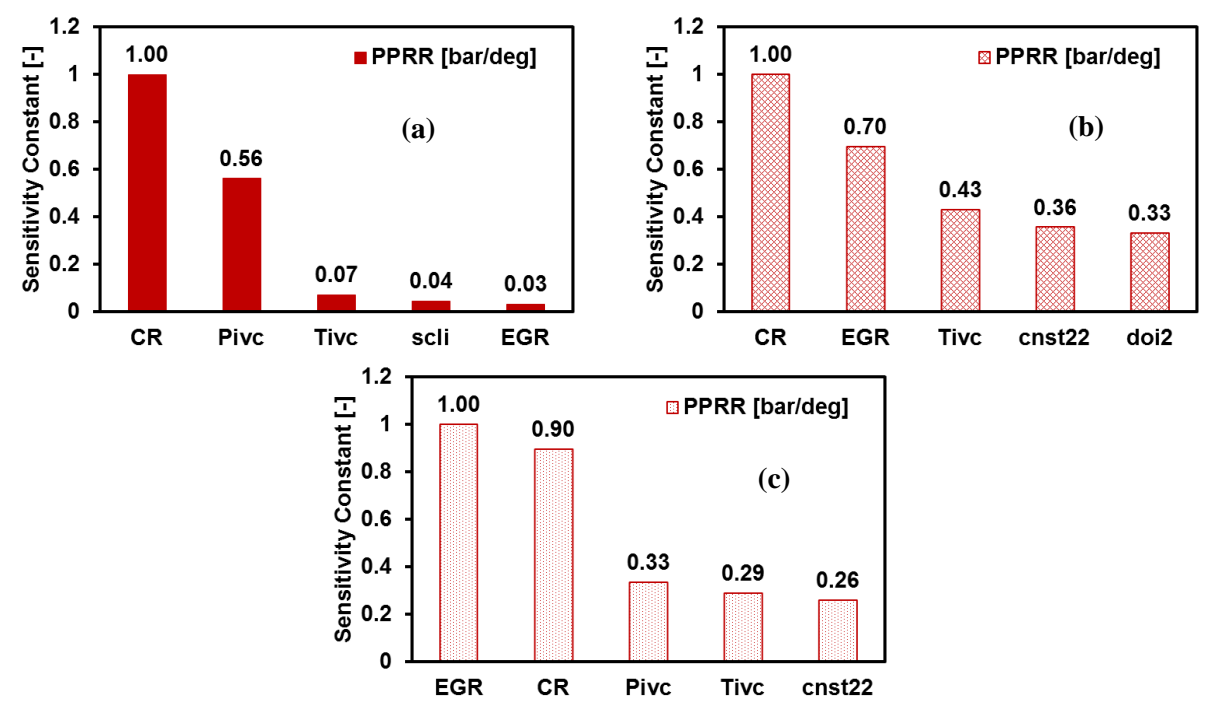


Figure 7-23. Input variable corresponding to the top five SCs of PPRR for the (a) CDC, (b) RCCI, and (c) GCI combustion strategies.

The PPRR for the CDC, RCCI, and GCI combustion strategies was found to be sensitive to CR. The RCCI and GCI strategies were additionally sensitive to EGR while the CDC strategy was sensitive to IVC pressure (Pivc). There was some sensitivity shown to IVC temperature and cnst22 as well for the RCCI and GCI strategies, but it was relatively insignificant as compared to the sensitivity shown to CR and EGR.

To verify the performance of the GPR model, the trends from the main effects of the top four SCs of PPRR for each combustion strategy were compared between the GPR model and CFD. As seen from Figure 7-24, there is a very good agreement in magnitude and trends between the GPR model and CFD. Figure 7-24 shows that PPRR increases with increasing CR for CDC, RCCI, and GCI cases. Secondly, the magnitude of PPRR is significantly lower for the CDC strategy relative to the RCCI and GCI strategies. For the RCCI and GCI strategies, PPRR was extremely sensitive to CR variation where a unit increase in CR results in 8 bar/deg and 38 bar/deg increase in PPRR for the RCCI and GCI strategies, respectively. The RCCI and GCI strategies were also found to be very sensitive to EGR with the GCI strategy being significantly more sensitive to EGR relative to the RCCI strategy.

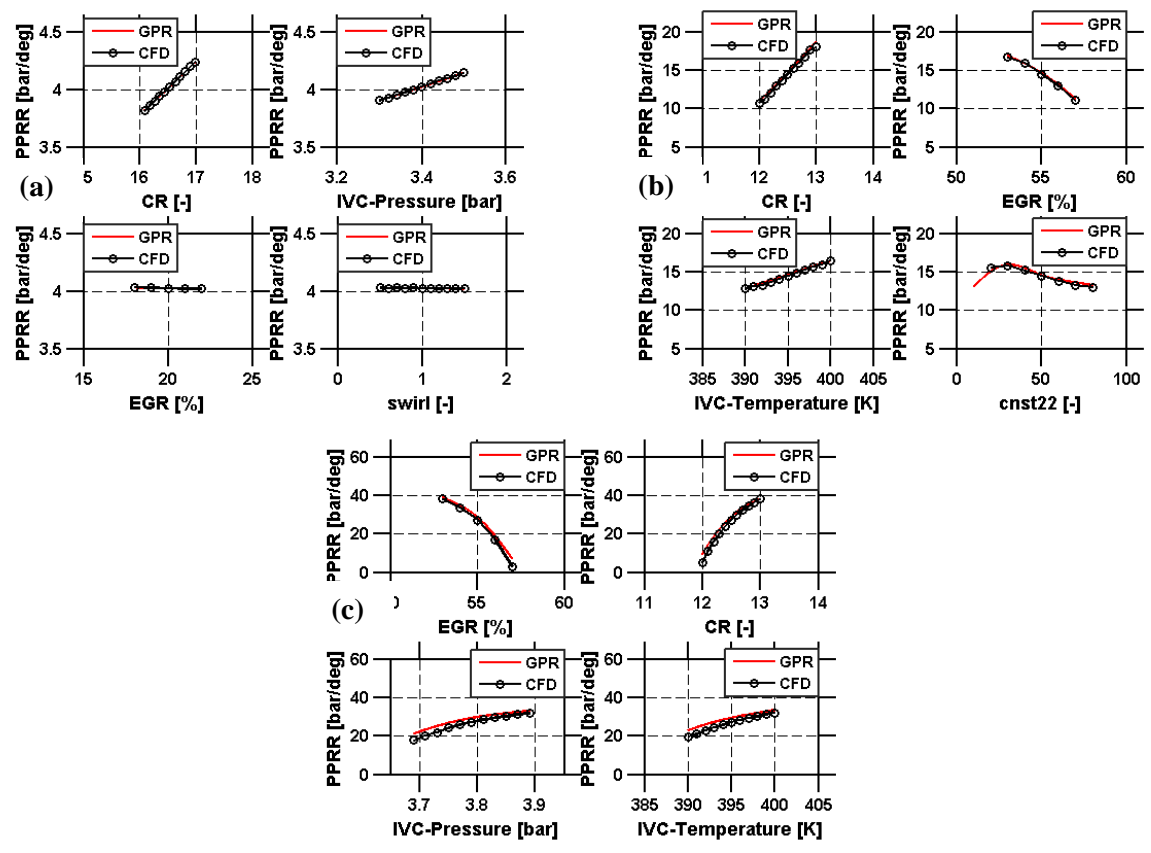


Figure 7-24. Trends of PPRR from the GPR model and CFD for the top four SCs of the (a) CDC, (b) RCCI, and (c) GCI combustion strategies.

Firstly, for all the three strategies, the increase in PPRR with increasing CR is a result of increased in-cylinder pressure and temperature. It leads to shortened ignition delay and advanced combustion phasing, which in turn causes higher PPRR. For the CDC strategy, the PPRR was mainly sensitive to CR, but in comparison to the RCCI and GCI strategies, the magnitude of PPRR and the variation in PPRR with CR was relatively small. Moreover, there is no premixed fuel in the CDC strategy, and the entire diesel fuel mass combusts in a mixing-controlled heat release. The high levels of fuel stratification prevent sharp increases in the heat release rate and result in a low PPRR. Therefore, although there was an increase in PPRR with increasing CR, the magnitude of increase was a small value of 1 bar/deg. However, the RCCI and GCI strategies have premixed gasoline with an ignition delay that is extremely sensitive to variations in temperature and pressure. Consequently, these strategies were more sensitive to CR variations. Secondly, the results shown in Figure 7-24 highlight the importance of using a low CR and high EGR combination for the baseline cases of RCCI and GCI strategies. It is seen that a small increase in CR or a minor reduction

in EGR increases the PPRR to unacceptable values. The increased sensitivity of the GCI strategy to variations in CR and EGR compared to the RCCI strategy was explained in §7.3.1 from Figure 7-14. The sensitivity of the GCI strategy to EGR and CR also explains why a significantly delayed combustion phasing of 10 °aTDC was used for the baseline case for the GCI strategy. That is, advancing the CA50 closer to TDC would require reducing the EGR or increasing the CR, which results in unreasonably high PPRR as shown from the PPRR trends for the GCI strategy in Figure 7-24.

To summarize this section, Table 7-5 shows the input variables with the maximum SCs for each output for the CDC, RCCI, and GCI strategies. The results of CA50 and PP are shown in Table 7-5, but were not explained in detail, as the results were similar to the GIE and PPRR results. From the comparison, it is seen that for high-load CDC operation, it is vital to get the correct injection profile and the mixing field (i.e., breakup and transport) to get reliable CFD predictions. For high-load RCCI and GCI strategies, it is essential to have accurate measurements of CR and intake conditions (i.e., Pivc, Tivc, EGR, etc.), as even the slightest error would result in large variations of cylinder pressure and emission predictions. It should be noted that these results are specific to the operating conditions studied. Notwithstanding, the main take away from this study is the potential of the GPR model to predict the results from a million simulations accurately in a short time which makes it possible to perform the uncertainty quantification analysis.

Table 7-5. Input variables with the maximum sensitivity constants for each output for the CDC, RCCI and GCI strategies.

Output	CDC Sensitivity	RCCI Sensitivity	GCI Sensitivity
GIE	cnst22, doi, swirl, dS	cnst22, doi2, EGR, CAaccord	EGR, CR, cnst22, Pivc
NOx	rsc, rpr, EGR, cnst22	EGR	EGR
Soot	dS, enst22, rsc, rpr	cnst22, doi2, EGR, CR	cnst22, doi2, EGR, CR
PPRR	CR, Pivc	CR, EGR, doi2	EGR, CR, Pivc, Tivc
PP	CR, Pivc, SOI	CR, EGR, doi2, cnst22	CR, EGR, Pivc, Tivc
CA50	cnst22, doi, SOI, swirl	CR, EGR, doi2, Pivc	CR, EGR, Pivc, Tivc

7.4. Stability Analysis in GA Optimization using GPR

In the previous section, baseline cases for high-load RCCI and GCI strategies were shown to be extremely sensitive to EGR. These baseline cases were the result of a high-load optimization study, as shown earlier in Chapter 4. Similar results were demonstrated in Chapter 4 as well where RSM, which is

also a form of regression analysis, was used to compare the stability of the optimum RCCI and GCI high-load strategies to fluctuations in operating conditions. It was concluded from that study that both the strategies showed high sensitivity to EGR fluctuations and the optimum obtained from the GA was not a stable optimum. If unstable optima were to be discouraged during the optimization process, it would avoid such outcomes from the GA and would result in a more reliable optimum strategy. Earlier, this could not be done, since the stability analysis was performed using RSM methodology, which does not work efficiently with non-parametric data. Therefore, a full factorial DOE was run on the final optima to perform this analysis. The COSSO tool worked well with non-parametric data, but could not be used due to the excessive time it takes to generate the response function. However, with the GPR model using the matern 3/2 kernel, stability analysis can be performed during the optimization process, since it overcomes the issues with the earlier regression approaches.

Figure 7-25 shows a flowchart outlining the procedure implemented to perform the stability analysis for each citizen of the GA. To summarize the flowchart, from every citizen of the GA, the input variables prone to cycle-to-cycle fluctuations or uncertainty (e.g., EGR, IVC Pressure, etc.) are identified. The expected fluctuation is estimated either from the experimental data or by intuition for each of these input variables. Within this fluctuation range, a Latin hypercube DOE dataset of 500 points (or more, based on the number of input variables) is generated. The input variables in each citizen that do not fluctuate cycle-to-cycle (e.g., CR, nozzle diameter, etc.) are set to the baseline value, which is the input value used in the citizen. Using the GPR model, the output variables are estimated for each data point of the DOE dataset. Based on the outputs at all the data points of the DOE, the standard deviation for each output variable is estimated. Similar to the constraints set for each output variable in the GA, constraints are set for the standard deviations as well, and a corresponding harshness factor is assigned. If the standard deviation of any output variable exceeds the constraint value, the objective function will be penalized based on the assigned harshness factor. Details on how the objective function is penalized with a harshness factor were explained in detail in Chapter 3 when explaining the GA methodology. The study is repeated individually for all the citizens of the GA. It should be noted that the stability analysis is performed only

on citizens evaluated with the GPR model in the GA. For those citizens simulated in KIVA, there is no penalty applied with respect to the stability constraints. This assumption is reasonable because these citizens if passed to future generations, will eventually be evaluated by the GPR model (i.e., once the GA covers the design space sufficiently). At this point, they will go through the stability check and be eliminated in future generations if they turn out to be unstable.

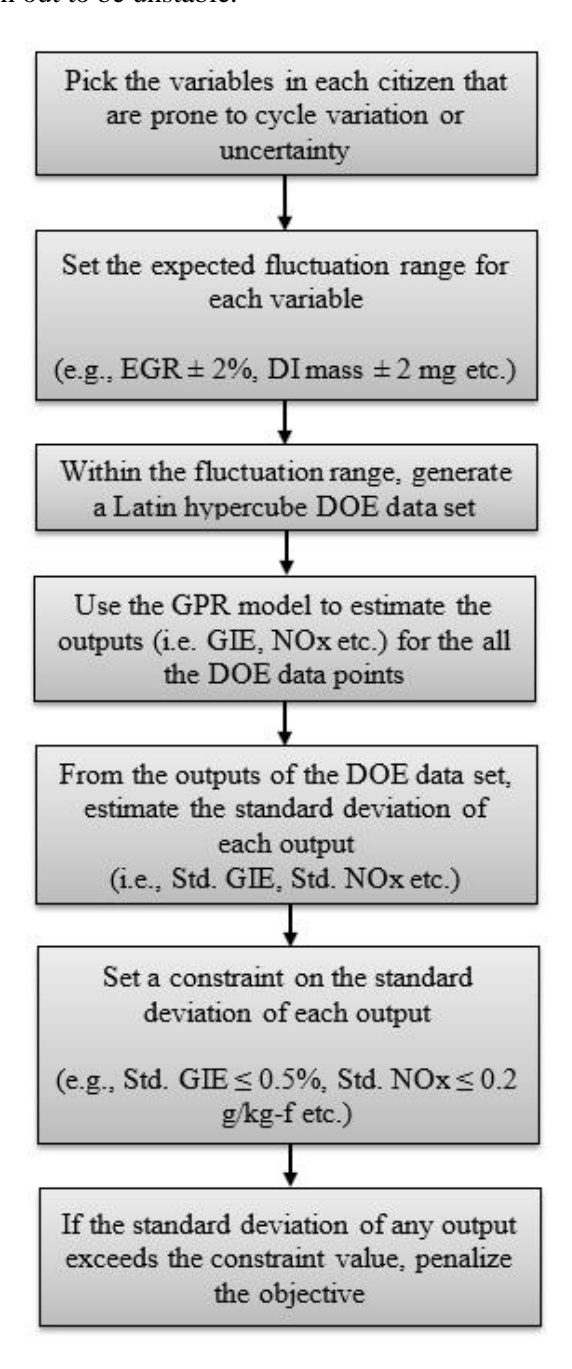


Figure 7-25. Flowchart outlining the stability analysis in GA optimization. This procedure is applied individually to every citizen of the GA.

To validate the approach, the optimization study shown in §7.2.1 was repeated with the stability constraints added. Since the motivation of this study was to test the potential of this approach, instead of using CFD, the optimization was run entirely with the GPR model. A combination of the optimization data from the study shown in §7.2.1 and the Latin hypercube data-set used in that study was used to train the GPR model. Based on the results shown in Figure 7-6, where the GPR model trained with the GA data predicted the outputs for a new data-set reasonably well, it is expected that the GPR model will perform efficiently (instead of CFD) in the current optimization. The optimization study was performed with and without the stability constraints, and the results from the two studies were compared. Though the optimization without the stability constraints was done earlier, it is repeated to estimate the standard deviations of the output variables (to input variable fluctuation) for every generation. This is necessary to perform a comparison and verify the effectiveness of adding the stability constraints in the optimization in achieving an optimum point with improved stability.

Table 7-6 shows the fluctuation assigned for each input variable and the constraint value chosen (for the optimization performed with stability constraints) for the standard deviation of each output variable.

Table 7-6. Fluctuations set for each input variable and the constraints set for the standard deviation of each output variable.

output variable.					
Parameter	Fluctuation/Constraint				
INPUTS					
Premix Gas. Mass [mg]	± 4				
DI-Gas. Mass [mg]	± 2				
DI-Diesel Mass [mg]	± 2				
SOI-Gas. [°aTDC]	± 1				
SOI-Diesel [°aTDC]	± 1				
EGR [%]	± 2				
OUTPUTS					
Std. GIE [%]	0.5				
Std. NOx [g/kg-f]	0.2				
Std. Soot [g/kg-f]	0.2				
Std. PPRR [bar/deg]	1				
Std. PP [bar]	4				

The constraint values were chosen randomly to test the approach. Reasonably low values of constraints were chosen so that the strategy can be considered stable. The ideal approach would be to choose these

values based on experimental CDC data. This approach shall be implemented in future studies. A harshness factor of 1 was assigned to each constraint to ensure that the GA meets the stability criteria. Although the GA does not cover essential input parameters (e.g., IVC temperature or pressure, wall temperatures, etc.), which are more prone to cycle-to-cycle fluctuations, it is to be noted that this study is a preliminary scoping study to verify the procedure. A more comprehensive GA inclusive of all the important variables will be explored in the future if this approach shows potential. Table 7-7 shows a comparison of the optima from the GA with and without the stability constraints.

Table 7-7. Comparison of the optimum value from the GA without and with the stability check.

Tuble 1 7. Comparison of the optimum value from the Gri without and with the stubility eneck.						
Parameter	GA without stability check GA with stability check		GA with stability check (KIVA Validation)			
INPUTS						
Premix Gas. Frac [-]	0.99	0.91	0.91			
Gas. Frac. [-]	0.96	0.72	0.72			
SOI-Gas. [°aTDC]	19.61	-100	-100			
SOI-Diesel [°aTDC]	-0.43	22.33	22.33			
EGR [%]	59.6	46.4	46.4			
Global Φ [-]	0.99	0.75	0.75			
OUTPUTS						
GIE [%]	45.63	44.68	44.26			
NOx [g/kg-f]	0.002	0.006	0.005			
Soot [g/kg-f]	0.003	1.97	1.86			
PPRR [bar/deg]	14.98	14.31	13.4			
PP [bar]	165.4	199.99	194.2			

Firstly, it is observed that, though the GPR model was used to perform the optimization, the final optimum obtained without the stability constraints is similar to the optimum presented in Table 7-3. This shows that the GPR model trained with the GA and Latin hypercube data-sets did a good job at replicating the CFD model over the design space covered in the GA. Removing the stability constraint resulted in a completely different optimum point. The optimum strategy with the stability check is a "mixed-mode" combustion strategy, which is a combination of gasoline PPC and a post TDC load extension injection. Similar operating strategy was found to be optimum for the high-load-low-speed operating point in Chapter 6 and was studied in detail in Appendix-B. Since the optimum obtained for the GA with the stability check was different from the optimum seen in Table 7-3, it was re-run in KIVA to validate the prediction of the

GPR model. As seen from Table 7-7, there is a reasonable agreement between the GPR and KIVA predicted outputs.

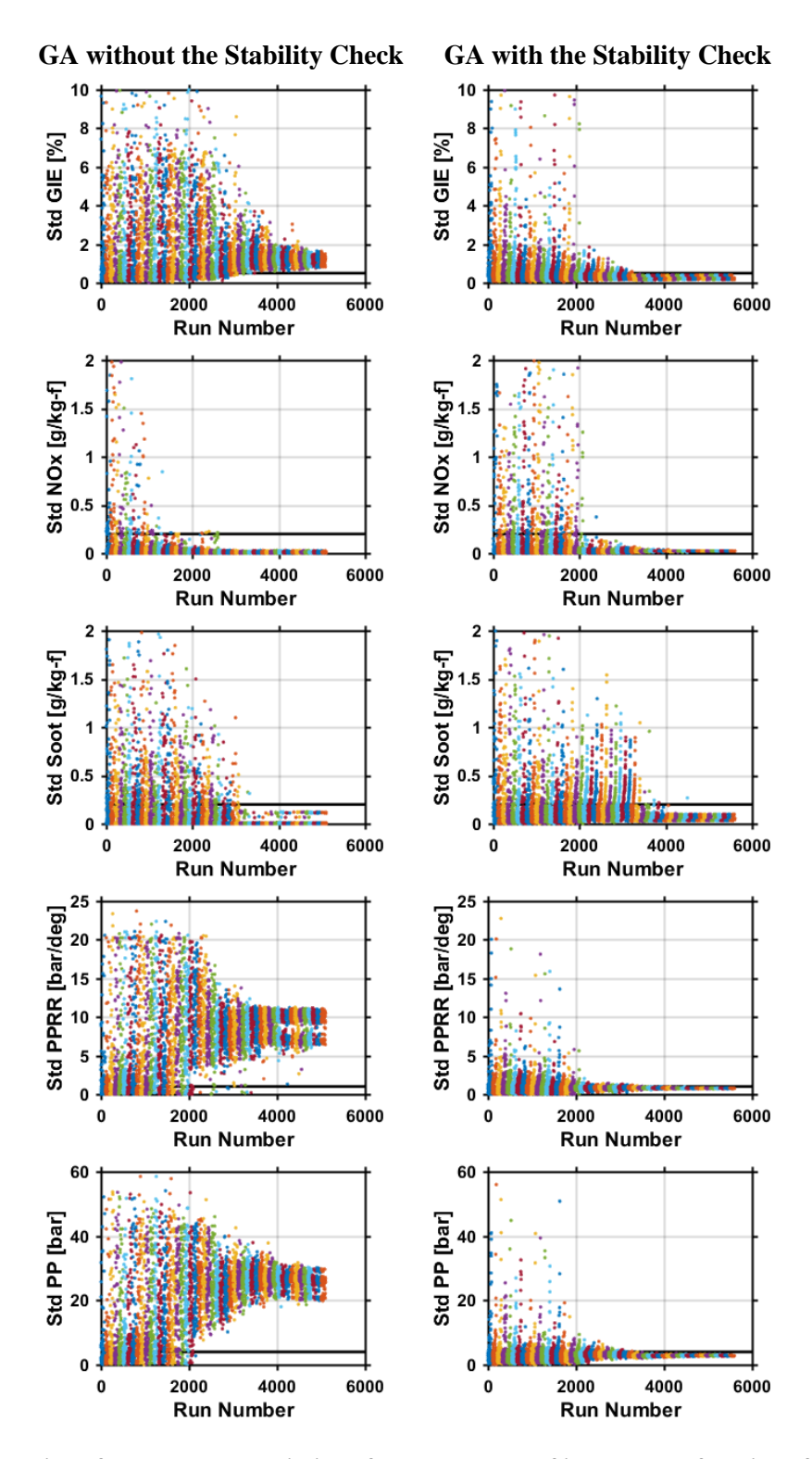


Figure 7-26. Evolution of the standard deviation of all the outputs of interest as a function of the run number for the GA (left) without and (right) with the stability check.

Figure 7-26 shows a comparison of the evolution of standard deviation as a function of the run number through the optimization for the GA with and without the stability check. The constraint value set for the standard deviation of each output variable is also shown on its corresponding plot. The optimum without the stability check is found to be highly unstable, which is evident from the large values of standard deviation in GIE, PPRR, and PP. Adding the stability constraints reduces the variation in the outputs significantly and ensures that all the output variables meet the stability criteria. To understand the source of instability for the optimum from the GA with the stability check, Figure 7-27 shows a comparison of the standard deviations for the optimum points from the two GA's with respect to each input variable variation included in Table 7-6. The standard deviation with respect to each input variable fluctuation was estimated based on the approach presented in §7.3.

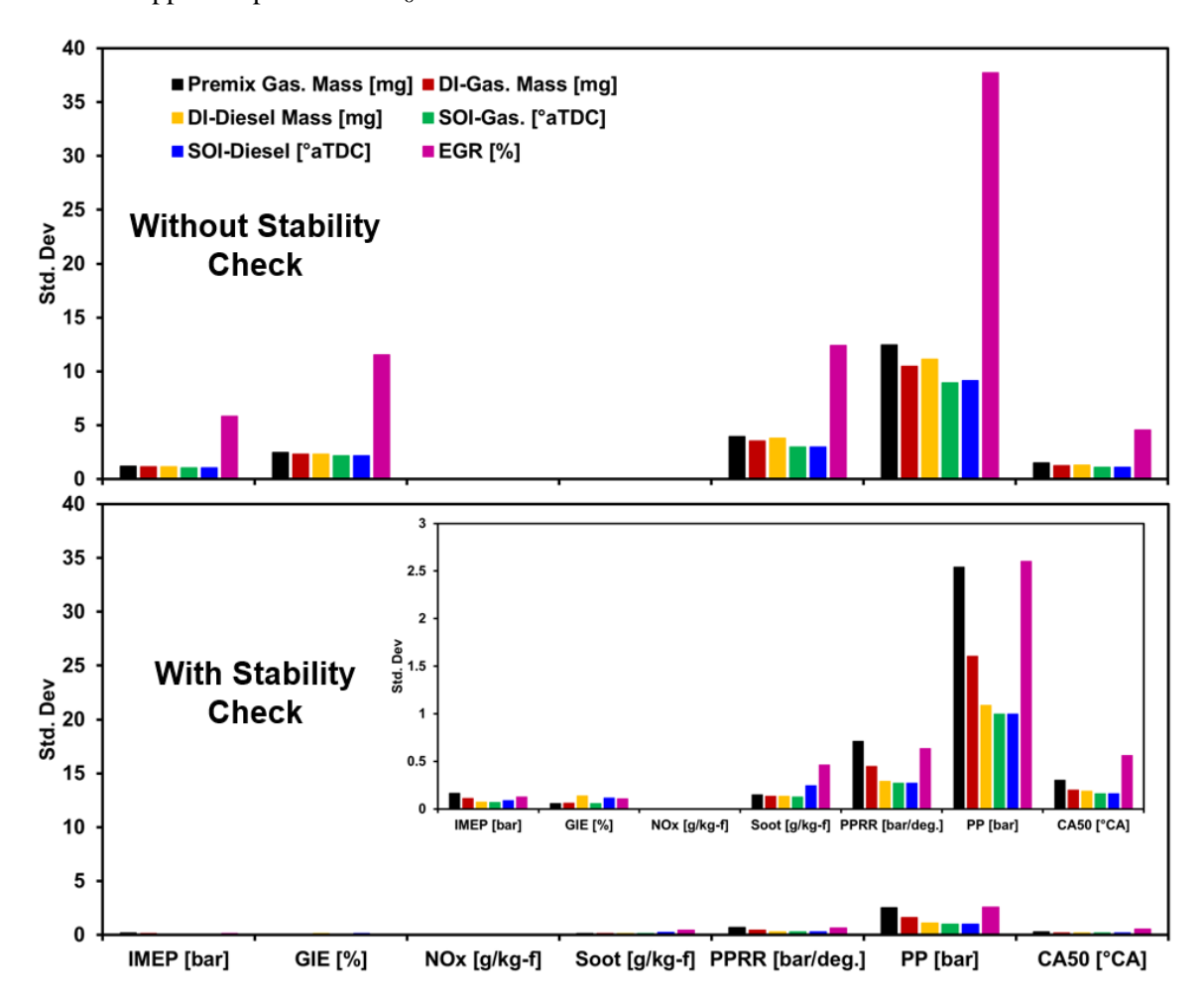


Figure 7-27. Standard deviation of the output variables with respect to fluctuations in the input variables for the optimizations (top) without and (bottom) with the stability check.

As seen from the figure, when the stability check was not included, the optimum was mainly unstable to fluctuations in EGR rate. From Table 7-7, it is seen that for the optimum without the stability check, the global Φ is ~1. The high sensitivity to EGR rate is due to operating at a near stoichiometric Φ . A similar observation was made previously as well with the high-load-low-speed optimum point in Chapter 4. Fluctuations (increases) in the EGR rate increases the global Φ beyond stoichiometric leading to fuel-rich operation. This results in a rapid increase in incomplete combustion and a drastic drop in GIE, PPRR, and PP. This trend with EGR fluctuation is shown in Figure 7-28, which clearly shows the sensitivity to positive fluctuations in EGR rate. The results presented in Figure 7-28 are from CFD simulations performed on the optimum point.

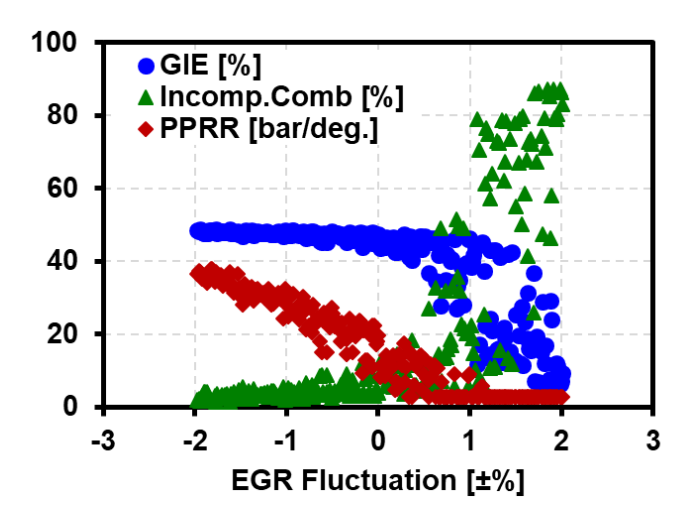


Figure 7-28. GIE, Incomplete Combustion, and PPRR as a function of EGR fluctuation.

When the stability check was added, the standard deviations reduced significantly (seen in Figure 7-27), and the operating strategy became relatively more stable. Since there was a substantial reduction in standard deviations, a plot with rescaled y-axis is also overlaid on the original plot in Figure 7-27 for the case with the stability check. As seen, the standard deviations for all the outputs are within the constraints used. However, the sensitivity of soot emissions increases relative to the optimum without the stability check. The differences in stability can be explained by comparing the operating strategies of the two optima. Both the strategies differ in terms of air-handling. The optimum with the stability check has a reduced EGR rate of 46.4% which results in a lean global Φ of 0.75. This reduces the sensitivity to EGR fluctuations

significantly. However, due to operating at a lower EGR rate, the chemistry timescales shorten. Consequently, the gasoline fuel mass (premixed and early DI) is reduced, to ensure that the constraints on PPRR and PP are met. Since the PPC combustion event is constrained by noise, the diesel fuel is injected as a load extension injection post TDC (after the PPC combustion event) to meet the load requirement. The SOI timing of the load-extension injection is constrained by soot emissions. That is, the SOI timing of the load-extension injection is as advanced as possible (upon the completion of the primary heat release), to maximize the efficiency while meeting the soot constraint. Similar results were also demonstrated in Kavuri et al. [100] where a detailed analysis on the constraining factors was presented while investigating mixed-mode combustion strategies as a pathway to enable stable high-load operation at reduced EGR rates.

Lastly, it is seen that including the stability check resulted in an operating strategy that has increased the sensitivity of soot emissions to input variable fluctuations. This is due to the increased DI fuel mass in the diesel fuel injection. Since the diesel fuel injection is combusting in a mixing-controlled heat release, it is prone to soot emissions. A detailed study on soot emissions from load extension injection was performed in Appendix-B. In this study, it was found that soot emissions are highly sensitive to the load-extension SOI timing. A similar observation is made in the current study as well. Secondly, it is also seen that soot emissions are sensitive to EGR fluctuations. This is contradictory to the results observed in Appendix-B where soot emissions in the post-TDC region were found to be independent of oxygen availability and were shown to be solely dependent on in-cylinder temperatures. To explain this result, Figure 7-29 shows the soot emissions response to fluctuations in EGR rate for the case with the stability check. It is observed that soot emissions are reducing with increased EGR rate. This shows that the temperature effect of EGR is dominating the oxygen availability effect, similar to the explanation provided earlier in Figure 7-21, in \$7.3.3. Therefore, the results seen in this study align with the results shown in Appendix-B.

In summary, based on the results shown in this section, using the GPR model to perform the stability analysis within the GA optimization seems to be a potential approach to achieve stable and reliable optima from the GA optimizations.

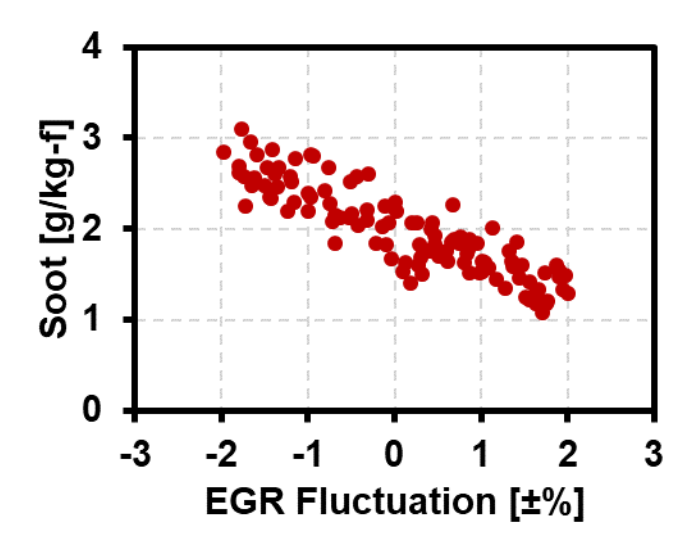


Figure 7-29. Soot emissions vs. EGR fluctuation for the optimum case with the stability check.

7.5. Conclusions

In this chapter, the potential of a GPR machine learning approach was tested in terms of its handling of large non-parametric datasets generated from the GA. Four different kernel functions for the GPR approach were compared, and the matern 3/2 kernel was shown to perform the best. Accordingly, the GPR approach with the matern 3/2 kernel was used to demonstrate three different applications of machine learning. The first was to speed up the GA optimization process. A new approach called the CFD+GPR approach was developed such that the GPR model could substitute some of the CFD runs and reduce the computational time. GA optimization was performed with the CFD+GPR approach and compared with the results from the GA run entirely with CFD. The CFD+GPR approach was shown to result in a similar optimum as the GA run completely with CFD while reducing the optimization time by 62%.

The GPR approach was then used to perform uncertainty quantification which identifies the input variables causing maximum uncertainty in the CFD model predictions for a combustion strategy. A total of 39 input variables, comprising of numerical and physical inputs, were considered and the uncertainty quantification study was performed with CDC, RCCI, and GCI strategies under high-load conditions. The results of this study showed that for high-load CDC operations, it is essential to have the correct injection profile and the mixing field (i.e., breakup and transport) to arrive at a reliable CFD prediction. For the high-load RCCI and GCI strategies, it is essential to take accurate measurements of CR and intake conditions

(i.e., Pivc, Tivc, EGR, etc.), as even the slightest error can result in result in significant variations in incylinder pressure and emission predictions.

Lastly, the GPR approach was used to further improve the optimization procedure by adding constraints on the stability of outputs to variations in inputs to ensure that the GA results in a stable and reliable optimum. The approach was verified by comparing the results from a GA that was run with and without the stability constraints. The results showed that adding the stability constraints reduces the standard deviations in all the outputs and results in an optimum with significantly improved stability to operating parameter variations.

Chapter 8 Summary and Future Work

The current study addresses the challenges of operating with advanced compression ignition combustion strategies at low-load-high-speed conditions and high-load-low-speed conditions of the engine operating map. A combination of CFD modeling, GA optimization, and machine learning was used to perform this study.

8.1. Addressing the challenges at High-Load Low-Speed Operating Condition

8.1.1. Optimization at High-Load-Low-Speed Conditions

Initially, targeting high-load-low-speed conditions, a GA optimization study was performed at 20 bar IMEP and 1300 rev/min. to identify feasible operating strategies at this load. The study was performed on a heavy-duty engine with a CR of 12:1 and a "bathtub" shaped piston geometry. In this study, RCCI and GCI combustion strategies were compared. The optimum operating strategies for RCCI and GCI cases were found to be similar. Most of the fuel (~70%) was introduced early into the combustion chamber in the form of premixed fuel and an early injection at -100 °aTDC and -78 °aTDC for the GCI and RCCI strategies, respectively. The rest of the fuel was injected as a stratified injection close to TDC at -14 °aTDC and -12 °aTDC for the GCI and RCCI strategies, respectively. The optimum air-handling parameters were also similar. Both required an EGR of 55% with the RCCI optimum having a slightly higher intake pressure.

The optimums were compared in terms of combustion and performance characteristics. Further analysis studied the effect of input and operating condition variation on combustion control, performance, and combustion stability. The results showed that both combustion strategies have similar combustion characteristics with a near TDC injection initiating and controlling the combustion. However, the RCCI strategy was found to have more control over combustion phasing than the GCI strategy. The increased control was found to be due to the shorter ignition delay of diesel fuel than gasoline. This benefit, however, comes at the expense of increased soot emissions as the combustion event occurs during the near TDC injection event. The longer ignition delay of the GCI strategy results in less control over combustion phasing but enables near-zero soot emissions. In terms of other performance parameters, both strategies were found to have high GIE (47%) with near zero NOx emissions. The RCCI strategy was found to have a higher PPRR than the GCI strategy due to advanced combustion phasing. Nevertheless, it was still within

reasonable operation level (PPRR \leq 20 bar/deg) for high-load operation in a heavy-duty engine. From the stability analysis, it was identified that both the strategies were most sensitive to variations in EGR, with the GCI strategy being more sensitive than the RCCI strategy. The high sensitivity to EGR was a result of operating at a high EGR level of 55% and near stoichiometric global Φ . Furthermore, achieving high EGR levels at high intake pressures in practice might be challenging due to the heavy burden it places on the air-handling equipment. These issues with high EGR operation motivated the need to investigate high-load operating strategies that work at reduced EGR rates and leaner global Φ . However, the results from the optimization study showed that the efficiency of the optimum strategy reduces as the EGR late is lowered. In the high-load-low-speed optimization study, the optimum strategies were identified under the constraints of NOx \leq 2g/kg-f, Soot \leq 2g/kg-f, and RI \leq 5 MW/m². Operating under these constraints could have negatively affected the efficiency at the low and moderate levels of EGR. The RI constraint is a necessity to prevent the structural damage of the engine parts. But, the constraints on NOx and soot emissions could be relaxed by using after-treatment devices if it offers significant efficiency benefits. Accordingly, the effect of removing these constraints on the efficiency in EGR- Φ operating space was investigated.

8.1.2. Constraint Analysis of High-Load-Low-Speed Operation with RCCI strategy

The NOx and soot emission constraints were removed while keeping the other constraints fixed, and the effect of removing the constraints on the optimum operating strategy and performance was studied. Results showed that the operation at low to moderate EGR levels (< 50%) was mainly constrained by the NOx emissions. Relaxing the NOx constraint enabled lower EGR operation with significant efficiency improvement. Allowing NOx emissions to increase to acceptable levels for SCR after-treatment, yielded an optimum at a moderate (\sim 45%) level of EGR and a lean global Φ of 0.8. The optimum case had near-zero soot emissions and a relatively higher NFE compared to the high EGR optima. The improved efficiency upon removing the NOx constraint was identified to be due to advancing the diesel fuel injection which resulted in a more optimal combustion phasing. Further comparison with the high EGR optima in terms of combustion control showed that the optimum with SCR after-treatment resulted in similar combustion control as the high EGR optima. However, due to operation at a reduced EGR rate and a leaner

global Φ , the optimum with SCR after-treatment resulted in significantly lower soot emissions compared to the high EGR strategy. Therefore, removing the NOx constraint and using SCR after-treatment addressed the tradeoff between combustion control and soot emissions. Lastly, comparison was made with the high EGR optimum in terms of stability to operating condition fluctuations. The optimum with SCR after-treatment was significantly more stable compared to the high EGR optimum. The improved stability was found to be due to the reduced sensitivity to EGR fluctuations from operating at a leaner global Φ . These results indicate that removing the NOx constraint and using SCR after-treatment addresses the issues of high soot emissions and sensitivity to EGR fluctuations while retaining the excellent combustion control observed with the high EGR GA optimum, under high-load-low-speed conditions.

8.2. Multi-Mode Optimization

Upon completing investigation of the high-load, low-speed operating conditions, the low-load, high-speed operating condition was targeted. When operation at 2 bar and 1800 rev/min. was investigated on the low CR engine used for the high-load study, it resulted in a poor efficiency. This was because of the low CR engine used for the high-load study, which was designed to perform well under high-load conditions. This shows that the optimum CR could be different when both loads are taken into consideration. In addition, the optimal injector configuration, bowl geometry, and air-handling could all be very different considering the vast difference in fuel mass associated with the low- and high-load operating conditions. Accordingly, a computational optimization study was performed using detailed CFD modeling in combination with a GA considering the performance at low-load-high-speed (2 bar, 1800 rev/min.) and high-load-low-speed (20 bar, 1300 rev/min.) operating conditions, simultaneously. The optimization study had 28 design inputs, which included parameters for piston bowl geometry, injector design, air-handling, and fueling strategy. When both conditions were equally weighted, the optimization study resulted in an optimum CR of 13.1 with a stepped piston bowl geometry that had two distinctive regions. Results also showed that a narrow spray angle for diesel fuel and a wide spray angle for gasoline would be necessary to target the two regions of the bowl. The optimal fueling strategy at low load was similar to diesel LTC. This strategy used very little premixed fuel and a low gasoline percentage (~15% of the total fuel mass). At highload, the optimum strategy was a mixed mode combustion strategy with 92% of the fuel being gasoline with most of it premixed. The small quantity of diesel fuel present was injected close to TDC. The diesel fuel injection along with the premixed fuel contributed to the primary heat release. The rest of the gasoline was injected as a load extension injection after TDC to achieve the necessary load. Thus, from this study, feasible operating strategies were identified for both the low-load-high-speed and high-load-low-speed operating conditions.

The COSSO response surface model was fit to the GA data and was used to study the effect of varying the weight assigned to each operating mode on the GA results. It was found that, when low-load is given a higher weight, a higher CR piston (CR ~ 15.7) was preferred as the optimum. Conversely, when giving a higher weight to high-load, a lower CR (CR ~ 11.8) piston was selected as the optimum. Results also showed that prioritizing one load highly over the other yielded a bowl geometry that affects the performance negatively at the other load condition. The results from the study indicated that advanced combustion optimizations must consider multiple loads simultaneously to achieve a realistic optimal design that yields good performance across a range of operating conditions. The multi-mode optimization study performed in this dissertation outlines the procedure for performing such studies.

8.3. RCCI Operating Strategy vs. Load

Based on previous research and the work presented in this dissertation, Figure 8-1 shows a summary of how to run a heavy-duty RCCI engine at different operating conditions. In the figure, fuel injected prior to IVC is classified as premixed fuel, fuel injected after IVC with the end of injection separated from the start of combustion is classified as a stratified injection, and the fuel injected close to TDC which combusts in a mixing-controlled heat release is classified as mixing-controlled injection. The aim of any advanced combustion strategy for a given load is to maximize the premixed fuel and to have any fuel injections as early in the cycle as possible. This is preferred because it increases the dilution and maximizes the efficiency while minimizing the NOx and soot emissions. Accordingly, for the operating strategy at every load, the factors limiting the advancement of the SOI timing (shown in green) and the factors limiting the increase in the fuel mass (shown in red) for each injection are highlighted in the figure.

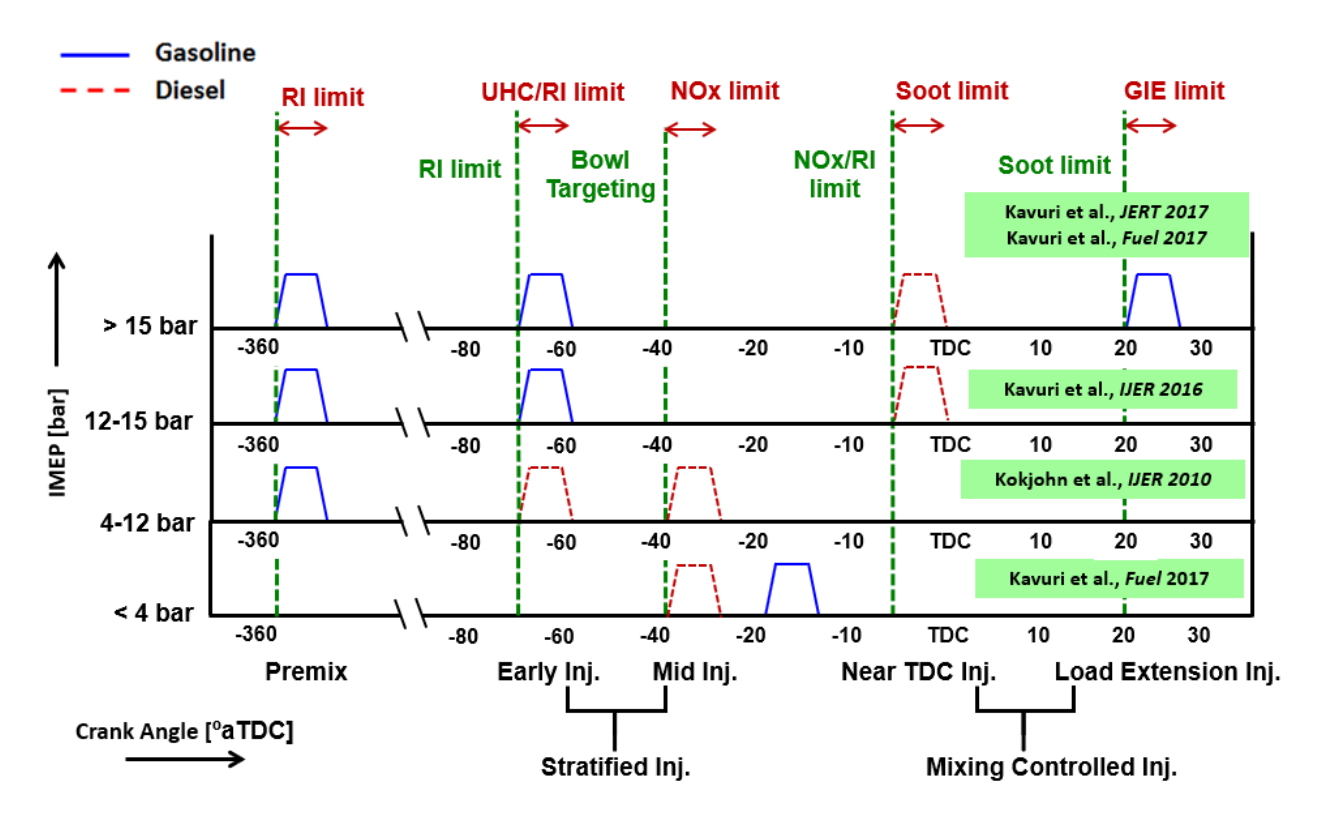


Figure 8-1. Summary of RCCI strategies as a function of nominal gross IMEP.

At the mid-load conditions in the range of 4 bar to 12 bar, the traditional RCCI strategy demonstrated by Kokjohn et al. [6] can be implemented. The gasoline fuel mass in this strategy is constrained by the RI limit. The early diesel fuel injection is targeted into the squish region and is used for conditioning the squish area. The diesel fuel mass in this injection is constrained by the UHC emissions from fuel deposited into the crevice region at the low-load conditions and gradually transitions to the RI limit as the load increases. The second diesel fuel injection can be early enough such that it is targeted into the bowl region. This injection acts as the ignition source. The fuel mass in this injection is constrained by the NOx emissions.

To explain why the same strategy cannot be used for loads less than 4 bar, Figure 8-2 shows the global Φ as a function of IMEP. As seen from the figure, at loads lower than 4 bar, the global Φ becomes overly lean, which causes high levels of incomplete combustion when the fuel is premixed. Hence, at loads less than 4 bar, the gasoline is direct-injected after the diesel fuel injection. This strategy was identified from the multi-mode optimization study presented in Chapter 6. The fuel mass in the DI gasoline is

constrained by NOx limit as was shown in Chapter 6. Since at loads less than 4 bar, it is preferred to delay the SOI timings as late as possible to achieve locally rich mixtures, it is of interest to know the limiting factor on retarding the SOI timing. Though, it is not shown in Figure 8-1, delaying the SOI timings of the two DI injections is constrained by NOx emissions. Since retarding the SOI timings increases the local Φ , it results in an increase in the peak combustion temperatures and consequently increases NOx emissions.

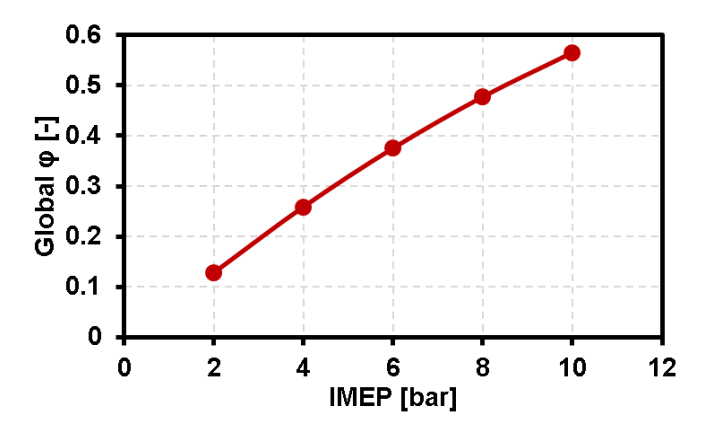


Figure 8-2. Global Φ as a function of IMEP.

To extend the load beyond 12 bar IMEP with the RCCI strategy proposed by Kokjohn et al. [6] would require excessively high EGR rates (~57%). Load extension at a reduced EGR rate with this strategy is not possible since it is constrained by the RI limit. The load can be extended from 13 bar to 15 bar IMEP by delaying the mid stratified diesel injection and injecting it as a near TDC mixing-controlled injection. The premixed gasoline can be split up into premixed gasoline and an early stratified DI gasoline. This strategy was demonstrated at a load of 13 bar IMEP in Kavuri et al. [100]. Adding the early DI gasoline has shown to reduce the impact of the RI constraint on load extension. That is, with the early DI gasoline added, a similar load as using the premixed fuel alone can be achieved at a relatively lower RI. The load that can be added from the mixing-controlled injection is constrained by soot emissions. The earliest the fuel can be injected is constrained by either the NOx or RI limit based on other operating parameters like EGR and IVC pressure.

Lastly, to achieve higher loads, a load extension injection of gasoline can be added post TDC to extend the load range from 15 bar to 20 bar IMEP, as was demonstrated in Chapter 6 and in Kavuri et al.

[100]. The earliest the load-extension injection can be injected is constrained by the soot emissions. The load that can be added through this injection is constrained by several factors like GIE, exhaust temperature, etc. Thus, the current study fills in the research gaps that exist in the low-load and the high-load operating regime by suggesting operating strategies at loads lower than 4 bar gross IMEP and in the high-load range of 13 bar to 20 bar gross IMEP.

8.4. Machine Learning in GA Optimization

Though the multi-mode optimization study showed the importance of considering multiple operating conditions during optimization to achieve the best output, it took nearly 3 months to complete the GA with two operating conditions. To consider all the points of a drive cycle, it would take significantly longer. This motivated the need to investigate ways to reduce the computational time of the GA optimization. To address this issue, machine learning through GPR with a Matern 3/2 kernel, was used in combination with CFD in GA optimizations, to speed up the optimization process. The approach was tested on a GA run with five input parameters. After every generation of the GA, the data from the prior generations was used to train the GPR model and then the GPR model was used to predict the outputs for the latest generation. To ensure that the GPR predictions are reliable, the data from a Latin hypercube DOE that was run prior to starting the GA was used. When the GA was run solely with CFD, the optimization took 50 days to complete. With the CFD and GPR approach, the computational time of optimization was reduced by 62%, and the optimization was completed in 19 days.

Additional applications of the GPR model were also demonstrated. One application was to perform uncertainty quantification. In this study, the GPR model was used to identify the key inputs which could contribute to uncertainty in the CFD model predictions. This study helps identify the inputs that should be chosen accurately to get reliable CFD predictions. It can also be used as a scoping study to identify the key operating variables that should be considered when optimizing a combustion strategy. An uncertainty quantification study was performed using the GPR model with CDC, RCCI, and GCI combustion modes under high-load conditions. The results of this study showed that for high-load CDC operation, it is essential to have the correct injection profile and the mixing field (i.e., breakup and transport) to achieve reliable

CFD predictions. For the high-load RCCI and GCI strategies, it was identified that it is important to take accurate measurements of CR and the intake conditions (i.e., Pivc, Tivc, EGR, etc.), as even the slightest error can result in result in significant variations in in-cylinder pressure and emission predictions.

The GPR model was also used to further improve the optimization process where it was used to check for the stability of the designs to operating parameter variations during the optimization. The approach was tested on the same GA used to verify the CFD+GPR approach. However, the optimization was run completely with the GPR model. The GA data from the earlier optimization study as well as the Latin hypercube DOE data-set used in the CFD+GPR approach, were used to train the GPR model. Initially, the GA was run without the stability constraint. Then the optimization was repeated with the CFD+GPR approach with the stability constraints added. Results from the study showed that adding the stability check resulted in a reliable and stable optimum.

8.5. Future Work

8.4.1. Machine Learning in Soot Modeling

With the two-step soot model used in the current study, the main concern is with changing operating conditions, though it predicts the trends accurately, the magnitudes are not always accurately predicted, and the soot formation constant has to be adjusted based on operating condition. The soot formation constant is a scaling factor for soot emissions. It is well known that soot emissions are a function of the local Φ and temperature. Hence, instead of using a global soot formation constant, what if the soot formation constant could be estimated and varied locally in each cell based on the local Φ and temperature, to predict the soot emissions in each cell. This would improve the soot predictions without having to adjust the soot formation constant manually. Constant volume soot data under different operating conditions for a variety of fuels is available from the engine combustion network (ECN) data provided by Sandia National Laboratory. The constant volume experiments can be modeled using CFD by using a randomly chosen set of soot constants. Obviously, the model predictions will not match with the experimental data completely. But, by comparing the images of soot contours from the experiments and CFD, we can know by how much the soot formation constant in each computational cell (each pixel of the image) should be scaled by. By scaling the global soot formation constant used with the scaling factor for each computational cell, we get the soot formation

constant for each computational cell. Similarly, the Φ and temperature in each computational cell can also be estimated from their respective contour images. This gives us a combination of Φ , temperature and the soot formation constant of each computational data. This data can be used to train the GPR model to predict the local soot formation constant in each computational cell based on the local Φ and temperature. Combining the data from multiple operating conditions could result in a robust GPR model for soot predictions.

8.4.2. Machine Learning in CFD Modeling

The applications of machine learning could also be extended to CFD modeling. For example, in engine CFD modeling, the majority of the computational expense is due to the expensive (refined) computational grids that are used to predict the spray structure and the momentum exchange between the liquid and gas phase. If the GPR model can be used instead to predict the in-cylinder spray evolution, it would save a lot of computational time and expense. Direct numerical simulation (DNS) data of diesel fuel sprays can be used to train the GPR model. The first step would be to compute the curvature and surface area of the interface between the gas and liquid phase present in each cell from the DNS data. This data at different time steps can be used to train the GPR model to predict the spray evolution. The GPR results could then be imposed into the Lagrangian framework to force the Lagrangian spray evolution to follow the GPR results. A simple approach would be to set the number of droplets in each spray parcels such that the GPR predicted interfacial area is captured.

8.4.3. Improving Engine Optimization

In the current study, existing optimization approaches were improved in several ways like considering multiple modes in optimizations, using machine learning to speed up the optimization and adding stability as a constraint to get stable and reliable optima. One other major concern with engine optimizations is the uncertainty in the model predictions. Having an error band on the optimization results and minimizing these error bands (uncertainties) in the results will give more confidence in the optimization predictions. This can be done by using the uncertainty analysis presented in Chapter 7. The top 4 model parameters that cause maximum uncertainty for each output can be included as input parameters in the GA optimization, and the uncertainty or standard deviation can be estimated with respect to each input. This

uncertainty can be used as an error on the optima presented and by setting a constraint value (to a low value) on the uncertainty, it can be minimized as the GA progresses, since the response to these variables changes as the operating strategy changes. Hence as the GA progresses the size of the error bands is expected to reduce, and the final optimum is expected to have a minimal error.

8.4.4. Optimization Study Considering Fuel Effects

Although most of the optimization studies shown so far were done with gasoline and diesel fuel, RCCI is a fuel flexible strategy and has been demonstrated on a wide range of fuels. Even in the present study, we found that using 87 AKI gasoline benefited combustion at low-load and aided in achieving higher efficiency relative to 93 AKI gasoline, which was used by Kokjohn et al. [7] at the same load conditions. However, at the higher loads, a higher-octane gasoline like 93 AKI gasoline would be preferred as the higher loads desire the additional ignition delay achievable with, the higher-octane gasoline. Accordingly, 93 AKI gasoline was used for the high-load optimization study. This clearly shows the impact fuel properties have on the optimum injection strategy at a given load condition. Fixing the fuels in the optimization process could be constraining the GA from arriving at strategies that would achieve higher efficiencies than what was seen in this study. Similar to gasoline there are other fuels like E10, E85, natural gas, etc. that can be used in RCCI combustion as alternatives to gasoline. A new optimization study can be setup, where the fuel in each injection can be varied within the chosen set of fuels.

References

- 1. 2017 and Later Model Year Light-Duty Vehicle Greenhouse Gas Emissions and Corporate Average Fuel Economy Standards, *Federal Register*, Vol. 77, No. 199, October 15, 2012.
- 2. Tier 3 Motor Vehicle Emissions and Fuel Standards, *Federal Register*, Vol.80, No. 33, February 19, 2015.
- 3. **Sharp, C., Webb, C., Yoon, S., Carter, M. et al.,** Achieving Ultra Low NOX Emissions Levels with a 2017 Heavy-Duty On- Highway TC Diesel Engine Comparison of Advanced Technology Approaches, *SAE Int. J. Engines*, 2017, 10(4), 1722-1735.
- 4. Global Transportation Scenarios 2050, London, 2011
- 5. **Liu, H., Yao, M., Zhang, B., and Zheng, Z.,** Effects of Inlet Pressure and Octane Numbers on Combustion and Emissions of a Homogeneous Charge Compression Ignition (HCCI) Engine, *Energy & Fuels*, 2008, 22(4), 2207-2215.
- 6. **Kokjohn, S.L., Hanson, R., Splitter, D., and Reitz, R.D.,** Fuel reactivity controlled compression ignition (RCCI): a pathway to controlled high-efficiency clean combustion, *Int. J. Eng. Res.*, 2011, 12(3), 209-226.
- 7. **Kokjohn, S.L., and Reitz, R.D.**, Reactivity Controlled Compression Ignition and Conventional Diesel Combustion: A Comparison of Methods to Meet Light-Duty NO_x and Fuel Economy Targets, *Int. J. Eng. Res*, 2013, 14(5), 452-468.
- 8. **Dempsey, A., and Reitz, R.,** Computational Optimization of Reactivity Controlled Compression Ignition in a Heavy-Duty Engine with Ultra Low Compression Ratio, SAE Int. J. Engines, 2011, 4(2), 2222-2239.
- 9. **Lim, J.H., and Reitz, R.D.,** High Load (21 Bar IMEP) Dual Fuel RCCI Combustion Using Dual Direct Injection, *J. Eng. Gas Turbines Power*, 2014, 137(11).
- 10. **Wissink, M., and Reitz, R.D,** Direct Dual Fuel Stratification, a Path to Combine the Benefits of RCCI and PPC, *SAE Int. J. Engines*, 2015, 8(2), 878-889.
- 11. **Li, T., and Ogawa, H.,** Analysis of the Trade-off between Soot and Nitrogen Oxides in Diesel-Like Combustion by Chemical Kinetic Calculation, *SAE Int. J. Engines*, 2012, 5(2), 94-101.
- 12. **Theis, J. R., Ura, J.A., Li, J.J., Surnilla, G.G., Roth, J.M., and Goralski Jr., C.T.,** NO_x Release Characteristics of Lean NO_x Traps During Rich Purges, *SAE Transactions Journals of Fuels and Lubricants*, 2003, vol. 12(4), 758-775.
- 13. **Johnson T.V.,** Diesel Emissions in Review, SAE Int. J. Engines, 2011, 4(1), 143-157.
- 14. **Marie-Luce, D., Di-penta, D., Bliman, P., and Sorine, M.,** Control-Oriented Modeling of a LNT-SCR Diesel After-Treatment Architecture, *SAE Int. J. Engines*, 2011, 4(1), 1764-1775.
- 15. **Henry, C., Langenderfer, D., Yezerets, A., Ruth, M., Chen, H.-Y., Hess, H., and Naseri, M.,** Passive Catalytic Approach to Low Temperature NO_x Emission Abatement, *DEER*, 2011, Detroit, MI, USA.
- 16. **Akihama, K., Takatori, Y., and Inagaki, K.,** Mechanism of the smokeless rich diesel combustion by reducing temperature, *SAE Technical Paper* 2001-01-0655, 2001.
- 17. **Diwakar, R., and Singh, S.,** NO_x and soot reduction in diesel engine premixed charge compression ignition combustion: a computational investigation, *Int. J. Eng. Res.*, 2008, 9(3), 195-214.

- 18. **Noehre, C., Andersson, M., Johansson, B., and Hultqvist, A.,** Characterization of Partially Premixed Combustion, *SAE Technical Paper* 2006-01-3412, 2006.
- Najt, P. M., and Foster, D. E., Compression-Ignited Homogeneous Charge Combustion, SAE Technical Paper 830264, 1983.
- 20. **Dec, J. E., and Yang, Y.,** Boosted HCCI for high power without engine knock and with ultra-low NOx emissions using conventional gasoline, *SAE Int. J. Engines*, 2010, 3(1), 750–767.
- 21. **Dec, J. E., Yang, Y., and Dronniou, N.,** Boosted HCCI Controlling Pressure-Rise Rates for Performance Improvements using Partial Fuel Stratification with Conventional Gasoline, *SAE Int. J. Engines*, 2011, 4(1), 1169–1189.
- Marriott, C.D., and Reitz, R.D., Experimental Investigation of Direct Injection-Gasoline for Premixed Compression Ignited Combustion Phasing Control, SAE Technical Paper 2002-01-0418, 2002
- 23. **Marriott, C.D., Kong, S.C., and Reitz, R.D.,** Investigation of Hydrocarbon Emissions from a Direct Injection-Gasoline Premixed Charge Compression Ignited Engine, *SAE Technical Paper* 2002-01-0419, 2002.
- 24. **Kalghatgi, G., Risberg, P., and Angstrom, H.,** Advantages of Fuels with High Resistance to Autoignition in Late-injection, Low-temperature, Compression Ignition Combustion, *SAE Technical Paper 2006-01-3385*, 2006.
- 25. **Risberg, P., Kalghatgi, G., Angstrom, H., and Wahlin, F.,** Auto-ignition quality of Diesel-like fuels in HCCI engines, *SAE Technical Paper 2005-01-2127*, 2005.
- 26. **Kalghatgi, G., Risberg, P., and Angstrom, H.,** Partially Pre-Mixed Auto-Ignition of Gasoline to Attain Low Smoke and Low NO_x at High Load in a Compression Ignition Engine and Comparison with Diesel Fuel, *SAE Technical Paper 2007-01-0006*, 2007.
- 27. **Ra, Y., Yun, J.E., and Reitz, R.D.,** Numerical Simulation Of Diesel And Gasoline-Fueled Compression Ignition Combustion With High Pressure Late Direct Injection, *Int. J. Vehicle design*, 2009, 50, 3-34.
- 28. **Ra, Y., Yun, J.E., and Reitz, R.D.,** Numerical parametric study of diesel engine operation with gasoline, *Combustion Science and Technology*, 2009, 181, 350-378.
- 29. **Christensen, M., Hultqvist, A., and Johansson, B.,** Demonstrating the Multi-Fuel Capability of a Homogeneous Charge Compression Ignition Engine with Variable Compression Ratio. *SAE* 1999-01-3679, 1999.
- 30. **Sellnau, M., Sinnamon, J., Hoyer, K., and Husted, H.**, Full-Time Gasoline Direct-Injection Compression Ignition (GDCI) for High Efficiency and Low NO_x and PM, *SAE Int. J. Engines*, 2012, 5(2), 300-314.
- 31. **Sellnau, M., Foster, M., Moore, W., Sinnamon, J., Hoyer, K., and Klemm, W.,** Second Generation GDCI Multi-Cylinder Engine for High Fuel Efficiency and US Tier 3 Emissions, *SAE Int. J. Engines*, 2016, 9(2), 1002-1020.
- 32. **Bessonette, P., Schleyer, C., Duffy, K., Hardy, W., and Lietchy, M.**, Effects of Fuel Property Changes on Heavy-Duty HCCI Combustion, *SAE Technical Paper 2007-01-0191*, 2007.

- 33. **Inagaki, K., Fuyuto, T., Nishikawa, K., Nakakita, K., and Sakata, I.**, Dual-Fuel PCI Combustion Controlled by In-Cylinder Stratification of Ignitability, *SAE Technical Paper 2006-01-0028*, 2006.
- 34. **Kokjohn, S.L., Hanson, R., Splitter, D., and Reitz, R.D.**, Experiments and Modeling of Dual-Fuel HCCI and PCCI Combustion Using In-Cylinder Fuel Blending, *SAE Inj. J. Eng.*, 2010, 2(2), 24-39.
- 35. **Kokjohn, S.L., and Reitz, R.D.**, A Modeling Study of Charge Preparation in a HCCI Engine using a Variable Pressure Pulse (VPP) Injection System and Optimized PRF Blends, *International Conference on Liquid Atomization and Spray Systems*, Vail, Colorado, USA, 2009.
- 36. **Hanson, R., Kokjohn, S.L., Splitter, D.**, and Reitz, R.D., An experimental investigation of fuel reactivity controlled PCCI combustion in a heavy-duty engine, *SAE Int. J. Eng.*, 2010, 3(1), 700-716.
- 37. **Splitter, D., Reitz, R. D., and Hanson, R. M.,** High efficiency, low emissions RCCI combustion by use of a fuel additive, *SAE Int. J. Fuel Lubr.* 2010, 3(2), 742-756.
- 38. **Hanson, R., Kokjohn, S.L., Splitter, D., and Reitz, R.D.,** Fuel effects on reactivity controlled compression ignition (RCCI) combustion at low load, SAE Technical Paper 2011-01-0361, 2011.
- 39. Wang, Y., Yao, M., Li, T., Zhang, W., and Zheng, Z., A parametric study for enabling reactivity controlled compression ignition (RCCI) operation in diesel engines at various engine loads, *Applied Energy*, 2016, 175, 389-402.
- 40. **Zhang, Y., Sagalovich, I., De Ojeda, W., Ickes, A. et al.,** Development of Dual-Fuel Low Temperature Combustion Strategy in a Multi-Cylinder Heavy-Duty Compression Ignition Engine Using Conventional and Alternative Fuels, *SAE Int. J. Engines*, 2013, 6(3), 1481-1489.
- 41. **Dempsey, A., and Reitz, R. D.,** Computational Optimization of Reactivity Controlled Compression Ignition in a Heavy-Duty Engine with Ultra Low Compression Ratio, *SAE Int. J. Engines*, 2011, 4(2), 2222-2239.
- 42. **Benajes, J., Pastor, V.J., Garcia, A., and Monsalve-Serrano, J.,** The potential of RCCI concept to meet EURO VI NO_x limitation and ultra-low soot emissions in a heavy-duty engine over the whole engine map, *Fuel*, 2015, 159, 952-961.
- 43. Curran, S., Hanson, R. M., Wagner, R. M., and Reitz R. D., Efficiency and emissions mapping of RCCI in a light-duty diesel engine, *SAE Technical Paper 2013-01-0289*, 2013.
- 44. **Wickman, D. D., Senecal, P. K., and Reitz R. D.,** Diesel engine combustion chamber geometry optimization using genetic algorithms and multi-dimensional spray and combustion modeling, *SAE Technical Paper 2001-01-0547*, 2001.
- 45. **Kim, M., Liechty, M. P., and Reitz, R. D.,** Application of micro-genetic algorithms for the optimization of injection strategies in a heavy-duty diesel engine, *SAE Technical Paper 2005-01-0219*, 2005.
- 46. **Tanner, F. X., and Srinivasan, S.,** Optimization of fuel injection configurations for the reduction of emissions and fuel consumption in a diesel engine using a conjugate gradient method, *SAE Technical Paper 2005-01-1244*, 2005.

- 47. **Shi, Y., Ge, H.W., and Reitz, R.D.,** Computational Optimization of Internal Combustion Engines, Springer, *ISBN 978-0-85729-618-4*, 2011.
- 48. **Shi, Y., and Reitz, R. D.,** Optimization of a heavy-duty compression-ignition engine fueled with diesel and gasoline-like fuels, *Fuel*, 2010, 89, 3416-3430.
- 49. **Kavuri, C., Paz, J., and Kokjohn, S.L.,** A Comparison of Reactivity Controlled Compression Ignition (RCCI) and Gasoline Compression Ignition (GCI) Strategies at High Load, Low Speed Conditions, *Energy Conversion and Management*, 2016, 127 (1), 324-341.
- 50. **Kavuri, C., Kokjohn, S.L., Klos, D.T., and Hou, D.,** Blending the Benefits of Reactivity Controlled Compression Ignition and Gasoline Compression Ignition Combustion using an Adaptive Fuel Injection System, *Int. J. Eng. Res.*, 2016, 17(8), 811-824.
- 51. **Shi, Y., and Reitz, R.D.**, Assessment of Optimization Methodologies to Study the Effects of Bowl Geometry, Spray Targeting and Swirl Ratio for a Heavy-Duty Diesel Engine Operated at High-Load, *SAE Int. J. Eng.*, 2008, 1(1), 537-557.
- 52. **Kokjohn, S. L.,** Reactivity Controlled Compression Ignition (RCCI) Combustion, *PhD Thesis*, University of Wisconsin-Madison, 2012.
- 53. **Dempsey, A. B., and Reitz, R. D.,** Computational Optimization of a Heavy-Duty Compression Ignition Engine Fueled with Conventional Gasoline, *SAE Int. J. Fuels Lubr.*, 2011, 4(1), 338-359.
- 54. **Klos, D.T.,** Investigations Of Low Temperature Combustion (LTC) Engine Design And Combustion Instability, *MS Thesis*, University of Wisconsin-Madison, 2015.
- 55. **Shi, Y., and Reitz, R. D.,** Optimization study of the effects of bowl geometry, spray targeting and swirl ratio for a heavy-duty diesel engine operated at low and high load, *Int J. Eng. Res.*, 2008, 9, 325–346.
- 56. **Ge, H. W., Shi, Y., and Reitz, R. D., and Willems, W.,** Optimization of a high-speed direct-injection diesel engine at low-load operation using computational fluid dynamics with detailed chemistry and a multi-objective genetic algorithm, *Proc. Inst. Mech. Eng. D: J. Auto. Eng.*, 2010, 224, 547–563.
- 57. **Klos, D.T., and Kokjohn, S.L.,** Investigation of the sources of combustion instability in low-temperature combustion engines using response surface models, *Int. J. Eng. Res.*, 2015, 16(3), 419-440.
- 58. **Kavuri, C., and Kokjohn, S.L.,** Investigating Air-handling Requirements of High Load Low Speed Reactivity Controlled Compression Ignition (RCCI) Combustion, *SAE Technical Paper 2016-01-0782*, 2016.
- 59. **Kavuri, C., and Kokjohn, S. L.,** Computational optimization of a reactivity controlled compression ignition (RCCI) combustion system considering performance at multiple modes simultaneously, *Fuel*, 2017, 207(1), 702-718.
- 60. **Herbrich, R.,** Machine Learning at Amazon, *Proceedings of the Tenth ACM International Conference on Web Search and Data Mining*, 2017, doi 10.1145/3018661.3022764.
- 61. **Lin, Y., and Zhang, H.H.,** Component Selection and Smoothing in Smoothing Spline Analysis of Variance Models, *Institute of Statistics Mimeo Series 2556*, NUCS, 2003.

- 62. **Ge, H. W., Shi, Y., Reitz, R. D., Wickman, D. D., Zhu, G. S., Zhang, H. S., and Kalish, Y.,** Heavy-duty diesel combustion optimization using multi-objective genetic algorithm and multi-dimensional modeling, *SAE Technical Paper 2009-01-0716*, 2009.
- 63. **Altman, N. S.,** An Introduction to Kernel and Nearest-Neighbor Nonparametric Regression, *The American Statistician*, 1992, 46 (3), 175–185.
- Kodavasal, J., Moiz, A., Ameen, M., and Som, S., Machine Learning Analysis of Factors Impacting Cycle-to-Cycle Variation in a Gasoline Spark-Ignited Engine, ASME ICEF2017-3604, 2017.
- 65. Breiman, L., Random Forests, Machine Learning, 2001, 45(1), 5-32.
- 66. **Bin, S., and Wenlai, Y.,** Application of Gaussian Process Regression to Prediction of Thermal Comfort Index, *ICEMI 2013*, 958-961.
- 67. **Rasmussen, C. E., and Williams, C. K. I.,** Gaussian Processes for Machine Learning. *MIT Press. Cambridge, Massachusetts*, 2006.
- 68. **Richardson, R., Osborne, M. A., and Howey, D. A.,** Gaussian Process Regression for Forecasting Battery State of Health, *Journal of Power Sources*, 2017, 357, 209-219.
- 69. **Shi, Y., and Reitz, R. D.,** Assessment of multi-objective genetic algorithms with different niching strategies and regression methods for engine optimization and design, *J. Eng. Gas. Turb. Power*, 2010, 132, 052801.
- 70. **Charalambous, C.,** Conjugate Gradient Algorithm for Efficient Training of Artificial Neural Networks, *IEEE Proceedings*, 1992, 139(3), 301–310.
- 71. **Buhmann, M. D.,** Radial Basis Functions on Compact Support, *Proc. of the Edinburgh Math. Society*, 2001, 41, 33-46.
- 72. Wissink, M.L., Lim, J.H., Splitter, D.A., Hanson, R.M., and Reitz, R.D., Investigation of Injection Strategies to Improve High Efficiency RCCI Combustion With Diesel and Gasoline Direct Injection, ASME Internal Combustion Engine Division Fall Technical Conference, Vancouver, ASME Paper No. ICEF2012-92107, 2012.
- 73. **Kavuri, C., Tiry, M., Paz, J., and Kokjohn, S.L.,** Experimental and Computational Investigation of Soot Production from a Premixed Compression Ignition Engine using a Load Extension Injection, *Int. J. Eng. Res.*, 2016, 18(5-6), 573-590.
- 74. **Amsden, A.A.**, KIVA-3V, Release 2, Improvement to KIVA-3V, Los Alamos, Report No. LA-13608-MS, 1999.
- 75. **Perini, F., Galligani, E., and Reitz, R.D.**, An Analytical Jacobian Approach to Sparse Reaction Kinetics for Computationally Efficient Combustion Modeling With Large Reaction Mechanisms, *Energy Fuels*, 2012, 26(8), 4804-4822.
- 76. Lim, J.H., Perini, F., and Reitz, R.D., High Load (21 bar IMEP) Dual Fuel RCCI Combustion Optimization, *International Multidimensional Engine Modeling User's Group Meeting at SAE Congress*, Detroit, 2013.
- 77. **Wang, H., Reitz, R. D., Yao, M., Yang, B., Jiao, Q., and Qiu, L.,** Development of an n-heptane-n-butanol-PAH mechanism and its application for combustion and soot prediction, *Combust. Flame*, 2013, 160(3), 504-519.

- 78. **Ra, Y., and Reitz, R.D.**, A Reduced Chemical Kinetic Model for IC Engine Combustion Simulations With Primary Reference Fuels, *Combust. Flame*, 2008, 155(4), 713-738.
- 79. **Wang, H., Dempsey, A. B., Yao, M., Jia, M., and Reitz, R. D.,** Kinetic and Numerical Study on the Effects of Di-tert-butyl Peroxide Additive on the Reactivity of Methanol and Ethanol, *Energy & Fuels*, 2014, 28 (8), 5480-5488.
- 80. **Sun, Y.**, Diesel Combustion Optimization and Emissions Reduction Using Adaptive Injection Strategies (AIS) with Improved Numerical Models, PhD Thesis in Mechanical Engineering, University of Wisconsin-Madison, 2007.
- 81. **Hiroyasu, H., and Kadota, T.**, Models for combustion and formation of nitric oxide and soot in DI diesel engines, *SAE Technical Paper 760129*, 1976.
- 82. Nagle, J., and Strickland-Constable, R. F., Oxidation of Carbon Between 1000-2000 C. Proc. of the Fifth Carbon Conf., Vol.1, 1962.
- 83. **Liu, Y., Tao, F., Foster, D.E., and Reitz, R.D.,** Application of A Multiple-Step Phenomenological Soot Model to HSDI Diesel Multiple Injection Modeling, *SAE Technical Paper 2005-01-0924*, 2005.
- 84. **Abraham, J.,** What is Adequate Resolution in the Numerical Computations of Transient Jets?, *SAE Technical Paper 970051*, 1997.
- 85. **Abani, N., Kokjohn, S.L., and Park, S.W. et al.**, An Improved Spray Model For Reducing Numerical Parameters Dependencies in Diesel Engine CFD Simulations", *SAE Technical Paper* 2008-01-0970, 2008
- 86. **Abani, N., Munnanur, A., and Reitz, R.D.**, Reduction of Numerical Parameter Dependencies in Diesel Spray Models, *J. Eng. Gas. Turb. Power*, 2008.
- 87. **Beale, J.C., and Reitz, R.D.**, Modeling Spray Atomization With the Kelvin-Helmholtz/Rayleigh-Taylor Hybrid Model, *Atomization Sprays*, 1999, 9(6), 623-650.
- 88. **Chuahy, F. D. F., and Kokjohn, S. L.,** Effects of the direct-injected fuel's physical and chemical properties on dual-fuel combustion, *Fuel*, 2017, 207(1), 729-740.
- 89. **Han, Z., and Reitz, R. D.**, Turbulence Modeling of Internal Combustion Engines Using RNG k-ε Models, *Combust. Sci. Technol.*, 1995, 106(4), 267-295.
- 90. **Munnanur**, A., Droplet Collision Modeling In Multi-Dimensional Engine Spray Computations, PhD Thesis in Mechanical Engineering, University of Wisconsin-Madison, 2007.
- 91. **O'Rourke, P.J., and Amden, A.A.**, A Spray/Wall Interaction Submodel For The KIVA-3 Wall Film Model, *SAE Technical Paper 2000-01-0271*, 2000.
- 92. **Deb, K., Pratap, A., Agarwal, S., and Meyarivan, T.**, A Fast and Elitist Multiobjective Genetic Algorithm: NSGA-II, *IEEE Transactions on Evolutionary Computation*, 2002, 6(2), 182-197.
- 93. **Dempsey, A.B.,** Dual-Fuel Reactivity Controlled Compression Ignition (RCCI) with Alternative Fuels, *PhD Thesis in Mechanical Engineering, University of Wisconsin- Madison*, 2013.
- 94. **Tiry, M.,** High Load Reactivity Controlled Compression Ignition (RCCI) Combustion, *MS Thesis in Mechanical Engineering, University of Wisconsin- Madison*, 2015.

- 95. **Vishwanathan, G., and Reitz, R. D.,** Development of a Practical Soot Modeling Approach and its Application to Low-Temperature Diesel Combustion, *Combustion Science and Technology*, 2010, 182(8), 1050-1082.
- 96. **Slavinskaya, N. A., Riedel, U., Dworkin, S. B., Thomson, M. J.,** Detailed numerical modeling of PAH formation and growth in non-premixed ethylene and ethane flames, *Combust. Flame*, 2012, 159(3), 979-995.
- 97. **Goodwin, D.G., Harry K., Moffat, and Speth, L.R.,** Cantera: An object- oriented software toolkit for chemical kinetics, thermodynamics and transport processes.
- 98. **Kokjohn, S., Hanson, R., Splitter, D., Kaddatz, J. et al.,** Fuel Reactivity Controlled Compression Ignition (RCCI) Combustion in Light- and Heavy-Duty Engines, *SAE Int. J. Engines*, 2011, 4(1), 360-374.
- 99. **Reitz, R.D., and Duaraisamy, G.,** Review of high efficiency and clean reactivity controlled compression ignition (RCCI) combustion in internal combustion engines, *Progress in Energy and Comb. Sci.*, 2015, 46(1), 12-71.
- 100. Kavuri, C., and Kokjohn, S.L., Computational Study to Identify Feasible Operating Space for a Mixed Mode Combustion Strategy: A Pathway for PCI High-load Operation, ASME ICEF 2017-3668, 2017.
- 101. **Lopez, A.H., Benajes, J., Novella, R., Pastor, J.M., and Kokjohn, S.L.,** Computational Optimization of the Combustion System of a Heavy Duty Direct Injection Diesel Engine Operating with Dimetyl-Ether, *Fuel*, 2018, 218, 127-139.
- 102. **Pei, Y., Shan, R., Som, S., Lu, T., et al.,** Global Sensitivity Analysis of a Diesel Engine Simulation with Multi- Target Functions, *SAE Technical Paper 2014-01-1117*, 2014.
- 103. **Kodavasal, J., Pei, Y., Harms, K., Ciatti, S., et al.,** Global Sensitivity Analysis of a Gasoline Compression Ignition Engine Simulation with Multiple Targets on an IBM Blue Gene/Q Supercomputer, *SAE Technical Paper 2016-01-0602*, 2016.
- 104. **Pal, P., Probst, D., Pei, Y., Zhang, Y., et al.,** Numerical Investigation of a Gasoline-Like Fuel in a Heavy-Duty Compression Ignition Engine Using Global Sensitivity Analysis, *SAE Int. J. Fuels Lubr.*, 2017, 10(1), 56-68.
- 105. **Zhou, D. Y., Davis, M. J., and Skodje, R. T.,** Multitarget Global Sensitivity Analysis of n-Butanol Combustion, *The Journal of Physical Chemistry A*, 2013, 117, 3569-3584.
- 106. **Nithyanandan, K., Hou, D., Major, G., and Lee, C.,** Spray Visualization and Characterization of a Dual-Fuel Injector using Diesel and Gasoline, *SAE Int. J. Fuels Lubr.*, 2014, 7(1), 144-158.
- 107. **Kenney, T.E., Gardner, T.P., and Low, S.S. et al.**, Overall Results: Phase I Ad Hoc Diesel Fuel Test Program, *SAE Technical Paper 2006-01-1145*, 2001.
- 108. Cooper, B., Penny, I., and Beasley, M. et al., Advanced Diesel Technology To Achieve Tier 2 Bin 5 Emissions Compliance in US Light-Duty Diesel Applications, *SAE Technical Paper 2006-01-1145*, 2006.
- 109. **Kaddatz, J., Andrie, M., Reitz, R. D., and Kokjohn, S. L.,** Light-Duty Reactivity Controlled Compression Ignition Combustion Using a Cetane Improver, *SAE Technical Paper 2012-01-1110*, 2012.

- 110. **Ra, Y., Loeper, P., Andrie, M., Krieger, R., Foster, D.E., Reitz, R.D., and Durret, R.**, Gasoline DICI Engine Operation in the LTC Regime Using Triple-Pulse Injection, *SAE Int. J. Engines*, 2012, 5(3), 1109-1132.
- 111. **Paz, J., and Staaden, D.,** Gasoline Compression Ignition Operation of a Heavy-Duty Engine at High Load as a Pathway to Lower Engine-Out Soot Emissions, *SAE Technical Paper*, 2018 (submitted).
- 112. **O'Connor, J., and Musculus, M.,** Post Injections for Soot Reduction in Diesel Engines: A Review of Current Understanding, *SAE Int. J. Engines*, 2013, 6(1), 400-421.
- 113. **Yun, H., and Reitz, R. D.,** An Experimental Investigation on the Effect of Post-Injection Strategies on Combustion and Emissions in the Low-Temperature Diesel Combustion Regime, *J. Eng. Gas Turb. Power*, 129(1), 279-286, 2007.
- 114. **Hotta, Y., Inayoshi, M., Nakakita, K., Fujiwara, K., and Sakata, I.,** Achieving Lower Exhaust Emissions and Better Performance in an HSDI Diesel Engine with Multiple Injection, *SAE Technical Paper 2005-01-0928*, 2005.
- 115. **O'Connor, J., and Musculus, M.,** Effects Of Exhaust Gas Recirculation And Load On Soot In A Heavy-Duty Optical Diesel Engine With Close-Coupled Post Injections For High-Efficiency Combustion Phasing, *Int. J. Eng. Res.*, 2014, 15(4), 421-443.

Appendix-A Light-Duty Cycle Optimization

In the literature review presented in Chapter 2, one of the main challenges identified with RCCI combustion was the low mode weighted gasoline percentage. Kokjohn and Reitz [7] investigated RCCI operation over a light-duty drive cycle and estimated that the RCCI engine would consume nearly equal proportions of gasoline and diesel fuel across the drive cycle. This is mainly an issue for light-duty applications since the need for two fuel tanks limits the practical application of the RCCI strategy. The high diesel quantity was primarily due to the lightest load operating point (2.3 bar IMEP and 1500 rev/min.) because the over-lean premixed charge of gasoline resulted in high UHC emissions. Marriott and Reitz [22] showed that low-load UHC emissions in a GCI engine could be reduced by stratifying the gasoline using late direct-injections. Accordingly, the present work will investigate the potential of direct-injection of gasoline and diesel fuel in improving the low-load combustion efficiency with RCCI combustion. The study performed by Kokjohn and Reitz [7] will be repeated by adding a DI gasoline to the injection strategy. A combination of CFD modeling and GA optimization will be used to identify the optimum operating strategy at each mode of the light-duty drive cycle. The goal of the study is to use direct-injection of gasoline to improve the mode weighted gasoline percentage of RCCI strategy. Addressing this issue could provide a pathway to practical implementation of RCCI engines.

A.1. Light-Duty Engine

In the following study, the engine modeled for the light-duty cycle optimization is the single cylinder version of the GM 1.9 L. four-cylinder light-duty engine. The modeling considered an injector capable of delivering two fuels through a single injector body, similar to the injector developed by QuantLogic Corporation [106]. The engine and injector specifications are shown in Table A-1. The computational grid used for the light-duty cycle simulations is shown in Figure A-1. The grid represents a 90° sector mesh, which includes two of the narrow-angle holes and one wide angle hole. The grid is made up of 34,080 cells at bottom dead center (BDC) with a cell size of 1.4 mm in the axial and the vertical directions and 1.5° in the azimuthal direction.

Table A-1. Engine and injector specification for the light-duty cycle optimization study.

Engine Specifications						
Displacement [L/cylinder]	0.48					
Bore x Stroke [mm]	82 x 90.4					
Connecting Rod [mm]	145.4					
Compression Ratio [-]	16.7:1					
Swirl Ratio [-]	1.5-4					
IVC [°ATDC]	-132					
EVO [°ATDC]	112					
Gasoline Injections						
Number of holes	8					
Hole Diameter [mm]	0.120					
Included Spray Angle [°]	90					
Diesel Injections						
Number of holes	4					
Hole Diameter [mm]	0.100					
Included Spray Angle [°]	140					

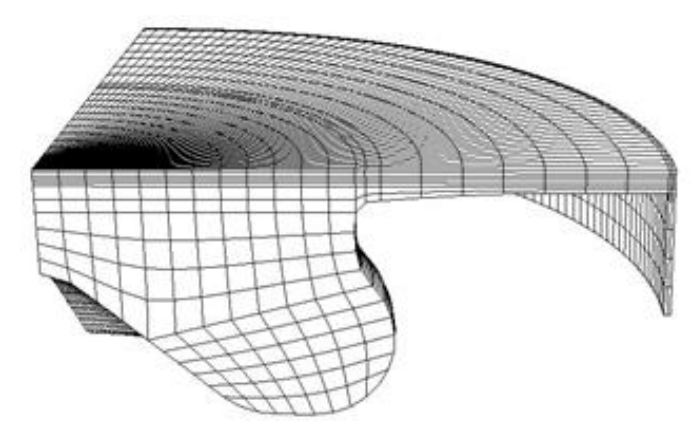


Figure A-1. Computational grid used for the light-duty cycle simulations.

A.2. Operating Conditions

The five operating points used by the ad hoc fuels working group [107] to evaluate fuel effects were chosen for the current study to approximate the light-duty drive cycle. The speed, load, and the relative weighting for drive cycle estimates of each mode are shown in Table A-2.

Table A-2. Operating conditions and the relative weights of each mode chosen for study.

Mode	Speed (rev/min.)	IMEP (bar)	Mode Weight
1	1500	2.3	400
2	1500	3.9	600
3	2000	3.3	200
4	2300	5.5	200
5	2600	9	75

A.3. Optimization Setup

The Adaptive Dual Fuel (ADF) injector enables stratification of the gasoline; however, it is not expected that gasoline stratification will always be desired. Therefore, the injection strategy was considered in the optimization by performing two sets of optimizations at each of the five operating modes. The injection strategies for both optimizations are shown in Figure A-2. The gasoline used for the study was 87 AKI gasoline. The design parameters for the optimization study are:

- 1. Fraction of the total fuel that is premixed (Premix);
- 2. Ratio of fuel injected in the first pulse to fuel injected in the second pulse (Inj1Frac) (Split Gasoline Injection Optimization Only);
- 3. Start of injection of the diesel injection (SOI-1);
- 4. Dwell time between the start of the diesel fuel injection and the start of the second gasoline injection (SOI-delta) (Split Gasoline Injection Optimization Only);
- 5. Exhaust gas re-circulation percent (EGR).

The ranges for each design parameter are shown in Table A-3. The ranges for SOI timings and EGR were chosen based on previous RCCI combustion research [7]. Note that the single gasoline injection RCCI optimization is a subset of the split gasoline injection RCCI optimization. That is, the split gasoline injection RCCI optimization parameters were allowed to vary across the design space such that all of the gasoline was premixed. This method of duplicating optimizations was chosen to ensure full coverage of the design space and enable comparisons between the optimum configurations for each injection strategy.

The engine parameters of Table A-3 were optimized at each of the five modes given in Table A-2 using the NSGAII code with the aim of minimizing six objectives: ISFC, NOx, soot, CO, UHC, and PPRR. The operating conditions are given in Table A-4. To fill the six-dimensional Pareto front, the GA's were allowed to run for 50 generations with 32 citizens per generation at each mode for each optimization.

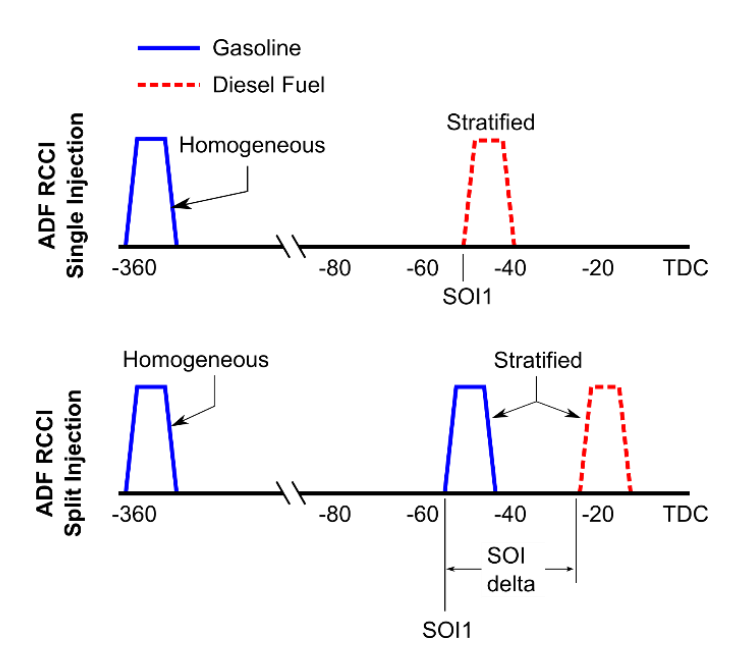


Figure A-2. Injection strategies considered in the two RCCI drive cycle optimizations. The simulations considered the port-injected or valve overlap injected fuel fully premixed at intake valve closure.

Table A-3. Range of variation allowed for each design parameter used in the GA optimization.

	Range				
Dogian Donomoton	Single Gasoline	Split Gasoline			
Design Parameter	Injection RCCI	Injection RCCI			
Premix (-)	0 to 1.00	0.25 to 1.00			
Inj1Frac (-)	N/A	0.00 to 1.00			
SOI-1 (ATDC)	-40 to 0	-50 to -30			
SOI-delta (CA)	N/A	10 to 30			
EGR (%)	0 to 50	0 to 45			

A.4. Results and Discussion

A.4.1. Light-Duty Drive Cycle Modes

The solutions for each injection strategy were combined, and the best cases were chosen as the cases with the lowest gross ISFC that meet the soot, NOx, and PPRR targets. NOx targets of 0.04, 0.1, 0.06, 0.24 and 0.32 g/kW-hr were chosen for modes 1-5, respectively, based on the work of Cooper et al. [108]. Unlike the NOx targets, soot targets in g/kW-hr were not available in the literature; thus, the optimum solutions were selected to have equal or lower soot values than the baseline CDC cases. For PPRR, from modes 1 to 3, a value of 5 bar/deg. was used as the upper limit and for modes 4 and 5, a PPRR of 10 bar/deg. was used as the upper limit. Based on these filters, an optimum case was chosen at each mode. The optimum cases were compared with the CDC cases from Kokjohn and Reitz [7]. The full comparisons are shown in Table A-4.

At mode 1 (2 bar IMEP and 1500 rev/min.) the split gasoline injection case (stratified gasoline) shows higher GIE than the single gasoline injection case (premixed gasoline). At modes 2 (3.9 bar IMEP and 1500 rev/min.) and 3 (3.3 bar IMEP and 2000 rev/min.), similar results are achieved using a single and a split gasoline injection. In the interest of simplicity, a single gasoline injection strategy is preferable for modes 2 and 3. At mode 4 (5.5 bar IMEP and 2300 rev/min.), the single gasoline injection strategy shows higher GIE and lower NOx emissions than the split injection strategy. At mode 5 (9 bar IMEP and 2600 rev/min.), both strategies show similar GIE, but the single gasoline injection strategy shows an order of magnitude lower NOx and soot emissions. These results suggest that the gasoline should be stratified at the lightest load conditions (mode 1) and made homogenous at higher loads.

Table A-4. Summary of best results from the optimization and comparison of the optimum RCCI results with CDC results of the corresponding mode. The emissions are shown on a gross indicated basis, and the GIE is defined as the (gross indicated work) / (fuel energy).

	Mode-1		Mode-2		Mode-3			Mode-4			Mode-5				
	Single Gas. RCCI	Split Gas. RCCI	CDC	Single Gas. RCCI	Gas.	CDC	Single Gas. RCCI	Split Gas. RCCI	CDC	Single Gas. RCCI	Gas.	CDC	Single Gas. RCCI	Split Gas. RCCI	CDC
Speed (rev/min.)	1500	1500	1500	1500	1500	1500	2000	2000	2000	2300	2300	2300	2600	2600	2600
IMEP (bar)	2	2	2	3.9	3.9	3.9	3.3	3.3	3.3	5.5	5.5	5.5	9	9	9
Total Fuel (mg/inj.)	5.3	5.3	5.3	9.6	9.6	9.6	8.8	8.8	8.8	14.5	14.5	14.5	20.9	20.9	20.9
Gasoline (Mass %)	65.3	86.2	0	92.1	90.9	0	95.8	92.5	0	89.4	92.6	0	93.0	71.6	0
Diesel Fuel (Mass %)	34.7	13.8	100	7.9	9.1	100	4.2	7.5	100	10.6	7.4	100	7.0	28.4	100
Premixed gasoline mass	65.3	28	0	92.1	85.9	0	95.8	87.8	0	89.4	62.6	0	93.0	67.4	0
Gasoline DI SOI (°ATDC)	N/A	-30.9	N/A	N/A	-30.8	N / A	N/A	-39.8	N/A	N/A	-36.7	N / A	N/A	-30.5	N / A
Diesel DI SOI (°ATDC)	-38.7	-14.6	-5.8/ 1.6	-38.5	-20.8	-7.2/ 0	-11.7	-22.2	-8.2/ 1.6	-23.9	-7.26	-11.7/ - 0.1	-1.57	-6.89	-15.4/ - 2.6
Inj1Frac	N/A	0.822	0.34	N/A	0.358	0.16	N/A	0.388	0.15	N/A	0.801	0.1	N/A	0.278	0.05
Inj. Pressure (bar)	330	330	330	400	400	400	500	500	500	500	500	780	500	500	1100
Intake Pressure (bar)	1	1	1	1.06	1.06	1.06	1.16	1.16	1.16	1.3	1.3	1.3	1.6	1.6	1.6
EGR (%)	17.5	31	47	41.5	41.9	45	20	16.4	46	48.5	43.9	29	48.2	44.4	19
						RES	ULTS								
GIE (%)	41.2	44.1	35.2	49.8	49.5	34.9	49.8	49.7	37.8	51.3	48.7	40.2	48.2	49.7	40
NOx (g/kW-hr)	0.01	0.04	0.74	0.02	0.04	0.23	0	0.01	0.56	0.18	0.3	2.06	0.04	0.3	3.89
Soot (g/kW-hr)	0.01	0.01	0.04	0.01	0.01	0.04	0.01	0.01	0.02	0.01	0.01	0.05	0.04	0.59	0.15
CO (g/kW-hr)	27.3	19.8	22.7	5.58	7.39	38	8.04	9.89	24.1	4.28	13.25	10.6	7.66	7.09	3.2
HC (g/kW-hr)	17.5	16.8	15.4	8.09	9.59	18.6	9.63	11.4	12.3	6.56	12.42	4.75	10.1	6.07	0.32
PPRR(bar/deg)	2.84	2.52	1.29	4.96	4.88	2.16	4.43	4.62	1.86	5.99	8.74	4.56	2.8	7.04	5.42

At the conditions studied, the primary benefit of DI gasoline is found at mode 1; thus, the discussion will focus on explaining the source of the benefit of stratified gasoline at the mode 1 conditions. Figure A-3 shows the GIE and combustion efficiency as a function of NOx emissions at mode 1 for the single and split injection cases. Direct-injecting part of the gasoline improves the combustion efficiency-NOx tradeoff. That is, at equal NOx levels, the combustion efficiency of the split gasoline injection case is 2% to 4% higher than the single gasoline injection case. Similarly, the GIE of the split gasoline injection case is ~4% higher than the single gasoline injection case at equal NOx levels.

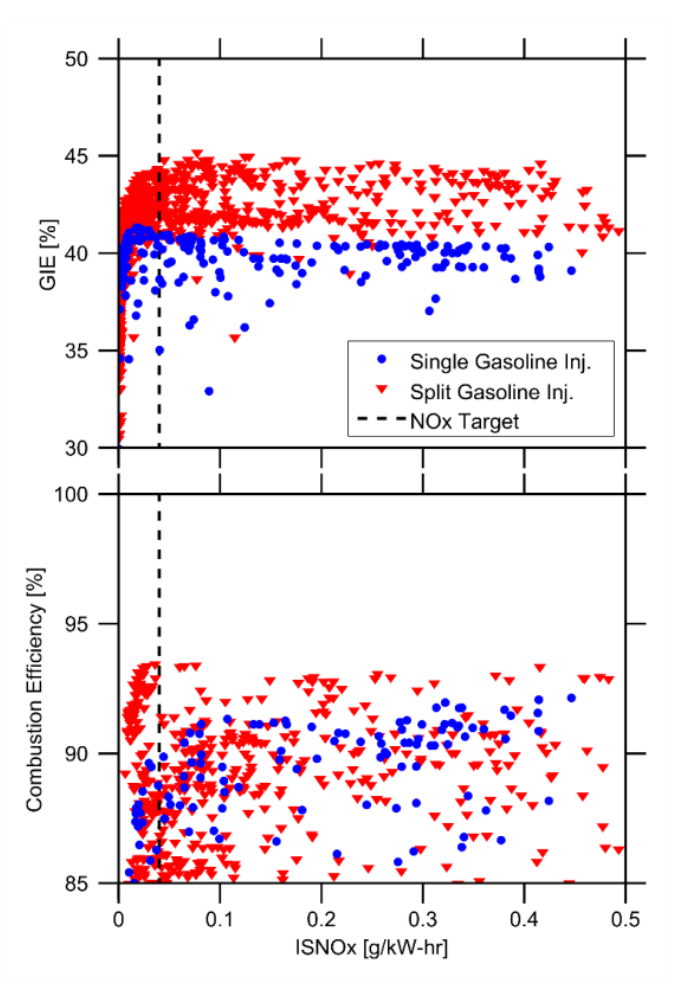


Figure A-3. GIE and combustion efficiency – NOx tradeoff for the optimization at Mode 1 (2 bar IMEP and 1500 rev/min.).

To evaluate the source of the efficiency improvement of split gasoline injection case at mode 1, the optimum mode 1 cases of the two RCCI strategies were analyzed. Figure A-4 shows the fuel energy flow for the two optimized cases. The optimum split injection strategy has a GIE of 44.2%, and the optimum

single injection strategy has a GIE of 41.2%. Both cases have identical incomplete combustion, but the split injection strategy has significantly lower wall heat transfer (WHT) losses than the single gasoline injection strategy. Thus, it appears that the improved GIE of the split gasoline injection case is at least partially due to reduced heat transfer losses.

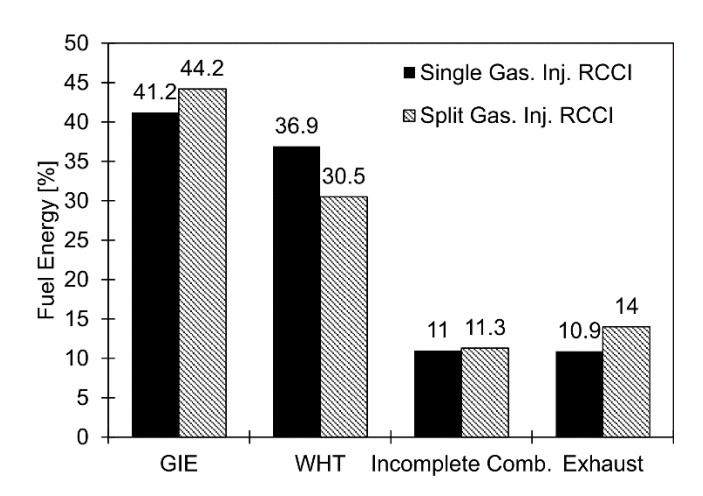


Figure A-4. Energy flow diagram for the optimum cases at Mode 1 (2 bar IMEP and 1500 rev/min.) with a single gasoline injection and split gasoline injection. All cases use DI of diesel fuel. The operating conditions are shown in Table A-4.

Figure A-5 shows the in-cylinder pressure and AHRR for the optimized cases. The optimum single gasoline injection strategy has a CA50 of -11.5 °aTDC and the optimum split gasoline injection strategy has a CA50 of -1.75 °aTDC. The advanced combustion phasing of the single injection strategy resulted in higher heat transfer losses and decreased work extraction efficiency (i.e., increased compression work). Of course, the combustion phasing of the single gasoline injection case could be retarded by increasing the gasoline percent to reduce heat transfer losses. To evaluate this approach, a third case was simulated where the operating conditions were set equal to the split gasoline injection case, but the DI gasoline was premixed. The in-cylinder pressure and AHRR for this case are included in Figure A-5. When the directinjected gasoline is premixed, ignition occurs at the same time as the split gasoline injection case. However, the premixed gasoline does not achieve complete combustion, and the results show a GIE of only 30% with a combustion efficiency of 55% (i.e., near misfire). These results show that when the gasoline is fully premixed, the combustion phasing must be advanced to yield temperatures high enough to oxidize the overlean ($\Phi = 0.15$) premixed gasoline. This overly advanced combustion phasing causes a fuel efficiency

penalty. Conversely, when the gasoline is stratified, the local Φ is high enough to achieve similar combustion efficiency at an optimal combustion phasing.

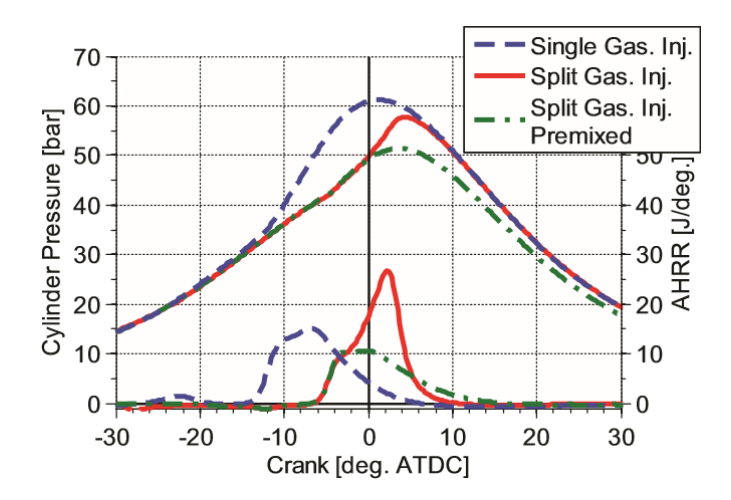


Figure A-5. Mode 1 in-cylinder pressure and AHRR for the optimum single gasoline injection case, optimum split gasoline injection case, and split gasoline injection case with the direct-injected gasoline premixed.

Figure A-6 shows the contours of in-cylinder Φ at several times prior to ignition for the single gasoline injection and split gasoline injection RCCI cases.

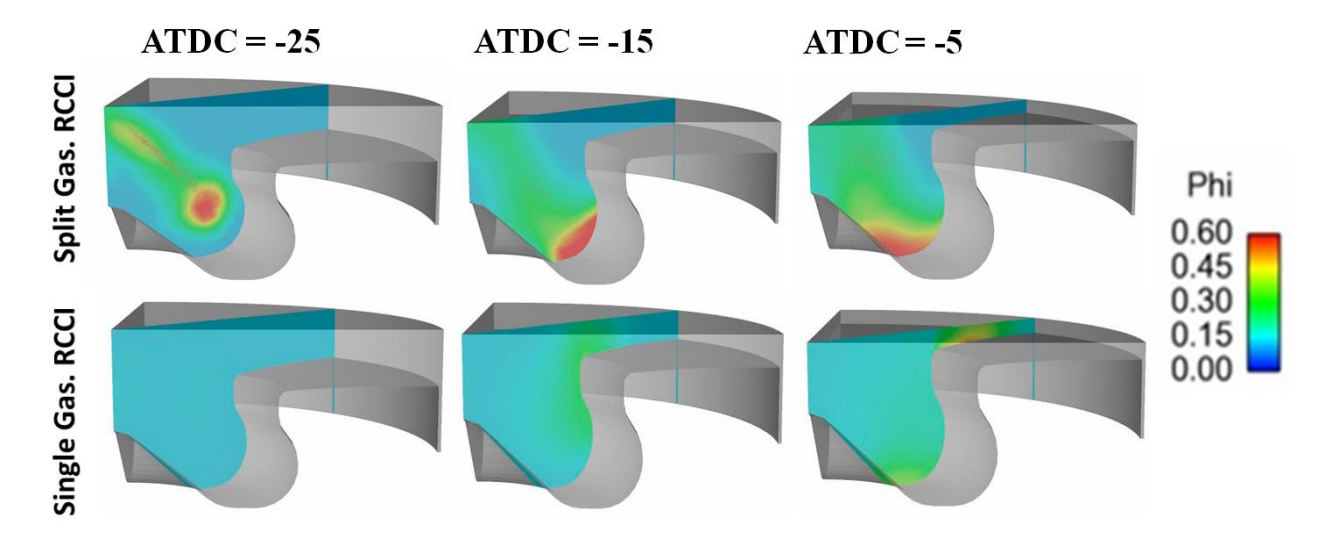


Figure A-6. Contours of in-cylinder Φ for the single gasoline injection and split gasoline injection RCCI cases at Mode 1. The contours are shown on a cut-plane coincident with the spray axis.

For the split injection case, the gasoline direct-injection begins at -30.9 °aTDC and ends at -25.8 °aTDC. The first image, -25 °aTDC, shows the gasoline injection event. Direct-injecting the gasoline with the narrow spray angle helps keep the gasoline within the piston bowl, forming a mixture rich enough to achieve complete combustion. At around -15 °aTDC, the diesel fuel injection event occurs and acts as the

ignition source. The late injection timings of both the gasoline and diesel fuel create relatively high Φ zones and ensure stable combustion. For the single gasoline injection case, the gasoline is fully premixed at a Φ of ~0.15. The diesel fuel injection at -38.7 °aTDC serves as an ignition source. However, the overly lean charge resulting from the high level of premixed fuel requires overly advanced combustion phasing to oxidize the premixed fuel, reducing thermal efficiency.

In addition to improved GIE, the optimum split injection strategy uses a much higher gasoline percentage than the optimum single injection strategy (86.2% and 65.3%, respectively). As discussed in Chapter 2, utilizing a high gasoline percentage is favorable to offset the transportation energy imbalance. To understand this trend, the impact of gasoline percentage on the optimum results was evaluated using the COSSO method [61]. Figure A-7 shows the effects of gasoline percentage on GIE, combustion efficiency, and NOx emissions. For both cases, the gasoline mass percentage has a strong impact on GIE due to its impact on combustion phasing. That is, increasing the gasoline percentage retards combustion phasing and decreasing the gasoline percentage advances combustion phasing. As the combustion phasing is retarded by increasing the gasoline percentage, NOx emissions, and combustion efficiency decrease. The optimum gasoline percentage at this operating condition is a balance between NOx emissions and combustion efficiency. The relatively low gasoline quantity for the single gasoline injection case is due to the need to advance combustion phasing to increase in-cylinder temperatures to enable oxidation of CO and UHC. Recall that the combustion phasing of the optimum single gasoline injection case is -11.5 °aTDC. If the combustion phasing is retarded beyond this value, the combustion efficiency deteriorates. Adding stratification by direct-injecting a portion of the gasoline (split gasoline injection), increases the optimum gasoline percentage to near 90%. The higher gasoline percentage is made possible by the improved combustion efficiency resulting from the stratified gasoline charge. That is, by confining the gasoline to the piston bowl, the gasoline quantity can be set to a higher value than the single injection case. This allows operation with combustion phasing near TDC because overly advanced combustion phasing is not required anymore to oxidize CO and UHC.

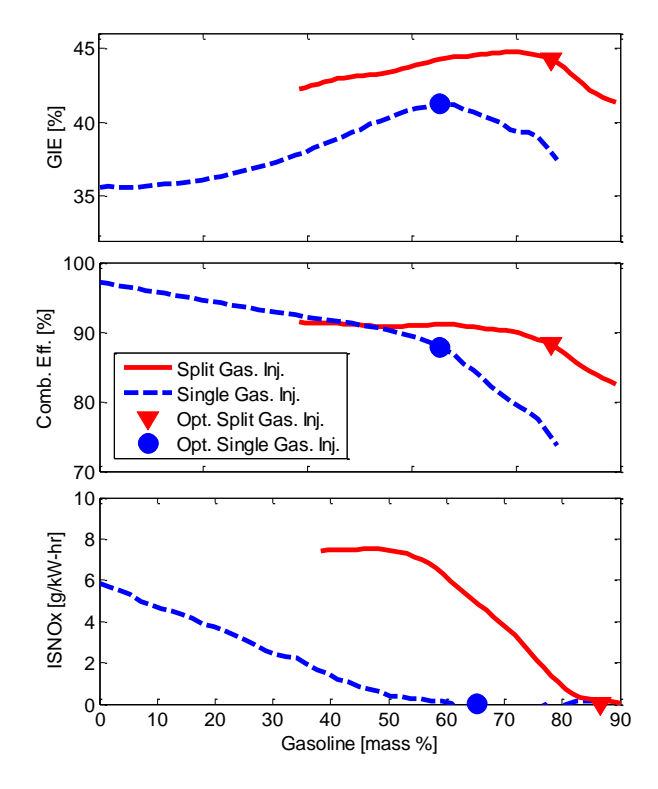


Figure A-7. Effect of gasoline mass on GIE, combustion efficiency, and NOx emissions at Mode 1 calculated using the COSSO method. The lines show COSSO predicted response and the symbols show the optimum solutions from the CFD study.

A.4.2. Cycle Averaged Emissions

Cycle averaged emissions and GIE are calculated from the optimum ADF-RCCI cases and compared to the baseline CDC case. As discussed, the optimum ADF-RCCI case uses a split gasoline injection at mode 1 and a single gasoline injection at modes 2 through 5. Cycle averaged emissions and GIE are calculated using a weighted average given by

$$E_{cycle} = \frac{\sum_{imode=1}^{5} E_{imode} Weight_{imode}}{\sum_{imode=1}^{5} Weight_{imode}},$$
(32)

where E_{cycle} is the cycle-averaged value of emissions or performance, E_{imode} is the value of emissions or performance at each operating mode, and $Weight_{imode}$ is the mode-weighting factor shown in Table A-2. Figure A-8 shows the comparison of cycle averaged GIE, NOx, and soot emissions for the optimum ADF-RCCI and CDC cases. Compared to CDC, the ADF-RCCI strategy gives a cycle-averaged improvement of 33% in GIE, and a reduction in NOx and soot emissions of 95% and 75%, respectively.

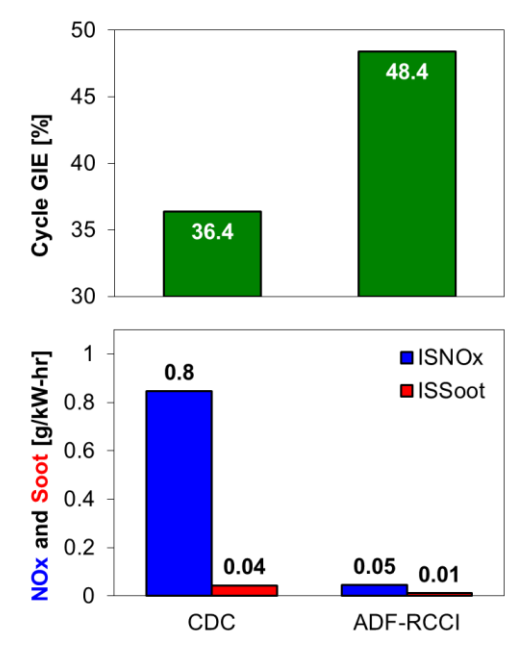


Figure A-8. Cycle averaged performance and emissions for RCCI combustion using DI gasoline (ADF-RCCI) and diesel fuel and the baseline conventional diesel combustion case.

The cycle averaged gasoline percentage for the optimized ADF-RCCI case of the present work, and the optimum case of Kokjohn and Reitz [7] were compared. The cycle averaged gasoline percent of the present work is increased from 58% to 91% by using a lower octane gasoline and by direct-injecting the gasoline at the light-load condition. The importance of enabling RCCI operation on a high gasoline percentage must be discussed. Therefore, we will assume a vehicle operating at an average of 50 miles per gallon over the light-duty drive cycle. With 91% by mass of the fuel supplied as gasoline, the total diesel fuel consumed over 5,000 miles of driving is approximately 8.4 gallons. Thus, if a standard sized diesel fuel tank were used, the diesel fuel would only need to be filled at oil change intervals. In comparison, if the vehicle operated with the same efficiency with a gasoline percentage of 58% by mass, the diesel fuel tank would need to be over 40 gallons or filled between oil changes. Further, Splitter et al. [37] and Kaddatz et al. [109] demonstrated RCCI combustion by doping DI gasoline with ~3% by volume of a cetane-improving additive. When operating under the conditions specified in this work, the additive tank size for a 5,000-mile fill interval would be only 0.27 gallons.

A.4.3. High-Speed-High-Load Optimization

The previous section demonstrated high efficiency and low emissions over conditions representative of a light-duty drive cycle; however, the engine must be able to achieve low emissions operation at full load conditions to be a viable combustion system. Accordingly, another optimization was performed at a high-speed-high-load (16 bar, 2500 rev/min.) condition. Because GCI combustion has shown promising results at high-load conditions [26], a GCI strategy was chosen for this load point. The operating conditions were selected based on the GCI model validation experiments [110]. The ranges of each input parameter for the study are shown in Table A-5.

Table A-5. Range of variation allowed for each design parameter in the high-load GCI optimization.

Design Parameter	Range
Premix (-)	0 to 1.00
Inj1Frac (-)	0 to 1.00
SOI-1 (ATDC)	-50 to 0
SOI-2 (ATDC)	-50 to 0
EGR (%)	0 to 50

From the optimization results, a best case was chosen as the case with the lowest gross ISFC with NOx below the mode 5 NOx target of 0.32 g/kW-hr and a PPRR below 15 bar/deg. Table A-6 shows the design parameters and results for the optimum case. The optimum case has a GIE of 46.4% with soot and NOx emissions of 0.08 g/kW-hr and 0.02 g/kW-hr, respectively, while meeting the PPRR constraint of 15 bar/deg. The high amount of premixed gasoline and EGR helps maintain the soot and NOx emissions to low values while achieving a high GIE. Thus, operation over the entire load range was demonstrated by blending the benefits of RCCI at low-load and mid-load with the benefits of GCI at full load conditions.

Table A-6. Optimum operating conditions for GCI combustion 16 bar IMEP and 2500 rev/min.

Design Parameter	Optimum				
Premix (-)	0.865				
Inj1Frac (-)	0.454				
SOI-1 (ATDC)	-44.68				
SOI-2 (ATDC)	-13.23				
EGR (%)	49.45				
Results					
GIE (%)	46.37				
NOx (g/kW-hr)	0.02				
Soot (g/kW-hr)	0.08				
PPRR (bar/deg)	14.62				
Inj1Frac (-) SOI-1 (ATDC) SOI-2 (ATDC) EGR (%) Results GIE (%) NOx (g/kW-hr) Soot (g/kW-hr)	0.454 -44.68 -13.23 49.45 46.37 0.02 0.08				

A.5. Conclusions

RCCI combustion using premixed gasoline and DI diesel fuel has shown promising results over a wide range of operating conditions. However, operation at low-loads has proven difficult. The results shown in this appendix address this issue by using an adaptive dual-fuel injector capable of direct-injecting gasoline and diesel fuel in a single cycle. A computational optimization study was conducted to identify the optimum fueling strategies for RCCI combustion at conditions representative of the light-duty drive cycle. The results showed that DI of gasoline is preferable at the lightest load conditions, but no benefit is found at mid-load conditions. The benefit of DI gasoline at light load conditions was shown to be due to the avoidance of overly lean regions that require overly advanced combustion phasing to achieve complete combustion. At light load conditions, direct-injecting gasoline improved the peak GIE from 41% to over 44%. A light-duty drive cycle RCCI strategy was demonstrated that enables operation on a drive cycle weighted average of 91% gasoline. In comparison, previous RCCI research [7] showed a drive cycle weighted average of 58% gasoline. The high drive cycle averaged gasoline quantity enables the second fuel (diesel fuel in the present work) to be treated as an additive with the potential to be filled at oil change intervals. At high-load conditions, direct-injecting gasoline enables a transition to GCI operation, enabling full load range coverage with high efficiency and low NOx and soot emissions. Enabling dual fuel operation at a high gasoline percentage provides a pathway to address the transportation fuel imbalance and achieve high efficiency, low emissions combustion.

Appendix-B Investigation of Soot Production from a Load Extension Injection

In Chapter 6, an optimization study was performed considering low-load-high-speed and high-load-low-speed operating conditions simultaneously. The study yielded feasible operating strategies for both the operating conditions. However, for the optimum operating strategy at high-load-low-speed, soot emissions were found to be reasonably high (~2 g/kg-f). The AHRR was a combination of a premixed main heat release (premixed gasoline ignited by a diesel fuel injection) followed by a mixing-controlled heat release from a load extension injection of gasoline. Investigation of the combustion characteristics of this 'mixed mode' strategy revealed that the main source of soot emissions was the load-extension injection. Accordingly, this appendix section will focus on understanding the soot formation and mitigation mechanisms from the load-extension injection of the mixed mode combustion strategy.

The mixed mode strategy at the high load operating condition resulted in high soot emissions. Consequently, this study will be performed at a mid-load condition of 13 bar and 1300 rev/min. so that the entire design space of interest for the load-extension injection can be covered, without causing issues of clogging in the soot filter. A detailed CFD analysis applying the results found in this study to high-load-low-speed conditions can be found in Kavuri et al. [100].

B.1. Operating Conditions and Computational Study Setup

The study uses engine experiments and CFD modeling to understand the effects of load extension injection SOI timing, EGR rate, and injection pressure on soot emissions. The engine experiments presented in this study were performed by Mike Tiry [94] and were guided by the CFD effort presented here. The operating conditions and parameters are shown in Table B-1.

For each parametric study, a premixed charge of gasoline and n-heptane was created using injections during the intake stroke. The quantity of gasoline and n-heptane was set to reach a load of 10 bar gross IMEP from the premixed fuel alone. A load extension injection consisting of 46 mg of gasoline was added at -10 °aTDC to reach a load of 13 bar gross IMEP. The ratio of gasoline and n-heptane in the premixed fuel was adjusted to set the 50 percent burn location of the premixed heat release to TDC. The load extension injection timing was swept from -10 °aTDC to +30 °aTDC in steps of 5 °CA while holding

all other parameters constant. The SOI timing mentioned is the start of the injector current and not the actual start of fuel delivery. Rate of injection bench measurements show a delay of 5 °CA between the start of injector current and the start of fuel delivery at these conditions.

Table B-1. Operating conditions for each parametric study.

Table B-1. Operating conditions for each parametric study.							
Parameter \ Effect	Load Extension	EGR	Injection				
Investigated	SOI	Lok	Pressure				
Nominal gross IMEP (bar)	13						
Speed (rev/min.)		1300					
Intake Temperature (°C)		60					
Coolant Temperature (°C)		90					
EGR Temperature (°C)		60					
Intake Pressure (bar)		2.31					
Load Extension SOI Timing (°ATDC)	-10 to +30						
Load Extension Mass (mg/cycle)	46						
Total Fuel Mass (mg/cycle)	175	175, 165	175				
EGR Rate (%)	46	30, 46	46				
Total Fuel Energy (kJ/cycle)	7.53	7.53, 7.10	7.53				
Load Extension Fuel Energy (kJ/cycle)	1.97	1.97	1.97				
Mole Fraction (O ₂ , N ₂ , CO ₂ , H ₂ O)	0.11, 0.76, 0.057, 0.064	(0.11,0.76, 0.057,0.064), (0.17, 0.77, 0.026, 0.029)	0.11, 0.76, 0.057, 0.064				
Injection Pressure (bar)	1000	1000	1000, 1500				
Mass Fraction of n-C ₇ H ₁₆ Premixed Fuel	0.1435	0.1435, 0.0279	0.1435, 0.1219				
Total Gasoline Mass (mg/cycle)	158	158, 160	158, 161				
Total n-heptane Mass (mg/cycle)	17	17, 5	17, 14				

B.2. Results

In this section, the results from the experimental study will be presented. The CFD model will be used to explain the experimentally observed results. Thorough validation of the CFD model with the experimental data from this study can be found in Chapter 3.

B.2.1. Effect of Load Extension SOI Timing

The effect of the load-extension injection SOI timing is evaluated for each parametric study. However, the general trends are found to be similar for all EGR, injection pressure, and fuel combinations. Accordingly, only the 46% EGR case at an injection pressure of 1000 bar is examined in detail. Figure B-

1 shows the measured and model predicted soot trends for this case as a function of load extension SOI timing.²

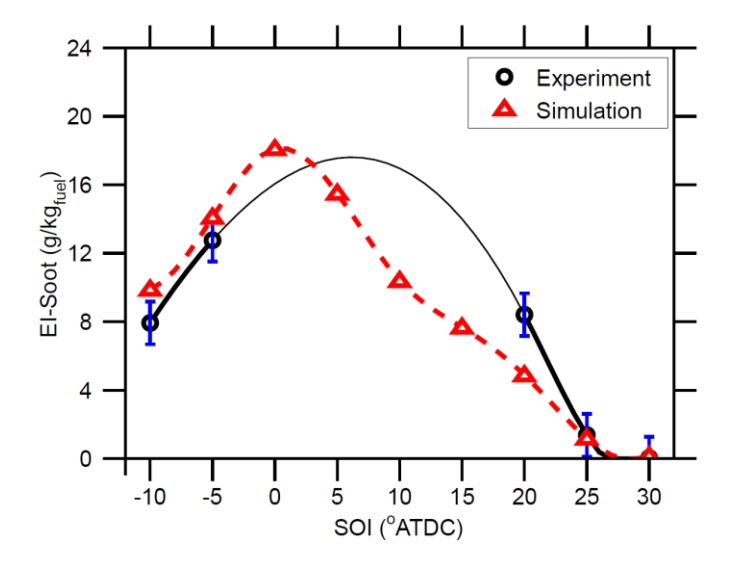


Figure B-1. Measured (○) and model predicted (△) soot emissions for EGR-46% and an injection pressure of 1000 bar using E0 fuel as a function of load extension injection SOI timing. The measured and simulation data are shown in symbols, and the lines show spline interpolation. The error bars are based on a 97.5% confidence interval from multiple repeats for the experiments with EGR-30% and an injection pressure of 1000 bar.

The model accurately captures the trends and magnitudes of soot emissions across the range of SOI timings. Though there was no measured soot data between -5 °aTDC and +20 °aTDC, simulations were performed at these intermediate SOI timings, and the results confirm that the experimental trend line shown is a reasonable approximation. The trend follows a downward parabola type profile. At the early SOI timings, soot increases as the injection timing is moved closer to TDC. It is known that soot formation is strongly dependent on the local Φ and temperature. Accordingly, the trends in soot are explained by investigating the state of the in-cylinder charge in Φ -T coordinates.

Figure B-2 shows the Φ-T diagrams for the cases with SOI timings of -10 °aTDC and -5 °aTDC at several crank angles after the start of injection (°ASOI). For the case with SOI at -10 °aTDC, the ignition delay is ~5 °CA. However, when the SOI timing is retarded to -5 °aTDC, the ignition delay shortens to ~0 °CA due to the elevated temperature and pressure resulting from the energy release of the premixed fuel.

² Note that measurements from SOI timings between -5 °aTDC and +20 °aTDC at this EGR and injection pressure could not be collected due to excessively high soot emissions that resulted in damage to laboratory equipment.

The longer ignition delay for the SOI of -10 °aTDC case allows more air to be entrained and forms a charge that is better mixed than the SOI of -5 °aTDC case. The increased air entrainment lowers the Φ and causes a shorter residence time in the soot formation zone and, thus, produces lower soot than the SOI of -5 °aTDC case. This analysis shows that the soot production for the early load extension SOI timings (i.e., SOI's of -10 °aTDC and -5 °aTDC) is highly dependent on mixing time. Increasing the mixing time increases the air entrainment, leading to lower soot levels.

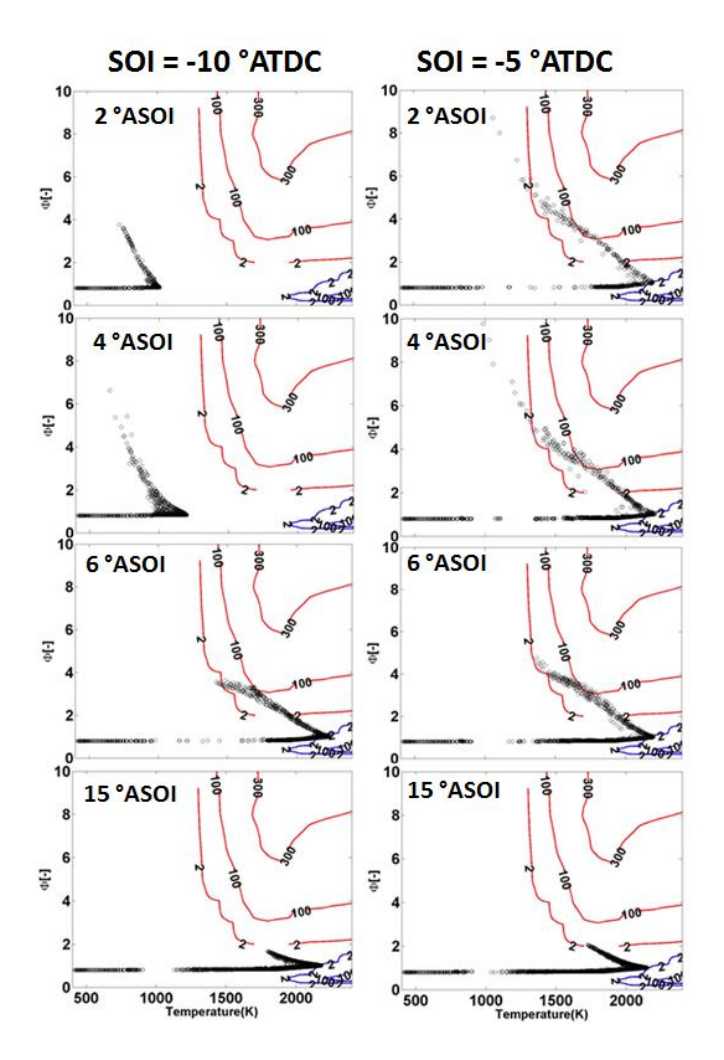


Figure B-2. Φ-T plots of the in-cylinder mixture at various crank angles after start of injection (°ASOI) for two load extension injection SOI timings at EGR-46% and injection pressure of 1000 bar. The symbols show the equivalence ratio, and temperature in each computational cell and the lines show NOx (lower right on each diagram) and soot (upper right on each diagram) islands calculated using HCCI simulations at the operating conditions of the present study.

The second trend that is noticed from Figure B-1 is that, as the load-extension injection timing is delayed beyond 20 °aTDC, the soot emissions begin to decrease. Figure B-3 shows the Φ -T diagrams for

the load-extension SOI timings of 20 °aTDC and 30 °aTDC for an EGR of 46% at several crank angles after the start of combustion (°ASOC) of the premixed fuel.

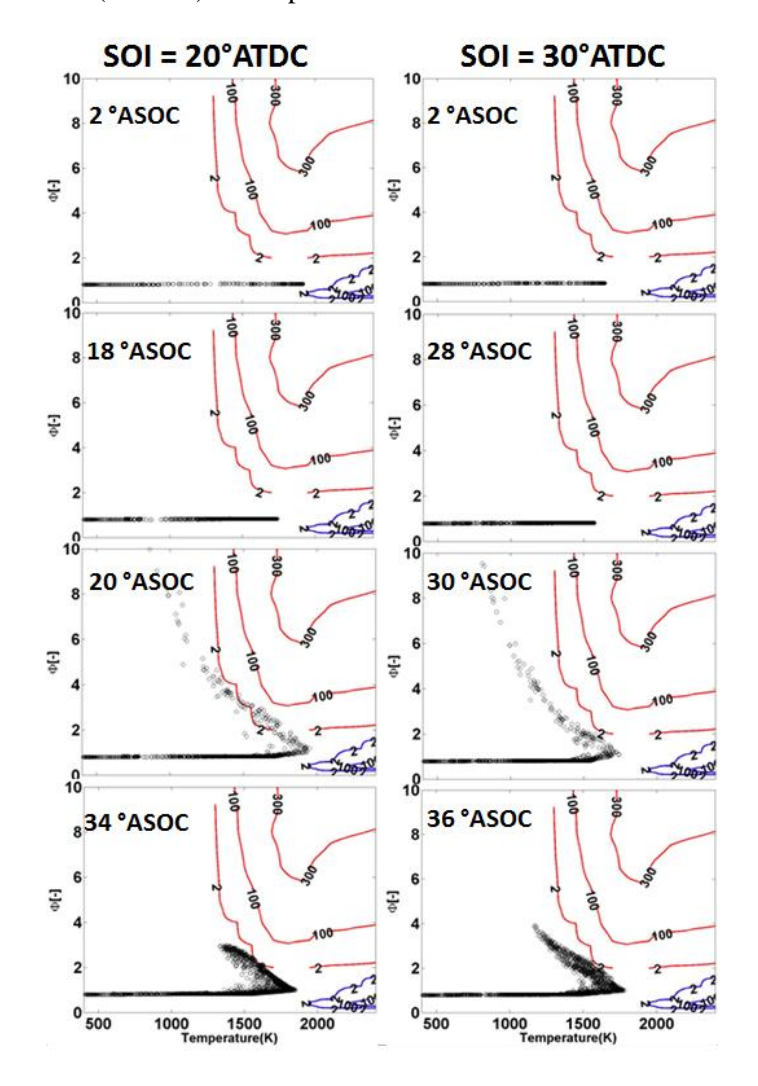


Figure B-3. Φ-T diagrams of the in-cylinder mixture at various crank angles after start of combustion (°ASOC) of premixed fuel for two load extension injection SOI timings at EGR-46% and an injection pressure of 1000 bar. The symbols show the equivalence ratio, and temperature in each computational cell and the lines show NOx (lower right on each diagram) and soot (upper right on each diagram) islands calculated using HCCI simulations at the operating conditions of the present study.

The crank angle location of 10% of total heat release (CA10) was used as a definition for start of combustion. As the injection event is delayed after the primary heat release, the in-cylinder temperature begins to decrease. For the case with an SOI of 30 °aTDC, though the in-cylinder Φ 's are high, the charge does not enter the soot formation zone due to the low combustion temperature. Advancing the SOI timing to 20 °aTDC results in higher temperatures and causes the charge to enter the soot formation zone. This

discussion explains the trend of increasing soot with advancing SOI timing for the cases with SOI timings well after TDC.

The trends in soot emissions with load extension SOI timing are further explained by examining the soot formation and oxidation. Figure B-4 shows the mass of soot formed and oxidized for the load-extension injection SOI timing sweep at an EGR rate of 46% and an injection pressure of 1000 bar.

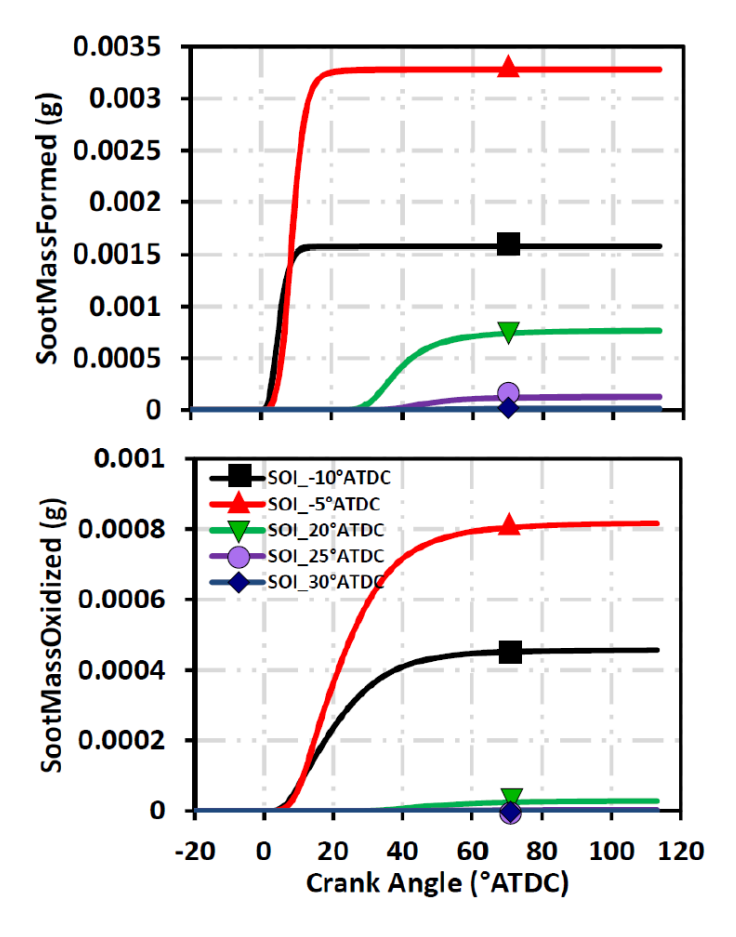


Figure B-4. Soot mass formed and oxidized for the load-extension injection SOI timing sweep at EGR-46% and an injection pressure of 1000 bar.

For the case with an SOI timing at -10 °aTDC, soot is rapidly formed during the combustion event (i.e., in the crank angle interval between TDC and 10 °aTDC) and soot formation ends around 10 °aTDC. Soot oxidation begins shortly after the initial soot formation, but proceeds at a slower rate and continues until approximately 60 °aTDC. When the injection timing is retarded to -5 °aTDC, more soot is formed during the combustion event due to the shorter ignition delay and higher local Φ. The higher mass of soot formed leads to more soot mass oxidized. However, the increase in soot oxidation does not make up for the

increase in soot formed resulting in an increase in the net soot mass (i.e., the mass of soot formed minus the mass of soot oxidized) (see Figure B-4). As the injection timing is further delayed into the expansion stroke, the mass of soot formed decreases due to the decreased temperature. However, because the primary combustion event consumes much of the available oxygen and the temperatures are low, most of the soot formed for the later SOI timings persists till the end of the cycle. Though load extension injections with late SOI timings have less access to oxygen and lower soot oxidation rates, they end up having lower net soot emissions than the load-extension injections with early SOI timings. This result indicates that the soot emissions of the late SOI cases do not depend on oxygen availability, but solely on the in-cylinder temperature.

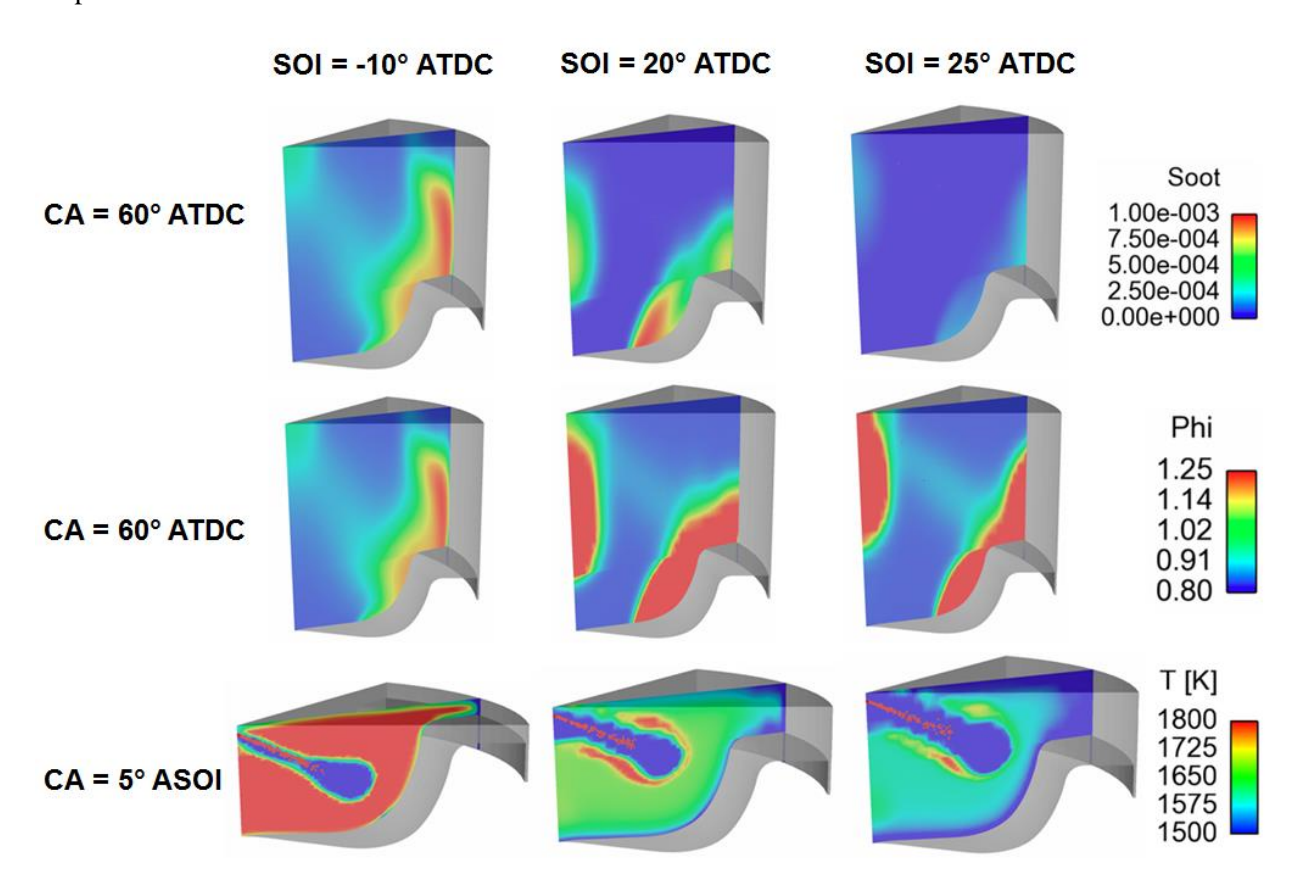


Figure B-5. In-cylinder images of soot, Φ , and temperature for the load-extension injection SOI timings of -10 °aTDC, 20 °aTDC and 25 °aTDC at EGR-46% and injection pressure of 1000 bar.

Figure B-5 shows in-cylinder images of soot, Φ , and temperature for the load-extension injection SOI timings of -10 °aTDC, 20 °aTDC, and 25 °aTDC at 46% EGR and injection pressure of 1000 bar. The images for soot and Φ are shown at a crank angle location of 60 °aTDC to show the correlation between

the location of soot and high Φ zones. The temperature contours are shown at 5 °CA after start of injection (°ASOI) to show the impact of temperature during the secondary combustion event. For all three SOI timings, soot is formed in the fuel rich zones. However, as the SOI timing is delayed beyond TDC, the incylinder soot produced decreases despite the presence of regions with Φ higher than the case with SOI timing before TDC. Comparing the temperature contours for the corresponding cases, it is seen that, for the SOI timings of 20 °aTDC and 25 °aTDC, the in-cylinder temperatures during combustion are significantly lower than the SOI of -10 °aTDC case. Hence, despite the existence of fuel-rich regions, these post TDC injection cases do not form as much soot as the pre-TDC injection case because the low temperatures inhibit soot formation. This reconfirms the result that soot emissions of the late SOI cases do not depend on oxygen availability, but solely on the in-cylinder temperature.

B.2.2. Effect of EGR

Figure B-6 shows the measured and predicted soot emissions as a function of the load-extension injection SOI timing for 30% and 46% EGR cases at an injection pressure of 1000 bar.

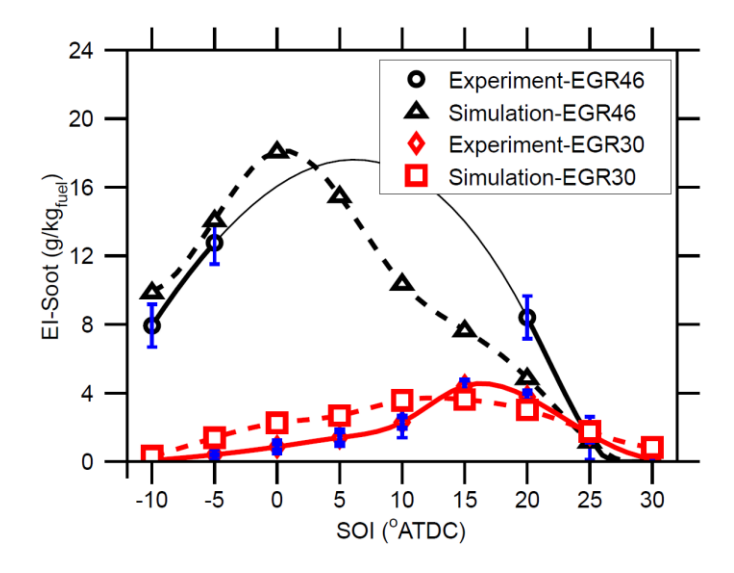


Figure B-6. Measured (○,○) and predicted (△,□) soot emissions for EGR-46% and EGR-30% using E0 fuel as a function of load extension SOI timing at an injection pressure of 1000 bar. The measured and simulation data are shown in symbols, and the lines show spline interpolation. The error bars show 97.5% confidence intervals for the EGR-30% from randomly ordered repeats on different days.

Decreasing the EGR from 46% to 30% resulted in an order of magnitude reduction in soot emissions at the early SOI timings. The magnitude of the soot reduction with decreased EGR decreases as the SOI timing is delayed beyond TDC. As shown earlier, the soot emissions for early and middle SOI

timings are dependent on oxygen availability. Due to the increased oxygen availability at 30% EGR, the soot formation reduces significantly, resulting in lower soot emissions than the 46% EGR cases. To illustrate this, Figure B-7 shows the CFD predictions of soot mass formed and oxidized for the 30% and 46% EGR cases. The reduced formation and increased oxidation rates at the lower EGR rate are evident.

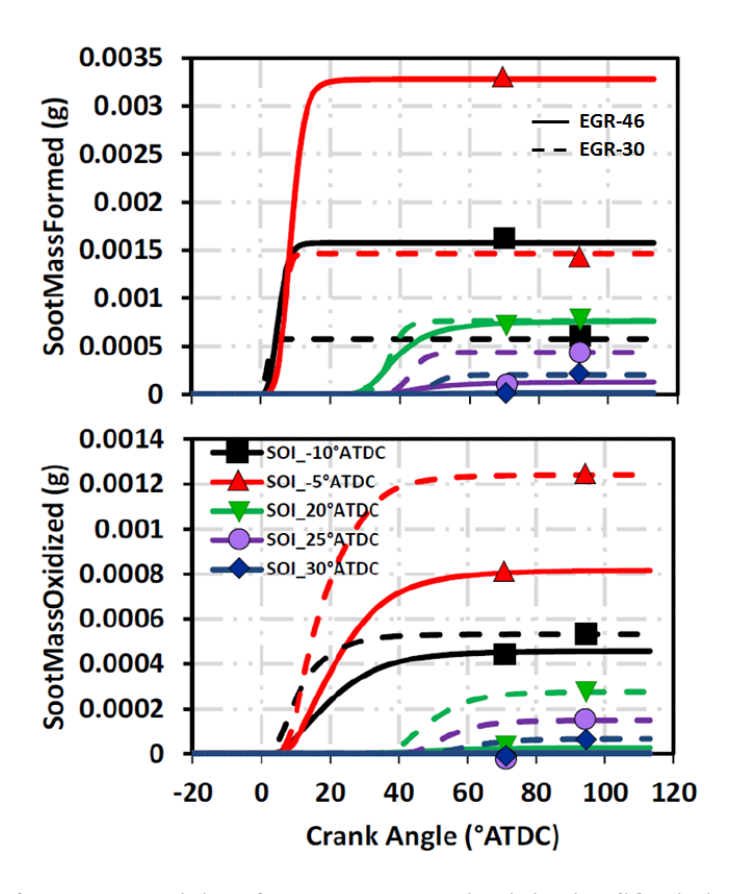


Figure B-7. Soot mass formed and oxidized for the load-extension injection SOI timing sweep at EGR-46% and EGR-30% at an injection pressure of 1000 bar.

At SOI timings of 20 °aTDC and later, the soot emissions are almost the same for both the EGR cases. In fact, for the cases with SOI timings of 25 °aTDC and 30 °aTDC, soot emissions for 30% EGR are slightly higher than those for 46% EGR. As mentioned earlier, the soot emissions for the late SOI timings are solely temperature dependent. For the 46% EGR case, the low availability of oxygen at the late SOI timings (3.53% at the start of the secondary heat release) reduces the peak combustion temperatures of the secondary heat release, causing near zero soot formation and oxidation. For the 30% EGR case, the higher oxygen availability (10.2% at the start of the secondary heat release) causes higher combustion temperatures from the secondary heat release. As a result, it forms slightly higher soot compared to the 46% EGR case.

This reconfirms the fact that the soot emissions of the late SOI timings are primarily controlled by temperature.

B.2.3. Effect of Injection Pressure

Figure B-8 shows the measured and predicted soot emissions for 46% EGR at injection pressures of 1000 bar and 1500 bar. At the early load extension injection timings, using a higher injection pressure reduces the soot emissions.

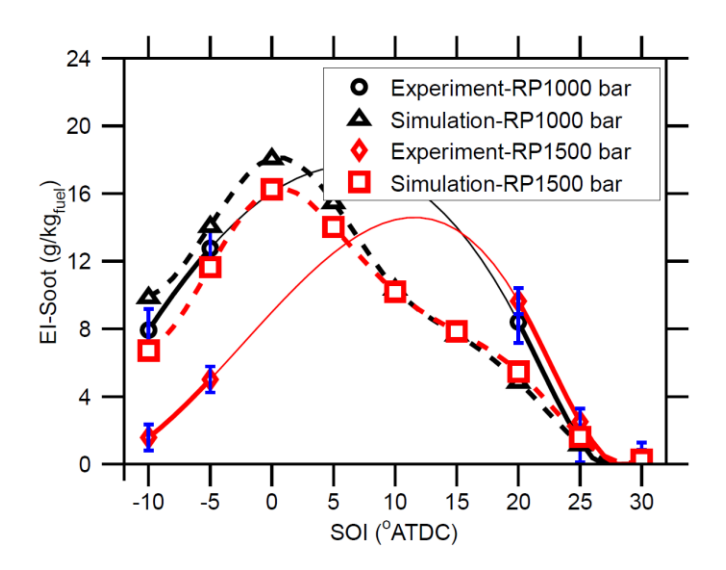


Figure B-8. Measured (\circ, \circ) and predicted (\triangle, \square) soot emissions for injection pressures of 1000 bar and 1500 bar for EGR-46% using E0 fuel. The measured and simulation data are shown in symbols, and the lines show spline interpolation. The error bars are based on a 97.5% confidence interval from multiple repeats for the experiments with EGR-30% and an injection pressure of 1000 bar.

Figure B-9 shows the Φ-T diagrams for both injection pressures at an SOI timing of -10 °aTDC and 46% EGR. The increased mixing of the higher injection pressure increases air entrainment and reduces the soot formation. It can be seen in Figure B-9 that, at every crank angle location, the higher injection pressure case has a slightly leaner charge than the lower injection pressure case. The leaner mixtures for the 1500 bar injection pressure cause the charge to exit earlier from the soot formation region than the 1000 bar injection pressure case; thereby resulting in lower soot emissions. However, for SOI timings of 20 °aTDC and later, the higher injection pressures show slightly higher soot emissions. The reason for the slight increase is due to increased temperature.

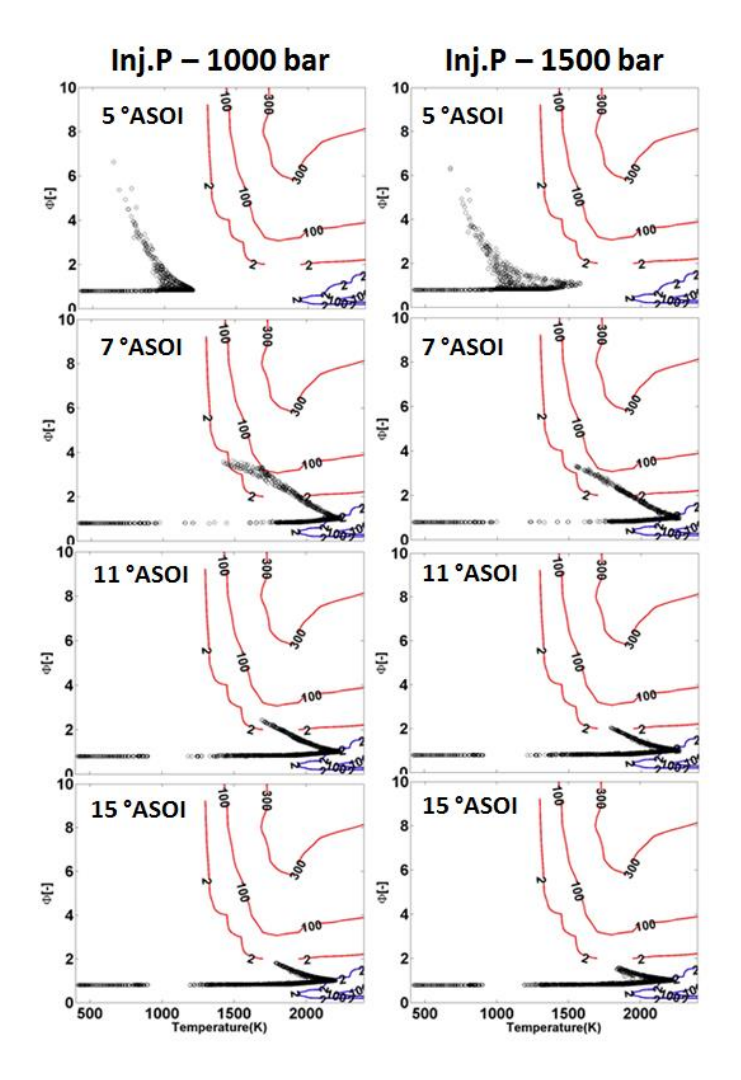


Figure B-9. Φ -T diagrams of the in-cylinder mixture at various crank angles after start of injection (°ASOI) for injection pressures of 1000 bar (left) and 1500 bar (right) at EGR-46% and SOI = -10 °ATDC. The symbols show the equivalence ratio, and temperature in each computational cell and the lines show NOx (lower right on each diagram) and soot (upper right on each diagram) islands calculated using HCCI simulations at the operating conditions of the present study.

Figure B-10 shows a comparison of the residence time in crank angles of the in-cylinder charge, in various temperature ranges, for the 46% EGR case at injection pressures of 1000 bar and 1500 bar and a SOI timing of 25 °aTDC. As can be seen from the figure, the shorter injection duration and increased mixing due to the higher injection pressure causes the fuel to reside in the high-temperature zones for a longer time than the lower injection pressure case. Hence, the higher injection pressure cases end up forming more soot at the late SOI timings than the lower injection pressure cases.

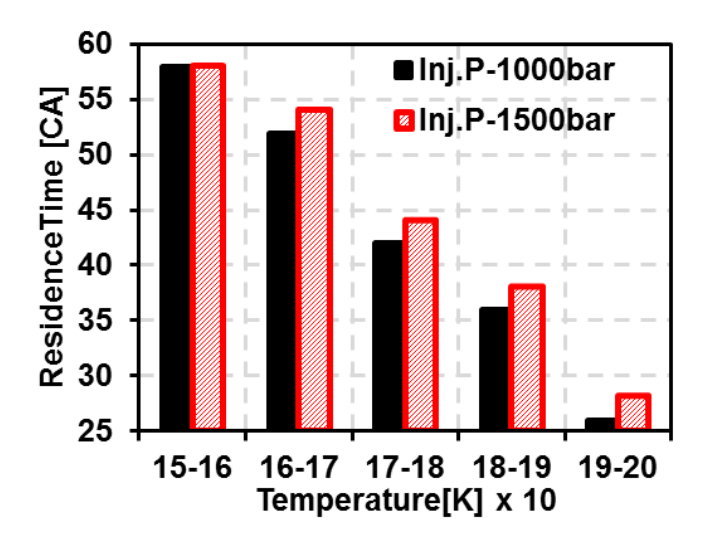


Figure B-10. Residence time (CA) of the in-cylinder charge in various temperature ranges for the EGR-46% case and E0 fuel at injection pressures of 1000 bar and 1500 bar and SOI = 25 °aTDC.

B.2.4. Feasible Operating Space for Load Extension Injection

The previous results showed that air entrainment has a significant impact on soot emissions for SOI timings near TDC. At these injection timings, oxygen concentration and injection pressure can effectively be used to control the soot emissions. However, as the injection timing is delayed beyond TDC, the effect of air entrainment reduces, and temperature becomes the dominant factor controlling soot emissions. As the SOI timing is delayed sufficiently late beyond the primary heat release, soot formation becomes dependent solely on temperature.

To summarize the results, Figure B-11 shows contours of GIE, NOx, and soot emissions as a function of EGR and SOI timing at an injection pressure of 1500 bar, generated from experimental data at EGRs of 30%, 38%, and 46%. The trends show that GIE is the highest at the earliest injection timings, with a maximum efficiency of 45%, and steadily decreases to just under 40% at the late injection timings. The decrease in GIE for the late SOI timings is mainly due to the expansion losses resulting from the late combustion phasing. High NOx levels are observed at injection timings before TDC at the lower EGRs. As the SOI timing is delayed beyond TDC, NOx levels decrease, but soot emissions begin to increase. With further delay in SOI timing, soot production peaks and eventually falls off. Combustion efficiency was fairly constant at 99.1% until the SOI timing was retarded beyond 20°aTDC. Since the study was performed at a fixed quantity of premixed fuel, the PPRR was fairly constant. Accordingly, the trends of PPRR are

not shown. Additional CFD studies were performed studying the effect of premixed fuel variation on the results from the mixed-mode strategy. The results of this study can be found in Kavuri et al. [100].

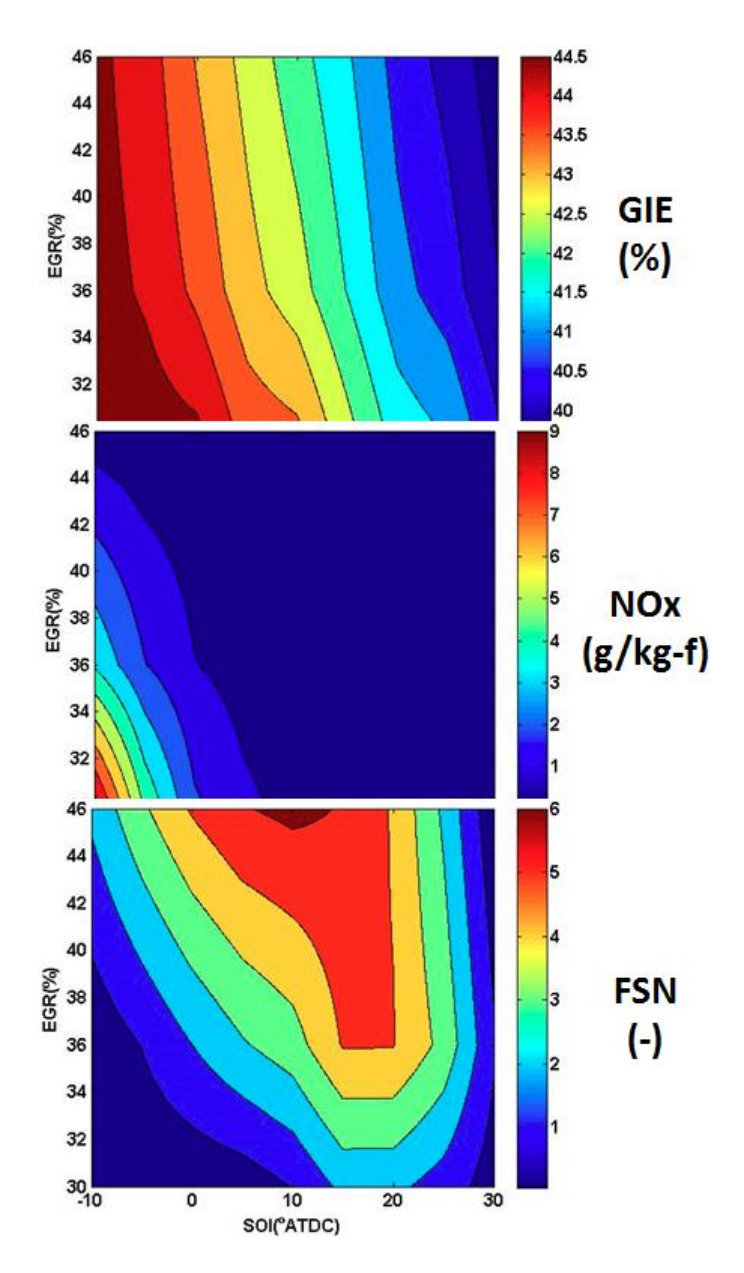


Figure B-11. Contours of GIE, NOx, and soot emissions as a function of EGR and SOI timing at an injection pressure of 1500 bar using E0 fuel.

These trends indicate two tradeoffs: the well-known soot-NOx tradeoff and a secondary tradeoff between soot and GIE. This offers two potential regions of operation that enable load extension. Figure B-12 shows the two regions in EGR-SOI operating space where the load-extension injection can be added to achieve low emissions (NOx and soot ≤ 2 g/kg-f) and reasonably high efficiencies (GIE $\geq 40\%$). At EGRs

below 40%, the operating space for load extension injections is relatively wide. That is, SOI timings between -5 °aTDC and 10 °aTDC show low NOx and soot emissions and high efficiency. Injection timings later than 20 °aTDC can also be used; however, thermal efficiency decreases. Therefore, splitting the load-extension injection into two separate injections in the two feasible regions can mitigate the soot emissions without compromising on the load.

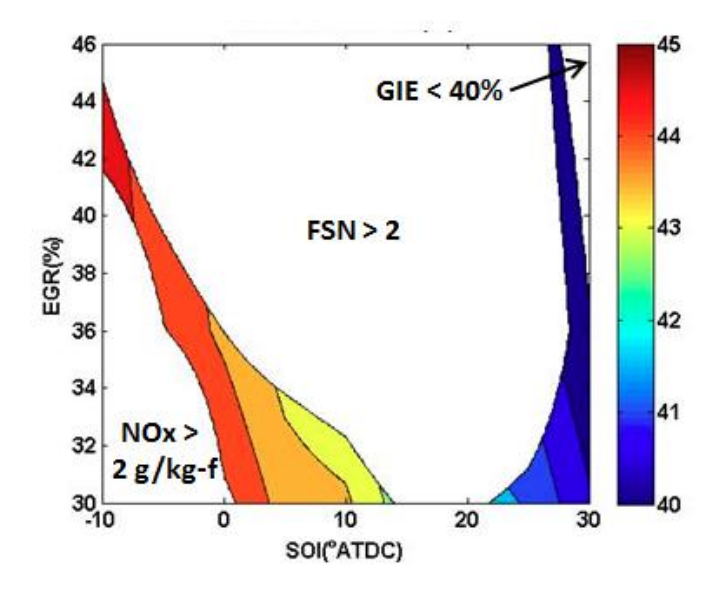


Figure B-12. Regions in EGR-SOI operating space which meet constraints of NOx < 2 g/kg-f, FSN < 2 and GIE > 40%. The regions are colored by contours of GIE.

B.3. Conclusions

The present work investigated soot formation and mitigation mechanisms using a combination of engine experiments and computational fluid dynamics modeling to help identify a pathway to enable efficient PCI load extension while minimizing soot emissions. A PCI combustion event was achieved using a premixed charge of gasoline and n-heptane to control combustion phasing, and a load extension injection of gasoline was added near top dead center. Detailed experiments were used to investigate the effects of load extension injection SOI timing, exhaust gas recirculation rate, injection pressure, and fuel type on soot emissions.

The results showed a strong impact of oxygen concentration and injection pressure for injection timings near top dead center; however, as the load-extension injection event was delayed beyond the end of the PCI heat release, the soot formation decreased and became independent of EGR. At these conditions,

the CFD modeling showed that soot formation is dependent solely on temperature. This analysis was then summarized to indicate potential regions of operation with high efficiency and low NOx and soot emissions. The results show that the operating space yielding high efficiency and low NOx and soot emissions increases as the EGR is decreased. At EGRs lower than 40%, a range of load extension SOI timings between -5° and 10° ATDC (near TDC injection) result in high efficiency and low emissions. Further reductions in NOx and soot are possible at injection timings later than 20° ATDC (late post-injection); however, thermal efficiency decreases. Therefore, by the splitting the load-extension injection into a near TDC (oxygen controlled) and a late post-injection (temperature controlled), soot emissions can be mitigated without reducing the load (fueling).

Appendix-C Thermodynamic Model - Open Cycle Work Calculation

A simple thermodynamic model was developed using Cantera [97] to estimate the pumping loop work required for each EGR and Φ combination. Figure C-1 shows a layout of the key components involved.

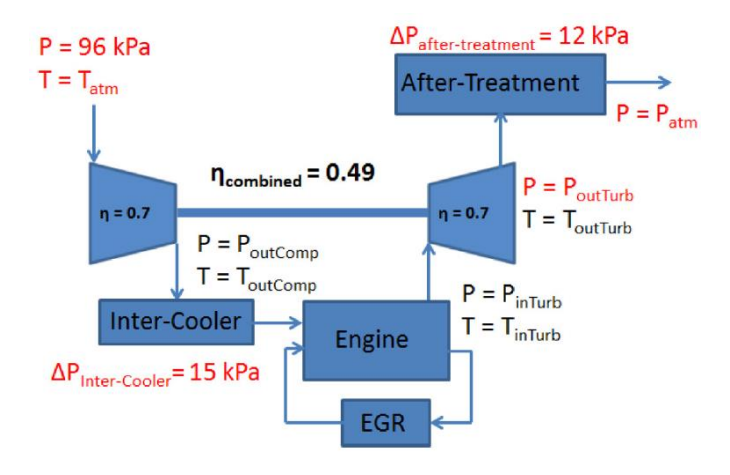


Figure C-1. Layout of the air-handling system for open cycle work calculation. Known values are shown in red font.

Compressor and turbine efficiencies of 70% were assumed, resulting in a combined turbomachinery efficiency of 49%. Isentropic compressor and turbine calculations were used with the specified turbine and compressor efficiencies to calculate the required exhaust backpressure for each operating condition.

C.1. Compressor Calculations

All the known states prior to starting the calculations are shown in red in Figure C-1. The inlet pressure for the compressor is assumed 4 kPa less than the ambient pressure of 100 kPa, considering pressure drop for piping. The inlet temperature is assumed to be at ambient temperature. From the pressure and temperature, the enthalpy and entropy at the inlet of the compressor can be calculated assuming intake air as an ideal gas. The pressure drop across the intercooler was assumed to be 15 kPa. The pressure and volume at IVC are known from the values initialized in KIVA, from which the entropy can be estimated. Considering isentropic compression from BDC to IVC gives

$$S_{IVC} = S_{RDC} \,, \tag{33}$$

where, S_{IVC} and S_{BDC} are the entropies at IVC and BDC respectively. The volume at BDC is known from the engine geometry which in combination with S_{BDC} can be used to estimate the pressure at BDC. The pressure at the outlet of the compressor can be calculated from the following equations:

$$P_{outIntercooler} = P_{RDC}, (34)$$

$$P_{inIntercooler} - P_{outIntercooler} = 15 \, kPa, \tag{35}$$

$$P_{outCompressor} = P_{inIntercooler}, \tag{36}$$

where $P_{outIntercooler}$, $P_{inIntercooler}$ are the pressures at the outlet and inlet of the intercooler and $P_{outCompressor}$ is the pressure at the outlet of the compressor. Considering isentropic compression for the compressor yields

$$S_{inCompressor} = S_{outCompressor}, \tag{37}$$

where $S_{inCompressor}$, $S_{outCompressor}$ are the entropies at the inlet and outlet of the compressor. From $S_{outCompressor}$ and $P_{outCompressor}$ the temperature at the outlet of the compressor can be calculated. Since ideal gas was assumed, from the temperature at the compressor outlet, the enthalpy at the outlet of the compressor can be estimated. Finally, the compressor power is calculated as

$$Power_{Compressor} = \dot{m}_{in} \left(\frac{h_{outCompressor,s} - h_{inCompressor}}{\eta_{compressor}} \right), \tag{38}$$

where \dot{m}_{in} is the mass flow rate at IVC, $h_{outCompressor,s}$ is the isentropic enthalpy at the outlet of the compressor, $h_{inCompressor}$ is the enthalpy at the inlet of the compressor and $\eta_{Compressor}$ is the compressor efficiency.

C.2. Turbine Calculations

At the turbine exit, a pressure drop of 12 kPa was assumed across the after-treatment devices. The exhaust from the after-treatment exits to the atmosphere. Hence, the pressure at the outlet of the turbine can be calculated from the following equations:

$$P_{outTurbine} = P_{inAfterTreatment}, (39)$$

$$P_{inAfterTreatment} - P_{outAfterTreatment} = 12 kPa, \tag{40}$$

$$P_{outAfterTreatment} = 100 \, kPa, \tag{41}$$

where, $P_{inAfterTreatment}$, $P_{outAfterTreatment}$ are the pressure at the inlet and outlet of the after treatment device and $P_{outTurbine}$ is the pressure at the outlet of the turbine. From the KIVA closed cycle simulation, the pressure, temperature, and mixture composition at EVO are known. From this, the entropy at EVO can be estimated. Assuming isentropic expansion from EVO to turbine inlet and from turbine inlet to turbine outlet gives

$$S_{outTurbine} = S_{inTurbine}, \tag{42}$$

$$S_{inTurbine} = S_{EVO}, (43)$$

where, $S_{inTurbine}$, $S_{outTurbine}$ and S_{EVO} are the entropies at the inlet, outlet of the turbine and at EVO respectively. Since the pressure and entropy at the outlet of the turbine are known, the temperature and enthalpy at the turbine outlet can be estimated. As the compressor and turbine are run on the same shaft, equating the power of compressor and turbine gives

$$Power_{Compressor} = Power_{Turbine}, \tag{44}$$

$$Power_{Turbine} = \eta_{Turbine} \dot{m}_{exh} (h_{inTurbine} - h_{outTurbine.s}), \tag{45}$$

where, \dot{m}_{exh} is the mass flow rate from EVO after deducting the EGR flow rate, $h_{inTurbine}$ is the enthalpy at the inlet of the turbine, $h_{outTurbine,s}$ is the isentropic enthalpy at the outlet of the turbine, and $\eta_{Turbine}$ is the turbine efficiency. Using these two equations, the enthalpy and the temperature at the inlet of the turbine can be estimated. Now that the entropy and the temperature are known, the pressure at the inlet of the turbine can be calculated. Finally, the pumping loop work is evaluated as

$$W_{pumping} = (P_{inTurbine} - P_{outCompressor}) * (V_{BDC} - V_{TDC}), \tag{46}$$

This approach avoids the complexity of turbo-machinery matching, by assuming that a turbine and compressor combination can be developed to achieve 49% combined efficiency at each EGR/intake pressure combination. Selecting specific hardware is beyond the scope of the work presented in this dissertation. It is assumed that the engine uses an intercooler and the intake temperature is fixed at 60 °C.

Appendix-D Post-Injection Strategies under High-Load Conditions

Based on the results seen in Chapter 4, with the objective of identifying high-load operating strategies that work at moderate EGR rates, Paz et al. [111] investigated high-temperature GCI operation at reduced EGR rates (< 30 %). They investigated a mixing-controlled CDC like strategy, but with gasoline. Due to the high fuel stratification resulting from the mixing-controlled injection, the PPRR was well controlled despite operating at a reduced EGR rate. However, combustion at locally rich Φ 's and high temperatures resulted in the classical tradeoff between soot and NOx emissions. They compared the GCI strategy with CDC under high-load conditions. Results from this study showed that operating with a relaxed NOx constraint at NOx emission levels suitable for production applications (~10 g/kg-f) yields significantly lower soot emissions (~ 1 FSN) at a higher efficiency (~42%) relative to CDC (~3 FSN, 40%) operation at similar levels of NOx emissions (~10 g/kg-f). However, even with gasoline, soot emissions were approximately 1 FSN, which remains to be higher than acceptable levels for no soot after treatment. Past research [112, 113, 114] in mixing-controlled strategies has shown post-injections as a viable mechanism to reduce soot emissions. However, most of these studies were done at low- to mid-load conditions. The current study adds to this research by investigating the use of post-injections to reduce soot emissions under high-load conditions in the range of 16 bar to 20 bar IMEP. A combination of experiments and CFD modeling will be used to isolate and understand the role of premixed, main, and post-injections on soot emissions. The effect of SOI timing and injection duration of the post-injection on soot emissions will also be investigated.

D.1. Operating Conditions

The study was performed using 91E10 gasoline. The engine was operated at 1300 rev/min. at a fixed intake pressure of 2.85 bar and 0% EGR rate. The three injection strategies investigated in the current study are shown in Figure D-1.

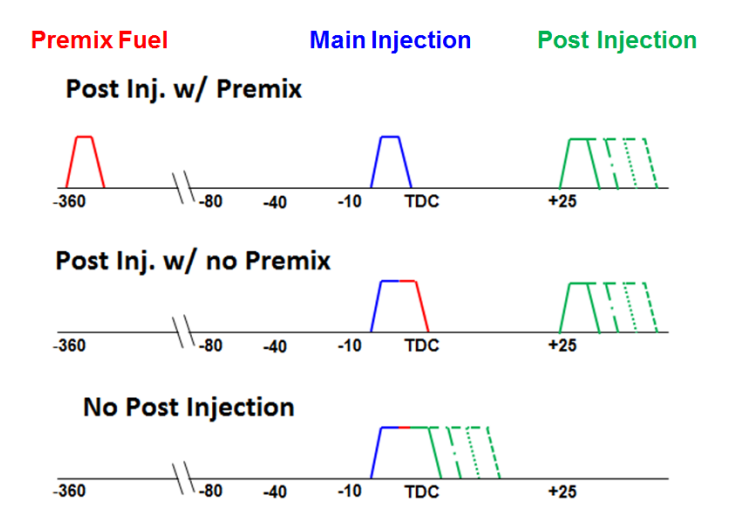


Figure D-1. Summary of the injection strategies investigated in the current study.

Initially, the baseline injection strategy was established which had just the main injection (named as No Post Injection in Figure D-1). The SOI timing of the main injection was fixed at -8 oaTDC, and the duration of the main injection was adjusted to vary the load in the range of 16 bar to 21 bar IMEP. For the second injection strategy (named as Post Inj. w/ no Premix in Figure D-1), the study was repeated by adding a post-injection. The duration of the main injection was fixed to achieve a load of 16 bar IMEP and load was varied by adjusting the duration of the post-injection to achieve a similar load range as the baseline strategy. The study was performed for three post-injection SOI timings of 16 °aTDC, 25 °aTDC, and 40 ^oaTDC. The earliest post-injection SOI was chosen to achieve the minimal dwell time between the main and post-injection while avoiding overlap with the main injection. For the final injection strategy (named as Post Inj. w/ Premix in Figure D-1), the same study was repeated by removing a part of the fuel from the main injection and adding it as premixed fuel. The premixed fuel is introduced into the combustion chamber as an early cycle injection, such that the combined load from the premixed and the main injection was 16 bar IMEP. The post-injection duration was once again varied to achieve the same load range as the baseline strategy. For this strategy, the earliest post-injection SOI timing was advanced from 16 °aTDC to 12 °aTDC. Since premixing a portion of the main injection fuel reduced the duration of the main injection, the postinjection could be advanced without overlapping with the main injection. The other two post-injection SOI

timings investigated remain the same as the second strategy. A detailed summary of the operating conditions for each injection strategy is shown in Table D-1.

Table D-1. Summary of operating conditions for the injection strategies shown in Figure D-1.

Parameter \ Injection Strategy	No Post- injection	Post Inj. w/ no Premix Fuel	Post Inj. w/ Premix Fuel
Fuel	91E10		
Nominal gross IMEP [bar]	16 to 21		
Engine Speed [rev/min.]	1300		
Intake Temperature [°C]	65		
Intake Pressure [bar]	2.85		
EGR [%]	0		
Injection Pressure [bar]	1360		
Main Inj. SOI Timing [°aTDC]	-8		
Total Fuel Mass [mg/cycle]	~ 215 to 290		
Premixed Fuel Mass [mg/cycle]	0	0	68
Main Inj. Fuel Mass [mg/cycle]	~ 215 to 290	215	147
Post Inj. Fuel Mass [mg/cycle]	0	~ 0 to 75	~ 0 to 75
Post Inj. SOI Timing [°aTDC]	N/A	16, 25, 40	12, 25, 40

The results from the three strategies were compared to first understand the role of premixed, main, and post-injections on soot emissions. Next, to study the effect of varying the SOI timing and injection duration of the post-injection on soot emissions.

D.2. Soot Trends

Figure D-2 shows the experimental and the simulation results of soot emissions as a function of the gross IMEP for the three injection strategies studied.

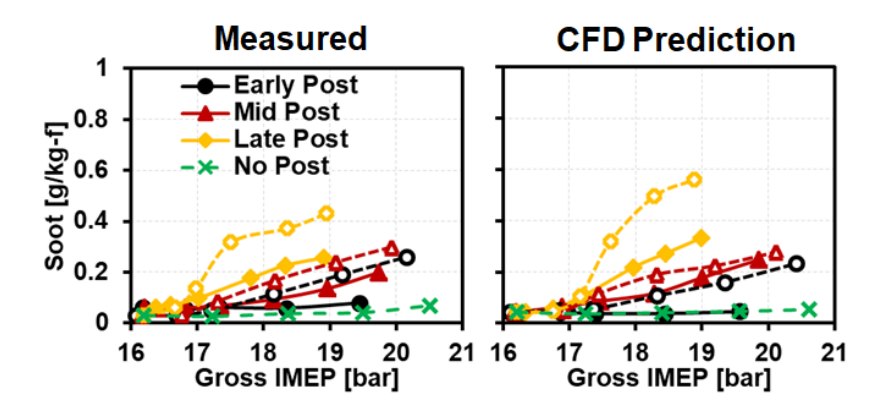


Figure D-2. Experiment and CFD predicted soot emissions vs. gross IMEP for all the cases studied. Post-injection cases with premixed fuel shown as solid lines with filled markers and post-injection cases without premixed fuel shown as dashed lines with unfilled markers.

In the figure, early post refers to SOI of 12 °aTDC for post-injection cases with premixed fuel and 16 °aTDC for post-injection cases without premixed fuel. Mid post refers to SOI of 25 °aTDC, and late post refers to 40 °aTDC cases. No post refers to the cases without post-injections. The post-injection cases with premixed fuel are shown in solid lines with filled markers. The post-injection cases without premixed fuel are shown in dashed lines with unfilled markers.

From the experimental trends, firstly it is seen that for both the post-injection strategies, as the post-injection SOI timing is delayed (i.e., the dwell time between the main and the post-injection increases), for the same gross IMEP, the soot emissions increase. Secondly, at each post-injection SOI timing, for the same gross IMEP, the cases with the premixed fuel have lower soot emissions than the cases without the premixed fuel. Lastly, comparing the post-injection strategies to the baseline strategy (no post) at the same gross IMEP, it is observed that adding post-injections does not give any benefit in terms of soot reduction. This is inferred since the post-injection strategy with the least soot emissions (i.e., the post-injection strategy with premixed fuel and SOI of 12 °aTDC), gives the same or slightly higher soot emissions relative to the baseline strategy.

Comparing the experimental trends with the CFD predicted trends, it is seen that there is a good agreement between the two. CFD does a decent job in predicting the experimental soot emissions in terms of trends and magnitude across the three injection strategies studied. All the trends observed in the experiments are observed to be intact in the CFD predictions as well. Accordingly, the CFD results will be used to explain the three experimental trends that were highlighted in the above discussion.

D.2.1. Effect of Dwell Time

The first trend that was highlighted from Figure D-2 was the effect of dwell time between main and post-injection SOI timings on soot emissions. It was found that for both the post-injection strategies, for the same gross IMEP, increasing the dwell time between the main and post-injection SOI timings increased the soot emissions. To explain this trend, the three post-injection SOI timings at a gross IMEP of ~18.5 bar are chosen from the post-injection cases with the premixed fuel. Figure D-3 shows the CFD predicted trends highlighting the cases that will be used to explain the trends.

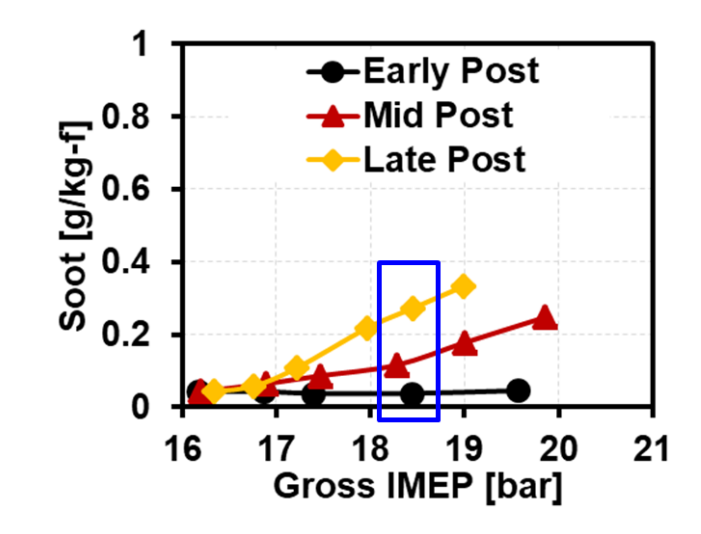


Figure D-3. CFD predicted trends for the post-injection cases with premixed fuel. The blue box highlights the cases that will be used to explain the soot trends as a function of the dwell time.

Figure D-4 shows the Φ and soot contours for the three cases highlighted in Figure D-3. For all the three cases, the fuel from the main injection hits the bowl and eventually ends up in the squish region due to the spray momentum. This is seen from the Φ contours from 24 °aTDC to 40 °aTDC where fuel-rich regions are visible in the squish region for the SOI of 40 °aTDC cases, and the post-injection is yet to be introduced. As a result, the soot emissions formed from the main injection which are yet to be oxidized also end up in the squish region. This is observed from the soot contours at the same crank angle locations of 24 ^oaTDC to 40 ^oaTDC for the SOI of 40 ^oaTDC case. Now focusing on the post-injections, for the SOI of 12 ^oaTDC case, it is seen from the Φ contours at 16 ^oaTDC that the entire fuel mass from the post-injection is targeted into the bowl. Eventually, this results in the fuel mass from the main and the post-injection being split up between the bowl and the squish region. This is evident from the two distinct fuel-rich regions in the Φ contours from 50 °aTDC to 70 °aTDC for the SOI of 12 °aTDC case. However, for the post-injection SOI timing of 25 oaTDC, a significant portion of the post-injection fuel mass is targeted into the squish region. Similarly, for the post-injection SOI timing of 40 °aTDC, the entire post-injection fuel mass is targeted into the squish region where it accumulates with the main injection fuel mass. This is seen from the Φ contours from 50 °aTDC to 70 °aTDC where the post-injection SOI timings of 25 °aTDC and 40 ^oaTDC have significantly richer regions in the squish relative to the post-injection SOI timing of 12 ^oaTDC.

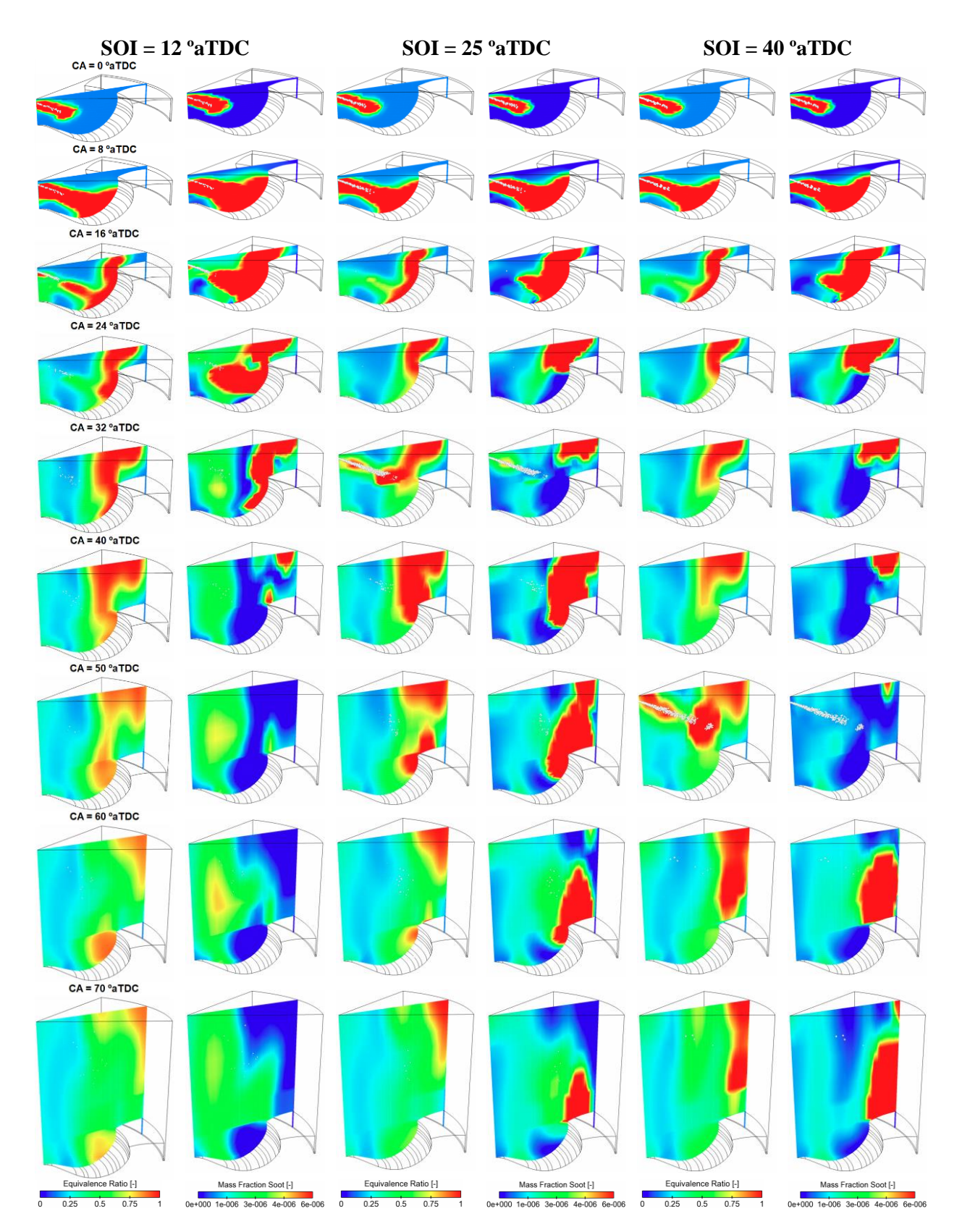


Figure D-4. Φ and soot emissions contours for the three cases highlighted in Figure D-3.

These results indicate that as the post-injection is delayed later into the expansion stroke, a larger portion of the fuel from the post-injection gets accumulated in the same region as the main injection fuel mass. Conversely, when the post-injection is early, the fuel mass from the two injections ends up in two distinct locations in the combustion chamber. Therefore, the earlier the post-injection, the better distributed the fuel is in the combustion chamber. Accordingly, the earliest post-injection SOI timing of 12 °aTDC results in the least soot emissions as it provides better access to oxygen for the main and the post-injections, resulting in improved soot oxidation rates. This is visible from the soot mass fraction contours from 50 °aTDC to 70 °aTDC for the post-injection SOI of 12 °aTDC cases, where most of the soot formed at the earlier crank angles gets oxidized. As the post-injection is delayed later into the expansion stroke, a larger portion of the post-injection is targeted into the squish region, leaving the majority of the oxygen in the bowl unused. Thus, the soot formed from the late post-injections gets accumulated with the soot formed from the main injection fuel mass, resulting in increased net soot emissions as the post-injection is delayed. This is evident from the soot mass fraction contours from 50 °aTDC to 70 °aTDC where, as the post-injection SOI timing is delayed, there is a higher soot mass fraction that does not get oxidized and ends up in the squish region.

Thus, the post-injection cases with a shorter dwell time with respect to the main injection result in lower soot emissions. This is because the fuel from the post-injection gets targeted into a different region of the combustion chamber relative to the main injection fuel which gives better access to oxygen to both the injections; thereby resulting in lower soot emissions.

D.2.2. Effect of Premixed Fuel

The second trend that was observed from Figure D-2 was that the post-injection cases where a portion of the main injection fuel is premixed resulted in lower soot emissions than the cases without the premixed fuel. To explain this trend, the cases at a gross IMEP of ~18.5 bar and post-injection SOI timing of 25 °aTDC were chosen from the two post-injection strategies. Figure D-5 shows the CFD predicted trends highlighting the cases that will be used to explain the trends.

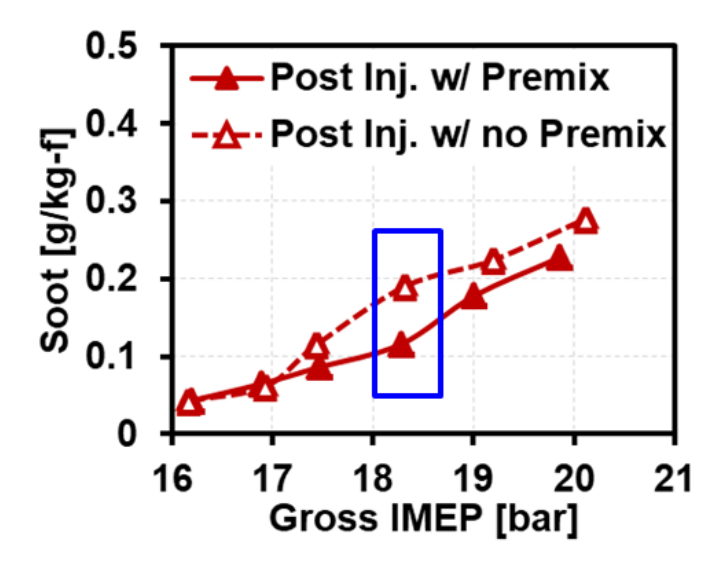


Figure D-5. CFD predicted trends for the post-injection SOI timing of 25 °aTDC cases with and without the premixed fuel. The blue box highlights the cases that will be used to explain the soot trends as a function of the dwell time.

Figure D-6 shows the Φ and the soot emissions contours for the two cases highlighted in Figure D-5. Not having premixed fuel creates a leaner background Φ when the main injection is introduced. This is seen from comparing the Φ contours at 0 °aTDC, in Figure D-6. When a portion of the main injection fuel is premixed, though the background Φ increases, the premixed fuel is well mixed and is locally lean during combustion. For the post-injection cases without the premixed fuel, though there is more oxygen available, not premixing the fuel increases the fuel quantity in the main injection which eventually combusts in a mixing-controlled heat release. Hence, not premixing the fuel increases the amount of locally rich regions in the combustion chamber during the mixing-controlled combustion of the main injection; thereby forming higher soot emissions. This is seen by comparing the Φ contours for crank angles locations of 8 °aTDC to 24 oaTDC. Similar to the cases shown in Figure D-4 the fuel from the main injection is targeted into the bowl and ends up in the squish. But when a portion of the fuel is premixed it reduces the fuel rich regions formed in the squish. This eventually results in less soot formation as is seen from comparing the soot emission contours at the crank angle locations of 8 °aTDC to 24 °aTDC. As a result, when the post-injection fuel is injected, there are relatively lower soot emissions in the combustion chamber for the case with premixed fuel. This is seen from comparing the soot emissions contours at 32 °aTDC. For the post-injection SOI timing of 25 °aTDC considered in Figure D-6, the fuel from the post-injection is split between the bowl and the squish regions as observed from the Φ contours at crank angles of 40 °aTDC and 50 °aTDC. The soot formed from the post-injection fuel targeted into the bowl gets oxidized almost completely as it accesses the oxygen present in the bowl. This is evident from the soot emissions contours where there is soot formed in the bowl at crank angles from 40 °aTDC to 50 °aTDC, but gets oxidized eventually by 70 °aTDC. The post-injection fuel that is targeted into the squish forms soot that gets accumulated with the soot mass from the main injection which is yet to be oxidized. This is seen from the soot emissions contours at 40 °aTDC and 50 °aTDC. Both the post-injection cases have the same fuel mass in the post-injection and end up forming nearly the same amount of soot from the post-injection eventually. This is observed by comparing the soot emissions contours for the two cases at 70 °aTDC. It is seen that there is nearly the same amount of soot from the post-injection that does not get oxidized and ends up in the squish region close to the crevice. However, for the case without the premixed fuel, there is additional soot mass that did not get oxidized. This soot mass ended up in the squish region close to the cylinder head as seen from the soot mass fraction contours at 70 °aTDC for the case without the post-injection. This is due to the additional fuel mass in the main injection which was not premixed and resulted in soot formation. This additional soot formed does not get oxidized and eventually ends up in the squish region close to the cylinder head.

The same result is shown quantitatively in Figure D-7, which shows a comparison of the trends of soot formation, soot oxidation, and soot production as a function of crank angle for the two cases compared in Figure D-6. The trends for the case with the premixed fuel are shown in solid lines while the trends for the case without the premixed fuel are shown in dashed lines. As seen from the figure, the peak soot produced prior to the post-injection is higher for the case without the premixed fuel. This is because at the peak soot location which occurs at in a crank angle range of ~12 °aTDC to 15 °aTDC, the soot mass oxidized is nearly the same for the two cases while the soot mass formed is significantly higher for the case without the premixed fuel. This difference in soot mass exists until late in the expansion stroke, resulting in higher soot emissions at EVO for the case without the premixed fuel.

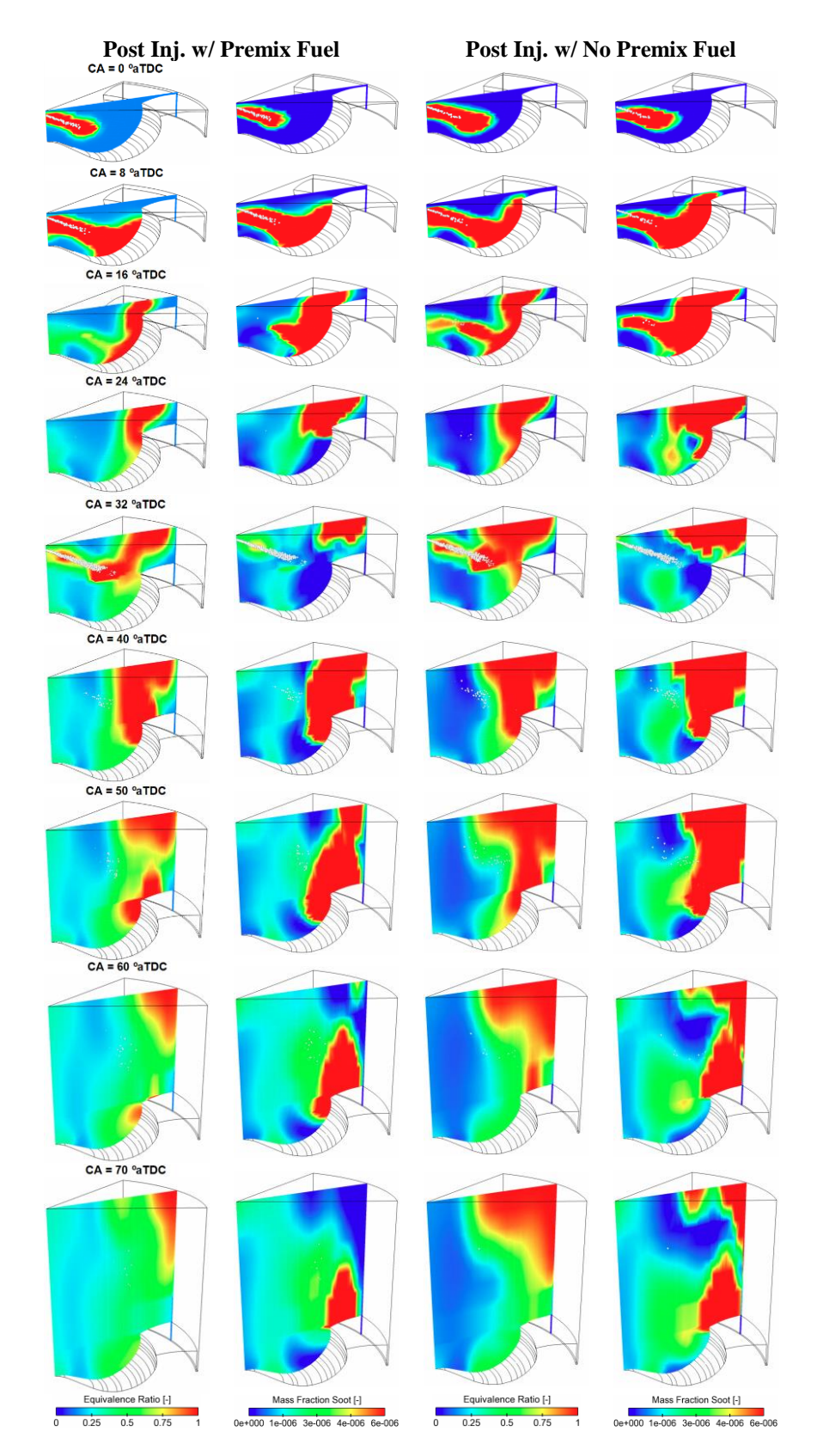


Figure D-6. Φ and soot emissions contours for the two cases highlighted in Figure D-5.

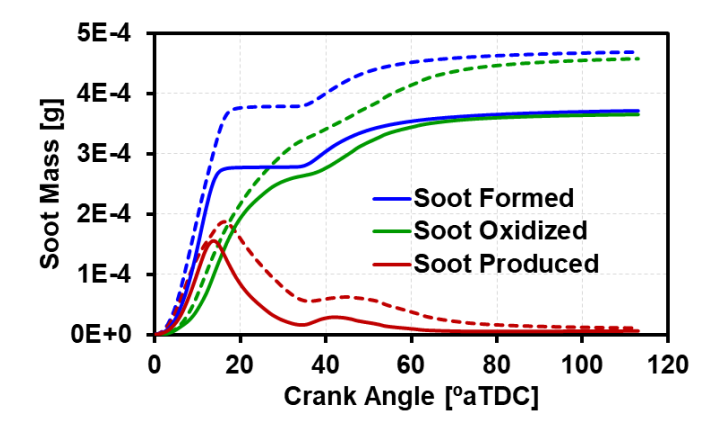


Figure D-7. Trends of soot formation, oxidation and production as a function of CA for the post-injection cases with (-) and without (- -) premixed fuel compared in Figure D-6.

D.2.3. Effect of Post-Injection

The last trend that was highlighted in Figure D-2 was that adding the post-injection did not result in any significant reduction in soot emissions relative to the baseline injection strategy. To explain this result, cases at a gross IMEP of ~18.5 bar are chosen from the no post-injection cases and the post-injection cases without premixed fuel having an SOI timing of 16 °aTDC. The post-injection case without the premixed fuel was chosen instead of the case with the premixed fuel, to isolate the effect of adding the post-injection. The earliest post-injection timing was chosen to make the comparison since it resulted in the least soot emissions. Figure D-8 shows the CFD predicted trends while highlighting the cases that will be used to explain the trends.

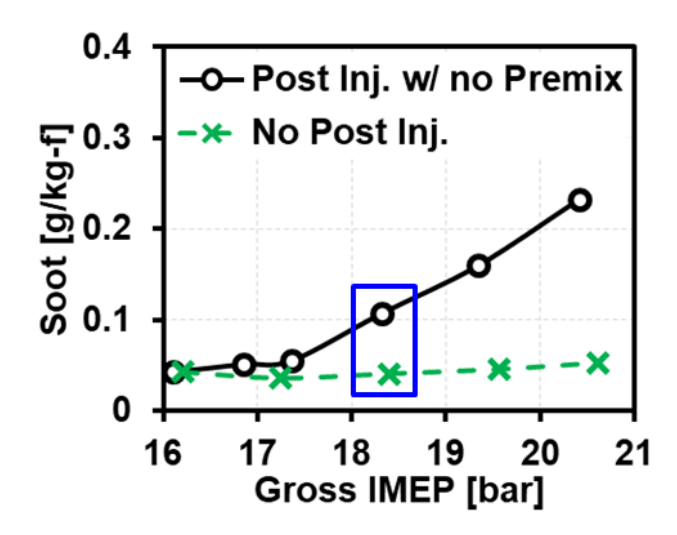


Figure D-8. CFD predicted trends for the post-injection SOI timing of 16 °aTDC cases without the premixed fuel and the cases without the post-injection. The blue box highlights the cases that will be used to explain the soot trends as a function of the dwell time.

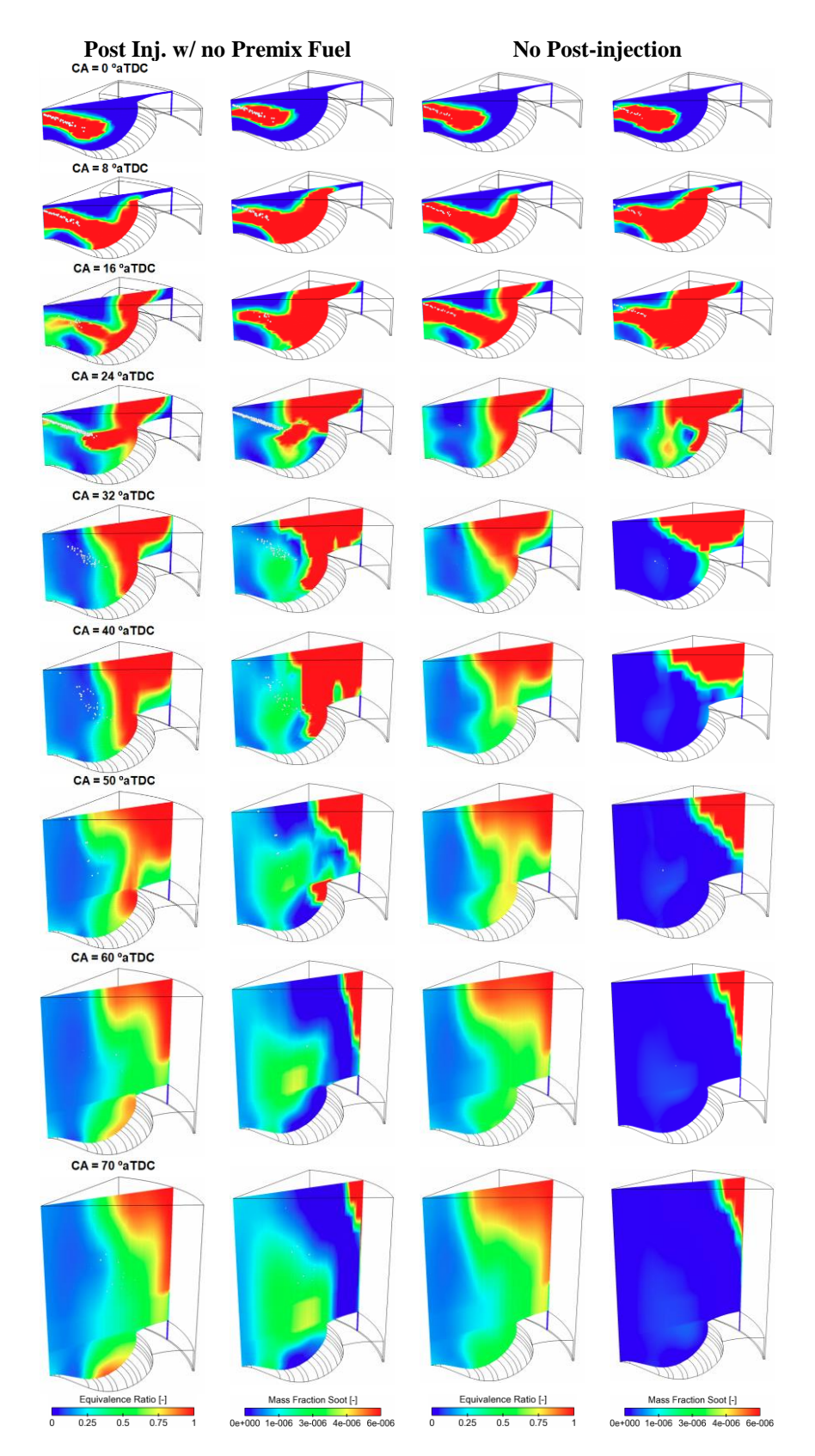


Figure D-9. Φ and soot emissions contours for the two cases highlighted in Figure D-8.

Figure D-9 shows the Φ and the soot emissions contours for the two cases highlighted in Figure D-8. The no post-injection case has a larger fuel mass in the main injection compared to the post-injection case. Hence, there are more locally rich regions during combustion for the no post-injection case. This is seen from comparing the Φ contours for the two cases in Figure D-9 at crank angle location of 16 °aTDC. This results in higher soot formation from the main injection fuel for the no post-injection case relative to the case with the post-injection. This can be observed from comparing the soot mass fraction contours for the two cases at crank angle location of 16 °aTDC. Figure D-10 shows the trends of soot formation, soot oxidation, and soot production for the two cases compared in Figure D-9. The trends for the case without the post-injection are shown in solid lines while the trends for the post-injection case without the premixed fuel are shown in dashed lines.

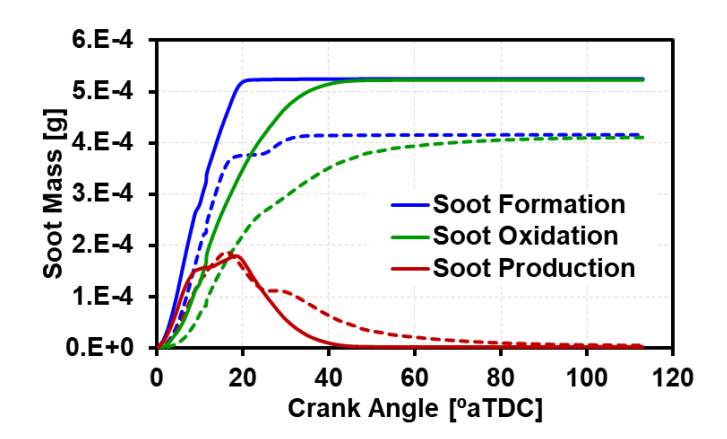


Figure D-10. Trends of soot formation, oxidation, and production as a function of CA for the no post-injection case (-) and the post-injection case without premixed fuel (- -) compared in Figure D-9.

From the soot formation trends, it is seen that of the two cases compared, the case without the post-injection forms more soot. However, there is abundant availability of oxygen, and since the combustion temperatures are high close to TDC, it results in high soot oxidation rates for both the cases. Hence most of the soot formed is oxidized, resulting in nearly the same amount of soot emissions for both the cases by 20 °aTDC, which is when the main injection for the no post-injection case ends. This can be visualized in Figure D-10 by comparing the soot production trends for the two cases around the crank angle timing of 20 °aTDC. Similar to the earlier cases, the soot formed from the main injections ends up in the squish region close to the cylinder head. As the expansion stroke proceeds, the soot formation reaches saturation for the

no post-injection case. However, the soot oxidation rate continues to increase and oxidizes the soot formed from the main injection in the squish region.

Conversely, for the post-injection case, soot formation increases at 20 °aTDC from the combustion of the post-injection fuel. Due to the high-load (~18.5 bar) operating condition the post-injection has a reasonably long duration (~ 7 °CA). This results in the soot formation continuing to increase till 30 °aTDC beyond which it reaches saturation. This is seen from the soot emissions contours at 24 °aTDC and 32 °aTDC for the post-injection case in Figure D-9 and from the soot formation trends in Figure D-10. However, at this point in the expansion stroke, the temperatures are decreasing quickly, and the oxygen concentration has reduced due to combustion of the main injection fuel. This slows down the soot oxidation rate, which is seen from the reduction in the slope of the soot oxidation curve in Figure D-10 beyond 20 °aTDC. Due to this the soot formed from the post-injection does not get oxidized completely. This is visible from the soot mass fraction contours at crank angle locations of 60 °aTDC and 70 °aTDC where the soot emissions formed in the bowl due to the post-injection are not completely oxidized. The amount of soot from the main injection that did not get oxidized ends up being nearly the same as the case with the no post-injection. Furthermore, it is found to occur in the same location of the squish region as the no post-injection case.

Hence, the post-injection cases do not give any benefit at high-load conditions due to the long duration of the post-injections which causes soot to form late in the cycle. At these late CA timings, the temperatures drop rapidly slowing down the soot oxidation rates and cause most of the soot from the post-injection to not get oxidized. This eventually results in increased soot emissions at EVO. Though the long main injections (where there is no post-injection) form more soot, since the soot is formed early in the cycle, the combustion temperatures are high and favorable for soot oxidation. As a result, most of the soot formed is oxidized. Therefore, based on the current study, it can be inferred that, when operating at high-load conditions close to 20 bar IMEP, post-injections will not be useful in reducing soot emissions.

The results seen from the post-injection study are contradictory to the results seen in literature where post-injections were found to be effective in reducing soot emissions. There are two differences between the studies in the literature and the present study. Firstly, most of the studies in literature were focused on the low- to mid-load conditions and secondly, they were performed with diesel fuel. Hence, to understand if the lack of benefits of post-injections in the present study was a result of changing these factors, a similar study was repeated under low- to mid-load conditions with diesel fuel using the validated CFD model. Validation of the model over a range of low to mid-load operating conditions with diesel fuel can be found in Kavuri et al. [50].

D.2.4. Effect of Post-Injection at Low to Mid-Load Conditions

The study at low to mid-load conditions was performed with the same engine and injector configuration that was used for the high-load study. The operating conditions were chosen from the study performed by O'Connor et al. [115]. This is because, in their study, they have shown post-injections to be beneficial for soot reduction and the setup of their study is very similar to the high-load study performed in the earlier section of this appendix. Both these factors make it an ideal data set to perform this study and compare with the results from the earlier high-load study. The operating conditions are shown in Table D-2.

Table D-2. Operating conditions for the study at low to mid-load conditions.

Parameter \ Injection Strategy	No Post- injection	Post Inj. w/ no Premix Fuel	
Fuel	Diesel		
Nominal gross IMEP [bar]	4 to 8		
Engine Speed [rev/min.]	1200		
Intake Pressure [bar]	1.61		
EGR [%]	0		
Injection Pressure [bar]	1200		
Main Inj. SOI Timing [°aTDC]	-13		
Total Fuel Mass [mg/cycle]	~ 6	2 to 124	
Main Inj. Fuel Mass [mg/cycle]	~ 62 to 124	62	
Post Inj. Fuel Mass [mg/cycle]	0	~ 0 to 43	
Post Inj. SOI Timing [°aTDC]	N/A	6	

For the baseline strategy, which has no post-injection, the main injection duration was adjusted to achieve a load range of 4 bar to 8 bar gross IMEP. The study was then repeated with the post-injection strategy where the main injection fuel mass was fixed to achieve a load of 4 bar gross IMEP, and the post-injection duration was varied to achieve the same load range as the baseline strategy. Understandably, the post-injection strategy with premixed fuel was not explored since the study was being performed with diesel fuel. Figure D-11 shows a comparison of the soot emissions results from the baseline and the post-injection strategy of the current study and the results from the study performed by O'Connor et al. [115].

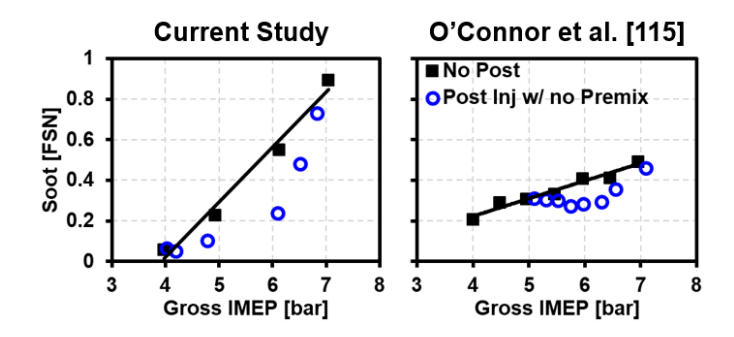


Figure D-11. Soot emissions results from the baseline and the post-injection strategy of the current study and the results seen from the study by O'Connor et al. [115].

From the results shown in Figure D-11, the current study yields similar results as seen from the original study by O' Connor et al. [115]. In both the studies, increasing load through post-injection resulted in a soot benefit initially. As the load is increased further, the soot emissions of the post-injection strategy eventually approached the soot emissions levels from the baseline strategy. The cases highlighted by the red box in Figure D-11 shall be used to understand why a soot benefit is seen from using post-injections at the low- to mid-load conditions. Figure D-12 shows the Φ and the soot mass fraction contours for the two cases highlighted in Figure D-11. Similar to the high-load cases, not having the post-injection increases the fuel mass in the main injection and therefore increases the amount of locally rich regions during combustion. This is seen from comparing the Φ contours of the two cases at 0 °aTDC and 6 °aTDC in Figure D-12. This results in increased soot emissions from the main injection fuel for the case with no post-injection. This is observed from comparing the soot mass fraction contours at 6 °aTDC between the two cases in Figure D-12. Similar to the high-load cases, due to the shape of the bowl and the spray momentum,

the majority of the main injection fuel is targeted into the squish region forming a fuel rich mixture in that region. Accordingly, the soot emissions formed from the main injection fuel also gets accumulated in the squish region. This is visible from the Φ and soot mass fraction contours for the no post-injection case at 24 °aTDC. However, for the post-injection case, the fuel from the post-injection is targeted into the bowl region. This causes the fuel from the two injections to be distributed between the bowl and the squish region. This is evident from the Φ contours at 12 °aTDC for the post-injection case, where the post-injection is targeted into the bowl region and from 12 °aTDC to 40 °aTDC the fuel from the two injection is distributed between the bowl and squish region. Since the main and the post-injection fuels are distributed between the squish and the bowl, the main injection has relatively higher oxygen availability in the squish region compared to the no post-injection case and the fuel in the post-injection that is targeted into the bowl utilizes the oxygen in the bowl that was otherwise unused. Since both the injections are getting better access to oxygen, the overall fuel mixture is better mixed in the post-injection case relative to the case without the post-injection. This was also seen in the high-load case where adding an early post-injection resulted in a better distributed and well-mixed fuel-air mixture. However, unlike the high-load case, we see that adding the post-injection results in a soot reduction here. This is because, in addition to reducing the soot emissions from the main injection, the soot formed from the post-injection also gets oxidized completely. This is seen from the soot mass fraction contours of the post-injection case in Figure D-12 at crank angle locations of 40 °aTDC to 70 °aTDC. The reason for this is the shorter injection durations of the main and the postinjection at low-load conditions. The fuel mass is relatively low compared to the high-load case. Hence, the injection duration of the post-injection (~ 3 °CA) is shorter compared to the high-load case (~ 7 °CA). Furthermore, since the main injection duration is also shorter, the post-injection is injected closer to TDC (SOI = 6 ° aTDC) relative to the high-load post-injection (SOI = 12 ° aTDC). The reduced fuel mass results in lower soot formation from the post-injection case and this reduction in soot formation combined with the early injection timing causes the soot formation to reach saturation relatively early in the cycle compared to the high-load case. This provides sufficient residence time in the high temperature regions to oxidize the soot formed from the post-injection completely.

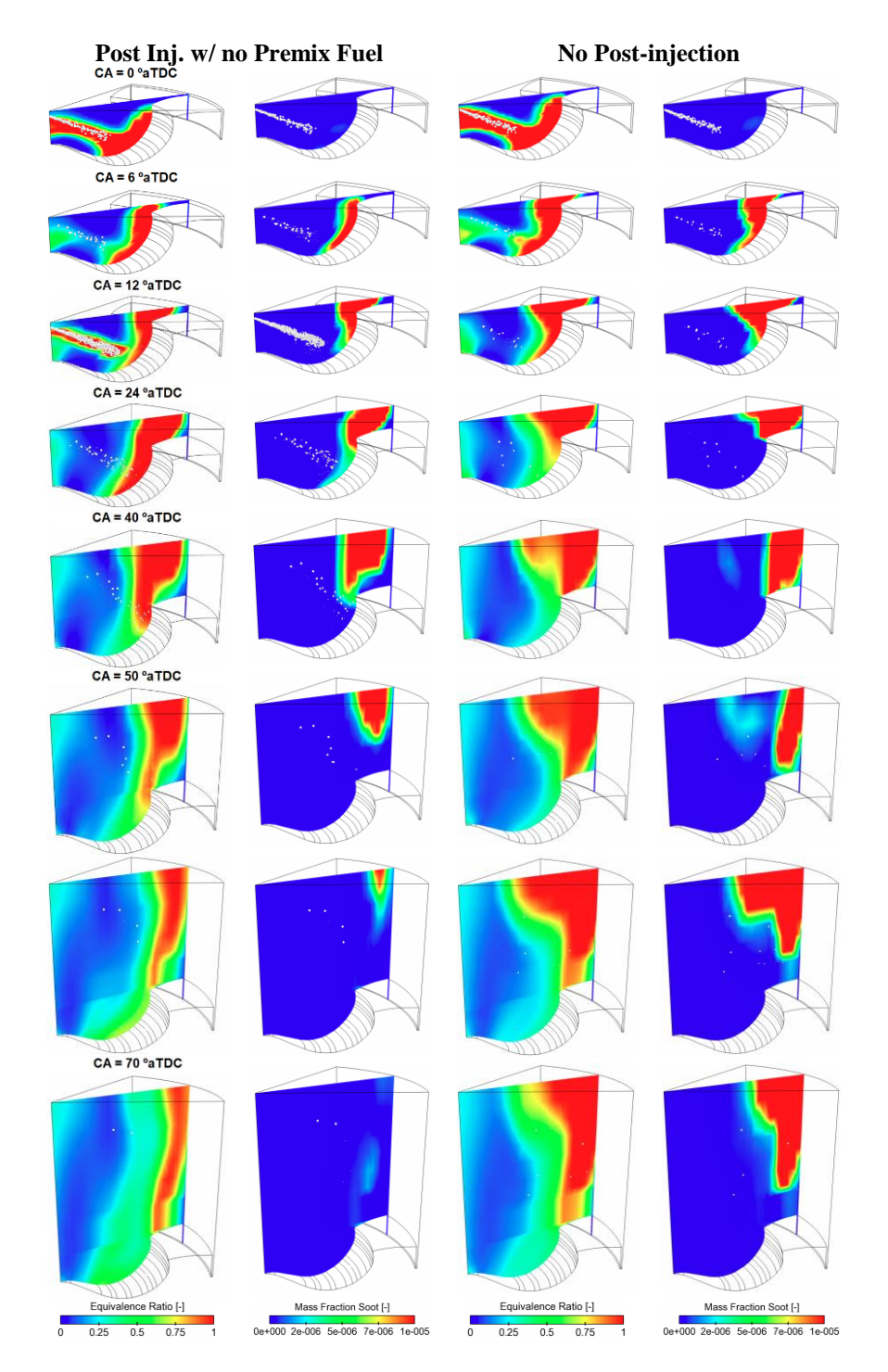


Figure D-12. Φ and soot emissions contours for the two cases highlighted in Figure D-11.

Hence, similar to the results seen in literature, using a post-injection at low- to mid-load conditions helps in reducing soot emissions. However, the reason for the soot benefit was not attributed to the enhanced mixing of main injection or the enhanced late cycle temperatures. It was found to be due to spray targeting. At low- to mid-load conditions, targeting the fuel from the post-injection at a different region in the

combustion chamber relative to the main injection provides better access to the oxygen to both the main and the post-injections. Additionally, since the duration of the main and the post-injection is shorter relative to the high-load conditions, it allows the SOI timing of the post-injection to be advanced closer to TDC without overlapping with the main injection. The combination of the advanced post-injection SOI timing and the shorter duration of the post-injection causes the fuel to be delivered sufficiently early in the cycle. All these factors combined provide an adequate residence time in the high temperature regions to oxidize the soot formed from the post-injection completely; thereby resulting in reduced soot emissions compared to the case without the post-injection.

D.3. Conclusions

In this appendix, the efficacy of post-injections under high-load operating conditions of 16 bar to 21 bar gross IMEP with GCI combustion was investigated. Results showed that minimizing the dwell time between the main and the post-injection resulted in the least soot emissions from the post-injection strategies. This is because the spray targeting allowed the fuel from the main and post-injections to be better distributed within the combustion chamber. Premixing a portion of the main injection fuel helped in further reducing the soot emissions for the post-injection cases. The well-mixed premixed fuel did not form any soot emissions and thereby reduced the soot that was otherwise being formed from the main injection. However, when compared to the soot levels from the baseline strategy which does not use a post-injection; it was found that adding the post-injection was not effective in reducing the soot emissions under high-load conditions. The reason for this is the increased fuel mass at high-load conditions, which caused the postinjection to end late in the cycle. At these late CA timings, the temperatures are rapidly decreasing, slowing the soot oxidation rates. Hence the soot formed from the post-injection was not oxidized completely. Not having the post-injection resulted in increased soot formation from the main injection, but since combustion was happening early in the cycle, the soot emissions formed have a longer residence time in the high temperature regions that favor soot oxidation. This caused most of the soot formed to be oxidized; thereby resulting in lower soot emissions than the post-injection cases.

Since these results were contrary to the results seen in literature at low to mid-load conditions, a similar study was repeated at lower load conditions of 4 bar to 8 bar gross IMEP with diesel fuel. At the low- to mid-load conditions, it was found that post-injections show a benefit in reducing soot emissions. This was because similar to the high-load conditions, targeting the fuel from the post-injection at a different region in the combustion chamber relative to the main injection provided better access to the oxygen to both the main and the post-injections. However, since the duration of the main and the post-injection is shorter relative to the high-load conditions, it allowed the SOI timing of the post-injection to be advanced closer to TDC without overlapping with the main injection. A combination of the advanced post-injection SOI timing and the shorter duration of the post-injection, caused the fuel to be delivered sufficiently early in the cycle. This provided an adequate residence time in high temperature regions to oxidize the soot formed from the post-injection completely; thereby resulting in reduced soot emissions compared to the case without the post-injection.